UNIVERSITÀ
DEGLI STUDI
FIRENZE

PhD in
EARTH SCIENCE

CYCLE XXXIII

COORDINATOR Prof. Francalanci Lorella

The contribution of Palaeomagnetism in Volcanology for dating of Holocene eruptions and estimating the emplacement temperature of pyroclastic flows.

Applications on Tenerife and El Hierro (Canary Islands) and on Volcán El Fuego (Guatemala)

Doctoral Candidate

Dr. Risica Gilda

Supervisors

Dr. Speranza Fabio
Prof. Rosi Mauro
Dr. Di Roberto Alessio

Coordinator
Prof. Francalanci Lorella

Years 2017/2020

UNIVERSITÀ
DEGLI STUDI
FIRENZE

PhD in
EARTH SCIENCE

CYCLE XXXIII

COORDINATOR Prof. Francalanci Lorella

The contribution of Palaeomagnetism in Volcanology for dating of Holocene eruptions and estimating the emplacement temperature of pyroclastic flows.

Applications on Tenerife and El Hierro (Canary Islands) and on Volcán El Fuego (Guatemala)

Doctoral Candidate

Dr. Gilda Risica

Supervisors

Dr. Fabio Speranza

Prof. Mauro Rosi

Dr. Alessio Di Roberto

Coordinator
Prof. Lorella Francalanci

Years 2017/2020

UNIVERSITÀ
DEGLI STUDI
FIRENZE

PhD in
EARTH SCIENCE

CYCLE XXXIII

Dissertation Reviewers

Prof. Michael Ort
(Northern Arizona University)

Dr. Laura Pioli
(University of Cagliari)

ABSTRACT

In this work, palaeomagnetism has been applied to get fundamental information useful to evaluate volcanic hazard in two different volcanic contexts: 1) to date the Holocene volcanic eruptions at Tenerife and El Hierro Islands (Canary Islands); 2) to estimate the emplacement temperature and investigate the origin of the pyroclastic density flows that occurred on June 2018 at Volcán El Fuego (Guatemala). Recent years, palaeomagnetism has been increasingly used in volcanology because it can provide high-quality data to reconstruct the chronology of the recent volcanism, and to estimate the emplacement temperatures of pyroclastic flows, and therefore to better understand their nature and origin.

Although the Holocene volcanism has been very intense in Tenerife and El Hierro islands, most of the eruptions have not been thoroughly studied or dated so far. Therefore, eighteen (nine for each island) poorly dated or undated volcanic eruptions have been studied: Boca Cangrejo, Montaña (Mña) Reventada, Mña Cascajo, Mña Bilma, Mña Botija, Abejera Alta, Pico Cabras and Roques Blancos eruptions in Tenerife island, and Lajal, Mña Chamuscada, Mña del Tesoro, Orchilla, Las Calcosas, Mña Negra, Cuchillo del Roque, Lomo Negro and Below Lomo Negro eruptions in El Hierro island.

Palaeomagnetic dating of lava flows in Tenerife allowed reconstructing a detailed chronology of the Holocene volcanic eruptions, showing better accuracy than other isotopic methods. A good agreement between previous and new ages was found specifically for two already dated eruptions (Boca Cangrejo and Mña Reventada), with narrower palaeomagnetic age ranges than the ones obtained by the ^{14}C technique. In another two cases (Abejera Alta and Roques Blancos eruptions) the palaeomagnetic ages are slightly different from the previous ^{14}C, instead. For the undated eruptions, much narrower age ranges were found if compared with the only stratigraphic evidence. Finally, for the Mña Grande eruption, a very high accuracy palaeomagnetic age (789-723 BC) has been obtained, adding it for the first time in the list of the Holocene eruptions. This updated chronological framework confirms the occurrence of alternating period with different eruptive frequencies, which the last 3 ka are characterized by mainly basaltic eruptions along the NE and NW rift zones.

On El Hierro island, palaeomagnetic dating, coupled with radiocarbon age determinations, showed different results: for the already dated eruption of Lomo Negro, the comparison between the new ^{14}C and palaeomagnetic ages with the previous ^{14}C dating showed a good agreement, whereas for Mña Chamuscada and Mña del Tesoro, the new ages agree with each other but they disagree with the previous ^{14}C and K/Ar ages from literature. For the undated eruptions (Orchilla, Las Calcosas, Lajal, Below Lomo Negro, Cuchillo del Roque and Mña Negra eruptions), due to the lack of previous age constraints, it was possible to define many palaeomagnetic ages; however, older ages (older than 5000 BC) can be discarded based on geomorphological features and the fresh volcanic landforms. As a whole, palaeomagnetic dating carried out on El Hierro Island indicates the occurrence of several Holocene eruptions in different sectors of the three rifts, most of which occurred probably between 2000 BC and 1600 AD.

Palaeomagnetism has been used also to estimate the emplacement temperature of pyroclastic deposits, helping to investigate the fundamental processes responsible for the generation of some type of pyroclastic density currents (PDCs). In this work, it has been applied to provide the

emplacement temperature and to unravel the origin of the explosive eruption of 3rd June 2018, at El Fuego volcano. The eruption produced convective clouds of volcanic ash and PDCs, which funnelled in the Las Lajas gorge, reached unexpected distances and caused the death of nearly two hundred people. The palaeomagnetic analyses of hand-samples and cores showed a homogeneous emplacement temperature of 220–280 °C; however, a small number of clasts recorded a very high temperature (>500 °C), whereas several clasts indicate T between 200 and 500 °C. Some cores recorded different temperatures between the outer and inner part of the same specimen; in some cases, lower temperatures were documented in the inner core section, and vice versa in other clasts. The study revealed that clasts embedded in the deposit have different thermal history and origin: those with intermediate temperatures (200-500 °C) have been interpreted as related to the still hot pyroclasts accumulated in the upper part of Las Lajas gorge, while few samples with a higher temperature (>500 °C) have been considered as "juvenile" and linked directly to the eruption of 3rd June 2018. These data, coupled by other independent evidences (the temporal gap between the most energetic phase of the eruption and the beginning of the pyroclastic flows; the appearance of a large scar at the head of Las Lajas gorge after the eruption; unburnt vegetation) and field observations of the deposits, allow interpreting the deposit as a "block-and-ash flow", produced by the gravitational collapse of unstable hot and cool volcanic materials (pyroclasts and lava flows) that were stacked on the upper segment of the Las Lajas gorge during the activity in the past years.

The results achieved in this work proved that the application of palaeomagnetism in volcanology can provide crucial information for a correct evaluation of the volcanic risk. Its application as a dating tool allowed obtaining narrower age ranges than other isotopic methods, essential for a detailed reconstruction of the recent volcanic activity of a volcano. It also showed that the use of multiple dating techniques is highly desirable. Its application to the pyroclastic flows provided not only the estimate of the emplacement temperature of the deposits but also essential data to unravel their origin. Therefore, this work shows that a more frequent use of paleomagnetism addressed to solve volcanological problems is desirable.

ABBREVIATIONS

v	volume
K_b	Boltzmann constant
T	temperature
T_b	blocking temperature
T_C	Curie Temperature
T_r	re-heating temperature
T_{emp}	Emplacement Temperature
H_c or B_c	coercive force
J_{sat}	saturation magnetization
H_{af}	alternating current
k	magnetic susceptibility
ChRM	Characteristic Remanent Magnetization
AMS	anisotropy of magnetic susceptibility
GAD	Geocentric Axial Dipole
AF	alternating field demagnetization
TH	thermal demagnetization
NRM	Natural Remanent Magnetization
TRM	Thermal Remanent Magnetization
DRM	Detrital Remanent Magnetization
pDRM	post-depositional Detrital Remanent Magnetization
CRM	Chemical Remanent Magnetization
VRM	Viscous Remanent Magnetization
IRM	Isothermal Remanent Magnetization
ARM	Anhysteretic Remanent Magnetization
PCA	Principal Component analysis
MAD	maximum angular deviation
SV	Secular Variation
PSV	Palaeo Secular Variation
HT	High-Temperature component
LT	Low-Temperature component
SQUID	Superconductive Quantum Interference Device
PDC	Pyroclastic density current

LIST OF FIGURES

PART I

Fig. 2.20 Overview of geomagnetic field models and dipole reconstructions for historical times through to 50 ka (from *Korte et al., 2019*). Model references: GEOMAGIA VADM (*Knudsen et al., 2008*); MS1982 (*McElhinny and Senanayake, 1982*); SHA.DIF.14k (*Pavón-Carrasco et al., 2014*); YOS2000 (*Yang et al., 2000*); HFMx, and HFM.OL1.A1 *(Panovska et al., 2015; Constable et al., 2016*); CALS10k.x (*Korte et al., 2011; Constable et al., 2016*); OH1993 (*Ohno and Hamano, 1993*); OH1992 (*Ohno and Hamano, 1992);* pfm9k.1, pfm9k.1a, and pfm9k.1b (*Nilsson et al., 2014*); DE_FNB, DE_FNBK, and DE_FNBKE (*Nilsson et al., 2010, 2011*); SCHA.DIF.8k (*Pavón-Carrasco et al., 2010*); ArcheoInt VADM (*Genevey et al., 2008*); ARCH-UK.1 (*Batt et al., 2017*); CALS7k.2 (*Korte and Constable, 2005*); SCHA.- DIF.3k (*Pavón-Carrasco et al., 2009*); CALS3k.x, ARCH3k.1, and SED3k.1 (*Korte and Constable, 2003, 2011, 2005; Korte et al., 2009*); COV-ARCH and COV-LAKE (*Hellio and Gillet, 2018*); AmR (*Sanchez et al., 2016*); A_FM, ASD_FM, and ASDI_FM (*Licht et al., 2013*); CJL2000 (*Constable et al., 2000*); VHLP2008 *(Valet et al., 2008*); GMADE2K.1 (*Lodge and Holme, 2009*); SCHA.DI.00-F (*Pavón-Carrasco et al., 2008a*); SCHA.DI.00 (*Pavón-Carrasco et l., 2008b*); HHK1998 (*Hongre et al., 1998*); gufm1 (*Jackson et al., 2000*).

Fig. 2.21 Declination, inclination and intensity values for the last 14 ka at Tenerife (Canary Islands), according to SHA.DIF.14K model (*Pavón-Carrasco et al., 2014*).

Fig. 2.22 Spatial and time distribution of palaeomagnetic data (declination, inclination and intensity) used to construct the SHA.DIF.14K model (from *Pavón-Carrasco et al., 2014*).

Fig. 2.23 Schematic model of palaeomagnetic categories and emplacement temperature (from *Porreca et al., 2008*). H is magnetic field. T_e is the deposit temperature. a) $T_e > T_c$ and clasts carry only 1 component, oriented along the magnetic field during the cooling; b) clast are reworked at ambient temperature (T_e=30 °C), then they record the first magnetic orientation, even if H is changed; c) clasts are reworked at intermediate temperature (T_e=350 °C), and then they have two magnetic components, HT (from 590° to 350 °C), representing the first component randomly oriented, and LT (from 350 °C to ambient temperature) oriented along H; d) clasts have two magnetic components, both randomly oriented.

Fig. 2.24 Deposit age plotted versus minimum paleomagnetic emplacement temperature as predicted by viscous magnetization theory for hematite, magnetite and titanomagnetite series (TM10–TM60) (from *Paterson et al., 2010).*

Fig. 2.25 Palaeomagnetic emplacement temperature versus directly measured emplacement temperature for the 1980 pyroclastic deposits at Mt. St. Helens, USA (from *Paterson et al., 2010*), and El Chichón (*Sulpizio et al. 2008*).

Fig. 2.26 Estimate of the T_{emp} of the Colli Albani phreatomagmatic deposit determined by the main overlap of individual clasts (from *Trolese et al., 2017*).

Fig. 3.1 a) and b) Palaeomagnetic sampling using a water-cooled, petrol-fuelled drill; c) hand-sampling of small pieces of rock embedded in a pyroclastic flow; d) Sun and magnetic compasses used to orient cores before the extraction; e) example of cores cut in a, b and c specimens; f) detail of a single core.

Fig. 3.2 Schematic representation of alternating-field demagnetization (from *Butler, 2004)*, with (a) generalized waveform of the magnetic field; H_{AF} represents the peak field. (b) Detailed examination of a portion of the AF demagnetization waveform.

Fig. 3.3 Construction of a vector component diagram, and equal-area projection (modified from *Butler, 2004*). a) and b) represent the projection of the NRM vector into the horizontal and vertical planes oriented north-south, respectively. c) combined horizontal and vertical projections in a single diagram. Black and white squares represent declination and inclination data, respectively. The scale on the axes is A/m. d) Equal-area projection of the direction of NRM. e) NRM intensity versus demagnetization level.

PART II

Fig. 4.51 a) Equal-area projection (lower hemisphere) of ChRMs, site-mean and flow-mean palaeomagnetic directions for all studied eruptions. The ellipses around the palaeomagnetic directions are the projections of the relative α_{95} cones. D, declination; I, inclination, α_{95}; statistical parameter. Red dots indicate the palaeomagnetic directions sampled by *Villasante-Marcos and Pavón-Carrasco (2014).* b) Equal-area projection (lower hemisphere) of site-mean palaeomagnetic directions for Lomo Negro eruption, including palaeomagnetic sites of *Villasante-Marcos and Pavón-Carrasco (2014)* (VPLN). Site-mean represents the mean palaeomagnetic direction obtained averaging all sites.

Fig. 4.52 Equal-area projection (lower hemisphere) of lava flow-mean palaeomagnetic directions from El Hierro. The ellipses around the palaeomagnetic directions are the projections of the relative α_{95} cones.

Fig. 4.53 Palaeomagnetic dating of Lajal, Mña Chamuscada, Orchilla and Cuchillo del Roque eruptions, according to the method and software by *Pavón-Carrasco et al. (2011*), and the PSV reference model by *Pavón-Carrasco et al. (2014).* Left-hand panel shows the PSV curves (red lines) for the declination and right-hand panel for the inclination (thin red lines for the associated errors, 95% confidence level), together with the probability density curves (in grey-shade). Palaeomagnetic declination and inclination values are shown in blue straight lines; the 95% associated errors are in green straight lines. In the probability density graphs the 95% confidence level is shown as a green line.

Fig. 4.54 a) Comparison of palaeomagnetically-inferred ages vs. literature stratigraphic/isotopic ages relative to the studied eruptions. b) Same diagram as in A) but with only the most probable ages for each eruption. Dashed red boxes and black arrows indicate previous isotopic dating and stratigraphic constraints, respectively. Green boxes are ^{14}C ages from this work.

Fig. 4.55 Eruptions occurred in the last 5 ka at the Canary Islands (ages of previously dated eruptions are according to *Carracedo et al., 2007* and *Carracedo and Troll, 2013* for Tenerife; *Global Volcanism Program* and *Troll and Carracedo, 2016* for La Palma; *Rodriguez-Gonzales et al., 2018* for Gran Canaria; *Global Volcanism Program* for Lanzarote).

PART III

Fig. 5.1 Volcanological framework of Central America from *Carr et al. (2007).* CM is Cerro Mercedes, AZ is Aguas Zarcas, GU is Guayacán and TO is Tortugero. Red circle indicated the position of El Fuego volcano.

Fig. 5.2 a) Fuego and nearby volcanoes (from GeoMapApp 3.6.1). Colours represent meters above and under sea level. Red and blue lines indicate the Central American volcanic arc (CAVA) and Fuego-Acatenango trends, respectively. b) Schematic illustration of the Fuego-Acatenango massif showing the main vents. (modified from *Basset, 1996*). Plumes indicate vents active in historic time.

Fig. 5.3 Total alkali-silica (TAS) rock classification diagram with pre-1999 and 1999–2013 rock compositions of Fuego magmas (from *Escobar-Wolf, 2013)*. 1999–2013 rock compositions are published by Berlo et al. (2012); pre-1999 whole-rock compositions are from the RU_CAGeochem database (http://www.iedadata.org/doi?id=100263).

Fig. 5.4 Photo of Las Lajas gorge after the 3rd June 2018 eruption (from https://medium.com/@UNDP/volc%C3%A1n-de-fuego-inside-the-emergency-response-e0f280834eff).

Fig. 5.5 The Visible Infrared Imaging Radiometer Suite (VIIRS) on Suomi NPP acquired this image of the ash plume at 1 p.m. local time (19:00 UT) on June 3, 2018, after the ash (brown) had

LIST OF TABLES

PART II

PART III

PART I

1 Introduction and Thesis organization

1.1 *Objectives and main goals*

Volcanic eruptions are one of the most beautiful natural phenomena but, at the same time, hazardous on Earth. Whether they are low energy effusive or more energetic explosive eruptions, they can affect several tens of square kilometres, and in inhabited areas can cause destruction and, in some cases, also death.

One of the principal purposes for volcanologists is to mitigate volcanic hazard by formulating, on a probabilistic base, the more likely scenarios for future eruptions; this should allow reducing the threatened population to minimum values. The volcanic hazard is closely connected with the type of volcano, time since the last eruption and geographical location (*Sigurdsson et al., 2015).* Therefore, it is extremely important to improve the quality of available data such as high-resolution stratigraphy calibrated by isotopic age determinations, and geophysical data associated with volcano monitoring.

Palaeomagnetism is a branch of geophysics increasingly applied during the recent years in volcanology. It can be used for different goals, such as to correlate and to date volcanic eruptions, to estimate the emplacement temperature of pyroclastic deposits, to infer eruptive source locations and to estimate flow fabric.

This work is aimed at using palaeomagnetism in two different volcanic areas and with two different purposes: 1) to date the Holocene effusive volcanic eruptions at Tenerife and El Hierro Islands (Canary Islands); and 2) to estimate the emplacement temperature and investigate the origin of pyroclastic flows occurred on June 2018 at Volcán El Fuego (Guatemala).

1) the first goal concerns the application of palaeomagnetism to date volcanic units. At Tenerife and El Hierro islands, Holocene effusive volcanism has been very intense; nevertheless, several Holocene eruptions have not been thoroughly studied or dated so far, even if they occurred in currently densely populates areas. The knowledge deriving from the study of volcanic records considerably increases the possibility to understand how active volcanic systems work and to elaborate more realistic future eruptive scenarios, including eruption type, intensity and frequency, and might document eruptive pattern behaviour such

as episodic eruptions, eruptive cycles or time/space eruptions clustering. Therefore, it is of primary importance to study and assess the recent volcanic history, including accurate ages of eruptions. The "palaeomagnetic dating method" relies upon the comparison between magnetic directions recorded by rocks during their emplacement with the expected directional values from reference Palaeo-Secular Variation curves (PSV), i.e. the directional variation of the geomagnetic field along time. To this respect, eighteen poorly dated and undated volcanic eruptions (nine for each island) were studied.

2) The second goal of the research is to provide the emplacement temperature of the pyroclastic flows from the explosive eruption of 3rd June 2018 at El Fuego volcano (Guatemala). El Fuego is one of the most active volcanoes of Guatemala, located in a densely inhabited area close to Antigua city, producing both effusive and explosive eruptions. On June 3rd, 2018, an explosive volcanic eruption occurred, generating a convective column of volcanic ash and lapilli and pyroclastic density currents (PDCs) and lahars that left almost no evacuation time, burying an entire village and causing the death of nearly two hundred people. The mechanism of PDC formation at El Fuego has not yet clearly understood. Palaeomagnetism can provide fundamental information, determining the emplacement temperature of pyroclastic density currents, useful to understand the mechanism from which they originated.

1.2 Thesis organization

The research presented here is divided into four Parts and six Chapters.

Part I includes three chapters in which theory, techniques and applications of palaeomagnetism in volcanology are presented. In particular: *Chapter 1* contains a brief introduction to the aim of this research and the thesis organization; in *Chapter 2,* an overview of the application of palaeomagnetism in Volcanology is presented, including basic concepts (*Chapter 2.1*) and the two applications in this research, i.e. palaeomagnetic dating, with an overview of the principles and the main pros and cons of this technique (*Chapter 2.2*), and the palaeomagnetic estimate of pyroclastic flow emplacement temperature (*Chapter 2.3*). In *Chapter 3*, a synthetic description of the sampling techniques (*Chapter 3.1*) and the palaeomagnetic instruments (*Chapter 3.2*) used in this work is shown.

Part II (*Chapter 4*) is focused on the palaeomagnetic dating of Holocene eruptions from the Canary Islands. *Chapter 4* is divided into four sub-chapters: *Chapter 4.1* shows a synthetic

overview of the geological setting of the Canary Islands; *Chapter 4.2* includes the palaeomagnetic dating of Holocene eruptions in Tenerife Island; *Chapter 4.3* is devoted to the palaeomagnetic dating of Holocene eruptions at El Hierro. Finally, *Chapter 4.4* is dedicated to an overview of the Holocene volcanic activity at the Canary Islands integrated with the new data provided by this work.

Part III contains *Chapter 5*, in which the palaeomagnetic estimate of the emplacement temperature of pyroclastic flows produced by El Fuego volcano (Guatemala) is presented.

Finally, in Part IV the main results of this thesis and the conclusive remarks are summarized in *Chapter 6.*

Parts of this thesis are published in two papers:

Risica, G., Di Roberto, A., Speranza, F., Del Carlo, P., Pompilio, M., Meletlidis, S., Rosi, M. (2020). Refining the Holocene eruptive activity at Tenerife (Canary Islands): the contribution of palaeomagnetism. *J. Volcanol. Geotherm. Res*. 401, 106930. https://doi.org/10.1016/j.jvolgeores.2020.106930

Di Roberto, A., Risica, G., Del Carlo, P., Pompilio, M., Speranza, F., Meletlidis, S., (2020). The forgotten eruption: the basaltic volcano of Montaña Grande, Tenerife. *J. Volcanol. Geotherm. Res*., 401, 106918. https://doi.org/10.1016/j.jvolgeores.2020.106918

2 Palaeomagnetism in Volcanology

2.1 Introduction to Palaeomagnetism

Palaeomagnetism (*Tarling, 1983; Tauxe, 1998; 2009; Butler, 2004*) is a branch of geophysics that studies the magnetic properties of rocks and the geomagnetic field behaviour over geological time. The applications of this discipline were multiple: in tectonics (e.g., *Torsvik et al., 2008*); in magnetostratigraphy and biostratigraphy (e.g., *Opdyke and Channell, 1996*); in the study of the physics of the Earth's interior (e.g., *Christensen and Wicht, 2007*), and recently in the study of the magnetic properties of atmospheric fine particles (PM10) (*Hofman et al., 2017; Winkler et al., 2019*). In volcanology (*Ort et al., 2015a*), palaeomagnetic and rock magnetic techniques have been applied to solve different problems, such as to estimate flow fabrics and source location using the anisotropy of magnetic susceptibility - AMS (e.g. *Ellwood, 1982; Cagnoli and Tarling, 1997; Ort et al., 1999, 2003; Giordano et al., 2008; Pioli et al., 2008; Ort et al., 2015b*); to estimate the emplacement temperature of pyroclastics deposits (e.g. *Aramaki and Akimoto, 1957; McClelland et al., 2004; Zanella et al., 2008*) and to date and correlate volcanic deposits using the palaeo-secular variation (PSV) of the geomagnetic field (e.g. *Holcomb et al., 1986; Hagstrum and Champion, 1994*; *Speranza et al., 2010; Mahgoub et al., 2017*). The last two applications are the subject of this study and will be analysed in detail in Chapter 2.

More than 90% of the Earth's geomagnetic field is generated by fluido-dynamic mechanisms taking place into the external fluid core of Earth and it can be related, in a first approximation, to a dipolar field (93%), resulting from an internal source (the dynamo in Earth's core-mantle). Other field sources (fields due to electric currents in the ionosphere and to crustal magnetic bodies) are subordinate. The simplest field model used in palaeomagnetism is the *Geocentric Axial Dipole* (GAD) model that considers the magnetic field produced by a single magnetic dipole aligned with the Earth's axis. According to this assumption, declination would be zero across the Earth's surface, whereas inclination (I) and field intensity are related to the latitude λ and the radius by:

$$\tan I = 2 \tan \lambda$$

Inclination is considered positive when pointing downward in the northern hemisphere and negative when pointing upward in the southern hemisphere (with zero inclination along the equator, I increases in absolute values toward the poles).

The field intensity (F) can be calculated using the relation between the dipole moment (M) of the geocentric axial dipole, λ and r_e (the mean Earth radius)

$$F = \frac{M}{re^3}\sqrt{1 + 3sin^2\lambda}$$

It is minimum at the equator (~30,000 nT) and increases toward the poles (~60,000 nT).

The magnetic poles do not correspond to the geographic pole and the magnetic equator swings around the geographic equator. For this reason, a better field description is the incline *geocentric dipole model*, in which the magnetic dipole is tilted by 11.5° (Fig. 2.1; *Butler, 2004*).

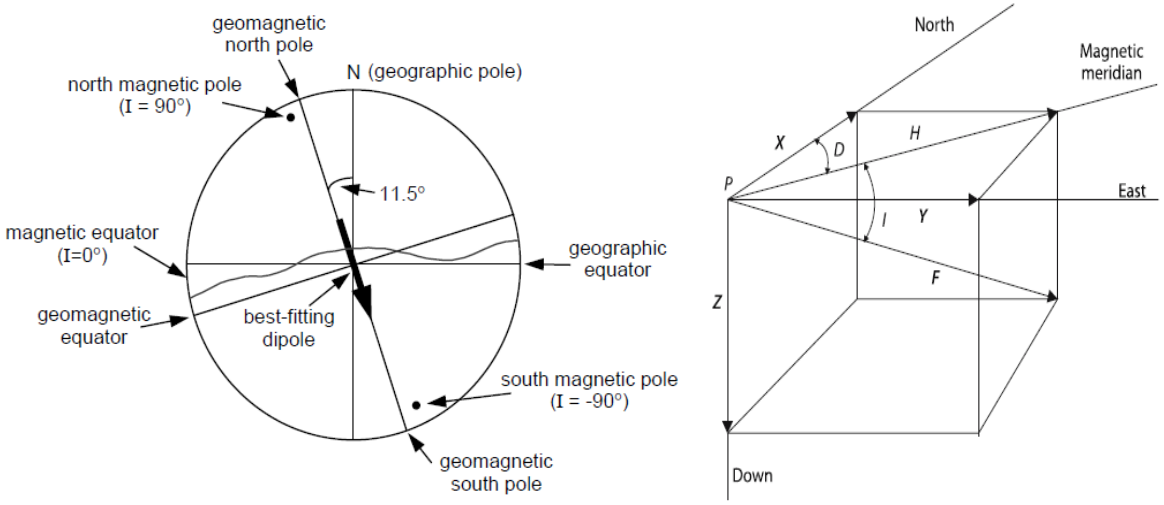

Fig. 2.1 Inclined Geocentric dipole model (*Butler, 2004*) and principal directions parameters (*Lanza and Meloni, 2006*).

The geomagnetic field is subject to variations in different timescales produced by transient changes or field interferences. Based on their origin, these variations can be divided into two principal groups (*Lanza and Meloni, 2006*):

1) internal origin, deriving from convective fluid motions within the external core and with periods between 1 yr and 10^5 yr. These variations constitute the *geomagnetic secular variation (SV)* that is called palaeo-secular variation *(PSV*) when is revealed by palaeomagnetism for periods older than the last 500 years, characterized by direct field observations: it concerns

both changes of the non-dipole field (dominating the shorter periods), and changes of the dipolar field (with longer periods). One of the most evident characteristics of these variations is the westward drift, i.e. a longitudinal shift toward the west (*Butler, 2004*). Considering longer time scales, another phenomenon is the *polarity inversion* or *geomagnetic reversal*. The present configuration is a normal polarity, with the field force lines point towards the geographic north; the last magnetic reversal occurred 778 ka ago and is called Brunhes-Matuyama reversal (*Doell and Dalrymple, 1966*);

2) external origin, generated by interactions with solar activity and characterized by short-lived variations (daily or less; *Butler, 2004*).

The magnetic field (H) is defined through a vector in which the directional parameters are D and I (Fig. 2.1): D represents the *declination*, i.e. the angle between the geographic north and the horizontal component, ranging from 0° to 360°, considered positive clockwise; I represents the inclination, i.e. the angle between the magnetic field and a horizontal plane, ranging from –90° to +90° and considered positive downward (*Butler, 2004*).

Rocks are composed of an aggregation of minerals, some of which can be able to record the magnetic characteristics of the geomagnetic field. Two types of magnetization exist: *induced* and *remanent* magnetization. The first is recorded when a material is exposed to a magnetic field and acquires an induced magnetization (*J)*, that is related to the *magnetic susceptibility* χ, according to:

$$J = \chi H$$

Typically, the action of the geomagnetic field causes the induced magnetization. Besides, rocks may also record a remanent magnetization that represents the record of the past magnetic field, active during the rock formation. The capability of a rock to record and preserve a remanent magnetization depends on the magnetic properties of minerals, and for this reason, they can be divided into three groups (*Butler, 2004*):

1) *diamagnetic minerals*, when they acquire only a little induced magnetization, opposite to the applied field, and drops to zero when the field is removed. Common diamagnetic minerals are calcite, dolomite and quartz.

2) *paramagnetic minerals*, when they acquire an induced magnetization, parallel to the applied magnetic field, but it is reduced to zero when field is removed. Examples of paramagnetic minerals are biotite, pyroxene and amphibole.

3) *ferromagnetic minerals,* characterized by the ability to record the remanent magnetization that persists beyond the removal of the magnetic field.

Ferromagnetic minerals are organized in magnetic structures with little volumes called *domain*. Each domain, according to the Néel relaxing theory (*1949*), acquires a magnetization parallel to the external magnetic field direction in a defined time called *the relaxing time*. It is related to the volume (v) of single domain grain, the Boltzmann constant (K_b), the absolute temperature (T), the coercive force (H_c o B_c) in each single domain grain and the saturation magnetization (J_{sat}) of the ferromagnetic material:

$$\tau = \frac{1}{C} e^{\frac{vHcJsat}{2KbT}}$$

It can be also defined as the needed time to reduce the magnetization to 1/e of the initial value. Therefore, the ability of the rocks to record a stable remanent magnetization depends on the relaxing time, deriving in turn by temperature and volume of magnetic grains (*Butler, 2004; Tauxe, 2009*).

Based on the granulometry, magnetic minerals are distinguished in grains with *single domain (SD)* and *multiple domain (MD)* (Fig. 2.2). The transition between these two categories depends on the shape and the saturation magnetization. Between these two main groups, another intermediate class exists called *pseudo-single domain (PSD).* The magnetic grains size is important because if grains are too small, they behave as superparamagnetic minerals, i.e. they have ferromagnetic characteristics but lose the magnetization before it can be measured. The efficient carriers of magnetization are mostly the SD grains, because they can preserve the magnetization over geological times. On the base of the arrangement of the magnetic domains, ferromagnetic minerals are distinguished also in: 1) *ferromagnetic s.s.*, characterized by magnetic moments parallel and adjacent; 2) *antiferromagnetic*, when magnetic moments are equal but opposite; 3) *ferrimagnetic,* when the magnetic moments are unequal and antiparallel.

Each magnetic mineral has a blocking Temperature (T_b) (Fig. 2.3), i.e. the temperature at which minerals lose the remanent magnetization and below which they preserve it. Increasing the temperature, the mineral remanent magnetization decreases until the *Curie Temperature (T_C) (*or *Néel Temperature* for the antiferromagnetic minerals*)* after which the minerals lose completely the remanent magnetization and assume a paramagnetic behaviour.

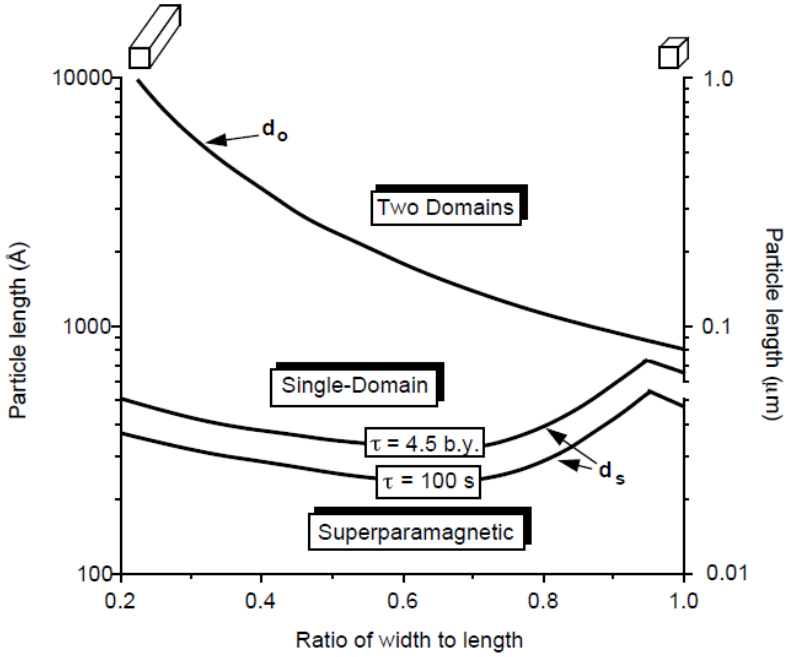

Fig. 2.2 Example of size and shape ranges of single-domain, superparamagnetic, and two-domain configurations for magnetite at 290° K. d_0 is the single-domain threshold grain size; d_s is the size and shape distribution of grains that have t = 4.5 b.yr and t = 100 s. Å, angstroms; µm, microns (from *Butler, 2004* and reference therein).

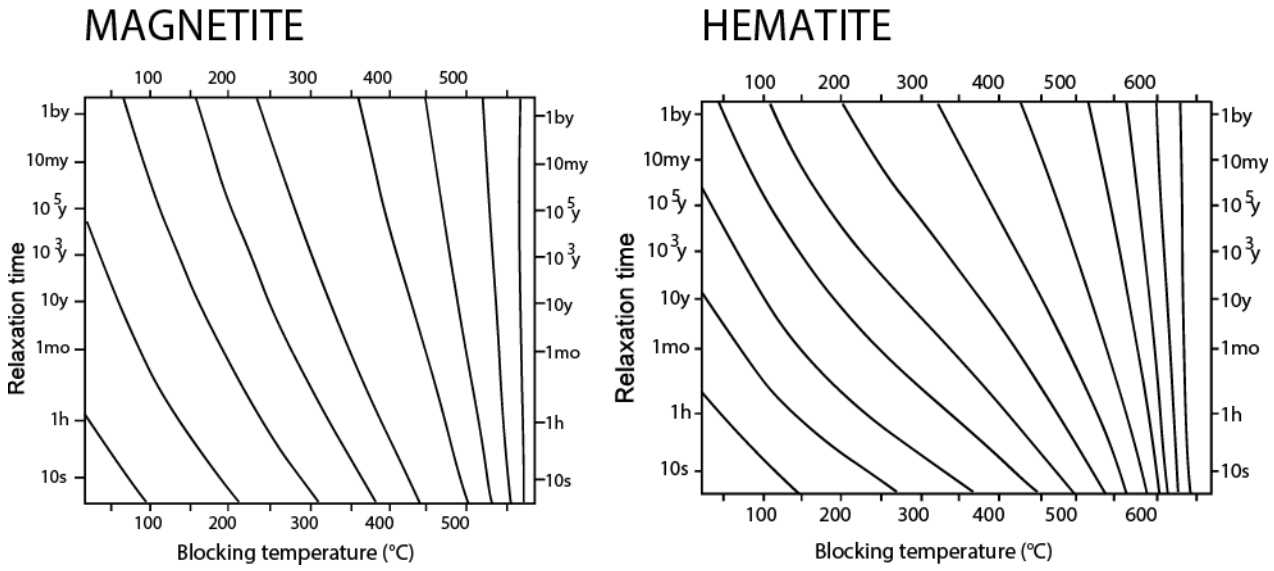

Fig. 2.3 Nomograms (*Pullaiah et al., 1975*) for magnetite and hematite (modified from *Butler, 2004*). Lines connect combined temperature and relaxing time conditions.

The most important ferromagnetic minerals are the iron-titanium (Fe-Ti) oxides, which crystallize in igneous rocks. When the T is above 980 °C, the iron oxides are in solid solution with the titanium oxides, forming two main solid solution series: *titanomagnetites and titanohematites* (Fig. 2.4a). The composition depends on the oxygen fugacity: titanomagnetites are the most frequent in the basic and ultra-basic rocks, whereas ilmeno-hematites are common in acid rocks. One of the most important minerals is magnetite (Fe_3O_4): it has strong ferrimagnetic characteristics, with a T_c of 578 °C. Its coercive force changes with size, up to a 0.2 T. When the Ti content increases in the solid solutions, the T_c typically decreases (Fig. 2.4b). Another important magnetic mineral is *hematite* (Fe_2O_3), a canted antiferromagnetic mineral produced by the alteration of the magnetite but is also possible to find it in an oxidizing environment. Its Néel Temperature is 680 °C, and its coercive force strongly depends on the grain size, up to 3.5-6.5 T for the SD grain. Also in this case, in the solid solutions with ilmenite, when the Ti content increases, the Néel temperature decreases. Unstable iron oxide is *maghemite* (γFe_2O_3), produced by the oxidation of magnetite at low temperature. Its characteristics are similar to those of magnetites, and its T_C is not well defined, in a range between 590-675 °C. Among iron hydroxides, only *goethite* (α-FeO*OH) has noticeable properties for palaeomagnetism. It is antiferromagnetic, but, it commonly displays weak ferromagnetism. Its Néel temperature is 120 °C. Finally, another important group of magnetic minerals are *iron sulphides* (the general formula is FeS_{1+x}), from pyrite (FeS_2) to troilite (FeS). *Pyrrhotite* is a ferrimagnetic mineral, common in basic igneous rocks, whose T_c is 320 °C. *Greigite* is another iron sulphide mineral, common in lacustrine sediments.

The *Natural Remanent Magnetization (NRM)* is the magnetization acquired by rocks when an external magnetic field (i.e. geomagnetic field) acts, and present in rock samples before laboratory treatments. It is a vector sum of more components, hopefully, one of which is the primary NRM, acquired during the rock formation (consolidation, diagenesis, cooling, etc). In this process, the assumption is that the original magnetization is parallel to the local Earth's magnetic field at the time of the rock formation. However, a *secondary NRM* can be acquired by rocks after their formation and in some cases, it can obliterate the primary magnetization completely.

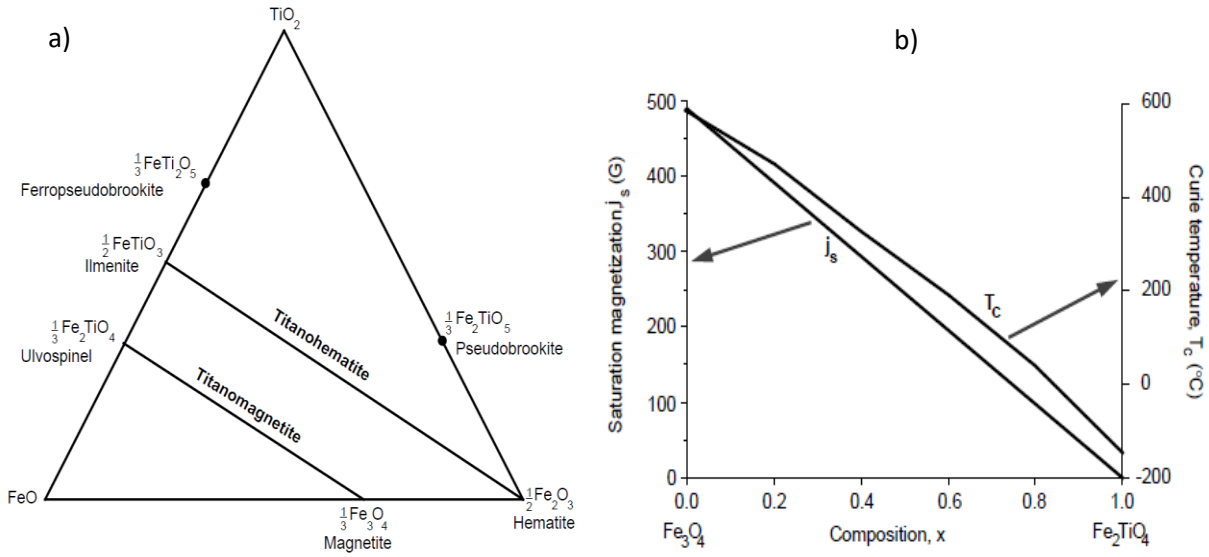

Fig. 2.4 a) TiO_2–FeO–Fe_2O_3 ternary diagram, in which titanomagnetites and titanohematites solid solution series are shown; b) Saturation magnetization (j_s) and Curie temperature (T_c) for titanomagnetite series (from *Butler, 2004)*.

Rocks can acquire the primary NRM in three main ways:

1) *Thermo-Remanent Magnetization* (TRM) is acquired by rocks during their cooling. From high temperatures above the T_c, minerals change from paramagnetic to ferromagnetic behaviour. The magnetization is acquired step by step while temperature goes below the T_b of different magnetic minerals. According to the relaxing time, the temperature decreases while the volume remains constant, and τ increases, recording the field palaeo-direction.

2) *Detrital Remanent Magnetization* (DRM) is acquired typically by sediments during the deposition and sedimentation, with the accumulation of magnetic minerals. According to the classic model, a ferromagnetic particle is aligned along the local magnetic field direction at the moment it encounters the sediment/water interface. Another DRM can form when diagenesis occurs (in this case it is called post-depositional detrital remanent magnetization-pDRM).

3) *Chemical Remanent Magnetization* (CRM) is acquired by rocks during the formation of magnetic minerals or with alteration of pre-existent magnetic minerals, with chemical alteration, recrystallization and/or T, P pH variations.

There are also other types of remanent magnetization: *Viscous Remanent Magnetization* (VRM), and *Isothermal Remanent Magnetization* (IRM). The first is acquired by rocks slowly

and continuously without T variations and under the constant action of the geomagnetic field. The latter is recorded when a strong magnetic field (much stronger than the Earth's field) is applied in a short time (for example by lightning). Both should be detected and rejected.

2.2 Palaeosecular variation (PSV) of the geomagnetic field as dating and correlating tool

As introduced in 2.1 paragraph, the *Secular Variation* (SV) of the geomagnetic field is due to internal core origin phenomena (*Korte et al., 2011; Finlay, 2012*), with periods changing from 1 to 10^5 yrs. Both magnetic direction and intensity of the dipole change over time. Although the intensity values can also be used as a dating and correlating tool, in this work I studied only the directional parameters.

The directional changes of the geomagnetic field are, in some cases, significant: in Fig. 2.5, it is possible to note that, as in London, the geomagnetic field directions changed considerably in only three centuries (from 1600 to 1950), up to 30° in declination (from 10°E to 25°W) and 10° in inclination (from 76° to 66°).

In the last four hundred years, the SV of the geomagnetic field has been studied with direct measurements of the magnetic field, in geomagnetic observatories and with scattered observations over the globe. For older ages, *palaeo-secular variation* (PSV) curves have been reconstructed using archaeomagnetic and palaeomagnetic data: archaeomagnetic data are palaeomagnetic data derived from archaeological finds (for examples terracotta and furnaces), in which their remanence is recorded commonly as a TRM; palaeomagnetic data originated from both volcanic rocks of well-dated eruptions or occurred in historical periods (their remanence is a TRM), and lake sediments and sedimentary rocks, which recorded the magnetization as a DRM (in some cases accurate ages can be obtained from lacustrine varves, *Lund and Barnerjee, 1985*).

Since 1910 and 1925 with *David's and Chevallier's* works (*David, 1910; Chevallier, 1925*), it was demonstrated that lavas can record the palaeo-directions of Earth's magnetic field: while the Earth's geomagnetic field changes its magnetic characteristics over time with a directional change rate of few degrees per century, lavas cooling down record an instantaneous snapshot of the geomagnetic field direction. For this reason, lavas have been used as dating and correlating tools (*Rutten & Wensink, 1960; Thompson & Turner, 1985; Rolph et al., 1987;*

Hagstrum & Champion, 1994; Ort et al., 1999; Carlut et al., 2000; Tanguy et al., 2003; Lanza et al., 2005a; Lanza and Zanella, 2006; Speranza et al., 2008; 2012; Vezzoli et al., 2009; Risica et al., 2019; among many others).

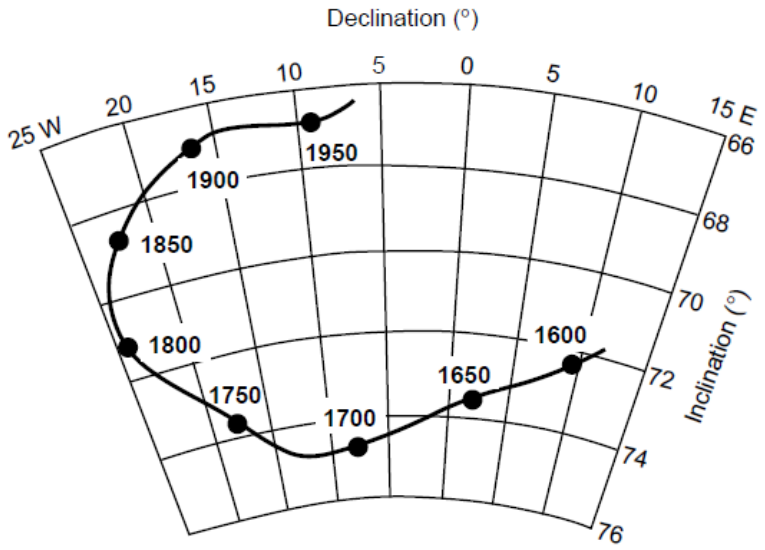

Fig. 2.5 Historic record of the geomagnetic field direction in England from 1600 to 1950 AD (from *Butler, 2004*).

Palaeomagnetic dating is obtained by comparing the palaeomagnetic directions "frozen" in volcanic rocks with independently built palaeosecular variation (PSV) reference curves. Since the non-dipole component of the geomagnetic field is not negligible, the SV shows similar directional characteristics over subcontinental regions, but displays different patterns when two continents are compared. For this reason, it is necessary to have a detailed reference PSV curve for the region where the sampled area is located (Fig. 2.6; *Merrill et al., 1996*).

The VGP method (*Noel and Batt, 1990*) is commonly used to relocate remanence vectors in subcontinental regions; nevertheless, due to the not completely dipolar nature of the geomagnetic field, data relocation can introduce small direction errors. *Lanza et al. (2005a)* demonstrated that the relocation of data by the pole method introduces small errors (1°-3°) for small distances (for example relocation from France to Italy, ~1100 km). Conversely, *Casas and Incoronato (2007)* argued that error for the present geomagnetic field increases linearly with the relocation distance (with a maximum of 7° for a 1700 km radius). Later, *Pavón-Carrasco and Villasante-Marcos (2010)*, investigating the relocation error from Madrid to the

Canary Islands, concluded that the error is generally smaller than the statistical errors affecting the palaeomagnetic directions themselves. This source of bias is eliminated when global models are used: temporally continuous global magnetic field models include the dipole and non-dipole fields and provide secular variation curves for any location on Earth (*Korte et al., 2019*).

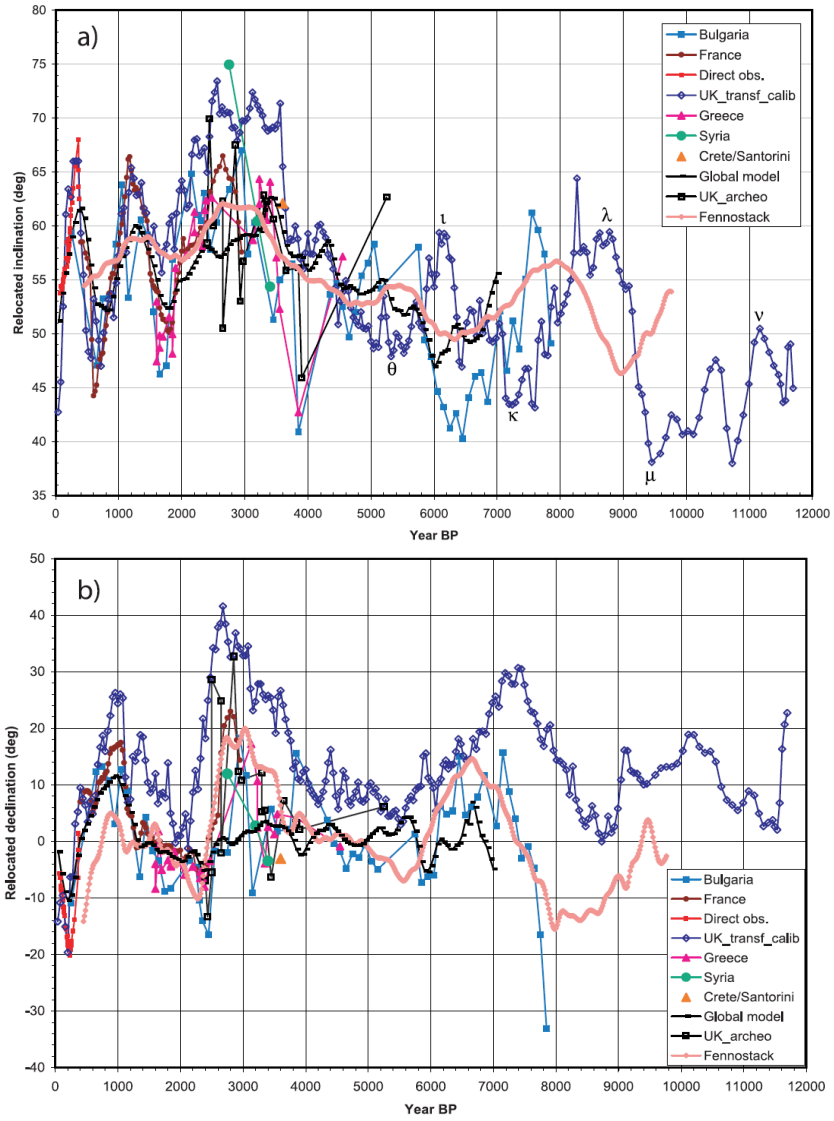

Fig. 2.6 Reference (a) inclination and (b) declination values from various PSV data sets, relocated by VGP method to Stromboli, Italy (from *Speranza et al., 2008*).

Approximately one hundred palaeomagnetic dating and correlating papers (to the best of my research) were carried out in the last century, of which 70% of them, with an average of 3-4 papers per year, were published in the last twenty years (Fig. 2.7). The palaeomagnetic dating tool has been applied on different volcanoes around the world in: Italy (Etna, *Tanguy et al., 1985*; 2003; *Rolph and Shaw, 1986; Rolph et al 1987*; *Incoronato et al., 2002; Speranza*

et al., 2006; Branca et al., 2019; Vulcano*, Zanella et al., 2001; Lanza and Zanella, 2003, 2006; Arrighi et al., 2006; Gurioli et al., 2012;* Stromboli*, Arrighi et al., 2004; 2005; Speranza et al., 2004, 2005, 2008; Risica et al., 2019;* Ischia island*, Incoronato et al., 2002; Tanguy et al., 2003; Vezzoli et al., 2009;* Vesuvius*, Hoye, 1981; Incoronato et al., 2002; Tanguy et al., 2003; Principe et al., 2004; Conte et al., 2006a, b;* Pantelleria*, Speranza et al., 2010*); Azores (*Di Chiara et al., 2012, 2014);* Canary Islands (*Soler et al., 1984; Pavón-Carrasco and Villasante-Marcos, 2010; Villasante-Marcos and Pavón-Carrasco, 2014; Kissel et al., 2015);* Mexico (*Urrutia-Fucugauchi et al., 2004, 2016; Böhnel et al., 2016; Mahgoub et al., 2017a, b, 2018; Juárez-Arriaga et al., 2018; Alva-Valdivia et al., 2019; Cifuentes-Nava et al., 2017, 2019; Larrea et al., 2019; Pérez-Rodríguez et al., 2020*); Georgia (*Vashakidze et al., 2019*); Iceland (*Rutten and Wensink, 1960*; *Thompson and Turner, 1985; Pintón et al., 2018*); Hawaii (*Doell and Cox, 1963*; *Holcomb et al., 1986; Hagstrum and Champion, 1994; Jurado-Chichay et al., 1996; Sherrod et al., 2006; Tema et al., 2017*); New Zealand (*Robertson, 1986; Downey et al., 1994; Greve et al., 2016; Greve and Turner, 2017; Lerner et al., 2019*); Chile (*Roperch et al., 2015; Di Chiara et al., 2017*); and Japan (*Matsumoto et al., 2007; Shitaoaka et al., 2019; Nitta et al., 2020; Yasuda et al., 2020).*

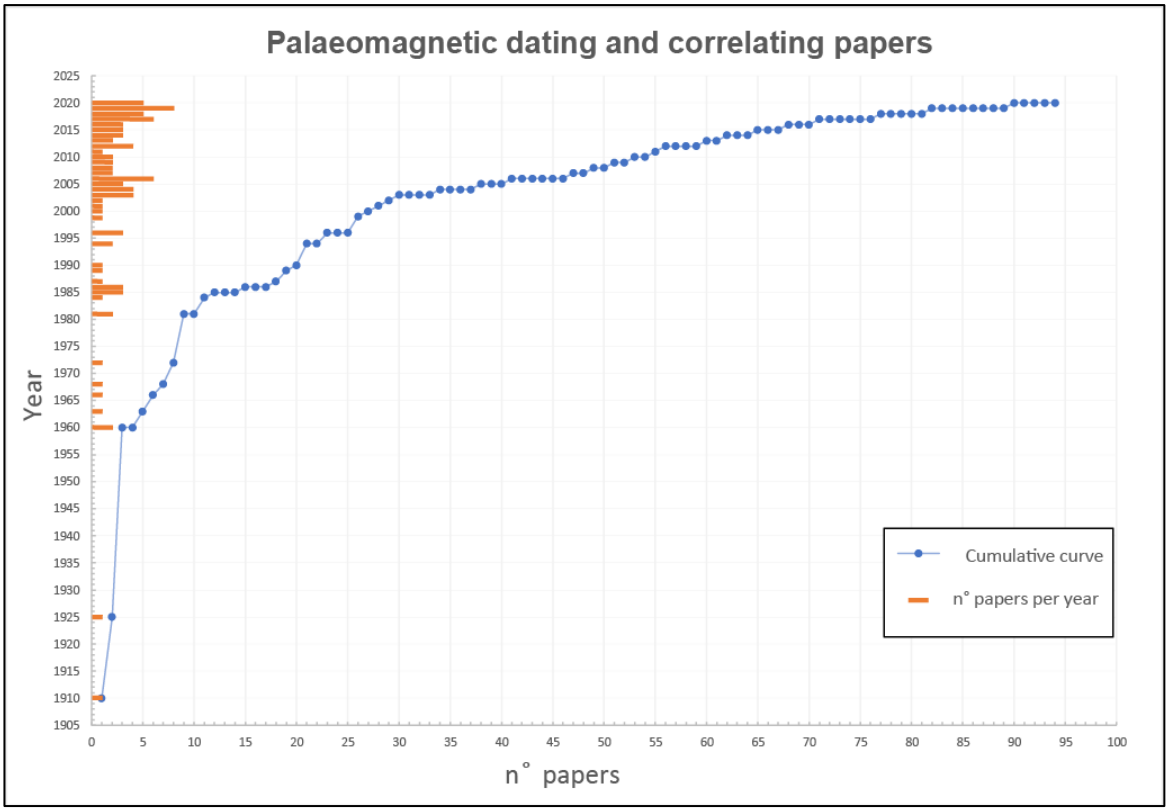

Fig. 2.7 Graph showing the number of palaeomagnetic dating and correlating papers per year (orange bars) of the last century, and the cumulative curve of papers (blue line). The flattening of the cumulative curve is due to the increasing numbers of published papers over time.

Hawaii

One of the first applications of palaeomagnetism to date lava flows is reported by *Holcomb et al. (1986).* They sampled 67 sites on lava flows of known ages, and 68 sites in undated flows in Hawaii, both to test the quality of the palaeomagnetic directions recorded in known age lavas and to date lava flows with unknown ages. They used also all palaeomagnetic directions to construct a PSV reference curve for Hawaii, with different degrees of reliability from 0 to 6,000 yr BP (Fig. 2.8).

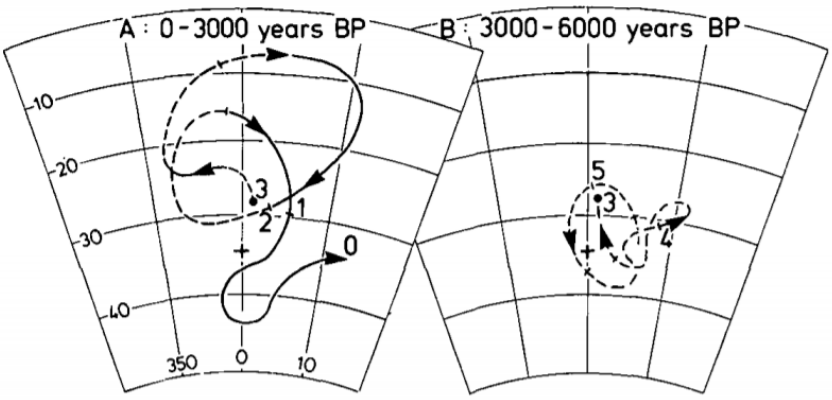

Fig. **2.8** Hawaiian PSV from 0 to 6,000 yr BP (from *Holcomb et al., 1986*).

Recently, *Sherrod et al. (2006)* studied the age and distribution of the latest Pleistocene and Holocene lava flows at Haleakalā volcano, Island of Maui. They combined the palaeomagnetic data and the PSV curve for the Hawaiian Islands with age limitations based on stratigraphic control to refine age estimates for some of the undated lava flows. They also calculated the volumetric rate, finding a nearly constant extrusion rate during the past 13,000 years, in the range 0.05–0.15 km^3/kyr. Their study allowed evaluation of as the Haleakalā's eruptive frequency as similar to that of Hualālai volcano (Island of Hawaii), even if its lava flows cover less area per unit time.

Herrero-Bervera and Valet (2007) investigated palaeomagnetically 13 sites of basaltic lava flows from Maui island with ^{14}C ages between 10.3 and 0.2 ka. They compared the inclination variations for the past 10 kyr found on Maui island with those previously obtained from the big island of Hawaii, finding an excellent agreement. Moreover, the authors noted that the inclinations from Lake Waiau sediments (big island) are shallower than those of the volcanic records (Mauna Kea, Hawaii) and interpreted it as due to the compaction. Therefore, *Herrero-*

Bervera and coauthors did not find striking evidence for an inclination anomaly under Hawaii during the analysed period, even if all studies reported a low dispersion of the VGPs which must reflect the low secular variation.

Tema et al. (2017) have compiled a detailed catalogue of palaeomagnetic data from historic and radiocarbon-dated Hawaiian lava flows of the last 10 kyrs, creating the first full geomagnetic field reference secular variation curves for central Pacific on the Bayesian statistics. The new Bayesian SV curves show three clear intensity maxima during the last 3000 yrs, accompanied by sharp directional changes, that have been interpreted as archaeomagnetic jerks.

Italy

In Italy, many works were performed on several volcanoes.

On Etna volcano, *Rolph et al. (1987)* studied over 40 historically dated lava flows. The palaeomagnetic analysis enabled authors to determine the change of the magnetic field in Sicily through historic times and to construct curves that show the secular variation of the field in direction and magnitude. The curves were then used to redate some of the Etna lavas attributed to the historic period. Finally, authors promoted the use of the secular variation curves also as a powerful archaeological dating tool by comparison with the NRM of fired artefacts.

Incoronato et al. (2002) focused on Mount Arso (Ischia Island), Etna and Vesuvius lava flows, to retrieve the local PSV curve. Palaeomagnetic analyses of the three volcanoes showed that they share the same PSV pattern, which they called the SISVC (Southern Italy Secular Variation Curve; Fig. 2.9). Thanks to this curve, authors proposed a reassessment of the age of several lavas from Etna: one lava flow, previously dated 812-1169 AD, was dated at 1169 AD; two flows, previously dated 1536 and 1595 AD, respectively, were emplaced at 1037 AD, instead; another three lavas, one dated at 1566 AD and two at 1595 AD, were emplaced between 1169 and 1284/85 AD. Finally, they also dated flows from Vesuvius within the same time windows.

Tanguy et al. (2003) applied the archaeomagnetic dating method to the Mediterranean volcanoes Etna, Vesuvius and Ischia, collecting a large number of oriented samples, weighing

0.5-1 kg each, both to reach a precision of a few degrees on the direction, with a Fisher 95 % confidence cone between 0.6° and 1.8°, and to avoid local field distortions. The authors palaeomagnetically dated sixty-three lava flows and pyroclastic units with a resolution increasing in younger ages from ± 100 to ± 40 years from 150 BC to 1,500 AD. The authors affirmed that the method can be safely extended to all of Europe to constrain eruption ages within the last 2 ka.

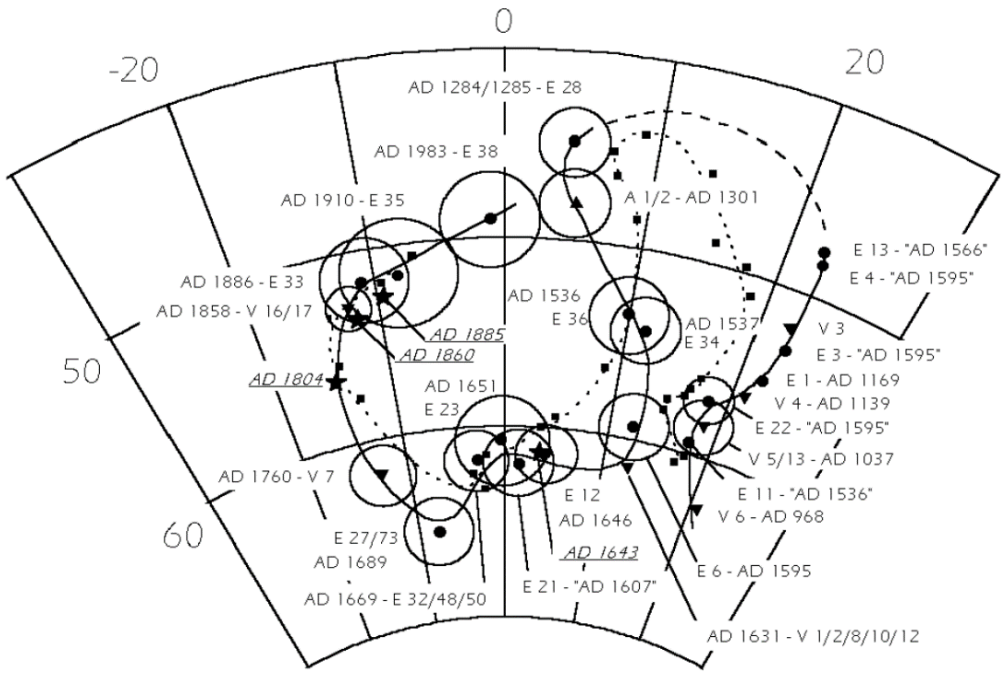

Fig. 2.9 Plot of site-mean directions of magnetization, and related circles of confidence, of Mount Arso (A) and Vesuvius (V), relocated to Etna, and Etna (E) lava flows (see details in *Incoronato et al., 2002*).

In recent years, a wide discussion arose about the sampling techniques. *Principe et al. (2004)* studied some medieval eruptions of Vesuvius (Italy), collecting and analysing big oriented blocks (using the so-called "big sample plaster method" of *Thellier, 1981*). Authors affirm this method allows obtaining very high precision (α_{95}~1°), and better time resolution (± 40 years) than the widely accepted classical core-drilling method. *Lanza and Zanella (2006)* replied to *Principe et al. (2004)* about the chronology of Vesuvius, discussing the high accuracy that can be reached using palaeomagnetic dating. Moreover, they argued that the reference curve used by *Principe et al. (2004)* is poorly constrained and not clearly indicated, and that they do not define parameters of the statistical approach used for the dating. Later, *Arrighi et al. (2004),* in a study about the recent deposits of Stromboli (Italy) adopted the same method of sampling of *Principe et al. (2004*), obtaining different results from *Speranza et al. (2004).*

Speranza et al. (2005) confirmed that the classical core-drilling method provides a more realistic estimate of dating and related uncertainties. They criticized the "big samples" procedure, which would not guarantee a realistic average of the palaeomagnetic field, and that the highly precise age-estimate is rather due to incorrect laboratory and statistical procedures. *Speranza et al. (2005)* showed that *Arrighi et al. (2004)* obtained the low α_{95} by rejecting samples arbitrarily or by an undersampling and that uncertainties of 2-4° better reflect the realistic values. Afterwards, *Arrighi et al. (2005)* supported again the "big sample method", affirming that the classical core-drilled method can cause a secondary drilling remanent magnetization (or DIRM).

Lanza et al. (2005a) studied the palaeomagnetic directions from Etna and Vesuvius volcanoes, finding higher dispersion for Vesuvius than for Etna. Therefore, they defined some possible sources of bias, such as the undersampling of the studied flows, a TRM anisotropy and the effect of magnetized rocks underlying the studied flow.

Tanguy et al. (2005) commented on the work of *Lanza et al. (2005a)*, interpreting their large dispersion due to collecting data in a very restricted area, and the use of inadequate drilling tools, which would produce a parasitic paramagnetization. Their compilation of data is also criticized as inadequate, and they underlined that their palaeomagnetic results from Vesuvius perfectly match with the French PSV curve. Moreover, *Tanguy et al. (2005)* argued on the validity of the PSV by *Incoronato et al. (2002),* which resembled Jackson's model *(Jackson et al., 2000)* for 1600, since it would be based on an inaccurate or wrong dating of some flows. *Lanza et al. (2005b)* replied to the comment by *Tanguy et al (2005),* defending their own work, pointing out a general agreement between the dataset published in *Lanza et al. (2005a)* and previous authors (e.g., *Rolph et al. 1987, Incoronato et al. 2002, and Tanguy et al. 2003*). Finally, they discussed the methodological problem, emphasising that the large sampling method is useable only for archaeological samples.

Lanza et al. (2005b) replied to the comment by *Tanguy et al. (2005),* pointing out the agreement between the dataset published for previous authors (*Rolph et al., 1987; Incoronato et al., 2002 and Tanguy et al., 2003*) and their dataset. Moreover, the authors showed that the thermal remanent magnetization direction of most flows deviates from the corresponding historical direction by a small angle θ, which in most cases is larger than the experimental

error (α_{95}). Therefore, the method used by Tanguy and co-authors provides smaller but unrealistic α_{95} values.

Speranza et al. (2006) studied historical lava flows from Etna to address again the controversy on the accuracy of the palaeomagnetic dating method and codify the technique. Studying 39 sites in 13 flows, authors compared palaeomagnetic directions with the archaeomagnetic data from the last 3 ka, from different areas (France, United Kingdom, Germany and Bulgaria) relocated to Etna coordinates. They discussed the method and the possible source of bias. According to *Principe et al. (2004),* the palaeomagnetic dating can achieve an age determination accuracy of even 20-30 years, whereas *Speranza et al. (2006)* found α_{95} values for the flow mean directions ranging between 3.3° and 5.7° (4.5° on average), which translate into accuracies of age determinations of 136–661 years (307 years on average).

Branca et al. (2019) investigated the age of the main lava flows forming the Alcantara River valley (Etna volcano). Moreover, through a multidisciplinary approach integrating stratigraphic and aeromagnetic data analysis, they reconstructed the length and volume of the main lava flow that impacted this area. They found that the valley was mainly affected by a few flank eruptions on the lower north flank during the activity of the Mongibello volcano. In particular, the Alcantara lava flow invaded the valley floor for 24 km between 13.9 and 9.7 ka BP; subsequently, another two flank eruptions occurred at 9.1–7.2 and 7.3–7.2 ka BP (respectively). The 3D magnetic modelling has been used by authors to calculate the total on- and off-shore volume of the Alcantara lava flow as 1 km^3.

Conte et al. (2006a) examined 14 undated lava flows of Somma-Vesuvius volcano. Characteristic magnetization directions determined for each flow unit gave palaeo-directions for 10 of the 14 lavas comparable with the early 17thcentury segment of the Italian PSV. For the other four sites, even if they found distinct mean directions, they did not correlate to any given sector of the reference curve, within the time frame expected for the activity. They supposed either these lava flows occurred in time intervals outside the period covered by the reference secular variation curve, or the palaeodirections recorded by these lava flows were affected by local structural disturbance.

Vezzoli et al. (2009) focused on Ischia Island, studying the volcanic field developed during the last 10 ka and constituted by alkali-trachytic to trachyandesitic lava domes, lava flows, tuff and scoria rings and pumice cones. They used the archaeomagnetic dating method to date 12 volcanic centres. The palaeo-field directions compared with the reference curve for secular variation in the western Mediterranean sea (for the last 3 ka) and eastern Europe (from 3 to 8 ka) gave ages between 4100 BC and 355 AD. These data, together with other geochronological information, allowed authors to define five periods of activity, separated by phases of quiescence and coeval with earthquake and landslide events. They propose a resurgence with a dome-shaped structure emplaced during the two oldest periods of activity (7200-6800 BC and 4100-2300 BC), which caused recurrent lateral collapses. During the last three younger periods (1800-1000 BC; 650 BC-350 AD; 1302 AD), resurgence affected a fault-bounded, asymmetric block.

At Pantelleria Island (Strait of Sicily, Italy), *Speranza et al. (2010)* studied the most recent silicic eruptive cycle, i.e. Serra della Fastuca fall deposit, pumice fall and agglutinate deposits from Cuddia del Gallo and Cuddia Randazzo, and the Khaggiar lava flow. The ages of these products, previously isotopically dated at 5–10 ka, were restricted considerably. Cuddia del Gallo agglutinate and Khaggiar flows were dated between 5.9 to 6.2 ka, whereas for the Fastuca pumices older age of 6.2–6.8 ka was obtained. Based on these data, the authors evaluated the duration of the most recent silicic eruptive cycle as at most a millennium and as little as a few centuries around 6.0 ka. Palaeomagnetically inferred ages, when compared with published data (^{14}C dates), showed a good agreement, whereas K/Ar data were more scattered and yielded ~30% older ages.

Palaeomagnetic dating was applied in Stromboli volcano (Aeolian Islands, Italy) *by Speranza et al. (2004, 2008)* and *Risica et al. (2019).* In *Speranza et al. (2004),* the authors have been focusing on the different spatter deposits spread over the northern and western flanks of the volcano produced by high-energy strombolian eruptions after the third-seventh century AD. Palaeomagnetic dating showed that most of them occurred during several eruptions between 1400 and 1600 AD, and during the powerful XX century eruptions. Later, *Speranza et al. (2008)* and *Risica et al. (2019)* focused on dating most of the eruptions belonging to the Neostromboli volcano (Fig. 2.10), the penultimate Holocene volcanic epoch, characterized by lava emissions both by summit craters and lateral vents situated in the western and eastern flank of the cone.

These datings improved the geochronological resolution of the Neostromboli activity, identifying the principal phases that have led to the repeated collapse events forming the Sciara del Fuoco formation, a large lateral collapse in the northwest sector of the island.

At Vulcano Island (Aeolian Islands, Italy), *Zanella et al. (2001)* studied the magnetic fabric and remanent magnetization of welded scoriae fall deposits to set the chronostratigraphic relationships. They considered the scoriae welded and cooled in situ, excluding en masse movement of welded scoriae on the base of the within-site consistency of the magnetic directions and the magnetic fabric and remanence. Moreover, they compared the ChRM directions of three units with the palaeosecular variation curve for the Aeolian Islands. For two of them, Spiaggia Lunga and Quadrara eruptions, previously dated with isotopic methods (but indistinguishable within the error), the authors found that they were emplaced at different times, and in particular, Spiaggia Lunga scoriae were set with a single eruption.

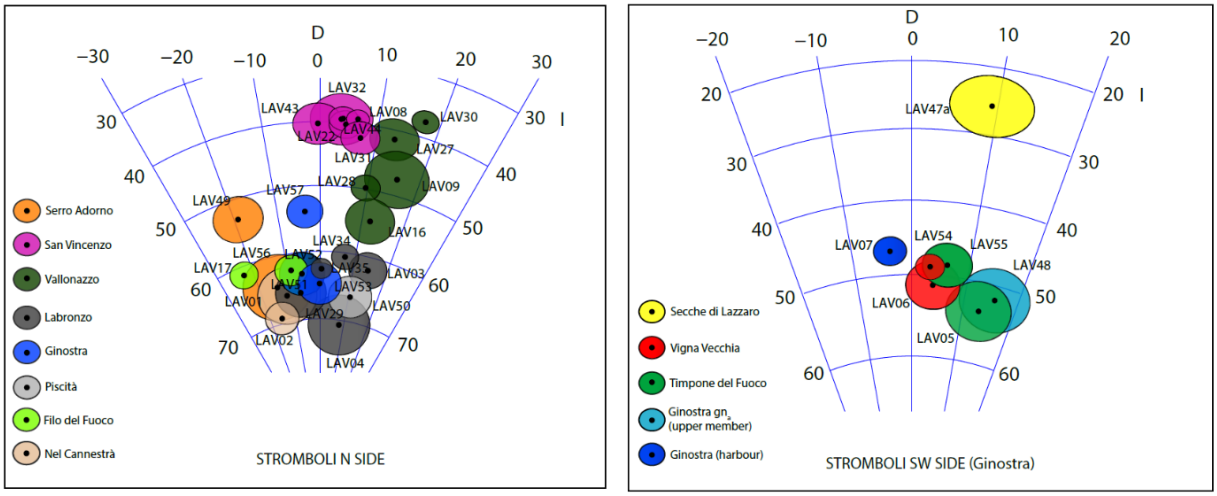

Fig. 2.10 Equal-area projection (lower hemisphere) of site-mean palaeomagnetic directions for all the studied units of the Neostromboli sequence (from *Risica et al., 2019*).

Lanza and Zanella (2003) investigated the palaeosecular variation of the Earth's magnetic field at Vulcano (Aeolian Islands, Italy) during the last 135 kyr, sampling lavas, scoriae and pyroclastic rocks from 25 distinct units previously dated with isotopic methods or constrained with stratigraphic relations. They found that the mean palaeomagnetic direction over the last 135 kyr differs from the geocentric axial dipole at Vulcano, and they interpreted it as probably due to the effect of a long-term, non-axial-dipolar component. Moreover, the authors compared the PSV record of Vulcano with the lacustrine sediments of Lago Grande di Monticchio and Lago di Mezzano, finding a good agreement. Subsequently, they analysed 113

repeat stations of the Italian Geomagnetic Network to find the optimum site to be used as a reference for PSV studies in Italy with the relocation via pole method, obtaining that the Viterbo station is the best, with a mean error of 0.3° for both declination and inclination. Finally, they proposed a preliminary, composite PSV curve for the last 30 kyr BP merging and relocating to Viterbo the data from Vulcano and the curve from Lago di Mezzano.

Arrighi et al. (2006) investigated the Vulcanello platform lavas and pyroclastic cones, and lava flows from the Fossa cone of Vulcano (Aeolian Islands) through the high-accuracy "large sample" archaeomagnetic method. They found a younger age than previously thought for the Vulcanello platform, which was built by nearly continuous activity between AD 1000 and 1250; moreover, they found a similar age range for the lavas emitted from the La Fossa cone. Lastly, they confirmed the age of 1720±30 for the "Pietre Cotte" obsidian flow.

Gurioli et al. (2012) focused on the historic Breccia di Commenda explosive eruption of Vulcano (Aeolian Islands, Italy), studying the stratigraphy, components and geochemistry of the deposits. The authors interpreted these deposits as generated by a magmatic-hydrothermal eruption produced by the ascent of new magma that interacted with fluid-saturated hydrothermally altered rocks residing in the conduit zone. They also analysed the magnetic temperature recorded by non-altered lithic clasts, defining a temperature between 200 and 260 °C. Finally, they dated the eruption at 1000-1200 AD age.

Azores

Di Chiara et al. (2012) provided the first palaeomagnetic directional record of the last 3 ka from the Atlantic Ocean, sampling 16 lava flows on São Miguel, the largest island of the Azores. Their data show inclination swings from 60° to 25° and declination between -10° to 20°, reflecting variations in the geomagnetic field. They compared the declination record with predictions from CALS3k.4 and gufm1 global field models, finding a good agreement. Conversely, they found lower inclination values than model predictions at two ages. By interpolating a cubic spline fit on declination/inclination versus age data, authors inferred the directional evolution of the geomagnetic field at the Azores from 1000 BC to 1600 AD.

Later, *Di Chiara et al. (2014)* studied the Faial island, one of the most volcanically active islands of the Azores Archipelago. Authors correlated scoria cones and lava flows yielded by

the same eruption on the Capelo Peninsula, recognizing at least six prehistoric clusters of volcanic activity, and dated them comparing the palaeomagnetic data with relocated Holocene reference curves of the palaeosecular variation of the geomagnetic field from France and the UK. The lava flows studied by *Di Chiara and co-authors* showed younger ages than previously believed, in the last 8 k.y.

Japan

Matsumoto et al. (2007) studied nine lava and pyroclastic flows from five dated volcanoes in Kagoshima Prefecture and Nansei Island. The analyses of the remanent magnetization allowed authors to construct a new secular variation curve for South Kyusyhu limited to ages younger than 700 AD (Fig. 2.11). The new curve was used to date three lava flows with unknown ages.

Shitaoaka et al. (2019) estimated the eruption age of Kannabe volcano (southwestern Japan), studying a basaltic lava flow and a soil layer above the scoriae both with palaeomagnetic and optically stimulated luminescence techniques. The soil layer was newly dated at 21 ± 6 ka, whereas palaeomagnetic data of 23 samples from six locations were compared with the PSV data of sediments in Lake Biwa, dating it at ca. 21.5 ka. The multi-dating approach allowed authors to date the Kannabe volcano eruption at ca. 22 ka.

Nitta et al. (2020) investigated the recent eruption history of Yokodake volcano (Japan) dating two recent lava flows with multi-dating techniques: palaeomagnetic and thermoluminescence dating methods for lavas and radiocarbon method for palaeosol. Results allowed distinguishing the eruption ages of the two lava flows, ca. 3.4 ka and 0.6 ka (Fig. 2.12), from the associated explosive eruptions that produced the tephra levels, ca. 2.4-2.2 ka. Their study showed that, since the recent lava effusion at 0.6 ka, Yokodake volcano should not be considered as an active volcano with low activity, but with some potential for eruption. Moreover, the use of multiple methods of dating is an effective tool for determining the age of young volcanic deposits.

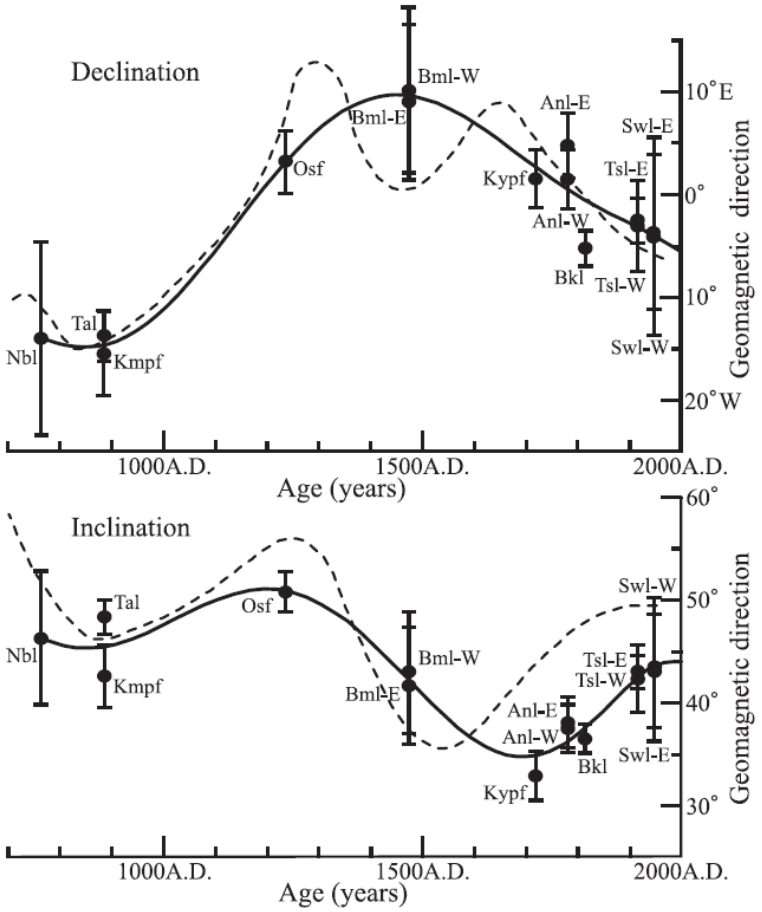

Fig. 2.11 Secular variation curve for South Kyushu (solid line), compared with the Kinki district curve (broken line) by *Hirooka (1971)* (from *Matsumoto et al., 2007)*.

Yasuda et al (2020) revised the stratigraphy of the proximal deposits around Ohachidaira volcano (central Hokkaido, Japan) and their palaeomagnetic directions. Authors identified four proximal pyroclastic members produced after the early edifice-building effusive volcanism: (1) vent-opening mafic PDC deposits; (2) maar-forming mafic tephra-ring deposits; (3) mafic to silicic caldera-forming deposits; and (4) mafic PDC deposits. Due to the well grouped palaeomagnetic direction, authors interpreted the first and the third deposit as emplaced in a short time interval, less than a century. Conversely, scattered palaeomagnetic directions of the maar-forming mafic tephra-ring deposits translated into a longer time interval, at least 750 yr or more. Lastly, the mafic PDC deposits showed a similar palaeomagnetic direction to the underlying Sounkyo Member, therefore they were produced during the Sounkyo eruption. The Ohachidaira volcano was interpreted as a maar-caldera complex volcano, in which the summit caldera is constituted by a flaring funnel formed incrementally by explosive erosion and syn-eruptive collapse of the vent walls.

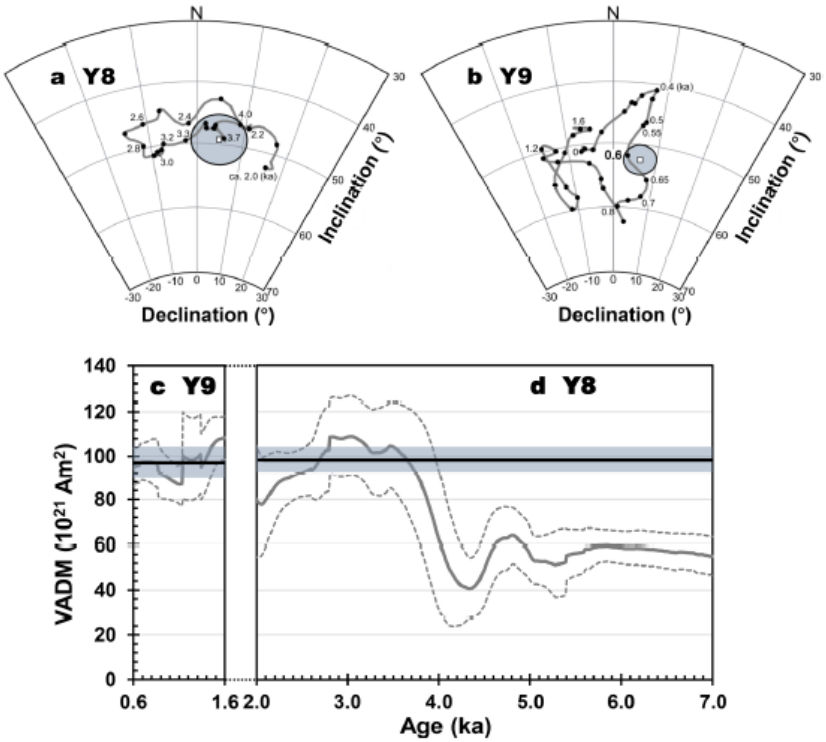

Fig. 2.12 PSV record and palaeomagnetic results for the two lava flows of Yokodake volcano, Japan (for details see *Nitta et al., 2020*).

New Zealand

One of the first applications of palaeomagnetism in New Zealand was done by *Robertson, (1986)*. In this work, *Robertson* sampled and analysed palaeomagnetic directions of the recent basalt lavas of Rangitoto Island. He compared the palaeomagnetic declinations with historically recorded declinations of the geomagnetic field, confirming the dating results previously obtained by the ^{14}C method. These results showed that Rangitoto volcano was active between A.D. 850 and A.D. 1800, with a maximum of activity between A.D. 1200 and A.D. 1500. Moreover, he inferred that near Auckland the geomagnetic field changed direction at approximately 2.87×10^{-2} deg/year eastwards, changing little in inclination, during the last 1000 years.

Downey et al. (1994) sampled lava flows from the Taranaki volcano and the parasitic cone Fanthams Peak and compared the palaeomagnetic directions with the palaeosecular variation curve for the region. Their results showed that the lava flows covering the main peak were extruded during two eruptive phases, of which the older occurred between 2800 and 7000 years B.P. and the younger between 400 to 700 years B.P. Moreover, they found that some of

the eruptive activity of Fanthams Peak probably occurred during the same time interval as the emplacement of the lavas of the northeast flank of Taranaki.

Greve et al. (2016) investigated the Tongariro Volcanic Centre (central North Island), studying palaeomagnetically 35 sites on Holocene lava flows, previously constrained to within a few thousand years with the Ar/Ar isotopic method. Correlating flow mean palaeomagnetic directions with the continuous sediment record from Lake Mavora (Fiordland), authors reduced the age uncertainty to 300–500 yr in some cases. The palaeomagnetic analysis of lavas belonging to Iwikau and Rangataua members showed that the effusive periods lasted up to thousands of years. In the last few millennia, Mt. Ruapehu was characterized by effusive activity, whereas Mt Tongariro, based on the Red Crater flow, dated at 200–500 BP, lasted into the past few centuries.

Greve and Turner (2017) added new PSV records obtained from post-glacial (≤15 kyrs BP) volcanic materials (mainly lavas) from New Zealand, in particular from the Taupo Volcanic zone, and critically assessed previous discrete PSV data and their age controls. The overall dataset presented by authors includes 23 directional and 10 absolute palaeointensity records primarily from lavas of rhyolitic or andesitic composition. The data set, with declination and inclination values ranging from 326.5° to 26.0° and −81.4 to −46.3°, and intensity values varying from 37.0 to 71.6 μT, fall into the range of PSV expected for this time-frame in New Zealand and reproduce features of continuous sediment records.

Another study on Mt. Taranaki was recently performed by *Lerner et al. (2019*). They focused on the study of the most recent eruption of Mt. Taranaki, which left a portion of a lava dome that now forms the 2518 m summit. Using the palaeomagnetic secular variation curve NZPSV1k, authors dated it between AD 1780 and 1800 (Fig. 2.13). Moreover, studying the geochemistry of this lava flow, they inferred that the summit cone was part of a large lava coulee. Furthermore, they reconstructed the thermal history of block and ash flow deposits formed by this dome/coulee collapse, finding temperatures > 500 °C more than 2 km from the source. Finally, the palaeomagnetic analyses allowed authors to identify a multiple-stage collapse, in which firstly the smaller portion of the lower dome collapsed, and later the thicker and hotter parts of the central dome.

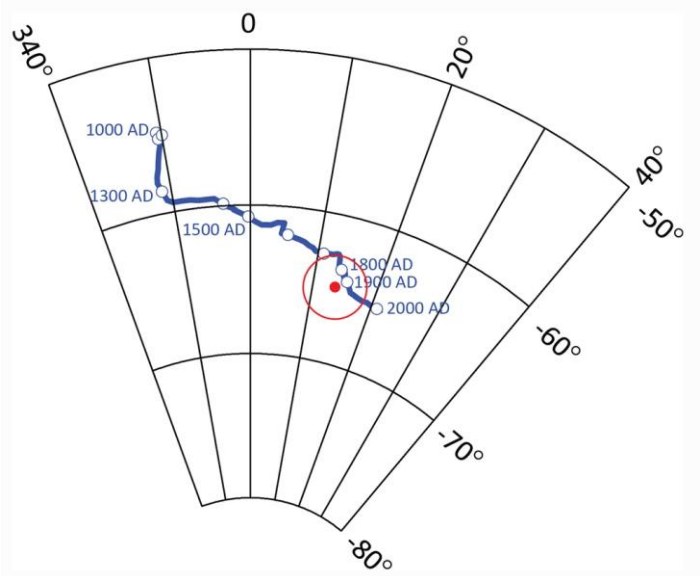

Fig. 2.13 Equal angle plot showing the mean direction (red dot) and α_{95} (red ring) for the current Taranaki summit dome compared with the magnetic field direction over the past 1000 years according to the NZPSV1K palaeosecular variation curve (blue line) (from *Lerner et al., 2019*).

Iceland

In Iceland, *Thompson and Turner (1985)* analysed sediments of the last 9 ka from the lake Vatnsdalsvatn, in northwest Iceland. Sediments, dated using ^{14}C dating, showed inclination of 76°, close to the expected axial dipole field, and direction fluctuations of around 20° from the mean. The pattern obtained by authors was similar to the British records and the central North American record, 2000 km and 5000 km distant respectively.

Pinton et al. (2018) studied palaeomagnetically 25 sites from the Reykjanes Peninsula and the Tungnaá lava sequence. They sampled also the precisely dated Laki and Eldgjà lavas, to test the method. The age window obtained for these two eruptions agrees with the true flow ages, whereas in the Reykjanes peninsula, they proposed an older emplacement age for Ogmundarhraun and Kapelluhraun lava fields. Finally, for pre-historical Tugnaá eruptions, the new palaeomagnetic ages showed higher precision of 300-400 years.

Chile

The first work that showed the presence of a large anomaly, the South Atlantic Magnetic Anomaly (SAMA) during the last centuries was performed by *Jackson et al. (2000)* in the geomagnetic model gufm1. However, South America is still characterized by the paucity of

palaeomagnetic data, which would be useful to understand the PSV of the geomagnetic field in this area. Here, two works are summarized.

In Chile, *Roperch et al. (2015)* analysed palaeomagnetically two well-dated lava flows, the 1835 AD eruption of the Osorno volcano and the 1751 AD eruption of the Llaima volcano, for which directions and palaeointensities were derived. Moreover, the authors studied also 14 samples from bricks of shelters built along the main road across the Andes from Santiago (Chile) to Mendoza (Argentina) in 1770 ± 5 AD. Their results confirmed the high reliability of the global geomagnetic model gufm1 (*Jackson et al., 2000*) for the last three centuries, showing a large amplitude in inclination (~20°) and intensity (~25 μT). Moreover, their study highlighted the importance to study well-dated lava flows to improve the reliability of global geomagnetic models. Finally, the authors applied palaeomagnetic dating in historical lava flows from the Antuco, Llaima and Villarrica volcanoes to refine the ages of the major historical effusive volcanic events.

Di Chiara et al. (2017) studied a lava flow (supposed to be the 1750 or 1957-58 AD lava flow) on the Llaima Volcano, one of the most active centres of the Chilean Andes, in the Southern Volcanic Zone, obtaining both palaeodirections and palaeointensity. The full magnetic vector obtained, compared to archaeomagnetic reference curves and the IGRF, allowed dating the lava flow at 1957–58 AD.

Mexico

In the last years, palaeomagnetic datings have been increasingly applied in Mexico.

Urrutia-Fugugauchi et al. (2016) studied the lava flows produced by the Xitle volcano, which covered the Cuicuilco archaeological site in the southern Basin of Mexico. The previous ages of this eruption obtained with the radiocarbon method have given contrasting results; therefore, authors determined a new age estimate correlating full vector data with the geomagnetic secular variation reference model and recalibrated the radiocarbon ages. The revised archaeomagnetic data gave ages from 1995 to 2177 cal yr BP, with a mean of 2086 yr BP. Bootstrap analysis of the calibrated radiocarbon and archaeomagnetic dates gave mean ages and confidence intervals of 2041 and 1968–2041 cal yr BP and 2035 and 1968–2073 cal yr BP, respectively. Finally, the authors inferred that the interval estimated of ~90 BC to ~AD

20 was probably linked with the abandonment of Cuicuilco site and the subsequent early development of Teotihuacan.

Mahgoub et al. (2018) studied four monogenetic Holocene lava flows (Fig. 2.14) located within the Michoacán-Guanajuato Volcanic Field (Mexico). One of these lava flows, previously dated with radiocarbon age, has been used by authors to validate the method. Using full-vector palaeomagnetic data and comparing them with the global palaeosecular variation model SHA-DIF.14K, they found for the already dated eruption a consistent age. For the other eruptions, they obtained two age ranges of 1340–1230 and 1030–940 BC for Malpaís Las Víboras, a younger age range of 200–80 BC for the Capaxtiro lava flow and an age range AD 830–960 for the Malpaís Prieto lava flow. This study enabled authors to identify a link between the ages of the eruptions and the abandonment of the area, especially in 900 AD, which coincides with the palaeomagnetic age of the Malpaís Prieto eruption. Finally, estimating an eruption recurrence interval of roughly 1000 years, the authors assume a new monogenetic eruption in the future.

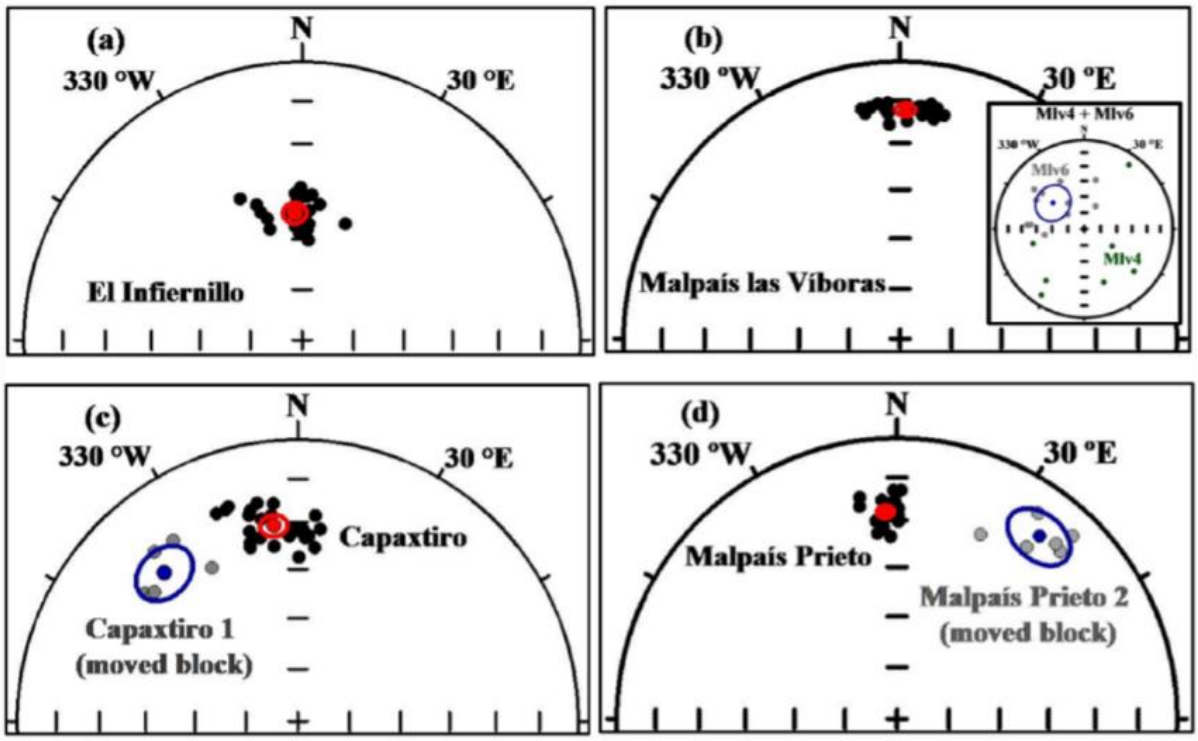

Fig. 2.14 Characteristic remanent magnetization directions for the four lava flows. (a) El Infiernillo, (b) Malpaís Las Víboras, (c) Capaxtiro, and (d) Malpaís Prieto (from *Mahgoub et al., 2018*).

Larrea et al. (2019) sampled two monogenetic volcanoes, El Astillero and El Pedregal located in the ~ 4400-km^2 Tancítaro-Nueva Italia region in the southwestern part of the Michoacán Guanajuato Volcanic Field (MGVF), only 25 km to the south of Paricutin volcano. They determined from palaeomagnetic and radiocarbon dating that El Astillero and El Pedregal most likely erupted one after the other between AD 500 and 700 (Fig. 2.15), emitting a dense rock equivalent (DRE) volume of magma of ~ 0.5 km^3, during an estimated eruption duration of ~ 6 years. The activity of this small cluster of eruptions formed firstly the El Astillero scoria cone and tephra deposits followed by its lava field and ended with the emplacement of the El Pedregal viscous lavas, passing in composition from basaltic andesite to andesite throughout the duration of the eruption. Although the eruptions probably had a limited impact on the small area affected and the surrounding human activities, the authors highlight that these two eruptions represent the initial stages of a new cluster, and therefore future eruptions in this area can be expected.

A refined and complete review about the use of palaeomagnetism and the palaeomagnetic dating tool has been recently provided by *Korte et al. (2019).*

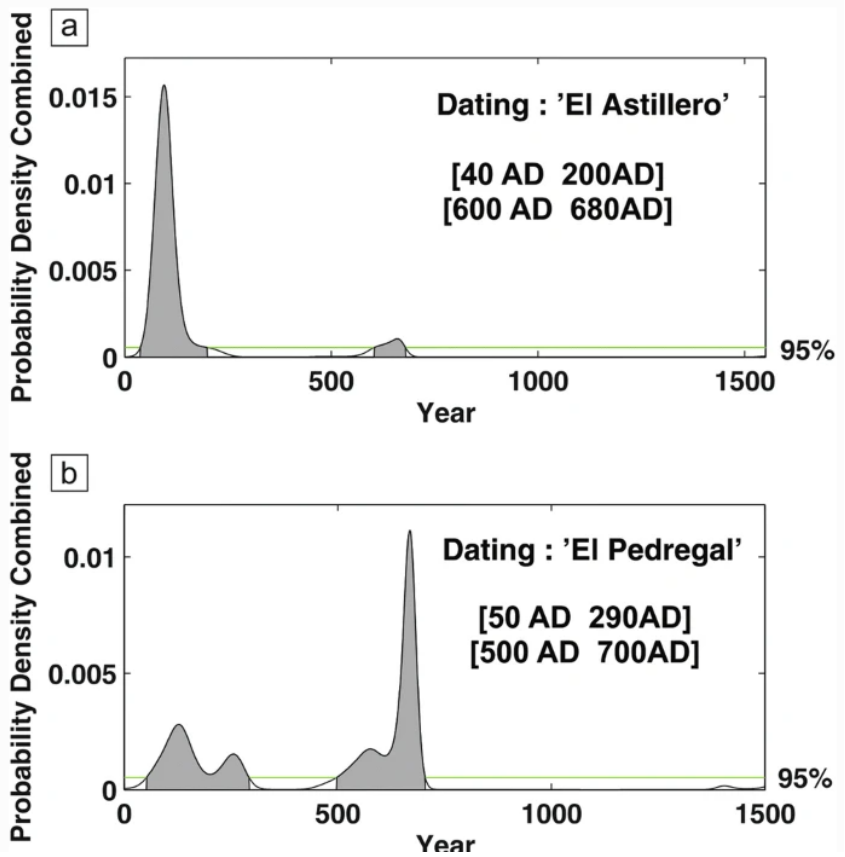

Fig. 2.15 Palaeomagnetic dating of El Astillero and El Pedregal lava flows (from *Larrea et al., 2019*).

The *palaeomagnetic correlation* is achieved by comparing palaeomagnetic directions (and palaeo-intensity, if available) from different volcanic outcrops and considering correlative those that share comparable values; volcanic rocks emplaced during the same eruption and/or eruptive event are subjected to the same geomagnetic field direction.

In volcanology, the palaeomagnetic correlation has been used to study both intrusive bodies (*Jones and McHlhinny, 1966; Chenet et al., 2008, 2009; Veselovskiy et al., 2012; Konstantinov et al., 2014; Peskov et al., 2018; Latyshev et al., 2018, 2020*) and volcanic deposits (*De Boer et al., 1968; Grommè et al., 1972; Bogue and Coe, 1981; Prévot and McWilliams, 1989; Hagstrum and Champion, 1994; Hayashida et al., 1996; Jurado-Chichay et al., 1996; Ort et al., 1999; 2013; Moulin et al., 2011; Riisager et al., 2003; Di Chiara et al., 2012; Speranza et al., 2012; Latyshev et al., 2013; Finn et al., 2016*).

Hagstrum and Champion (1994) used palaeomagnetism to correlate historic lava flows at Kilauea Volcano. Their results showed that remanent magnetization for historic flows was not influenced by local magnetic anomalies, with angular differences within flows less than 5°. The palaeomagnetic grouping of flows into eruptive events allowed identifying a different eruptive history for the lower east rift zone, with probably lower event frequency.

Jurado-Chichay et al. (1996) palaeomagnetically studied the Pohue Bay flow (Mauna Loa Volcano, Hawaii islands) with the associated cones (Fig. 2.16) to determine the cone origin (primary or secondary processes) and the temporal relations between flows and cones. Their results showed also in this case that the remanent magnetization from correlative flows yields small angular dispersion and well-defined characteristic magnetizations. The authors define a littoral origin for the cones, and using the secular variation curve and the comparison with age-dated flows with similar palaeomagnetic directions, estimate an eruptive age of approximately 1300 years ago for the Pohue Bay flow.

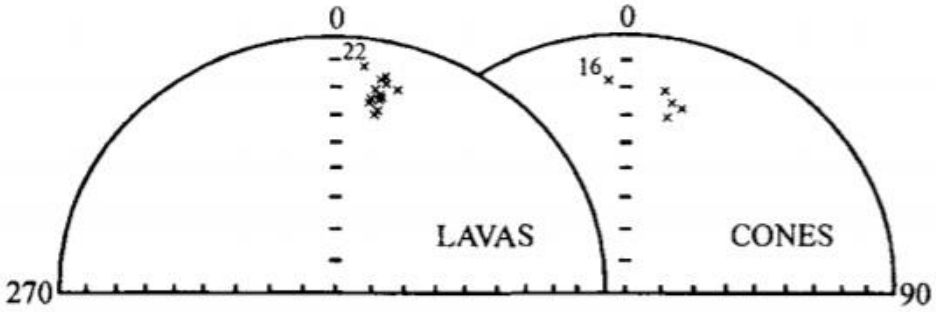

Fig. 2.16 Equal area stereograms of flow sites and cone sites (from *Jurado-Chichay et al., 1996*).

Ort et al. (1999) used this technique to correlate deposits of the proximal Campanian Ignimbrite deposits (Breccia Museo and the Piperno Tuff), using the NRM, and to identify the vent locations using the AMS technique (Fig. 2.17). This method proved to be extremely useful in cases in which the field correlation is complicated by the lack of medial exposures and/or limited proximal stratigraphic sections and lateral facies changes.

According to *Di Chiara et al. (2012)* and *Speranza et al. (2012)*, palaeomagnetic directions are considered as correlative when they are virtually in overlap, and with a cut-off angular distance <10°. However, in some cases, volcanic deposits can share the same palaeomagnetic directions, and nevertheless, they do not belong to the same volcanic event. The geomagnetic field, swinging around the same directions, can yield similar palaeomagnetic directions several times along the centuries/millennia. Thus several possible ages and possible wrong correlations can occur, if other geological constraints (for example upper or lower dated eruptions, stratigraphy, petrographic and geochemical analysis, etc.) are not considered.

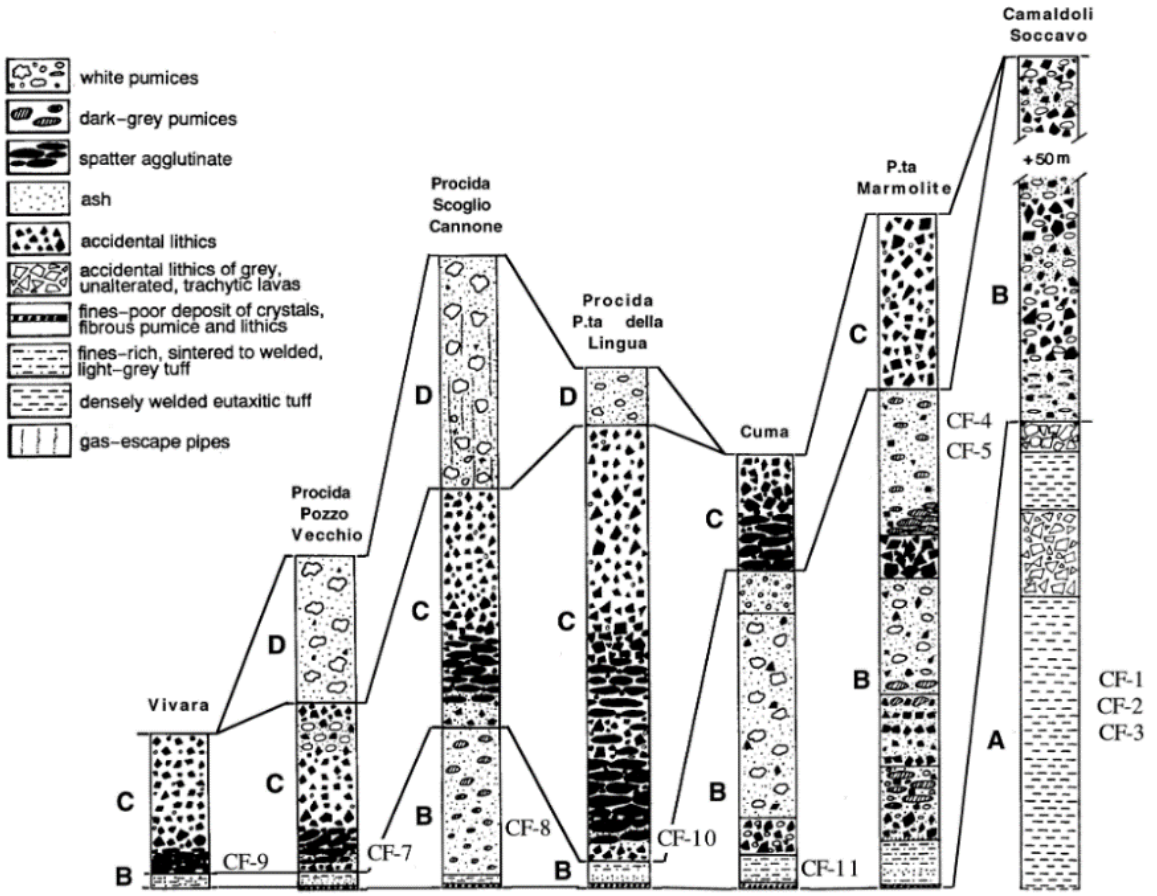

Fig. 2.17 Palaeomagnetic correlation of stratigraphic columns of Campi Flegrei deposits, studied *by Ort et al. (1999).*

Recently, *Finn et al. (2016)* applied palaeomagnetic, geochemical, mineralogical and geochronologic evidence for a correlation of the mid-Miocene Cougar Point Tuff in southwest Snake River Plain (Idaho). The palaeomagnetic characterization of eruption units shows a resolution on the order of a few centuries. To obtain reliable palaeomagnetic directions, the authors measured the anisotropy of anhysteretic remanence to correct for magnetic anisotropy. Moreover, *Finn and co-authors* found in most sampled ignimbrites a gyroremanent magnetization, that is a spurious magnetization component acquired from AF application. This component can hamper attempts to demagnetize rock samples with standard three-axis static AF methods. To remove it, they used a new method proposed by *Finn and Coe (2016),* that involves permutation of the AF axes order with progressively higher AF steps and subsequent smoothing of the resultant demagnetization data.

2.2.1 Reference curves and SHA.DIF.14K Global Model

The availability of PSV reference curves is a fundamental requirement to safely use palaeomagnetism as a dating tool for Holocene volcanic rocks. There are mainly three different sources of reference PSV curves:

1) the regional PSV curves determined for a specific area: they are built for a specific region in which well-dated data are available; then, assuming an ideal dipolar geomagnetic field, directional data are transferred to another locality using the VGP (*Noël and Batt, 1990*). During the last years, several detailed PSVCs from several countries were obtained (archaeomagnetic curves: Austria, *Schnepp and Lanos, 2006;* Bulgaria*, Kovacheva, 1980; Kovacheva et al., 1998, 2004; 2009*; France, *Thellier, 1981; Bucur, 1994; Chauvin et al., 2000; Gallet et al., 2002;* Germany*, Schnepp and Lanos, 2005;* Greece*, De Marco et al., 2008;* Hungary*, Márton, 2010; Tema and Kondopoulou, 2011;* Iberia*, Gómez-Paccard et al., 2006; Molina-Cardín et al., 2018*; Italy, *Evans and Hoye, 2005; Tema et al., 2006, 2020*; the United Kingdom and Britain*, Aitken, 1958; Clark et al., 1988; Zananiri et al., 2007; Batt et al., 2017;* western North America, *Hagstrum and Blinman, 2010*; the United States of America*, DuBois, 1975; Eighmy et al., 1980; Sternberg, 1982; Lengyel and Eighmy, 2002;* Japan*, Watanabe, 1958; Hirooka, 1971;* sedimentary palaeomagnetic curves: Britain, *Thompson and Turner, 1979; Turner and*

Thompson, 1982; Sweden, *Snowball et al., 2007;* Black sea, *Creer, 1974;* Germany*, Stockhausen, 1998;* Greece*, Creer et al., 1981;* Finland*, Ojala and Tiljander, 2003*) were made.

Bucur (1994) obtained complete directional archaeomagnetic data for France from backed clay for the last 21 centuries (Fig. 2.18). *Kovacheva et al. (1998)* also developed archaeomagnetic curves of the direction and intensity of the geomagnetic field during the last 8000 yr for the Bulgaria region (Fig. 2.18). *Snowball et al. (2007)* built a Holocene palaeomagnetic secular variation master curve, called Fennostack, for Fennoscandia, using laminated and non-laminated lake sediment sequences (varves) (Fig. 2.19).

2) regional models: they are constructed when high-density reference data are available for a larger area, e.g. SHA.DIF.3K and SHA.DIF.8K (by *Pavón-Carrasco et al., 2009* and *2010*, respectively). The first is built only with archaeomagnetic data, whereas the second only with lake sediment and archaeomagnetic data.

3) global models: usually called CALS models, are a new generation of global models. Examples are *Korte et al. (2009), Donadini et al. (2009*). ARCH3K.1 was developed using archaeomagnetic input data; SED3K.1, built using only a lake sediment database, and finally, the CALS3K.3 model, in which all typologies (archaeomagnetic, volcanic and lake sediments) data were used.

In the early archaeo- and palaeomagnetic models (*Ohno and Hamano, 1993; Hongre et al., 1998; Constable et al., 2000*) only snapshots in time were provided. Later, the subsequent generation of models is temporally continuous.

In the CALSxk (e.g., *Korte and Constable, 2003; Korte et al., 2011; Constable et al., 2016*), pfm9k (*Nilsson et al., 2014*), HFM families of models (*Panovska et al., 2015; Constable et al., 2016)*, the ASD_FM and ASDI_FM (*Licht et al., 2013*) models and the COV-LAKE model (*Hellio and Gillet, 2018*), all three data types are used. Conversely, only archaeomagnetic and volcanic data are used in the ARCHxk (*Korte et al., 2009; Constable et al., 2016*) and S(C)HA (*Pavón-Carrasco et al., 2008b, a, 2014*) families and the A_FM (*Licht et al., 2013*), AmR (*Sanchez et al., 2016*) and COV-ARCH (*Hellio and Gillet, 2018*) models, instead. In Fig. 2.20, a complete overview of the geomagnetic field models for the 50 ka is available (from *Korte et al., 2019* and reference therein).

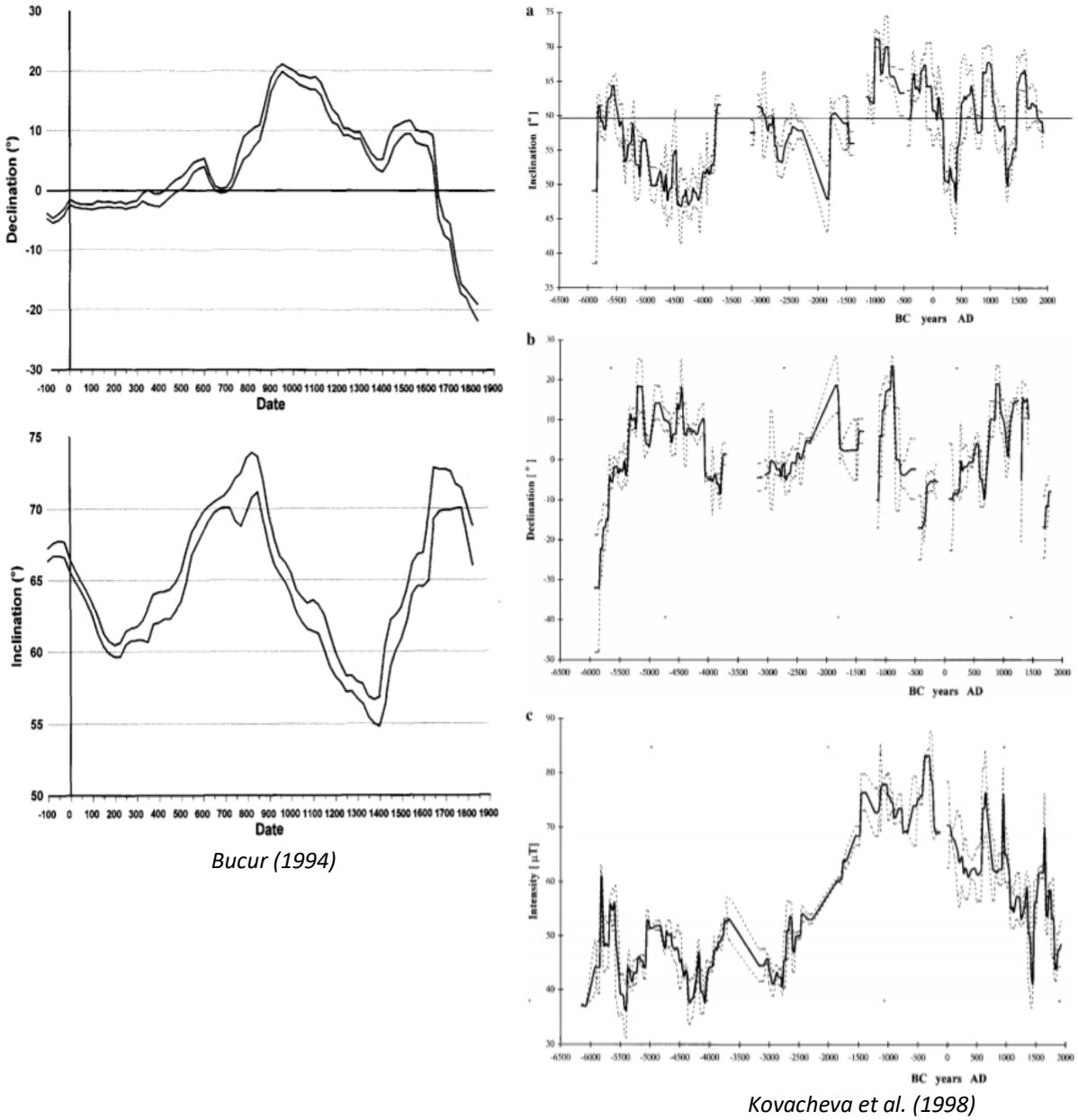

Bucur (1994)

Kovacheva et al. (1998)

Fig. 2.18 In the left side, declination and Inclination curves for France with 95% confidence band (from *Bucur, 1994*); in the right side, inclination (a), declination (b) and intensity (c) for Bulgaria for the last 8000 years obtained from archaeomagnetic measurements (from *Kovacheva et al., 1998*).

In this work, the *SHA.DIF.14K* (*Pavón-Carrasco et al., 2014*) global model was used. The name SHA.DIF.14K is an acronym: SHA is the Spherical Harmonic Analysis technique; DIF represents the elements of the geomagnetic field; 14K is the temporal range covered by the curve. The model is built with the database GEOMAGIA50v2 (*Donadini et al., 2006; Korhonen et al., 2008*), which contains more than 13 thousand data. As explained above, there are three principal sources of palaeomagnetic data used to reconstruct the PSV curves: heated

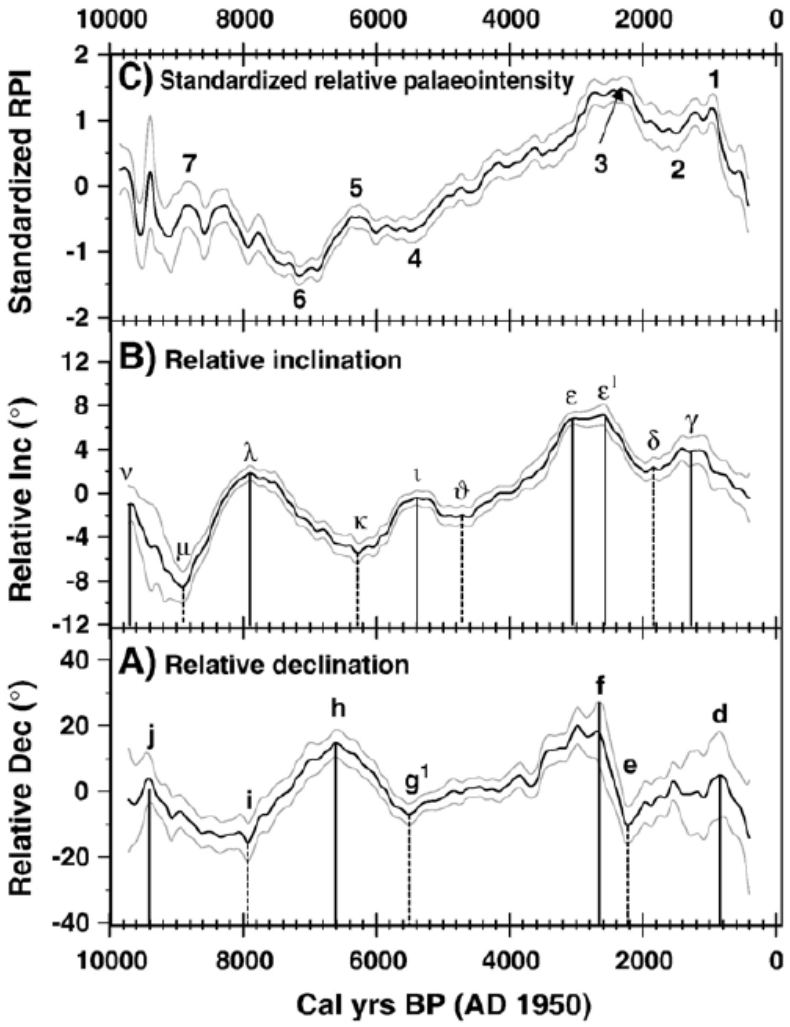

Fig. 2.19 Smoothed declinations, inclinations and standardized relative palaeointensity for Fennoscandia (details in *Snowball et al., 2007*).

archaeological artefacts and volcanic rocks that record the palaeomagnetic direction as a TRM, and the lake sediments that record as a DRM. The first two kinds of data can be considered as an instantaneous photograph of the geomagnetic field, whereas in the last the remanence is acquired in a "longer" time. When these data are processed together, a strong smoothing of the curve is produced. Discarding the sedimentary data, the SHA.DIF.14K model supplies an improvement in the resolution of the time evolution of the geomagnetic field. Moreover, while other models allow dating only the last few thousands of years, the SHA.DIF.14K model investigates the whole Holocene epoch, until 14 ka (Fig. 2.21). However, it is important to highlight that the time resolution of this curve decreases going backwards: the time variability for the interval between 6000 BC and 1900 AD is higher than for the older time interval (12000 – 6000 BC), where the non-dipolar contribution of the geomagnetic field

is not constrained. Moreover, the spatial distribution of all data is very heterogeneous, because ca. 97% of the total is located in the northern hemisphere, and in particular, most of the intensity data are located in the European continent (Fig. 2.22). For this reason, the model is not well constrained in the southern hemisphere.

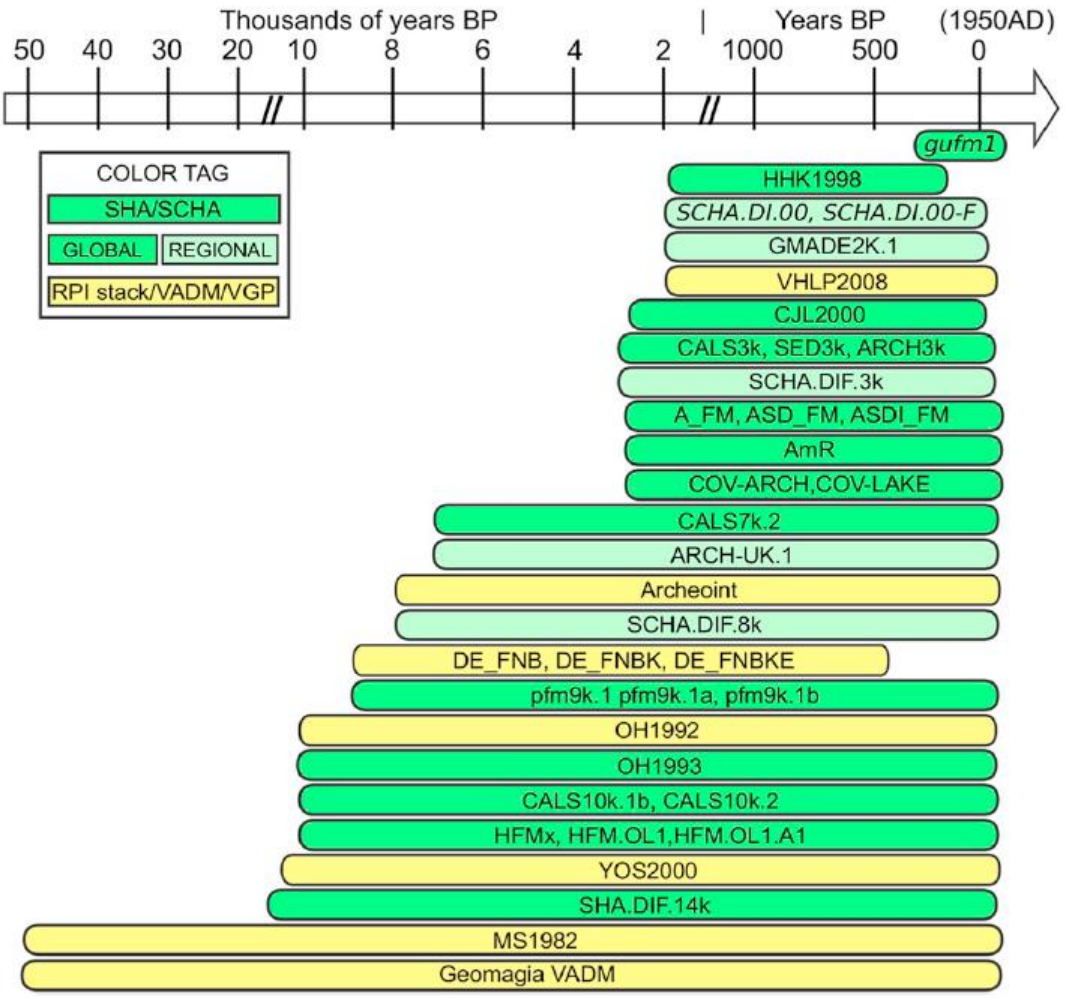

Fig. 2.20 Overview of geomagnetic field models and dipole reconstructions for historical times through to 50 ka (from *Korte et al., 2019*). Model references: GEOMAGIA VADM (*Knudsen et al., 2008*); MS1982 (*McElhinny and Senanayake, 1982*); SHA.DIF.14k (*Pavón-Carrasco et al., 2014*); YOS2000 (*Yang et al., 2000*); HFMx, and HFM.OL1.A1 *(Panovska et al., 2015; Constable et al., 2016*); CALS10k.x (*Korte et al., 2011; Constable et al., 2016*); OH1993 (*Ohno and Hamano, 1993*); OH1992 (*Ohno and Hamano, 1992);* pfm9k.1, pfm9k.1a, and pfm9k.1b (*Nilsson et al., 2014*); DE_FNB, DE_FNBK, and DE_FNBKE (*Nilsson et al., 2010, 2011*); SCHA.DIF.8k (*Pavón-Carrasco et al., 2010*); ArcheoInt VADM (*Genevey et al., 2008*); ARCH-UK.1 (*Batt et al., 2017*); CALS7k.2 (*Korte and Constable, 2005*); SCHA.- DIF.3k (*Pavón-Carrasco et al., 2009*); CALS3k.x, ARCH3k.1, and SED3k.1 (*Korte and Constable, 2003, 2011, 2005; Korte et al., 2009*); COV-ARCH and COV-LAKE (*Hellio and Gillet, 2018*); AmR (*Sanchez et al., 2016*); A_FM, ASD_FM, and ASDI_FM (*Licht et al., 2013*); CJL2000 (*Constable et al., 2000*); VHLP2008 *(Valet et al., 2008*); GMADE2K.1 (*Lodge and Holme, 2009*); SCHA.DI.00-F (*Pavón-Carrasco et al., 2008a*); SCHA.DI.00 (*Pavón-Carrasco et l., 2008b*); HHK1998 (*Hongre et al., 1998*); gufm1 (*Jackson et al., 2000*).

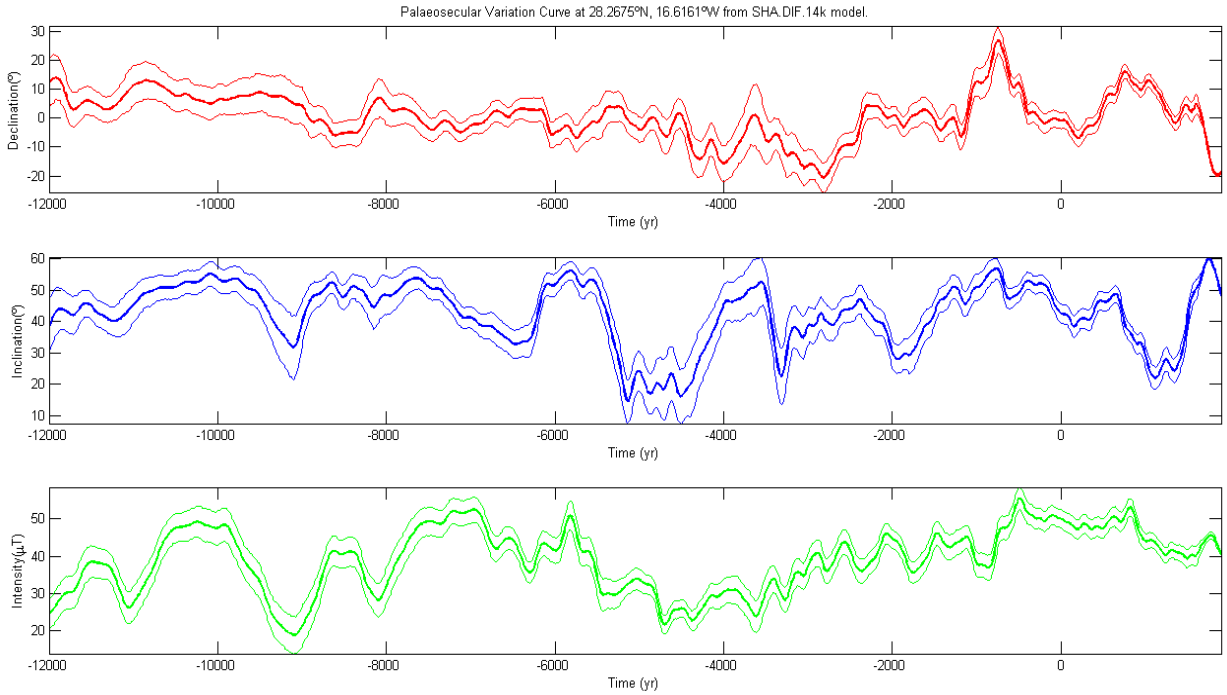

Fig. 2.21 Declination, inclination and intensity values for the last 14 ka at Tenerife (Canary Islands), according to SHA.DIF.14K model (*Pavón-Carrasco et al., 2014*).

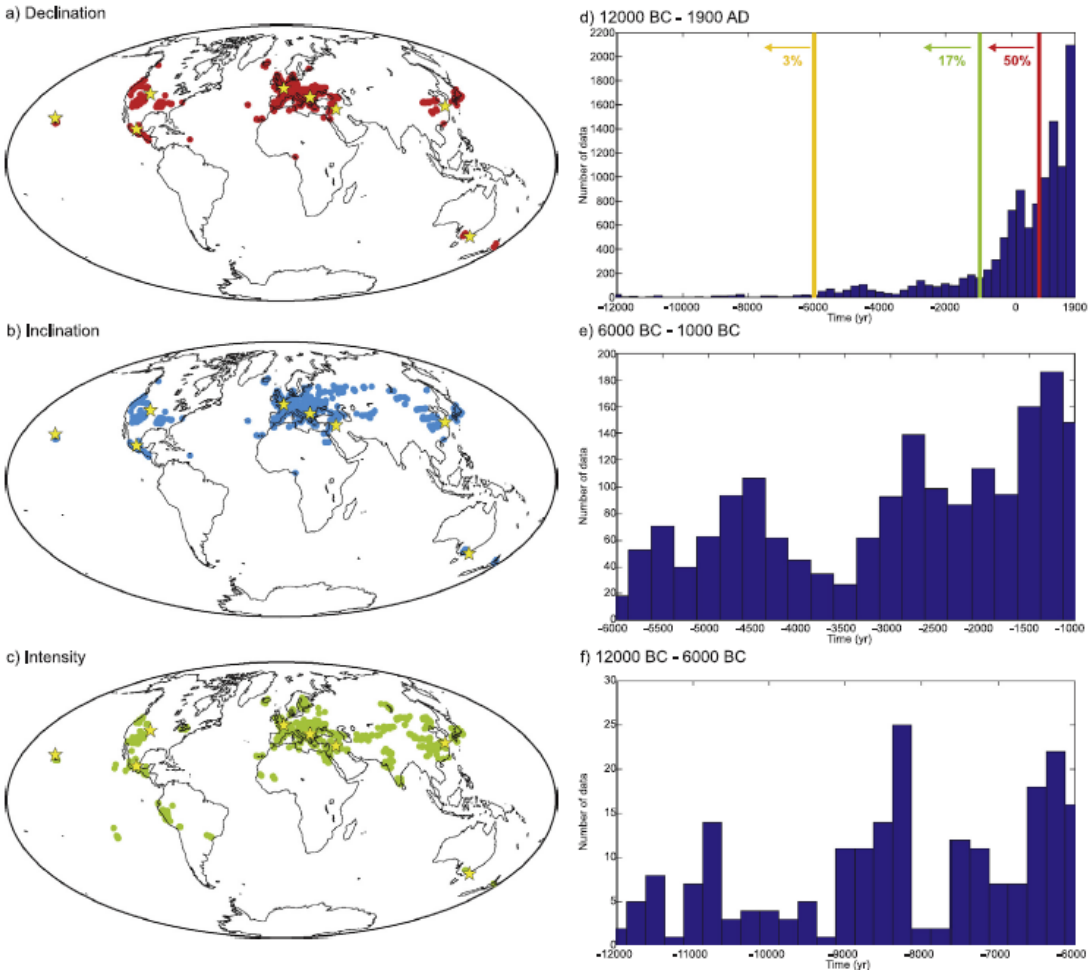

Fig. 2.22 Spatial and time distribution of palaeomagnetic data (declination, inclination and intensity) used to construct the SHA.DIF.14K model (from *Pavón-Carrasco et al., 2014*).

2.2.2 Pros and cons of the palaeomagnetic dating and reliability of the method

Palaeomagnetic dating has some unquestionable advantages, which include:

1) the possibility to get whole-rock samples: samples are usually taken from the rock and are cut into specimens and analysed without further treatment. Conversely, other dating techniques need to isolate crystals, which can be a difficult and time-consuming task;

2) the application to nearly all lava types (from acid to basic) because magnetic minerals are present in all lava compositions, from rhyolite to basanite;

3) previously gathered palaeomagnetic directions can be re-dated as soon as new reference PSV data and curves are available;

4) palaeomagnetic dating provides in most cases higher accuracy dating than other isotopic methods (of course considering only the Holocene epoch).

However, palaeomagnetic dating does not provide absolute ages, as the radiometric methods do, but gives compatibility age windows that depend upon the availability and quality of archaeo- and palaeomagnetic reference PSV data for the same temporal window. Moreover, palaeomagnetic dating can be used only to date rocks of the last 14 thousand years (*Pavón-Carrasco et al., 2014)*, because the available PSV curves are reconstructed and/or modelled only for the Holocene epoch.

It is important also to highlight that several possible sources can yield scatter of palaeomagnetic directions, that may translate into wrong ages:

1) local magnetic anomalies generated by the strongly magnetized underlying terrain and cooling lava flow (*Baag et al., 1995; Valet and Soler, 1999; Speranza et al., 2006*). The presence of these anomalies can produce significant deviations of the magnetic needle, which is apparent when sun and magnetic compass readings are compared. *Baag et al. (1995) and Valet and Soler (1999)* confirmed it by field measurements carried out at Hawaii and Canary Islands, where field deflections up to 15°–20° than the expected values were observed. Nevertheless, *Valet and Soler (1999)* showed that sampling over large distances within each lava flow would provide the best way to average out the contribution of the anomalies. Finally,

Tanguy and Le Goff (2004) documented much smaller (<3°) field deviations at a dozen measurement sites at Etna (*Speranza et al., 2006; 2010; 2012*);

2) Regional magnetic anomalies due to strongly magnetic bodies lying at depth;

3) variability of the magnetic mineralogy and magnetic anisotropy;

4) internal viscous deformation of lava flows and/or movement of blocks and lava during flow advance;

5) local tectonic effects and block tilting.

2.3 The palaeomagnetic estimate of emplacement temperature of pyroclastic flows

For two decades at least, palaeomagnetism has been considered one of the best methods to quantitatively assess the emplacement temperature (T_{emp}) of one of the most hazardous volcanic phenomena for populations, i.e. PDCs. Since the 1902 eruptions of Mount Pelée (Martinique), which killed 30,000 people, the perception of the danger and devastating power of PDC produced resulting from different types of explosive volcanic activity has grown dramatically (*Sigurdsson et al., 2000*). PDCs are a mixture of hot volcanic particles and gas, originated by a plethora of different phenomena and processes, such as eruptive column collapse, lateral blasts and/or lava-domes collapse (*Druitt, 1998; Branney and Kokelaar, 2002; Sulpizio et al., 2014*). PDCs can be generated also from the collapse of a part of volcanic edifices, due to the unstable conditions characterizing the craters rim and/or the slopes, or to gravitational instability of piled materials (*Salvatici et al., 2016*). They can transport large volumes of hot debris for many kilometres with high velocity and temperatures. The T_{emp} of a pyroclastic flow is the combined result of several factors, such as the starting magmatic temperature (directly linked with the magmatic composition of the magma), the eruptive style and the interaction with external factors, like air, water and vegetation during their travel (*McClelland and Druitt, 1989*).

The technique is based on the palaeomagnetic analysis of lithic clasts that contain ferromagnetic minerals (*Bardot and McClelland, 2000; Paterson et al., 2010*). During a pyroclastic eruption, a large amount of lithic clasts can be torn away from both the conduit system, magma chamber, vents and/or picked up from the ground surface. Lithic clasts are

supposed to possess an original magnetic remanence acquired during their formation and/or before the volcanic event considered (Fig. 2.23a, b). When they are incorporated into a PDC, they can be heated up to a temperature close to the mean temperature of the flow (thermal equilibration). The heating process erases a portion of the magnetic remanence carried by ferromagnetic grains having blocking temperatures (T_b) lower than the PDC temperature. The time to reach the equilibrium temperature depends on the volume and temperature of the deposit compared to lithic fragment size (*Zanella et al., 2015* and reference therein). Obviously, if the pyroclastic flow has a temperature higher than the T_c of the magnetic grains, all the original magnetic remanence will be completely unblocked and erased.

When the PDC halts and drops off the clasts, lithic clasts start to cool along with the ignimbrite and acquire a new, partial Low-T_b (LT) thermal magnetization, oriented along the local Earth's magnetic field direction at the time of emplacement (Fig. 2.23c). Consequently, lithic clasts will have two magnetic components: the High-T_b (HT) component, that is the primary magnetic component randomly oriented (as clasts were incorporated in the PDC and rotated from their original setting), and the LT component, the second magnetic component acquired after deposition and oriented along the local geomagnetic field direction. The re-heating temperature (T_r) of each clast is estimated between the highest Tb of the LT component and the lowest Tb of the HT component.

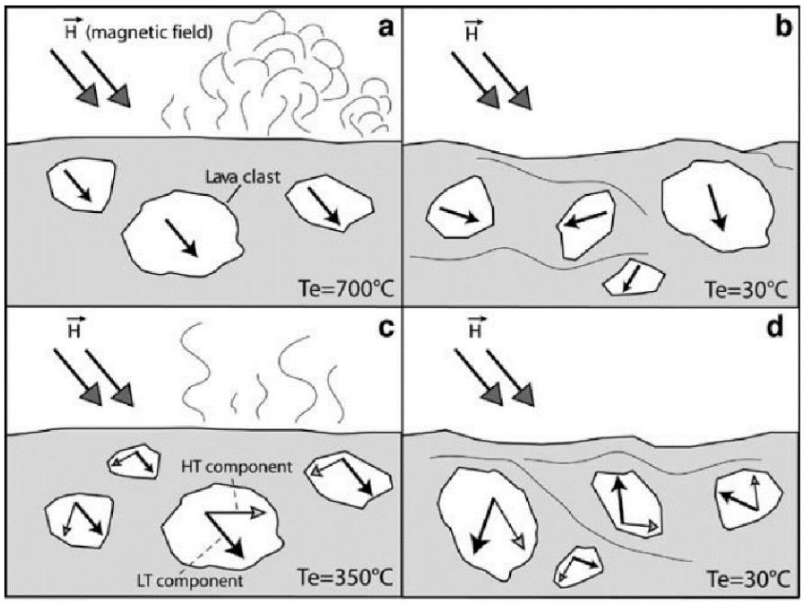

Fig. 2.23 Schematic model of palaeomagnetic categories and emplacement temperature (from *Porreca et al., 2008*). H is magnetic field. T_e is the deposit temperature. a) $T_e > T_c$ and clasts carry only 1 component, oriented along the magnetic field during the cooling; b) clast are reworked at ambient temperature (T_e=30 °C), then they record the first magnetic orientation, even if H is changed; c) clasts are reworked at intermediate temperature (T_e=350 °C), and then they have two magnetic components, HT (from 590° to 350 °C),

representing the first component randomly oriented, and LT (from 350 °C to ambient temperature) oriented along H; d) clasts have two magnetic components, both randomly oriented.

To establish the mean T_{emp} of the deposit, two different approaches can be followed: 1) *McClelland et al. (2004),* and 2) *Cioni et al. (2004).*

1) *McClelland et al. (2004)* collected and analysed lithic clasts from the 1.8 -ka Taupo ignimbrite (New Zealand) to determine the palaeotemperature and the thermal structure of the deposit. In this study, they assumed that clasts with initial temperatures lower than the mean deposit temperature will heat up to the mean temperature of the deposit, before cooling to ambient temperature, and that re-magnetization of grains with T_b values less than the mean temperature will occur. Therefore, clasts will record the T_{emp} values, ranging from the mean temperature of the deposits at emplacement to the maximum initial temperature of a clast. According to the authors, the T_{emp} is the temperature at which the deposit starts to cool as a whole, close to the lowest value of the T_r of the sampled clasts in a particular location, and represents the equilibrium state at which all the different thermal populations start to cool.

2) *Cioni et al. (2004)* evaluated the emplacement temperature of the deposits produced by the PDCs of the AD 79 "Pompei" eruption of Vesuvius (Italy), analysing both lava and roof tile fragment clasts. They suggested that clasts could record different cooling conditions as a function of their position in the deposit, especially in thin pyroclastic flows or near the boundaries of the deposits. For this reason, they considered as deposit temperature the mean value given by the overlap of several T_r.

Furthermore, it is important to keep in mind some conditions to correctly estimate the T_{emp}: 1) not all the clasts embedded in the deposit will reach thermal equilibrium. It depends on the size of the lithic clasts (big clasts of several tens of cm in diameter will remain cool in their cores; *Marti et al., 1991; Bardot, 2000*); 2) after deposition, clasts can be subjected to several reworking, possibly recording the temperature of each reworking; 3) the different time scale between the laboratory analyses and the natural processes causes an overestimation of the T_{emp} of the deposit, which increases with increasing thickness. However, this correction is not necessary for deposits <10 m in thickness (*Porreca et al., 2008,* and reference therein). Finally, especially for old deposits, it is important to consider the possible presence of a VRM. According to *Bardot and McClelland (2000)*, using the nomograms of *Pullaiah et al. (1975*; see

Fig. 2.3) the temperature at which the VRM is erased can be exactly calculated with the relation between the relaxing time (τ) and the T_b:

$$T_b = 75+15\log \tau.$$

For example, the VRM unblocking temperature of the magnetite for a 50-60 ka deposit is ~150 °C (Fig. 2.24). Therefore, the T_{emp} estimate is valid only above the temperature value unaffected by the VRM, which can be calculated considering the age of the deposit (*Bardot and McClelland, 2000)*.

Although other techniques exist to evaluate the T_{emp} of a pyroclastic flow, such as the direct measurements of the flow with thermal probe or by satellite (*Banks and Hoblitt 1981; Cole et al. 1998; Denniss et al., 1998; Calder et al. 1999; Druitt et al. 2002*), the study of the oxidation colours of pumices (*Tsuboi and Tsuya 1930*), the infrared spectroscopy of wood fragments (*Maury, 1971*), the analysis of bone fragments (*Capasso et al., 2000; Mastrolorenzo et al., 2001, 2010*), the melting points of plastic bottles (*Voight and Davis, 2000*), the H/C ratio of carbonized wood (*Sawada et al., 2000*) and above all the reflectance analysis of charred wood (*Scott and Glasspool, 2005; McParland et al., 2009; Ascough et al., 2010; Hudspith et al., 2010; Caricchi et al., 2014; Pensa et al., 2015b; Pensa et al., 2019*), the palaeomagnetic method has been probably the most applied at several volcanoes (Mount St. Helens, *Mullineaux and Crandell, 1962*; *Crandell, 1971*; *Crandell and Mullineaux, 1973; Hoblitt and Kellogg, 1979;* Greece, *Wright, 1978; McClelland and Druitt, 1989; McClelland and Thomas, 1993; Bardot et al., 1996; Bardot, 2000; Bardot and McClelland, 2000; Paterson et al., 2010;* Gallatin Mountains*, Chadwick, 1971;* Italy, *Kent et al., 1981; De Gennaro et al., 1996; Cioni et al., 2004; Porreca et al., 2006, 2008; Di Vito et al., 2009; Paterson et al., 2010; Zanella et al., 2008; 2015; Trolese et al., 2017;* Azores, *Pensa et al., 2015a, 2015b*; Spain, *Pares et al., 1993*; Mexico, *Urrutia-Fugugauchi, 1983; Clement et al., 1993; Alva-Valdivia et a., 2005; Paterson et al., 2010; Sulpizio et al., 2008, 2015; Pérez-Rodríguez et al., 2019;* New Mexico, *Moore et al., 1997;* Oregon Cascades*, Grubensky et al., 1998;* Guadeloupe*, Zlotnicki et al., 1984;* Indonesia, *Mandeville et al., 1994;* Australia, *van Otterloo et al., 2016*; Argentina, *Lesti et al., 2011;* Japan, *Yamazaki et al., 1973; Tamura et al., 1991; Sawada et al., 2000; Saito et al., 2003; Tanaka et al., 2004; Furukawa et al., 2014; Uheara et al., 2015;* Indonesian*, Mandeville et al., 1994;* New Zealand, *Smith et al., 1999*; *McClelland and Erwin, 2003*; *McClelland et al., 2004*; *Turner et al., 2018; Cole et al., 2019)*.

Bardot and McClelland (2000) examined the reliability of the emplacement temperature estimates. The palaeomagnetic technique is accurate if the low-T_b component of remanence is of thermal origin and acquired during transport and cooling in a pyroclastic flow. If It is not, the low-T_b component can be due to a VRM, resulting from a lightning strike, or a CRM. The authors applied palaeointensity experiments on samples from pyroclastic deposits from Santorini (Greece), in order to assess the magnetic origin of the low-T_b. Their experiments showed that some of their samples passed the stringent tests, while for others they found magnetic alteration. However, these cases display that, if a CRM is present, it has a direction parallel to the applied field that is different from the direction of the parent grain; therefore, it does not affect the estimate of emplacement temperature necessarily. Moreover, in two cases they found curvature between their two components of magnetization and ascribed it to the presence of MD grains.

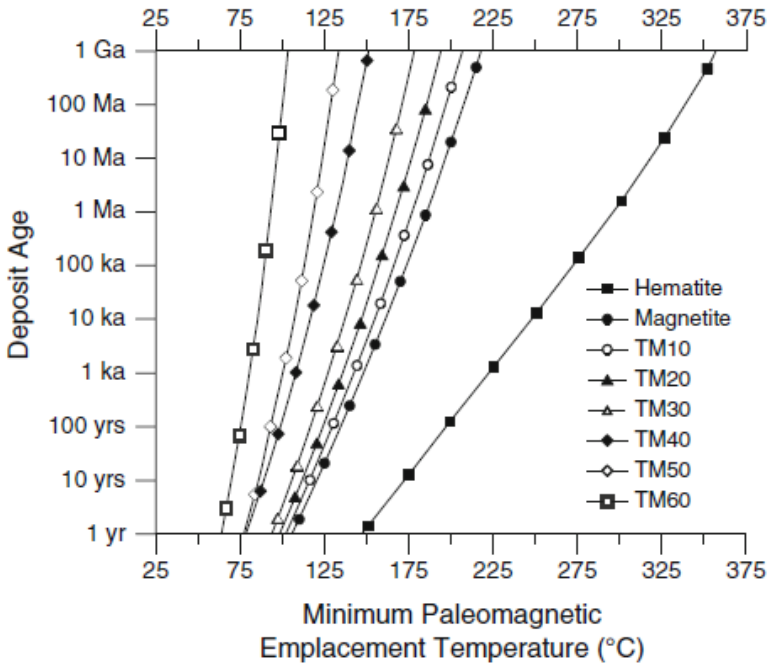

Fig. **2.24** Deposit age plotted versus minimum palaeomagnetic emplacement temperature as predicted by viscous magnetization theory for hematite, magnetite and titanomagnetite series (TM10–TM60) (from *Paterson et al., 2010*).

Paterson et al. (2010) studied lithic clasts collected from Mt. St. Helens (USA), Láscar volcano (Chile), Colima volcano (Mexico) and Vesuvius (Italy), to determine the emplacement temperature of pyroclastic deposits, and highlighted the usefulness of the palaeomagnetic technique for evaluating the emplacement temperatures in different types of deposit. The palaeomagnetic temperatures found for Mt. St. Helens are in agreement with the direct

measurements previously published (Fig. 2.25), with a temperature ≥509 °C. Lithic clasts from the pyroclastic deposits of Láscar volcano showed a complete remagnetization above the T_c, giving a minimum of emplacement temperature of the deposit of 397 °C. Conversely, the studied samples of the Colima volcano showed a cold temperature, probably linked with the lahar emplacement, common in such area. Finally, the pyroclastic deposits of the 472 AD deposits of Vesuvius showed two different temperatures: the lower section recorded a 280-340 °C, while the upper part recorded a higher temperature > 520 °C.

Trolese et al. (2017) studied the emplacement temperature of large-volume caldera-forming ignimbrites related to magmatic and phreatomagmatic eruptions at the Colli Albani volcano (Italy), collecting both juvenile and lithic clasts. To identify the mean T_{emp} for each site, they used the definition of *Cioni et al. (2004)*, i.e. the main overlap of T_{emp} of each clast at one site. They showed that all the magmatic ignimbrites were emplaced at high temperature, whereas the phreatomagmatic ignimbrite range between 200 and 400 °C (Fig. 2.26). They attributed such temperature difference due to the magma-water interaction, which can produce strong thermal dissipation even in large-volume eruptions.

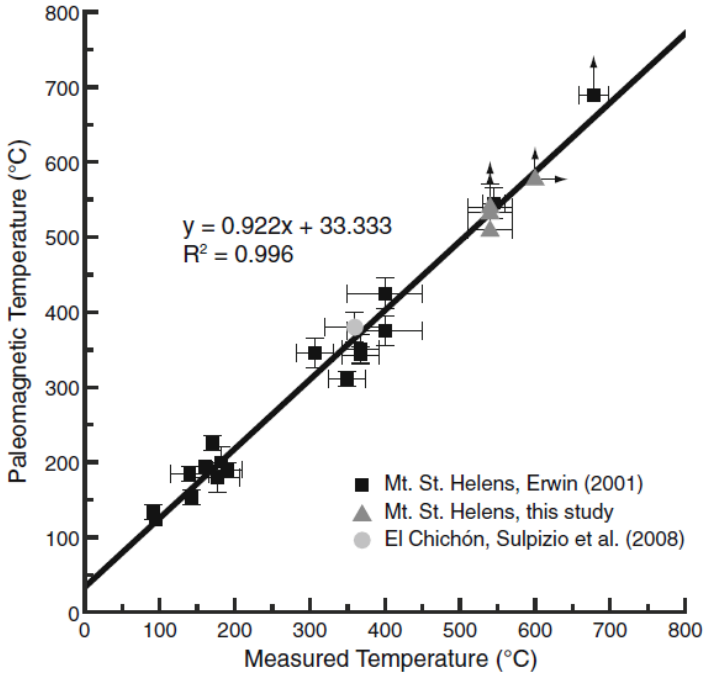

Fig. 2.25 Palaeomagnetic emplacement temperature versus directly measured emplacement temperature for the 1980 pyroclastic deposits at Mt. St. Helens, USA (from *Paterson et al., 2010*), and El Chichón (*Sulpizio et al. 2008*).

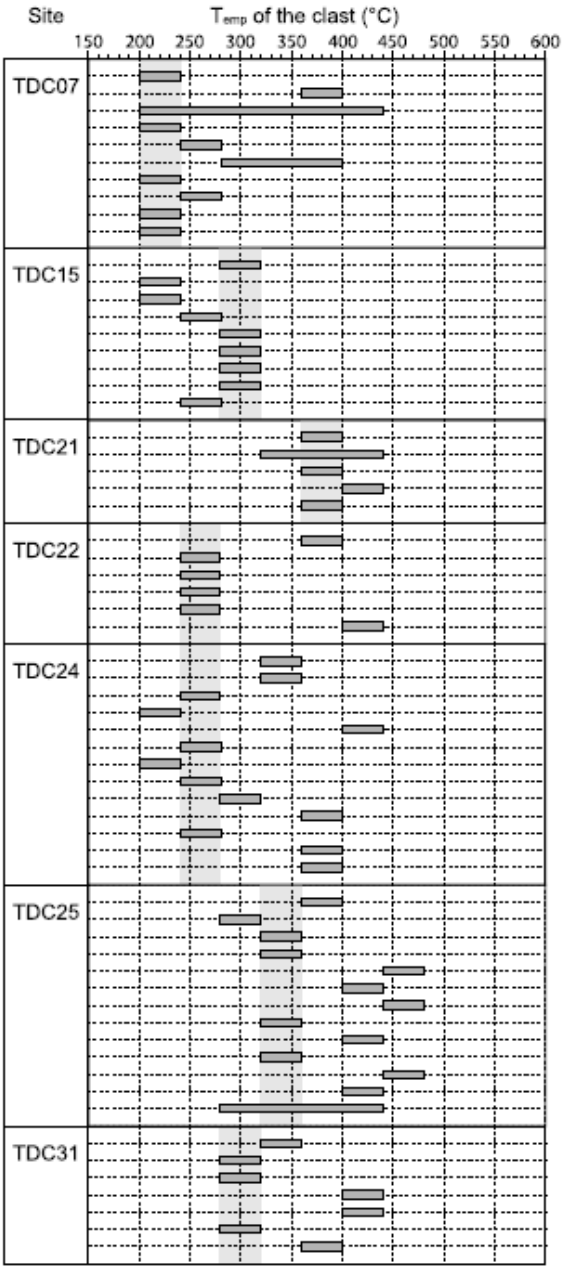

Fig. 2.26 Estimate of the T_{emp} of the Colli Albani phreatomagmatic deposit determined by the main overlap of individual clasts (from *Trolese et al., 2017*).

3 Sampling, methods and instruments

3.1 *Palaeomagnetic sampling*

One of the most important phases of a correct palaeomagnetic study is the sampling procedure. Techniques and sampling criteria vary with the different applications and investigations. However, some guidelines must be carefully followed to avoid possible disturbances caused by external factors.

Generally, fresh and unaltered outcrops must be chosen; in this way, alteration and/or oxidation of ferromagnetic minerals in hematite or other iron hydroxides can be avoided. These minerals, grown after the emplacement, can modify the remanent magnetization recorded by magnetite, with a possible secondary CRM overprinting. Attention should also be paid to avoiding areas in which lighting may frequently strike. The intense electric currents generated by lighting bolts generate a strong magnetic field that can produce secondary IRMs. For this reason, topographic height as crests and peaks must be avoided. Moreover, during cooling, fractures and tilting often occur, and for this reason, it is recommended to sample in the inner part of the lava flow, avoiding the external crust, tilted after cooling. Finally, local magnetic anomalies due to the topographic features at the surface of the flow should be avoided, spacing sites as much as possible along with the whole lava flow (*Valet and Soler, 1999)*.

A suitable sampling procedure involves the collection of many samples yielding a robust statistic data set from which to obtain the mean palaeomagnetic direction of the studied volcanic unit. For this reason, it is important to define a hierarchy of sampling strategy: 1) eruptive unit (or volcanic eruption); 2) site; 3) samples. In this work, samples have been named with three letters indicating the location, two numbers specifying the site number, and the other two numbers indicating the sample number. For example, TEN0105 will be sample 05, belonging to site 01, sampled on Tenerife island.

For the application in volcanology, the palaeomagnetic sampling can be done in three ways: 1) sampling cores in situ directly; 2) sampling blocks of rock, oriented in situ, in which cores will be drilled in the laboratory; 3) hand-sampling of small rock pieces, oriented in situ with a compass and a clinometer.

For consolidated rocks, the most common method to sample (used also in this work) is using a high-speed petrol-powered portable drill cooled by water, with a diamond drill stem of 2.5 cm in internal diameter drill (Fig. 3.1a, b). Drilled samples are usually from 3 to 10 cm in length. Once the cores have been obtained, they must be oriented before removal from the outcrop. Usually, a fiducial line is drawn lengthwise on the upper side, using an inclinometer and a magnetic compass. Due to the strong magnetization of volcanic rocks that sometimes can influence the compass needle, a solar compass is used jointly (Fig. 3.1d). The solar compass allows calculating the azimuth of each core reading the angle of the solar ray in the

specific ring. In this way, comparing the solar and magnetic readings, it is possible to correct any magnetic needle deviations. For each selected eruptive unit of Tenerife and El Hierro islands, four sites were sampled, spacing them as much as possible along the whole lava flow; at each site, ten to eleven cores were collected.

Fig. 3.1 a) and b) Palaeomagnetic sampling using a water-cooled, petrol-fuelled drill; c) hand-sampling of small pieces of rock embedded in a pyroclastic flow; d) Sun and magnetic compasses used to orient cores before the extraction; e) example of cores cut in a, b and c specimens; f) detail of a single core.

For unconsolidated sediments, such as recent ignimbrites, a common procedure is to carve cube-shaped samples and cover them with a plastic box, which is oriented in the same way as above. In this work, to sample the pyroclastic flow at El Fuego, both drilling cores (as above) and oriented small pieces (1-3 cm wide) of rocks, were collected. Concerning “hand-samples”

measurement, the dip azimuth and dip value of a roughly flat clast surface were measured in situ by a magnetic compass and a clinometer (Fig. 3.1c).

Finally, cores and hand samples are cut (Fig. 3.1e) into standard 2 cm-long cylindrical and 2 cm edge cubes specimens, respectively. Specimens were labelled with the letter *a*, *b*, and when possible *c* (Fig. 3.1f), from the outer to the inner section of the core. Usually, the outer section *a* is stored as a backup sample, and the *b* and/or *c* sections are used for doing magnetic experiments.

Analyses were done in the shielded room of the Palaeomagnetic Laboratory of the Instituto Nazionale di Geofisica e Vulcanologia (INGV-Rome).

3.2 Methods and Instruments

As described in the 2.1 paragraph, the main goal of the palaeomagnetic analyses is to isolate the primary NRM recorded by the rock. The NRM of a sample generally is composed of several components, carried by grains in different parts of the blocking temperature spectrum. To isolate and determine the characteristic component, specimens are progressively demagnetized, with incremental steps able to remove the magnetization through the coercivity spectrum or blocking temperature. The demagnetization can be done with the *alternating field (AF)* and *thermal (TH) cleaning.*

The *AF demagnetization* is based on the gradual exposition of a specimen to an alternating magnetic field, with a sinusoidal waveform linearly decreasing in magnitude with time (Fig. 3.2). This technique operates a progressive elimination of the weakest components of the remaining total magnetization depending on the coercivity spectrum. The amplitude of the alternating current (H_{AF}) is increased up to a chosen maximum value: typically, instruments can reach fields up to 120-150 mT. Each magnetic grain has a coercivity force that is directly connected with the size and grain itself: only the magnetic moments with coercivity force H_c smaller than H_{AF} value will be forced to re-orient along the magnetic field direction. This technique is efficient with rocks in which Ti-magnetite grains are present, whereas it is not suitable when there is hematite, due to the high coercivity force of this mineral that overtakes the H_{AF} values achievable with the instruments. After each step of AF demagnetization, the remanent component is measured.

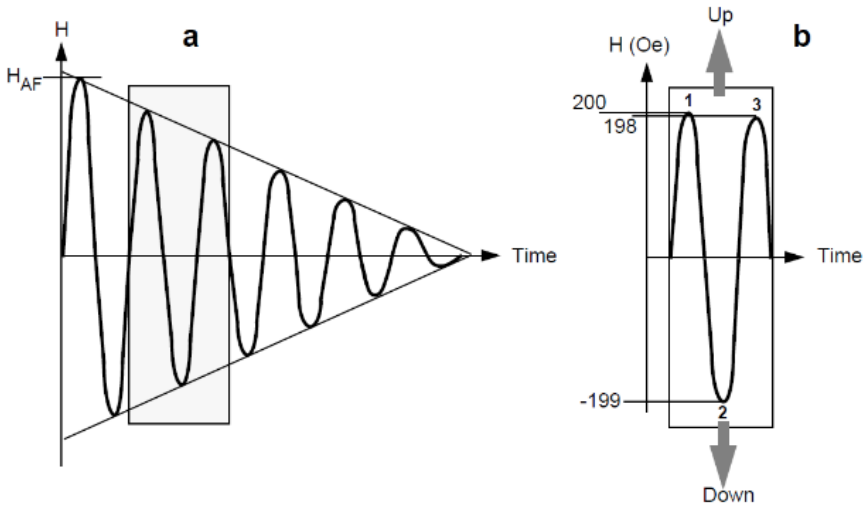

Fig. 3.2 Schematic representation of alternating-field demagnetization (from *Butler, 2004)*, with (a) generalized waveform of the magnetic field; H_{AF} represents the peak field. (b) Detailed examination of a portion of the AF demagnetization waveform.

The *TH cleaning* directly acts to the blocking temperature spectrum of the ferrimagnetic grains. It works taking advantage of the relaxing time, which is inversely proportional to the temperature (see 2.1 paragraph). Specimens are heated using predetermined temperatures, and cooled back to room temperature, in a zero magnetic field location. During the heating, the magnetic grains with blocking temperatures smaller than the instrumental temperature become superparamagnetic, losing the original remanent magnetization. For each increasing temperature step, higher blocking temperatures are eliminated, up to the Curie temperature of the principal magnetic minerals. After each heating and cooling step, the remanence magnetization is measured. The thermal cleaning is performed using special ovens, in which it is possible to heat and to cool in a zero magnetic field environment (as the shielded oven available at the Palaeomagnetic Laboratory of INGV).

Typically, the demagnetization data are shown using different graphical displays (Fig. 3.3). The most powerful diagram is the orthogonal diagram, also called *Zijderveld diagram (Zijderveld, 1967*), because it is possible to display simultaneously directional and intensity information on a single diagram, by projecting the vector into two orthogonal planes. Another way to show the directional data is using the equal-area projection; however, the stereographic projection contains no information regarding the intensity of magnetization, and it is essential to add a plot with the NRM intensity variation.

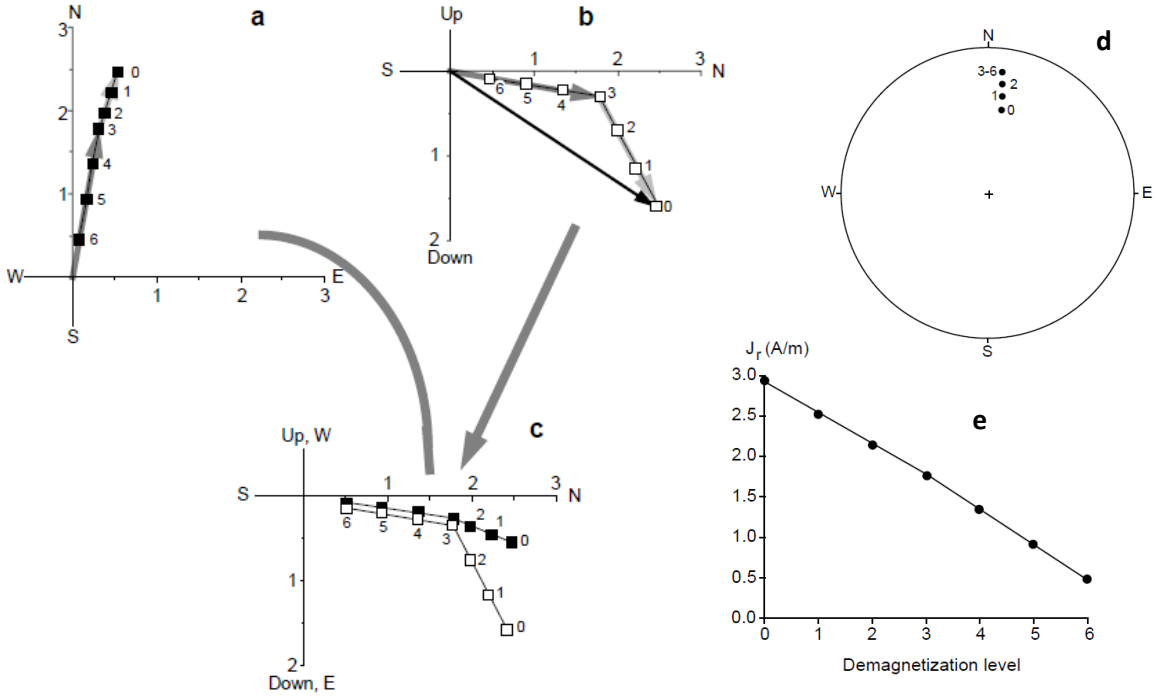

Fig. 3.3 Construction of a vector component diagram, and equal-area projection (modified from *Butler, 2004*. a) and b) represent the projection of the NRM vector into the horizontal and vertical planes oriented north-south, respectively. c) combined horizontal and vertical projections in a single diagram. Black and white squares represent declination and inclination data, respectively. The scale on the axes is A/m. d) Equal-area projection of the direction of NRM. e) NRM intensity versus demagnetization level.

Once the demagnetization data are obtained, principal component analysis, or PCA (*Kirschvink, 1980*) must be done for each specimen; it provides a rigorous way of estimating all magnetization components.

In PCA, the best-fit direction is computed to a preselected sequence of demagnetization data by analysis of a 3X3 matrix made up from the vector components. The best-fit direction is given by the eigenvector, and a statistic of the quality of the fit (i.e. the 'maximum angular deviation' or MAD) is derived from principal eigenvalues. Finally, palaeomagnetic data are analysed with Fisher's distribution (*Fisher, 1953*), i.e. the three-dimensional probability density distribution function, which is similar to a 2-D Gaussian or normal distribution. This statistical treatment is useful to estimate the reliability of the data, through two parameters, i.e. *k* and α_{95}. The first is the best estimate of the precision parameter and measures the dispersion of the population of directions about the mean direction. The increase of the k value indicates an increased clustering of the distribution of the directions around the mean direction, so high values of k are desirable. The α_{95} is the angle within which the unknown true

mean lies at 95% confidence level. It is possible to calculate it using the k value and N (number of samples), according to this formula:

$$\alpha_{95} = \frac{140}{\sqrt{(kN)}}$$

The Palaeomagnetic Laboratory of INGV is one of the most equipped laboratories worldwide. It is shielded from the Earth's magnetic field to operate in a protected environment: the intensity of the magnetic field inside the room screen is reduced to a few hundred nT (the Earth's magnetic field intensity in Rome is about 45,000 nT). Moreover, the instruments inside the room are protected by additional *μ-metal* shields to further insulate them from variable magnetic fields.

The instruments able to measure the NRM are the magnetometers. For this study, two types of magnetometers have been used, the *AGICO Dual Speed Spinner magnetometer (JR-6A) Spinner* (Fig. 3.4) and *2G Enterprises SQUID (Superconductive Quantum Interference Device) Cryogenic magnetometer* (Fig. 3.5). Generally, the *spinner magnetometer* takes advantage of electromagnetic induction: the sample rotates up to 90 cycles/s inside a pair of coils, producing an induced electromotive force proportional to the remanent magnetization of the sample. One specimen at a time can be analysed and for each step of demagnetization, it must be turned about at least two axes to obtain three orthogonal components of the magnetic moment and so calculate the total vector. This instrument is very reliable, especially recommended for high magnetized samples, but much more time-consuming than cryogenic magnetometers.

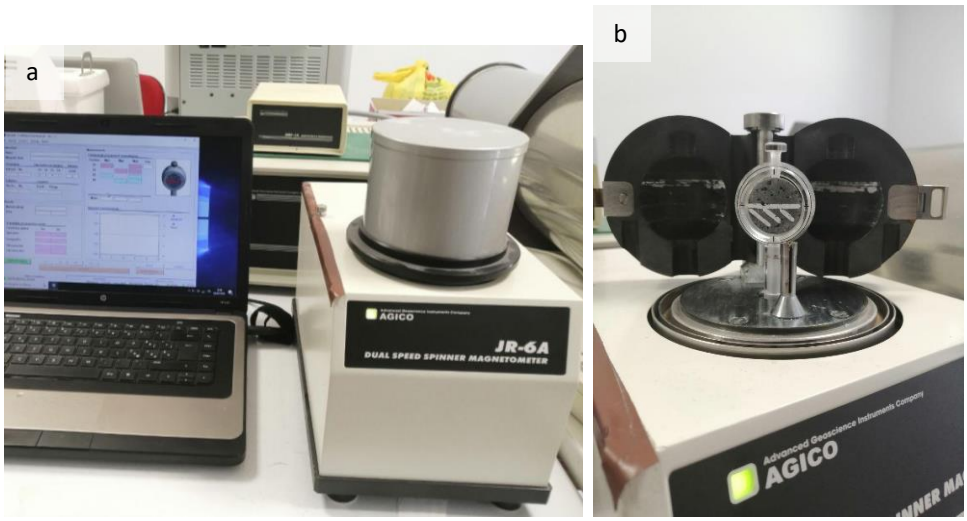

Fig. 3.4 AGICO Dual Speed Spinner magnetometer (JR-6A) Spinner at INGV Palaeomagnetic Laboratory; b) detail with the housing for the sample.

The *SQUID Cryogenic magnetometer* offers several improvements over other similar instruments: it is highly sensitive, with high speed of measurement and measuring several samples simultaneously. A magnetometer with DC SQUID sensors is based on the superconductivity of junctions at liquid helium temperature (4K). It can measure both standard discrete (cylinders of rock to 2.5 cm in diameter 2.2 cm high) and continuous palaeomagnetic samples (u-channels of up to 1.5 m in length and a square section of 1.9 cm side). Moreover, it is equipped with in-line apparatus that includes a system of three orthogonal coils for alternating magnetic field (AF) degaussing of the samples, with the possibility of imparting anhysteretic remanent magnetization (ARM- the magnetization produced for simultaneous application of a magnetic alternate field and a constant magnetic field) and a pulsed magnet that can produce a maximum axial magnetic field of 0.9 T. To ensure maximum shielding from external magnetic fields, the instrument is dressed in μ-metal, able to deflect the lines of force of the external magnetic field. Samples are arranged in a tray, and when they enter within the instrument, they generate an electric current due to the magnetic flux variation that is proportional to the magnetic momentum of the samples, according to Faraday's law:

$$\varepsilon = d\Phi/dt$$

where ε is the electromotive force, Φ is the magnetic flux and t is time.

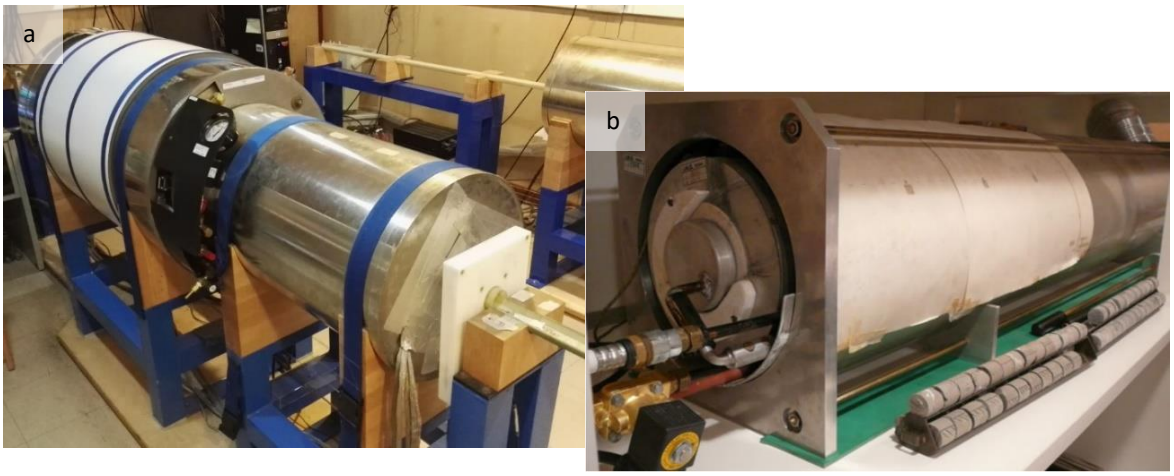

Fig. 3.5 a) 2G Enterprises SQUID Cryogenic magnetometer and b) Pyrox shielded oven, at the INGV Palaeomagnetic Laboratory.

The produced electric current is measured by SQUID sensors and converted in Am^2 (magnetic momentum) and A/m (intensity of magnetization).

To study and characterize the magnetic mineralogy of the sampled volcanic rocks, the *hysteresis cycles* and *k-T curves* were measured on representative samples.

Hysteresis properties (Fig. 3.6) are evaluated by submitting a sample to an increasing magnetic field in one direction and then in the opposite direction, with a constant temperature. It is possible to evaluate important parameters as saturation magnetization (M_s), saturation remanence (M_{rs}), coercive force (B_c) and remanent coercive force (B_{cr}). When the remanence (M_{rs} /M_s) versus coercivity (B_{cr}/B_c) ratios are plotted in a dedicated diagram, called Day-plot (*Day et al., 1977*), SD, MD and PSD magnetic minerals can be distinguished. Over the years, several theoretical curves for magnetites and Ti-magnetites were computed (*Dunlop, 2002a and 2002b* and reference therein).

The instrument used in this work to determine the hysteresis parameters is a Princeton Measurement Corporation MicroMag alternating gradient magnetometer (AGM, model 2900) with a maximum applied field of 1 T (Fig. 3.6).

Another method to identify the ferromagnetic minerals is through the k-T curves. These curves are obtained by measuring the magnetic susceptibility k at different temperatures. The powdered sample (Fig. 3.7) is exposed before a heating cycle (up to 700 °C) and later cooled back to room temperature, measuring the variation of the low-field magnetic susceptibility.

As the temperature increases, the T_C of the magnetic minerals is reached, and above this temperature minerals become paramagnetic, and consequently, a drop in the susceptibility is recorded (*Butler, 2004*). Therefore, because each magnetic mineral has a characteristic T_C, is possible to infer the magnetic mineral present in the sample. Samples were powdered using a Planetary Ball Mill PM 100 CM, and experiments were done using a Kappabridge MK1-FA coupled with a CS-3 furnace.

Finally, palaeomagnetic dating was obtained by comparing the palaeomagnetic directions of the studied eruptions to the SHA.DIF.14K PSV directional curve (*Pavón-Carrasco et al., 2014*), with the aid of the Matlab tool by *Pavón-Carrasco et al. (2011).* Through this software, it is possible to input the palaeomagnetic direction data, intensity, α_{95} and the location data, and to choose the PSV master curve (Fig. 3.8a).

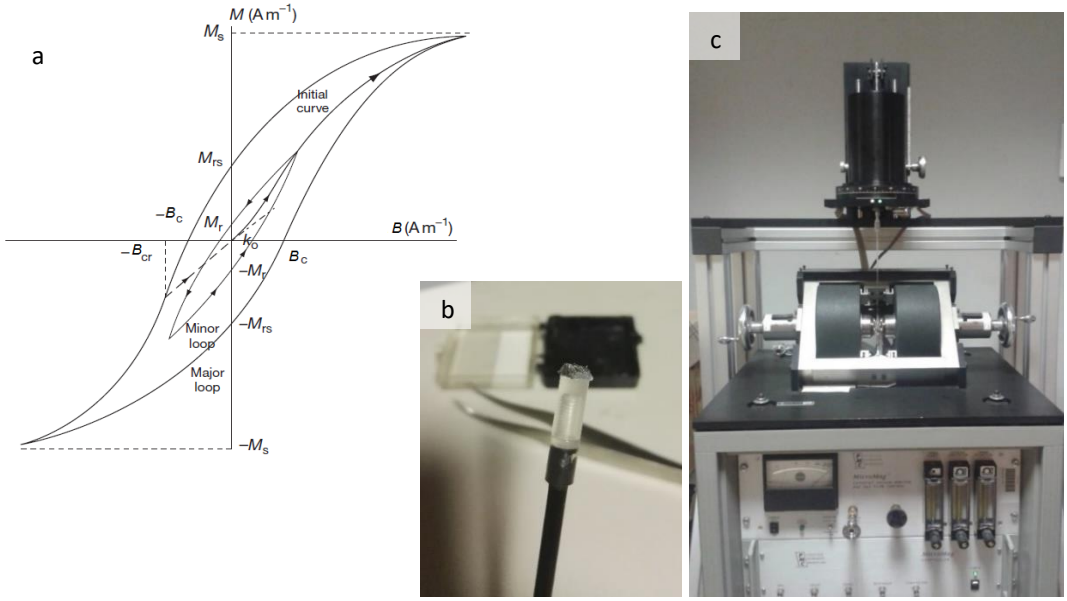

Fig. 3.6 a) Hysteresis loops. k_o (initial susceptibility), M_s (saturation magnetization), M_{rs} (saturation remanence), M_r (isothermal remanence, minor loop), H_c (coercive force), and H_{cr} (or B_{cr} remanent coercive force). Modified from *Kono (2015);* b) detail with the small piece of the specimen glued to the stick; c) Princeton Measurement Corporation MicroMag alternating gradient magnetometer (AGM, model 2900) at INGV Palaeomagnetic Laboratory.

Moreover, the whole time-interval covered by the curve (i.e. the last 14 ka) or defined age ranges can be investigated. The result is shown in a graph (Fig. 3.8b), in which several diagrams display the localization data in a map, the comparison between the palaeomagnetic direction and the PSV curve, and the probability density vs. years graphs, which represent the probability density for each variable. Finally, a combined graph shows the inferred age(s).

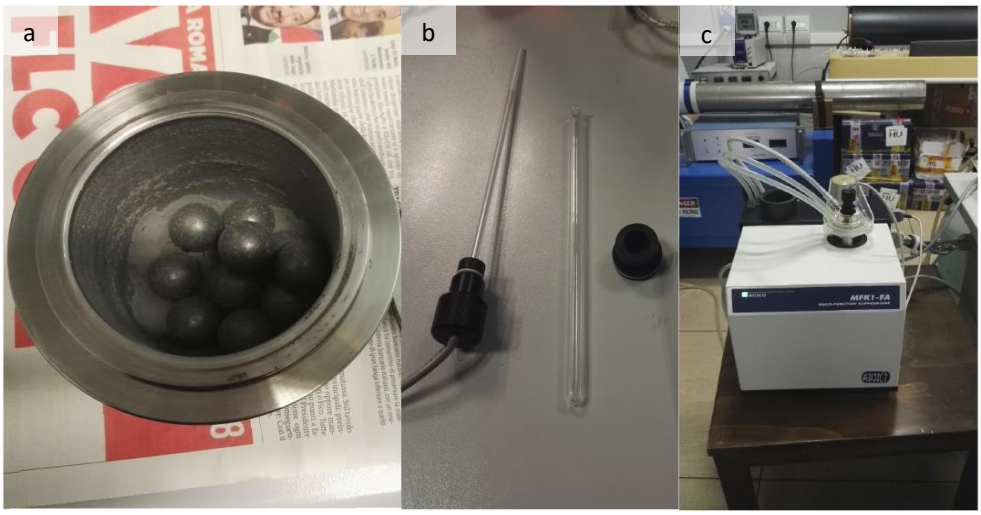

Fig. 3.7 a) Powdered sample with a Planetary Ball Mill PM 100; b) thermometer and glass tube used for the experiments; c) MFK1-FA instrument at INGV Palaeomagnetic Laboratory

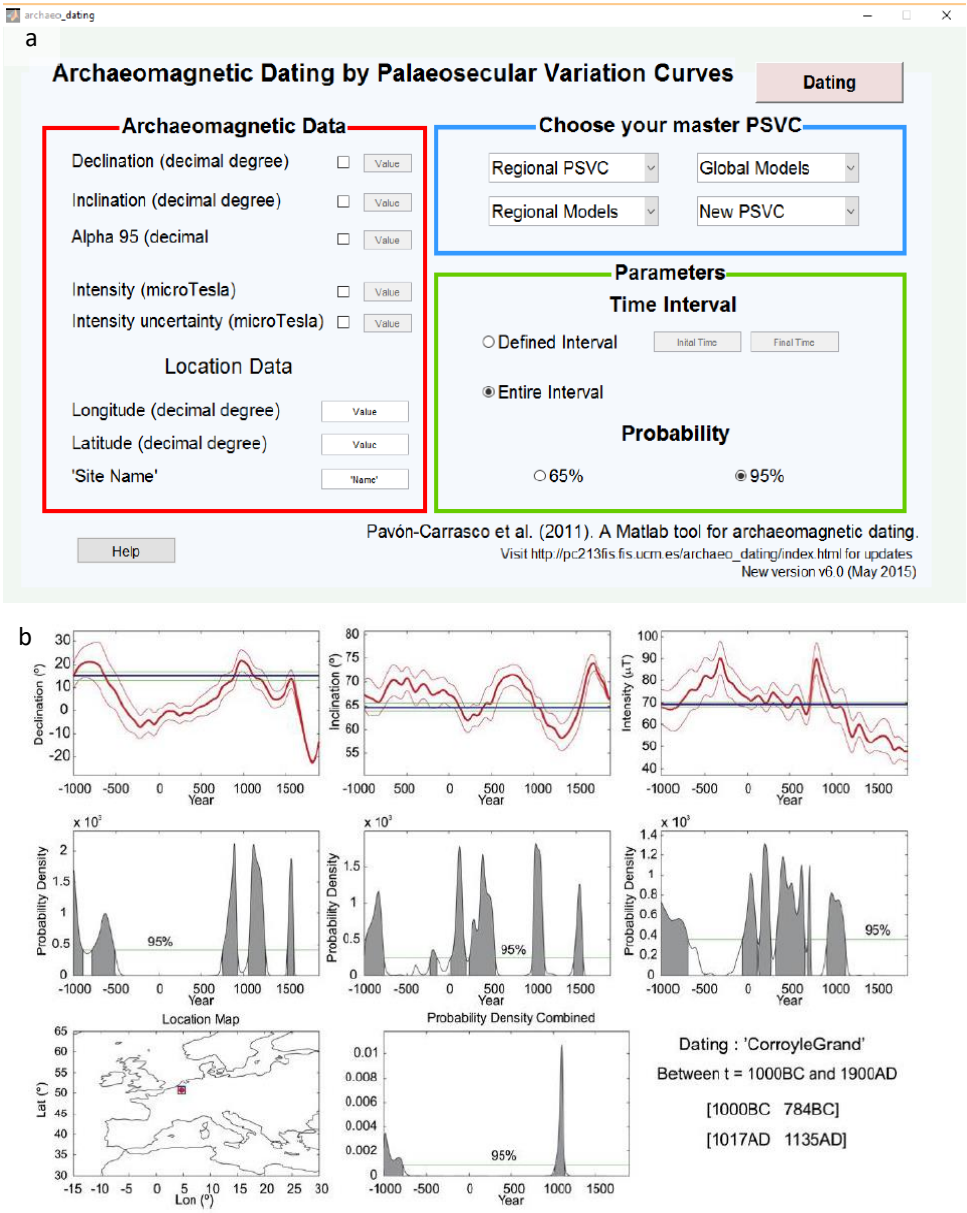

Fig. 3.8 a) Interactive window of the archaeo-dating Matlab tool of *Pavón-Carrasco et al. (2011)*; b) example of a dating result (from *Pavón-Carrasco et al., 2011).*

References

Aitken, M.J. (1958). Magnetic dating I. Archaeometry 1, 16–20.

Alva-Valdivia, L.M., Rosas-Elguera, J., Bravo-Medina, T., Urrutia-Fucugauchi, J., Henry, B., Caballero, C., Rivas-Sanchez, M.L., Goguitchaichvili, A., Lopez-Loera, H. (2005) Paleomagnetic and magnetic fabric studies of the San Gaspar ignimbrite, western Mexico—constraints on emplacement mode and source vents. J. Volcanol. Geotherm. Res. 147:68–80. doi:10.1016/j.jvolgeores.2005.03.006

Alva-Valdivia, L. M., Rodríguez-Trejo, A., Vidal-Solano, J. R., Paz-Moreno, F., Agarwal, A. (2019). Emplacement temperature resolution and age determination of Cerro Colorado tuff ring by paleomagnetic analysis, El Pinacate Volcanic Field, Sonora, Mexico. Journal of Volcanology and Geothermal Research, 369, 145-154.

Aramaki, S., Akimoto, S. (1957). Temperature estimation of pyroclastic deposits by natural remanent magnetism. Am. J. S., 255, 619–627.

Arrighi, S., Rosi, M., Tanguy, J.C., Courtillot, V. (2004). Recent eruptive history of Stromboli (Aeolian Islands, Italy) determined from high-accuracy archeomagnetic dating. Geophys. Res. Lett. 31, L19603.

Arrighi, S., Tanguy, J. C., Courtillot, V., LeGoff, M. (2005). Reply to comment by F. Speranza et al. on "Recent eruptive history of Stromboli (Aeolian Islands, Italy) determined from high-accuracy archeomagnetic dating". Geophysical Research Letters, 32(23).

Arrighi, S., Tanguy, J.C., Rosi, M. (2006). Eruptions of the last 2200 years at Vulcano and Vulcanello (Aeolian Islands, Italy) dated by high-accuracy archeomagnetism. Phys. Earth Planet. Inter. 159, 225–233.

Ascough, P.L. et al. (2010). Charcoal reflectance measurements: Implications for structural characterization and assessment of diagenetic alteration. J. Arch. S. 37, 1590–1599

Baag, C., C. E. Helsley, S. Xu, Lienert B. R. (1995). Deflection of paleomagnetic directions due to magnetization of the underlying terrain. J. Geophys. Res., 100(B6), 10,013–10,027.

Banks, N.G., Hoblitt, R. (1981). Summary of temperature studies of 1980 deposits. In: Lipman PW, Mullineaux DR (eds) The 1980 eruptions of Mount St. Helens, Washington. US Geol. Surv. Prof. Pap. 1250:295–313

Bardot, L. (2000). Emplacement temperature determinations of proximal pyroclastic deposits on Santorini, Greece, and their implications. Bull. Volcanol. 61, 450–467. http://dx.doi.org/10.1007/PL00008911.

Bardot, L., McClelland, E. (2000). The reliability of emplacement temperature estimates using palaeomagnetic methods: a case study from Santorini, Greece. Geophys. J. Int., 143, 39–51.

Bardot, L., Thomas, R., McClelland, E. (1996) Emplacement temperatures of pyroclastic deposits on Santorini deduced from palaeomagnetic measurements: constraints on eruption mechanisms. In: Morris A, Tarling DH (eds) Palaeomagnetism and tectonics of the Mediterranean region. Geol. Soc. London. Spec. Pub. 105:345–357

Batt, C.M., Brown, M.C., Clelland, S.J., Korte, M., Linford, P., Outram, Z. (2017). Advances in archaeomagnetic dating in Britain: new data, new approaches and a new calibration curve. J. Archaeol. Sci. 85, 66–82

Bogue, R.W., Coe R. S. (1981). Paleomagnetic correlation of Columbia River Basalt using Secular Variation. Journal of Geophysical Research, 86(B12), 883-897.

Böhnel, H., Pavón-Carrasco, F.J., Sieron, K., Mahgoub, A.N. (2016). Palaeomagnetic dating of two recent lava flows from Ceboruco volcano, western Mexico. Geophys. J. Int. 207 (2), 1203–1215.

Branca, S., D'Ajello Caracciolo, F., Malaguti, A. B., Speranza, F. (2019). Constraining age and volume of lava flow invasions of the Alcantara valley, Etna volcano (Italy). New insights from paleomagnetic dating and 3D magnetic modeling. J. Volcanol. Geoth. Res., 374, 13–25. https://doi.org/10.1016/j.jvolgeores.2019.02.009

Branney, M. J., Kokelaar, P. (2002). Pyroclastic Density Currents and the Sedimentation of Ignimbrites. Geol. Soc.., London, Memoirs, 27

Bucur, I. (1994), The direction of the terrestrial magnetic field in France, during the last 21 centuries. Recent progress, Phys. Earth Planet. Inter., 87, 95–109.

Butler, R.F. (2004). Paleomagnetism: Magnetic Domains to Geological Terranes

Cagnoli, B., Tarling, D. H. (1997). The reliability of anisotropy of magnetic susceptibility (AMS) data as flow direction indicators in friable base surge and ignimbrite deposits: Italian examples. J. Volcanol. Geoth. Res., 75, 309–320.

Calder, E.S., Cole, P.D., Dade, W.B., Druitt, T.H., Hoblitt, R.P., Huppert, H.E., Ritchie, L., Sparks, R.S.J., Young, S.R. (1999). Mobility of pyroclastic flows and surges at the Soufriére Hills Volcano, Montserrat. Geophys Res Lett 26:537–540. doi:10.1029/1999GL900051

Capasso, L., Caramiello, S., D'Anastasio, R., Di Domenicantonio, L., Di Fabrizio, A., Di Nardo, F., La Verghetta, M. (2000). Paleobiologia della popolazione di Ercolano (79 dC). Recenti Prog Med 91:288–296

Caricchi, C., Vona, A., Corrado, S., Giordano, G. & Romano, C. (2014). 79 AD Vesuvius PDC deposits' temperatures inferred from optical analysis on woods charred in-situ in the Villa dei Papiri at Herculaneum (Italy). J. Volcanol. Geoth. Res. 289, 14–25

Carlut, J., Quidelleur, X., Courtillot, V., & Boudon, G. (2000). Paleomagnetic Directions And K/Ar Dating of 0 To 1 Ma Lava Flows From La Guadeloupe Island (French West Indies): Implications For Time-Averaged Field Models. J. Geoph. Res., 105(B1), 835. Doi:10.1029/1999jb900238

Casas, Ll., and Incoronato, A. (2007) Distribution analysis of errors due to relocation of geomagnetic data using the 'conversion via pole' (CVP) method: Implications on archaeomagnetic data: Geophysical Journal International, v.169, p.448–454, doi:10.1111/j.1365-246X.2007.03346.x.

Chadwick, R.A. (1971) Paleomagnetic criteria for volcanic breccia emplacement. Geol Soc Amer Bull 82:2285–2294. doi:10.1130/0016-7606(1971)82[2285:PCFVBE]2.0.CO;2

Chauvin, A., Garcia, Y., Lanos, Ph., Laubenheimer, F. (2000). Paleointensity of the geomagnetic field recovered on archaeomagnetic sites from France. Phys. Earth Planet. Int. 120, 111-136.

Chenet, A. L., Fluteau, F., Courtillot, V., Gérard, M., Subbarao, K. V. (2008). Determination of rapid Deccan eruptions across the Cretaceous-Tertiary boundary using paleomagnetic secular variation: Results from a 1200-m-thick section in the Mahabaleshwar escarpment. Journal of Geophysical Research: Solid Earth, 113(B4).

Chenet, A. L., Courtillot, V., Fluteau, F., Gérard, M., Quidelleur, X., Khadri, S. F. R., et al. (2009). Determination of rapid Deccan eruptions across the Cretaceous-Tertiary boundary using paleomagnetic secular variation: 2. Constraints from analysis of eight new sections and synthesis for a 3500-m-thick composite section. Journal of Geophysical Research: Solid Earth, 114(B6).

Chevallier, R. (1925). L'aimantation des laves de l'Etna et l'orientation du champ terrestre en Sicile du XIIeme au XVIIeme siècle. thèse, 163 pp., Univ. of Paris, Paris.

Christensen, U. R., Wicht, J. (2007). Numerical dynamo simulations. G. Schubert (Ed.), Treatise of Geophysics, 8, Elsevier, Amsterdam, 245–282.

Cifuentes-Nava, G., Goguitchaichvili, A., López-Loera, H., Cervantes, M., Cortés, A., Sánchez-Bettucci, L., et al. (2017). Full vector magnetic dating of some pyroclastic rocks associated to the Colima volcano, western Mexico. Boletín de la Sociedad Geológica Mexicana, 69(3), 577-590.

Cifuentes-Nava, G., Cervantes-Solano, M.Á, Díaz-Ortega, U., Goguitchaichvili, A., López-Loera, H., Rosas-Elguera, J., Delgado-Granados, H., Morales-Contreras, J., Cejudo-Ruíz, R., Urrutia-Fucugauchi, J. (2019) Archeomagnetic dating of Holocene lava flows from Ceboruco volcano, western Mexico. Boletin de la Sociedad Geologica Mexicana, Volume 71, Issue 2, 2019, Pages 445-455

Cioni, R., Gurioli, L., Lanza, R., Zanella, E. (2004). Temperatures of the AD 79 pyroclastic density current deposits (Vesuvius, Italy). J. Geophys. Res., Solid Earth109, B02207. http://dx.doi.org/10.1029/2002JB002251.

Clark, A. J., Tarling, D. H., Noel, M. (1988). Developments in archaeomagnetic dating in Great Britain, J. Archaeol. Sci., 15, 645– 667.

Clement, B.M., Connor, C.B., Graper, G. (1993). Paleomagnetic estimate of the em-placement temperature of the long-runout Nevado de Colima volcanic de-bris avalanche deposit, Mexico. Earth Planet. Sci. Lett.120, 499–510. http://dx.doi.org/10.1016/0012-821X(93)90260-G.

Cole, P.D., Calder, E.S., Druitt, T.H., Hoblitt, R., Robertson, R., Sparks, R.S.J., Young, S.R. (1998). Pyroclastic flows generated by gravitational instability of the 1996–97 lava dome of Soufriére Hills Volcano, Montserrat. Geophys. Res. Lett. 25:3425–3428. doi:10.1029/98gl01510

Cole, R. P., Ohneiser, C., White, J. D. L., Townsend, D. B., & Leonard, G. S. (2019). Paleomagnetic evidence for cold emplacement of eruption-fed density current deposits beneath an ancient summit glacier, Tongariro volcano, New Zealand. Earth Planet Sc. Lett., 522, 155-165.

Constable, C.G., Johnson, C.L., Lund, S.P., (2000). Global geomagnetic field models for the past 3000 years: transient or permanent flux lobes? Phil. Trans. Roy. Soc. Lond. 358, 991–1008.

Constable, C., Korte, M., Panovska, S. (2016). Persistent high paleosecular variation activity in Southern Hemisphere for at least 10 000 years. Earth Planet Sci. Lett. 453, 78–86

Conte, G., Urrutia-Fucugauchi, J., Goguitchaichvili, A., Incoronato, A. (2006a). Paleomagnetic dating of lava flows of uncertain age, Somma-Vesuvius volcanic complex (Southern Italy). International Geology Review, 48(4), 349-359.

Conte, G., Urrutia-Fucugauchi, J., Goguitchaichvili, A., Incoronato, A., Tiano, P. (2006b). Lava identification by paleomagnetism: a case study and some problems surrounding the 1631 eruption of Mount Vesuvius, Italy. Earth, planets and space, 58(8), 1061-1069.

Crandell, D. (1971) Postglacial lahars from Mount Rainier Volcano, Washington. US Geol Surv Prof Pap 677:1–75

Crandell, D.R., Mullineaux, D.R. (1973) Pine creek volcanic assemblage at Mount St. Helens, Washington. US Geol. Surv. Bull. 1383-A:1–23.

Creer, K.M. (1974). Geomagnetic variations for the interval 7000-25,000 yr B.P. as recorded in a core of sediment from station 1474 of the Black Sea cruise of “Atlantis II”. Earth Planet Sci. Lett. 23, 34–42.

Creer, K.M., Readman, P.W., Papamarinopoulos, S. (1981). Geomagnetic secular variation in Greece through the last 6000 years obtained from lake sediment studies. Geophys. J. Roy. Astron. Soc. 66, 147–193.

David, P. (1910). Sur la stabilité de la direction d’aimantation dans quelques roches volcaniques. C. R. Acad. Sci.,Paris, 138, 41–42.

Day, R., Fuller, M., Schmidt, V.A. (1977). Hysteresis properties of titanomagnetites: grain-size and compositional dependence. Physics of the Earth and planetary interiors, 13(4), 260-267.

De Boer, J. (1968). Paleomagnetic differentiation and correlation of the Late Triassic volcanic rocks in the central Appalachians (with special reference to the Connecticut Valley). Geological Society of America Bulletin, 79(5), 609-626.

De Gennaro, M., Naimo, D., Gialenella, P., Incoronato, A., Mastrolorenzo, G. (1996) Palaeomagnetic controls on the emplacement of the Neapolitan Yellow Tuff (Campi Flegrei, Southern Italy). In: Morris A, Tarling DH (eds) Palaeomagnetism and tectonics of the Mediterranean region. Geol. Soc. London. Spec. Pub. 105:359–365

De Marco, E., Spatharas, V., Gómez-Paccard, M., Chauvin, A., Kondopoulou, D. (2008). New archaeointensity results from archaeological sites and variation of the geomagnetic field intensity for the last 7 millennia in Greece. Phys. Chem. Earth 33, 578-595.

Denniss, A. M., Carlton, R. W. T., Harris, A. J. L., Rothery, D. A., Francis, P. W. (1998). Satellite observations of the April 1993 eruption of Láscar Volcano. Int. J. Remote Sens. 19:801–821. doi:10.1080/014311698215739

Di Chiara, A., Speranza, F., Porreca, M. (2012). Paleomagnetic secular variation at the Azores during the last 3 ka. J. Geophys. Res. 117, B07101. https://doi.org/ 10.1029/2012JB009285.

Di Chiara, A., Speranza, F., Porreca, M., Pimentel, A., D'Ajello Caracciolo, F., Pacheco, J. (2014). Constraining chronology and time-space evolution of Holocene volcanic activity on the Capelo Peninsula (Faial Island, Azores): the paleomagnetic contribution. Geol. Soc. Am. Bull. 126, 1164–1180. https://doi.org/10.1130/B30933.1.

Di Chiara, A., Moncinhatto, T., Hernandez Moreno, C., Pavón-Carrasco, F.J., Trindade, R.I.F. (2017). Paleomagnetic study of an historical lava flow from the Llaima volcano, Chile Journal of South American Earth Sciences, 77, pp. 141-149. doi: 10.1016/j.jsames.2017.04.014

Di Vito, M.A., Zanella, E., Gurioli, L., Lanza, R., Sulpizio, R., Bishop, J., Tema, E., Boenzi, G., Laforgia, E. (2009). The Afragola settlement near Vesuvius, Italy: the destruction and abandonment of a bronze age village revealed by archaeology, volcanology and rock-magnetism. Earth Planet. Sci. Lett. 277:408–421. doi:10.1016/j.epsl.2008.11.006

Doell, R. R., and Cox, A. (1963) The accuracy of the paleomagnetic method as evaluated from historic Hawaiian lava flows: Journal of Geophysical Research, v. 68(7), p. 1997-2009, https://doi.org/10.1029/JZ068i007p01997.

Doell, R.R., Dalrymple, G.B. (1966). Geomagnetic polarity epochs – A new polarity event and the age of the Brunhes–Matuyama boundary. Science 152: 1060–1061.

Donadini, F., Korhonen, K., Riisager, P., Pesonen, L. (2006). Database for Holocene geomagnetic intensity information. Eos Trans. AGU87(14),137.

Donadini, F., Korte, M., Constable, C.G. (2009). Geomagnetic field for 0e3 ka: 1. New data sets for global modelling. Geochem. Geophys. Geosyst. 10 (Q06007). doi:10.1029/2008GC002295.

Downey, W. S., Kellett, R. J., Smith, I. E. M., Price, R. C., Stewart, R. B. (1994). New palaeomagnetic evidence for the recent eruptive activity of Mt. Taranaki, New Zealand. JVGR, 60(1), 15-27.

Druitt, T. H. (1998). Pyroclastic density currents. In: Gilbert, J.S., Sparks, R.S.J. (eds) The physics of explosive volcanic eruptions. Geolog. Soc., London, Special Publications, 145(1), 145-182.

Druitt ,T.H., Calder, E.S., Cole, P.D., Hoblitt, R.P., Loughlin, S.C., Norton, G.E., Ritchie, L.J., Sparks, R.S.J., Voight, B. (2002). Small volume, highly mobile pyroclastic flows formed by rapid sedimentation from pyroclastic surges at Soufriere Hills Volcano, Montserrat; an important volcanic hazard. In: Druitt, D.H., Kokelaar, B. (eds) The eruption of Soufriére Hills Volcano, Montserrat, from 1995 to 1999. Mem. Geol. Soc. Lond. 21:263–279

DuBois, R.L. (1975). Secular variation in southwestern United States as suggested by archaeomagnetic studies. In: Fischer, R.M., Fuller, M., Schmidt, V.A., Wasilewski, P.J. (Eds.), Takesi Nagata Conference - Magnetic Fields: Past and Present. Goddard Space Flight Center, Greenbelt, Maryland.

Dunlop, D. J. (2002a). Theory and application of the Day plot (Mrs/Ms versus Hcr/Hc): 1. Theoretical curves and tests using titanomagnetite data. J. Geophys. Res., 107(B3), 2056, doi:10.1029/2001JB000486.

Dunlop, D. J. (2002b). Theory and application of the Day plot (Mrs/Ms versus Hcr/Hc): 2. Application to data for rocks, sediments, and soils. J. Geophys. Res., 107(B3), doi:10.1029/2001JB000487.

Eighmy, J.L., Sternberg, R.S., Butler, R.F. (1980). Archaeomagnetic dating in the American southwest. Am. Antiq. 45, 507–517

Ellwood, B. B. (1982). Estimates of flow direction for calc-alkaline welded tuffs and paleomagnetic data reliability from anisotropy of magnetic susceptibility measurements: central San Juan Mountains, southwest Colorado. Earth Planet Sc. Lett., 59, 303–314.

Evans, M. E., Hoye G. S. (2005). Archaeomagnetic results from southern Italy and their bearing on geomagnetic secular variation, Phys. Earth Planet. Inter., 151, 155– 162.

Finlay, C. C. (2012). Earth's eccentric magnetic field. Nat. Geosci. 5, 523–524.

Finn, D. R., Coe R. S. (2016). A new protocol for three-axis static alternating field demagnetization of rocks, Geochem. Geophys. Geosyst., 17, 1815– 1822, doi:10.1002/2015GC006178.

Finn, D. R., Coe, R. S., Brown, E., Branney, M., Reichow M., Knott, T., Storey, M., Bonnichsen B. (2016). Distinguishing and correlating deposits from large ignimbrite eruptions using paleomagnetism: The Cougar PointTuffs (mid-Miocene), southern Snake River Plain, Idaho, USA, J. Geophys. Res.Solid Earth, 121, 6293–6314,doi:10.1002/2016JB012984

Fisher, R. A. (1953). Dispersion on a sphere, Proc.R.Soc.Ser.A and Ser.B, 217, 195-305.

Furukawa K., Uno K., Shinmura T., Miyoshi M., Kanamaru T., Inokuchi H. (2014). Origin and mode of emplacement of lithic-rich breccias at Aso Volcano, Japan: Geological, paleomagnetic and petrological reconstruction. J. Volcanol. Geoth. Res. 276 (22-31).

Gallet, Y., A. Genevey, Le Goff, M. (2002). Three millennia of directional variation of the earth's magnetic field in western Europe as revealed by archaeological artefacts, Phys. Earth Planet. Inter., 131, 81– 89.

Genevey, A., Gallet, Y., Constable, C., Korte, M., Hulot, G. (2008). ArcheoInt: an upgraded compilation of geomagnetic field intensity data for the past ten millennia and its application to the recovery of the past dipole moment. Geochem. Geophys. Geosys. 9, Q04038. https://doi.org/10.1029/2007GC001881.

Giordano, G., Porreca, M., Musacchio, P., Mattei, M. (2008). The Holocene Secche di Lazzaro phreatomagmatic succession (Stromboli, Italy): evidence of pyroclastic density current origin deduced by facies analysis and AMS flow directions. Bull. Volcanol., 70(10), 1221-1236.

Gómez-Paccard, M., Lanos, Ph., Chauvin, A., McInstosh, G., Osete, M.L., Catanzariti, G., Ruiz-Martínez, V.C., Núñez, J.I. (2006). The first archaeomagnetic secular variation curve for the Iberian Peninsula. Comparison with other data from Western Europe and with global geomagnetic field models. Geochem. Geophys. Geosyst. 7 (Q12001). doi:10.1029/2006GC001476.

Greve, A., Turner, G. M. (2017). New and revised palaeomagnetic secular variation records from post-glacial volcanic materials in New Zealand. Phys. Earth Planet. Inter. 269, 1–17.

Greve, A., Turner, G. M., Conway, C.E., Townsend, D.B., Gamble, J.A., Leonard, G.S. (2016). Palaeomagnetic refinement of the eruption ages of Holocene lava flows, and implications for the eruptive history of the Tongariro Volcanic Centre, New Zealand. Geophys. J. Int. 207 (2), 702–718. https://doi.org/10.1093/gji/ggw296.

Grommè, C. S, McKee, E. H., Blake M. C. (1972). Paleomagnetic Correlations and Potassium-Argon Dating of Middle Tertiary Ash-Flow Sheets in the Eastern Great Basin, Nevada and Utah. GSA Bulletin, 83, 6, 1619-1638, doi: 10.1130/0016-7606

Grubensky, M.J., Smith, G.A., Geissman, J.W. (1998) Field and paleomagnetic characterization of lithic and scoriaceous breccias at Pleistocene Broken Top volcano, Oregon Cascades. J Volcanol Geotherm Res 83:93–114. doi:10.1016/S0377-0273(98)00006-7

Gurioli, L., Zanella, E., Gioncada, A., Sbrana, A. (2012). The historic magmatic-hydrothermal eruption of the Breccia di Commenda, Vulcano, Italy. Bulletin of volcanology, 74(5), 1235-1254.

Hagstrum, J.T., Champion, D.E. (1994). Paleomagnetic correlation of Late Quaternary lava flows in the lower east rift zone of Kilauea Volcano, Hawaii. J. Geophys. Res. 99:21,679–21,690.

Hagstrum, J.T., Blinman, E. (2010). Archeomagnetic dating in western North America: an updated reference curve based on paleomagnetic and archeomagnetic data sets. Geochem. Geophys. Geosyst. 11 (Q06009). doi:10.1029/2009GC002979.

Hayashida, A., Kamata, H., Danhara, T. (1996). Correlation of widespread tephra deposits based on paleomagnetic directions: link between a volcanic field and sedimentary sequences in Japan. Quaternary International, 34, 89-98.

Hellio, G., Gillet, N. (2018). Time-correlation-based regression of the geomagnetic field from archeological and sediment records. Geophys. J. Int. 214, 1585–1607.

Hirooka, K. (1971). Archaeomagnetic study for the past 2,000 years in southwest Japan. In: Memoirs of the Faculty of Science, Kyoto University, Series of Geol. & Mineral. XXXVIII, pp. 167–207.

Hoblitt, R. P., Kellogg, K. S. (1979). Emplacement temperature of unsorted and unstratified deposits of volcanic debris as determined by palaeomagnetic techniques, Geol. Soc. Am. Bull., 90, 633–642.

Hofman, J., Maher, B.A., Muxworthy, A.R., Wuyts, K., Castanheiro, A., Samson, R. (2017). Biomagnetic monitoring of atmospheric pollution: a review of magnetic signatures from biological sensors. Environ. Sci. Technol., 51 (12), pp. 6648-6664

Holcomb, R., Champion, D., & McWilliams, M. (1986). Dating recent Hawaiian lava flows using paleomagnetic secular variation. Geol. Soc. Am. Bull., 97(7), 829-839.

Hongre, L., Hulot, G., Khokhlov, A. (1998). An analysis of the geomagnetic field over the past 2000 years. Phys. Earth Planet. In. 106, 311–335.

Hoye, G. S. (1981), Archaeomagnetic secular variation record of Mount Vesuvius, Nature, 291, 216–218.

Hudspith, V.A., Scott, A.C., Wilson, C. J.N., Collinson, M.E. (2010). Charring of woods by volcanic processes: An example from the Taupo ignimbrite, New Zealand. Palaeogeogr. Palaeoclimatol. Palaeoecol. 291, 40–51

Incoronato, A., Angelino, A., Romano, R., Ferrante, A., Sauna, R., Vanacore, G., Vecchione, C. (2002). Retrieving geomagnetic secular variations from lava flows: evidence from Mounts Arso, Etna and Vesuvius (southern Italy). Geophys. J. Int. 149, 724–730.

Jackson, A., Jonkers, A.R.T., Walker, M.R. (2000). Four centuries of geomagnetic secular variation from historical records. Phil. Trans. Roy. Soc. Lond. 358, 957–990.

Juárez-Arriaga, E., Böhnel, H., Carrasco-Núñez, G., Mahgoub, A. N. (2018). Paleomagnetism of Holocene lava flows from Los Humeros caldera, eastern Mexico: Discrimination of volcanic eruptions and their age dating. J. S. Am. Earth Sci., 88, 736-748.

Jurado-Chichay, Z., Urrutia-Fucugauchi, J., Rowland, S. K. (1996). A paleomagnetic study of the Pohue Bay flow and its associated coastal cones, Mauna Loa volcano, Hawaii: constraints on their origin and temporal relationships. Phys. Earth Planet. Inter. 97 (1–4), 269–277. https://doi.org/10.1016/0031-9201 (95)03135-9.

Kent, D.V., Ninkovich, D., Pescatore, T., Sparks, R.S.J. (1981). Palaeomagnetic determination of emplacement temperature of Vesuvius AD 79 pyroclastic deposits, Nature, 290, 393–396

Kirschvink, J.L. (1980). The least-squares line and plane and the analysis of palaeomagnetic data. Geophys. J. R. Astron. Soc. https://doi.org/10.1111/j.1365-246X.1980.tb02601.x

Kissel, C., Gonzalez, A., Laj, C., Perez-Torrado, F., Carracedo, J., Wandres, C., Guillou, H. (2015). Paleosecular variation of the earth magnetic field at the Canary Islands over the last 15 ka. Earth and Planetary Science Letters. 412. 10.1016/j.epsl.2014.12.031.

Kono, M. (2015). Geomagnetism: an introduction and overview. Chapter 5. In: Schubert, G. (Ed.), Treatise on Geophysics. 2015. Elsevier.

Konstantinov, K. M., Bazhenov, M. L., Fetisova, A. M., Khutorskoy, M. D. (2014). Paleomagnetism of trap intrusions, East Siberia: Implications to flood basalt emplacement and the Permo–Triassic crisis of biosphere. Earth and Planetary Science Letters, 394, 242-253.

Korhonen, K., Donadini, F., Riisager, P., Pesonen, L. (2008). GEOMAGIA50: an archeointensity database with PHP and MySQL. Geochem. Geophys. Geosyst. 9. http://dx.doi.org/10.1029/2007GC001,893.

Korte, M., Constable, C. (2003). Continuous global geomagnetic field models for the past 3000 years. Phys. Earth Planet. In. 140, 73–89.

Korte, M., Constable, C.G. (2005). Continuous geomagnetic field models for the past 7 millennia: 2. CALS7K. Geochem., Geophys., Geosys. 6, Q02H16. https://doi.org/10. 1029/2004GC000801.

Korte, M., Constable, C. G. (2011). Improving geomagnetic field reconstruction for 0–3 ka, Phys. Earth Planet. Inter., 188, 247–259, doi:10.1016/j.pepi.2011.06.017.

Korte, M., Donadini, F., Constable, C.G. (2009). Geomagnetic field for 0e3 ka: 2. A new series of time-varying global models. Geochem. Geophys. Geosyst. 10 (Q06008). doi:10.1029/2008GC002297

Korte, M., C. G. Constable, Donadini F. (2011). Reconstructing the Holocene geomagnetic field, Earth Planet. Sci. Lett., 312(3–4), 497–505, doi:10.1016/j.epsl.2011.10.031.

Korte, M., Brown, M. C., Gunnarson, S. R., Nilsson, A., Panovska, S., Wardinski, I., Constable, C. G. (2019). Refining Holocene geochronologies using palaeomagnetic records. Quat. Geochronol., 50, 47-74.

Kovacheva, M. (1980). Summarized results of the archaeomagnetic investigation of the geomagnetic field variation for the last 8000 yr in south-eastern Europe. Geophys. J. Int. 61 (1), 57–64.

Kovacheva, M., Jordanova, N., Karloukovski, V. (1998). Geomagnetic field variations as determined from Bulgarian archaeomagnetic data. Part II: The last 8000 years, Surv. Geophys., 19, 431–460.

Kovacheva, M., Boyadziev, Y., Kostadinova, M., Jordanova, N., Donadini, F. (2009). Updated archeomagnetic data set of the past 8 millennia from the Sofia laboratory Bulgaria. Geochem. Geophys. Geosyst. 10 (Q05002). doi:10.1029/ 2008GC002347.

Kovacheva, M., Kostadinova-Avramova, M., Jordanova, N., Lanos, P., and Boyadzhiev, Y. (2014). Extended and revised archaeomagnetic database and secular variation curves from Bulgaria for the last eight millennia, Phys. Earth Planet.Int., 236, 79–94.

Knudsen, M.F., Riisager, P., Donadini, F., Snowball, I., Muscheler, R., Korhonen, K., Pesonen, L.J., Jacobsen, B.H. (2008). Variations in the geomagnetic dipole moment during the Holocene and the past 50 kyr. Earth Planet Sci. Lett. 272, 319–329.

Lanza, R., Zanella, E. (2003). Paleomagnetic secular variation at Vulcano (Aeolian Islands) during the last 135 kyr. Earth Planet. Sci. Lett. 213, 321–336.

Lanza, R., Zanella, E. (2006). Comments On "Chronology Of Vesuvius' Activity From A.D. 79 To 1631 Based On Archeomagnetism Of Lavas And Historical Sources" By C. Principe Et Al., Bull Volcanol. Bull. Volcanol., 68(4), 394–396. Doi:10.1007/S00445-005-0030-9

Lanza, R., Meloni, A., (2006). The Earth's magnetism, an introduction for geologists. Springer edition,

Lanza, R., Meloni, A., Tema, E. (2005a). Historical measurements of the Earth's magnetic field compared with remanence directions from lava flows in Italy over the last four centuries. Physics of the Earth and Planetary Interiors, 148(1), 97–107. https://doi.org/10.1016/j.pepi.2004.08.005

Lanza, R., Meloni, A., Tema, E. (2005b). Reply to Comment on "Historical measurements of the Earth's magnetic field compared with remanence directions from lava flows in Italy over the last four centuries", by Tanguy, J.C., Principe C., Arrighi S. Physics of the Earth and Planetary Interiors, 152, 121–124.

Larrea, P., Siebe, C., Juárez-Arriaga, E., Salinas, S., Ibarra, H., Böhnel, H. (2019). The~ AD 500–700 (Late Classic) El Astillero and El Pedregal volcanoes (Michoacán, Mexico): a new monogenetic cluster in the making?. Bulletin of Volcanology, 81(10), 59.

Latyshev, A. V., Veselovskiy, R. V., Ivanov, A. V., Fetisova, A. M., Pavlov, V. E. (2013). Short intense bursts in magmatic activity in the south of Siberian Platform (Angara-Taseeva depression): the paleomagnetic evidence. Izvestiya, Physics of the Solid Earth, 49(6), 823-835.

Latyshev, A. V., Veselovskiy, R. V., Ivanov, A. V. (2018). Paleomagnetism of the Permian-Triassic intrusions from the Tunguska syncline and the Angara-Taseeva depression, Siberian Traps Large Igneous Province: Evidence of contrasting styles of magmatism. Tectonophysics, 723, 41-55.

Latyshev, A. V., Rad'ko, V. A., Veselovskiy, R. V., Fetisova, A. M., Pavlov, V. E. (2020). Correlation of the Permian-Triassic ore-bearing intrusions of the Norilsk region with the volcanic sequence of the Siberian Traps based on the paleomagnetic data. Economic Geology, 115(6), 1173-1193.

Lengyel, S. N., Eighmy, J. L. (2002). A revision to the US Southwest archaeomagnetic master curve. Journal of archaeological science, 29(12), 1423-1433.

Lesti, C., Porreca, M., Giordano, G., Mattei, M., Cas, R.A.F., Wright, H.M.N., Folkes, C.B., Viramonte, J. (2011). High-temperature emplacement of the Cerro Galán and Toconquis Group ignimbrites (Puna plateau, NW Argentina) determined by TRM analyses. Bull. Volcanol.73, 1535–1565. http://dx.doi.org/10.1007/s00445-011-0536-2.

Lerner, G. A., Cronin, S. J., Turner, G. M., Rowe, M. C. (2019). Paleomagnetic determination of the age and properties of the 1780–1800 AD dome effusion/collapse episode of Mt. Taranaki, New Zealand. Bulletin of Volcanology, 81(3), 15.

Licht, A., Hulot, G., Gallet, Y., Thébault, E. (2013). Ensembles of low degree archeomagnetic field models for the past three millennia. Phys. Earth Planet. In. 224, 38–67

Lodge, A., Holme, R. (2009). Towards a new approach to archaeomagnetic dating in Europe using geomagnetic field modelling. Archaeometry 51, 309–322.

Lund, S., Banerjee, S. K. (1985). Late Quaternary paleomagnetic field secular variation for two Minnesota lakes, J. Geophys. Res., vol. 90, pp.803-825.

Mahgoub, A. N., Böhnel, H., Siebe, C., Chevrel, M. O. (2017a). Paleomagnetic study of El Metate shield volcano (Michoacán, Mexico) confirms its monogenetic nature and young age (~ 1250 CE). J. Volcanol. Geoth. Res., 336, 209-218.

Mahgoub, A. N., Böhnel, H., Siebe, C., Salinas, S., Guilbaud, M. N. (2017b). Paleomagnetically inferred ages of a cluster of Holocene monogenetic eruptions in the Tacámbaro-Puruarán area (Michoacán, México): implications for volcanic hazards. Journal of Volcanology and Geothermal Research, 347, 360-370.

Mahgoub, A. N., Reyes-Guzmán, N., Böhnel, H., Siebe, C., Pereira, G., Dorison, A. (2018). Paleomagnetic constraints on the ages of the Holocene Malpaís de Zacapu lava flow eruptions, Michoacán (Mexico): implications for archeology and volcanic hazards. The Holocene, 28(2), 229-245.

Mandeville, C. W., S. Carey, H. Sigurdsson, King J. (1994). Paleomagnetic evidence for high-temperature emplacement of the 1883 subaqueous pyroclastic flows from Krakatau Volcano, Indonesia, J. Geophys. Res., 99, 9487– 9504.

Marti, J., Diez-Gil, J. L., Ortiz, R. (1991). Conduction model for the thermal influence of lithic clasts in mixtures of hot gases and ejecta, J. Geophys. Res., 96, 21,879– 21,885.

Márton, E., T. Zelenka, Márton P. (2007). Paleomagnetic correlation of Miocene pyroclastics of the Bükk Mts and their forelands. Central European Geology, 50/1, 47–57, doi:10.1556/CEuGeol.50.2007.1.4.

Márton, P. (2010). Two thousand years of geomagnetic field direction over central Europe revealed by indirect measurements. Geophys. J. Int. 181 (1), 261-268.

Mastrolorenzo, G., Petrone, P. P., Pagano, M., Incoronato, A., Baxter, P. J., Canzanella, A., Fattore, L. (2001). Herculaneum victims of Vesuvius in AD 79. Nature, 410(6830), 769-770.

Mastrolorenzo, G., Petrone, P., Pappalardo, L., Guarino, F. M. (2010). Lethal thermal impact at periphery of pyroclastic surges: evidences at Pompeii. PLoS One, 5(6), e11127.

Matsumoto, T., Ueno, H., Kobayashi, T. (2007). A new secular variation curve for South Kyushu, Japan, and its application to the dating of some lava flows. Rep. Fac. Sci., Kagoshima Univ., No. $0, pp. 35-49.

Maury, R. (1971). Application de la spectrometrie infra-rouge a l'etude des bois fossilises dans les formations volcaniques. Bull Soc Geol Fr 5:280.

McClelland, E.A., Druitt, T.H. (1989), Palaeomagnetic estimates of emplacement temperatures of pyroclastic deposits on Santorini, Greece, Bull. Volcanol., 51, 16–27.

McClelland, E., Thomas, R. (1993) A palaeomagnetic study of Minoan age tephra from Thera. In: Hardy D (ed) Thera and the Aegean world III, vol 2. Thera Foundation, London, pp 129–138.

McClelland. E., Erwin. P.S. (2003). Was a dacite dome implicated in the 9,500 BP collapse of Mt Ruapehu? A palaeomagnetic investigation. Bull Volcanol 65:294–305.doi:10.1007/s00445-002-0261-y.

McClelland, E., Wilson, C. J., Bardot, L. (2004). Palaeotemperature determinations for the 1.8-ka Taupo ignimbrite, New Zealand, and implications for the emplacement history of a high-velocity pyroclastic flow. Bull. Volcanol., 66(6), 492-513.

McElhinny, M.W., Senanayake, W.E. (1982). Variations in the geomagnetic dipole: I. The past 50 000 years. J. Geomagn. Geoelectr. 34, 39–51.

McParland, L. C., Collinson, M. E., Scott, A. C., Campbell, G. (2009). The use of reflectance values for the interpretation of natural an anthropogenic charcoal assemblages. Archaeological and Anthropological Sciences. 1(4), 249.

Merrill, R. T., Mcelhinny, M. W., Mcfadden, P. (1996). The Magnetic Field of The Earth: Paleomagnetism, The Core And The Deep Mantle. Elsevier, New York.

Molina-Cardín, A., et al. (2018), Updated Iberian archaeomagnetic catalogue: New full vector paleosecular variation curve for the last three millennia, Geochemistry, Geophysics, Geosystems, 19, https://doi.org/10.1029/2018GC007781

Moore, J.D., Geissman, J.W., Smith, G.A. (1997) Paleomagnetic emplacement-temperature and thermal-profile estimates for nonwelded pyroclastic-flow deposits, Miocene Peralta Tuff, Jemez Mountains, New Mexico. EOS Trans AGU 78:178

Moulin, M., Fluteau, F., Courtillot, V., Marsh, J., Delpech, G., Quidelleur, X., et al. (2011). An attempt to constrain the age, duration, and eruptive history of the Karoo flood basalt: Naude's Nek section (South Africa). Journal of Geophysical Research: Solid Earth, 116(B7).

Mullineaux, D.R., Crandell, D.R. (1962) Recent lahars from Mount St. Helens, Washington. Geol Soc Amer Bull 73:855–870

Nasser Mahgouba, A., Böhnela, H., Siebeb, C., Oryaëlle Chevrelc, M. (2017). Paleomagnetic study of El Metate shield volcano (Michoacán, Mexico) confirms its monogenetic nature and young age (~1250 CE). J. Volcanol. Geotherm. Res. 336, 209–218.

Néel, L. (1949). Théorie du traînage magnétique des ferromagnéniques en grains fins avec applications aux terres cuites. Ann. Géophys., 5, 99–136.Opdyke, N. D., and J. E. T. Channell (1996). Magnetic Stratigraphy. Academic Press.

Nilsson, A., Muscheler, R., Snowball, I. (2011). Millennial scale cyclicity in the geodynamo inferred from a dipole tilt reconstruction. Earth Planet Sci. Lett. 311 299–205.

Nilsson, A., Snowball, I., Muscheler, R., Uvo, C.B. (2010). Holocene geocentric dipole tilt model constrained by sedimentary paleomagnetic data. Geochem. Geophys. Geosys. 11, Q08018.

Nilsson, A., Holme, R., Korte, M., Suttie, N., Hill, M. (2014). Reconstructing Holocene geomagnetic field variation: new methods, models and implications. Geophys. J. Int. 198, 229–248.

Nitta, H., Saito, T., Shitaoka, Y. (2020). Recent eruption history inferred from eruption ages of the two latest lava flows using multi-dating at Yokodake Volcano, Japan. Earth, Planets and Space, 72(1), 1-15.

Noël, M., Batt, C.M. (1990). A method for correcting geographically separated remanence directions for the purpose of archaeomagnetic dating. Geophys. J. Int. 102, 753e756.

Ohno, M., Hamano, Y. (1992). Geomagnetic poles over the past 10,000 years. Geophys. Res. Lett. 19, 1715–1718.

Ohno, M., Hamano, Y. (1993). Spherical harmonic analysis of paleomagnetic secular variation curves. Central Core of the Earth 3, 205–212.

Ojala, A.E.K., Tiljander, M. (2003). Testing the fidelity of sediment chronology: comparison of varve and paleomagnetic results from Holocene lake sediments from central Finland. Quat. Sci. Rev. 22, 1787–1803.

Opdyke, N.D., Channell, J.E.T. (1996). Magnetic Stratigraphy. Academic Press.

Ort, M. H., Rosi, M., Anderson, C. D. (1999). Correlation of deposits and vent locations of the proximal Campanian Ignimbrite deposits, Campi Flegrei, Italy, based on natural remanent magnetization and anisotropy of magnetic susceptibility characteristics. J. Volcanol. Geoth. Res., 91(2-4), 167-178.

Ort, M.H., Orsi, G., Pappalardo, L. et al. (2003). Anisotropy of magnetic susceptibility studies of depositional processes in the Campanian Ignimbrite, Italy. Bull Volcanol 65, 55–72. https://doi.org/10.1007/s00445-002-0241-2

Ort, M. H., De Silva, S. L., Jiménez C, N., Jicha, B. R., Singer, B. S. (2013). Correlation of ignimbrites using characteristic remanent magnetization and anisotropy of magnetic susceptibility, Central Andes, Bolivia. Geochemistry, Geophysics, Geosystems, 14(1), 141-157.

Ort, M.H., Porreca, M., Geissman, J.W. (2015a) The use of palaeomagnetism and rock magnetism to understand volcanic processes: Introduction. Geological Society Special Publication, 396, pp. 1-11. doi: 10.1144/SP396.17

Ort, M.H., Newkirk, T.T., Vilas, J.F., Vazquez, J.A. (2015b). Towards the definition of AMS facies in the deposits of pyroclastic density currents. Geological Society Special Publication, 396, pp. 205-226. doi: 10.1144/SP396.8

Panovska, S., Korte, M., Finlay, C.C., Constable, C.G. (2015). Limitations in paleomagnetic data and modelling techniques and their impact on Holocene geomagnetic field models. Geophys. J. Int. 202, 402–418.

Pares, J. M., Marti, J., Garces, M. (1993) Thermoremanence in red sandstone clasts and emplacement temperature of a Quaternary pyroclastic deposit (Catalan Volcanic Zone, NE Spain). Stud Geophys Geod 37:401–414

Paterson, G.A., Roberts, A.P., Mac Niocaill, C., Muxworthy, A.R., Gurioli, L., Viramonté, J.G., Navarro, C., Weider, S. (2010). Paleomagnetic determination of emplacement temperatures of

pyroclastic deposits: an under-utilized tool. Bull. Volcanol. 72, 309–330. http://dx.doi.org/10.1007/s00445-009-0324-4.

Pavón-Carrasco, F.J., and Villasante Marcos, V. (2010) Geomagnetic secular variation in the Canary Islands: Paleomagnetic data, models and application to paleomagnetic dating: Física de la Tierra, v. 22, p. 59–80.

Pavón-Carrasco, F., Osete, M., Torta, J., Gaya-Piqué, L., (2008a). A regional archaeomagnetic model for the palaeointensity in Europe for the last 2000 years and its implications for climatic change. Pure Appl. Geophys. 165, 1209–1225.

Pavón-Carrasco, F., Osete, M., Torta, J., Gaya-Piqué, L., Lanos, P. (2008b). Initial SCHA.DI.00 regional archaeomagnetic model for Europe for the last 2000 years. Phys. Chem. Earth 33, 596–608.

Pavón-Carrasco, F.J., Osete, M.L., Torta, J.M., Gaya-Piqué, L.R. (2009). A regional archeomagnetic model for Europe for the last 3000 years, SCHA.DIF.3K: applications to archeomagnetic dating. Geochem. Geophys. Geosyst. 10 (Q03013). doi:10.1029/2008GC002244.

Pavón-Carrasco, F.J., Osete, M.L., Torta, J.M. (2010). Regional modelling of the geomagnetic field in Europe from 6000 BC to 1000 BC. Geochem. Geophys. Geosyst. doi:10.1029/2010GC003197.

Pavón-Carrasco, F.J., Rodríguez-González, J., Osete, M.L., Torta, J.M. (2011). A Matlab tool for archaeomagnetic dating. J. Archaeol. Sci. 38, 408–419.

Pavón-Carrasco, F.J., Osete, M.L., Torta, J.M., De Santis, A. (2014). A geomagnetic field model for the Holocene based on archaeomagnetic and lava flow data. Earth Planet Sc. Lett. vol. 388, pp. 98–109.

Pensa, A., Giordano, G., Cas, R.A.F., Porreca, M. (2015a). Thermal state and implications for eruptive styles of the intra-Plinian and climactic ignimbrites of the 4.6 ka Fogo A eruption sequence, São Miguel, Azores. Bull. Volcanol.77 (99). http://dx.doi.org/10.1007/s00445-015-0983-2.

Pensa, A., Porreca, M., Corrado, S., Giordano, G., Cas, R. (2015b). Calibrating the pTRM and charcoal reflectance (Ro%) methods to determine the emplacement temperature of ignimbrites: Fogo A sequence, São Miguel, Azores, Portugal, as a case study. Bull. Volcanol.77 (18). http://dx.doi.org/10.1007/s00445-015-0904-4.

Pensa, A., Capra, L., & Giordano, G. (2019). Ash clouds temperature estimation. Implication on dilute and concentrated PDCs coupling and topography confinement. Scientific Reports, 9(1), 1-14.

Pérez-Rodríguez, N., Morales, J., Goguitchaichvili, A., García-Tenorio, F., (2019). A comprehensive paleomagnetic study from the last Plinian eruptions of Popocatepetl volcano: absolute chronology of lavas and estimation of emplacement temperatures of PDCs. Earth Planets Space. 71: 80. https://doi.org/10.1186/s40623-019-1059-x

Pérez-Rodríguez, N., Morales, J., Guilbaud, M.N, Goguitchaichvili, A., Cejudo-Ruiz, R., Hernández-Bernal, M.D.S. (2020). Reassessment of the eruptive chronology of El Metate shield volcano (central-western Mexico) based on a comprehensive rock-magnetic, paleomagnetic and multi-approach paleointensity survey. Quaternary Geochronology, 55, 101031

Peskov, A. Y., Didenko, A. N., Guryanov, V. A. (2018). Paleoproterozoic evolution of mafic–ultramafic magmatism of the Kun-Manie Ore Field (Aldan-Stanovoy Shield): evidence from paleomagnetic data. Russian Journal of Pacific Geology, 12(5), 341-353.

Pinton, A., Giordano, G., Speranza, F., Þórðarson, Þ. (2018). Paleomagnetism of Holocene lava flows from the Reykjanes Peninsula and the Tungnaà lava sequence (Iceland): implications for flow correlation and ages. Bull. Volcanol. 80, 10. https://doi.org/ 10.1007/s00445-017-1187-8.

Pioli, L., Lanza, R., Ort, Rosi, M. (2008). Magnetic fabric, welding texture and strain fabric in the Nuraxi Tuff, Sardinia, Italy. Bulletin of Volcanology, 70(9), 1123-1137.

Porreca, M., Giordano, G., Mattei, M., Musacchio, P. (2006). Evidence of two Holocene phreatomagmatic eruptions at Stromboli volcano (Aeolian Islands) from paleomagnetic data. Geophys. Res. Lett.33, 1–6. http://dx.doi.org/10.1029/2006GL027575.

Porreca, M., Mattei, M., MacNiocaill, C., Giordano, G., McClelland, E., Funiciello, R. (2008). Paleomagnetic evidence for low-temperature emplacement of the phreatomagmatic Peperino Albano ignimbrite (Colli Albani volcano, Central Italy). Bull. Volcanol.70, 877–893. http://dx.doi.org/10.1007/s00445-007-0176-8.

Prévot, M., McWilliams, M. (1989). Paleomagnetic correlation of Newark Supergroup volcanics. Geology, 17, 11, 1007-1010.

Principe, C., Tanguy, J.C., Arrighi, S., Paiotti, A., Le Goff, A., Zoppi, U. (2004). Chronology of Vesuvius activity from AD 79 to 1631 based on archeomagnetism of lavas and historical sources. Bull. Volcanol. 66 (8), 703–724

Pullaiah, G., Irving, E., Buchan, K. L., Dunlop, D.J. (1975), Magnetization changes caused by burial and uplift, Earth Planet. Sci. Lett., 28, 133–143.

Riisager, J., Riisager, P., Pedersen, A. K. (2003). The C27n-C26r geomagnetic polarity reversal recorded in the west Greenland flood basalt province: How complex is the transitional field? Journal of Geophysical Research: Solid Earth, 108(B3).

Risica, G., Speranza, F., Giordano, G., De Astis, G., Lucchi, F. (2019). Palaeomagnetic dating of the Neostromboli succession, J. Volcanol. Geoth. Res., 371, 229–244. https://doi.org/10.1016/j.jvolgeores.2018.12.009.

Robertson, D. J. (1986). A paleomagnetic study of Rangitoto Island, Auckland, New Zealand. New Zealand Journal of Geology and Geophysics, 29(4), 405-411.

Rolph, T. C., Shaw J. (1986), Variations of the geomagnetic field in Sicily, J. Geomagn. Geoelectr., 38, 1269– 1277.

Rolph, T. C., Shaw, J., Guest, J. E. (1987). Geomagnetic field variations as a dating tool: Application To Sicilian Lavas. J. Arch. Sc., 14(2), 215–225. Doi:10.1016/0305-4403(87)90008-2

Roperch, P., Chauvin, A., Lara, L.E., Moreno, H., (2015). Secular variation of the Earth's magnetic field and application to paleomagnetic dating of historical lava flows in Chile. Phys. Earth Planet. In. 242, 65–78.

Rutten, M. G., & Wensink, H. (1960). Paleomagnetic Dating, Glaciations and The Chronology Of The Plio-Pleistocene In Iceland. In Copenhagen, Denmark, Xxi International Geological Congress, 62 Norden, Part Iv, N. 53 (P. 62).

Saito, T., Ishikawa, N., Kamata, H. (2003) Identification of magnetic minerals carrying NRM in pyroclastic-flow deposits. J Volcanol Geotherm Res 126:127–142. doi:10.1016/S0377-0273(03)00132-X.

Salvatici, T., Di Roberto, A., Di Traglia, F., Bisson, M., Morelli, S., Fidolini, F., et al. (2016). From hot rocks to glowing avalanches: Numerical modelling of gravity-induced pyroclastic density currents and hazard maps at the Stromboli volcano (Italy). Geomorphology, 273, 93-106.

Sanchez, S., Fournier, A., Aubert, J., Cosme, E., Gallet, Y. (2016). Modelling the archaeomagnetic field under spatial constraints from dynamo simulations: a resolution analysis. Geophys. J. Int. 207, 983–1002.

Sawada, Y., Sampei, Y., Hyodo, M., Yagami, T., Fukue, M., (2000). Estimation of emplacement temperatures of pyroclastic flows using H/C ratios of carbonized wood. J Volcanol Geotherm, Res 104:1–20. doi:10.1016/S0377-0273(00)00196-7

Schnepp, E., Lanos, P.H. (2005). Archaeomagnetic secular variation in Germany during the past 2500 years. Geophys. J. Int. 163, 479e490.

Schnepp, E., Lanos, P.H. (2006). A preliminary secular variation reference curve for archaeomagnetic dating in Austria. Geophys. J. Int. 166 (1), 91-96.

Schnepp, E., Pucher, R., Reinders, J., Hambach, U., Soffel, H. C., Hedley, I. (2004). A German catalogue of archaeomagnetic data, Geophys. J. Int., 157, 64– 78.

Scott, A. C. Glasspool, I. J. (2005). Charcoal reflectance as a proxy for the emplacement temperature of pyroclastic flow deposits. Geology. 33, 589–592

Shitaoka, Y., Saito, T., Yamamoto, J., Miyoshi, M., Ishibashi, H., Soda, T. (2019). Eruption age of Kannabe volcano using multi-dating: Implications for age determination of young basaltic lava flow. Geochronometria, 46(1), 49-56.

Sherrod, D. R., Hagstrum, J. T., McGeehin, J. P., Champion, D. E., Trusdell, F. A. (2006). Distribution, 14C chronology, and paleomagnetism of latest Pleistocene and Holocene lava flows at Haleakalā volcano, Island of Maui, Hawaii: a revision of lava flow hazard zones. Journal of Geophysical Research: Solid Earth, 111(B5).

Sigurdsson, H., Houghton, B., McNutt, S., Rymer, H., & Stix, J. (Eds.), (2000). The encyclopedia of volcanoes. Elsevier.

Sigurdsson, H., Houghton, B., McNutt, S., Rymer, H., & Stix, J. (Eds.). (2015). The encyclopedia of volcanoes. Elsevier.

Smith, G.A., Grubensky, M.J., Geissman, J.W. (1999) Nature and origin of cone-forming volcanic breccias in the Te Herenga Formation, Ruapehu, New Zealand. Bull. Volcanol. 61:64–82.doi:10.1007/s004450050263

Snowball, I., Zillén, L., Ojala, A., Saarinen, T., Sandgren, P. (2007). FENNOSTACK and FENNOPRIS: varve dated Holocene palaeomagnetic secular variation and relative palaeointensity stacks for Fennoscandia. Earth Planet Sci. Lett. 255, 106–116.

Soler, V., Carracedo, J.C., Heller, F., (1984), Geomagnetic secular variation in historical lavas from the Canary Islands: Geophysical Journal of the Royal Astronomical Society, v. 78, p. 313–318, doi: 10 .1111 /j .1365 -246X.1984 .tb06487.x.

Speranza, F., Pompilio, M., Sagnotti, L. (2004). Paleomagnetism of spatter lava from Stromboli volcano (Aeolian Islands, Italy): implications for the age of paroxysmal eruption. Geophys. Res. Lett. 31 (2). https://doi.org/10.1029/2003GL018944.

Speranza, F., L. Sagnotti, Meloni A. (2005). Comment on ‘‘Recent eruptive history of Stromboli (Aeolian Islands, Italy) determined from high-accuracy archeomagnetic dating’’ by S. Arrighi et al., Geophys. Res. Lett., 32, L23305, doi:10.1029/2005GL022590.

Speranza, F., Branca, S., Coltelli, M., D'ajello Caracciolo, F., Vigliotti, L. (2006). How accurate is “paleomagnetic dating”? New evidence from historical lavas from Mount Etna. J. Geophys. Res. 111 (B12). https://doi.org/10.1029/2006JB004496.

Speranza, F., Pompilio, M., D'Ajello Caracciolo, F., Sagnotti, L. (2008). Holocene Eruptive history of the Stromboli volcano: constraints paleomagnetic dating. J. Geophys. Res. 113 (B9). https://doi.org/10.1029/2007JB005139.

Speranza, F., Landi, P., D'Ajello Caracciolo, F., Pignatelli, A. (2010). Paleomagnetic dating of the most recent silicic eruptive activity at Pantelleria (Strait of Sicily). Bull. Volcanol. 72, 847–858. https://doi.org/10.1007/s00445-010-0368-5.

Speranza, F., Di Chiara, A., Rotolo, S.G. (2012). Correlation of welded ignimbrites on Pantelleria (Strait of Sicily) using paleomagnetism. Bull. Volcanol. 74, 341–357. https://doi. org/10.1007/s00445-011-0521-9.

Sternberg, R.S. (1982). Archaeomagnetic Secular Variation of Direction and Paleointensity in the American Southwest. Ph.D. thesis. The University of Arizona.

Stockhausen, H. (1998). Geomagnetic palaeosecular variation (0–13 000 yr BP) as recorded in sediments from three maar lakes from the West Eifel (Germany). Geophysical Journal International, 135(3), 898-910.

Sulpizio, R., Zanella, E., Macías, J.L. (2008) Deposition temperature of some PDC deposits from the 1982 eruption of El Chichón volcano (Chiapas, Mexico) inferred from rock magnetic data. J Volcanol Geotherm Res 175:494–500. doi:10.1016/j.jvolgeores.2008.02.024

Sulpizio, R., Dellino, P., Doronzo, D. M., Sarocchi, D. (2014). Pyroclastic density currents: state of the art and perspectives. Journal of Volcanology and Geothermal Research, 283, 36-65.

Sulpizio, R., Zanella, E., Macias, J.L., Saucedo, R. (2015). Deposit temperature of pyro-clastic density currents emplaced during the El Chichon 1982 and Colima 1913 eruptions. Geol. Soc. (Lond.) Spec. Publ. 396, 35–49. http://dx.doi.org/10.1144/sp396.5.

Tarling, D.H. (1983). Palaeomagnetism: Principles and applications in geology, geophysics, and archaeology.

Tamura, Y., Koyama, M., Fiske, R.S. (1991). Paleomagnetic evidence for hot pyroclastic debris flow in the shallow submarine Shirahama Group (Upper Miocene-Pliocene) Japan. J. Geophys. Res. 96:21779–21787. doi:10.1029/91jb02258

Tanaka, H., Hoshizumi, H., Iwasaki, Y., Shibuya, H. (2004) Applications of paleomagnetism in the volcanic field: a case study of the Unzen Volcano, Japan. Earth Planets Space 56:635–647

Tanguy, J.C., Le Goff, M. (2004). Distorsion of the geomagnetic field in volcanic terrains: an experimental study of the Mount Etna stratovolcanos. Physic of the Earths and Planetary Interiors, 141, 59-70.

Tanguy, J.-C., I. Bucur, J., Thompson F. C. (1985), Geomagnetic secular variation in Sicily and revised ages of historic lavas from Mount Etna, Nature, 318, 453–455.

Tanguy, J. C., Principe, C., Arrighi, S. (2005). Comment on "Historical measurements of the Earth's magnetic field compared with remanence directions from lava flows in Italy over the last four centuries" by R. Lanza, A. Meloni, and E. Tema. Physics of the Earth and Planetary Interiors, 152(1-2), 116-120.

Tanguy, J. C., Le Goff, M., Principe, C., Arrighi, S., Chillemi, V., Paiotti, A., La Delfa, S., Patanè, G. (2003). Archaeomagnetic dating of Mediterranean volcanics of the last 2100 years: validity and limits. Earth Planet. Sci. Lett. 211, 111–124.

Tauxe, L. (1998). Paleomagnetic principles and practice, Kluwer acad., pp. 312.

Tauxe, L. (2009). Essentials of Paleomagnetism, University of California Press, Berkeley.

Tema, E., I. Hedley, Lanos, P. (2006), Archeomagnetism in Italy: A compilation of data including new results and a preliminary Italian secular variation curve, Geophys. J. Int., 167, 1160– 1171.

Tema, E., Kondopoulou, D. (2011). Secular variation of the Earth's magnetic field in the Balkan region during the last eight millennia based on archaeomagnetic data. Geophysical Journal International, 186(2), 603-614.

Tema, E., Herrero-Bervera, E., Lanos, Ph. (2017). Geomagnetic field secular variation in Pacific Ocean: A Bayesian reference curve based on Holocene Hawaiian lava flows, Earth Planet Sc. Lett., 478, 58-65, https://doi.org/10.1016/j.epsl.2017.08.023.

Tema, E., Lanos, P. (2020). New Italian directional and intensity archaeomagnetic reference curves for the past 3000 years: Insights on secular variation and implications on dating. Archaeometry.

Thellier, E. (1981). Sur la direction du champ magnétique terrestre, en France, durant les deux derniers millénaires. Phys. Earth Planet. In. 24 (2–3), 89–132

Thompson, R., Turner, G.M. (1979). British geomagnetic master curve 10,000-0 yr BP for dating European sediments. Geophys. Res. Lett. 6 (4), 249–252.

Thompson, R., Turner, G. M. (1985). Icelandic Holocene Palaeolimnomagnetism. Phys. Earth Planet In., 38(4), 250–261. Doi:10.1016/0031-9201(85)90072-X

Torsvik, T. H., R. D. Muller, R. Van der Voo, B. Steinberger, C. Gaina (2008). Global plate motion frames: Toward a unified model. Rev. Geophys., 46, RG3004, doi:10.1029/2007RG000227.

Trolese, M., Giordano, G., Cifelli, F., Winkler, A., Mattei, M. (2017). Forced transport of thermal energy in magmatic and phreatomagmatic large volume ignimbrites: Paleomagnetic evidence from the Colli Albani volcano, Italy. Earth Planet Sc. Lett., 478, 179-191.

Tsuboi, S., Tsuya, H. (1930). On the temperature of the pumiceous ejecta of Komagatake, Hokkaidò, as inferred from their modes of oxidation. Bull. Earth. Res. Inst. Univ. Tokyo 8:271– 273

Turner, G.M., Alloway, B.V., Dixon, B.J., Atkins, C.B. (2018). Thermal history of volcanic debris flow deposits on the eastern flanks of Mt. Taranaki, New Zealand: Implications for future hazards. Journal of Volcanology and Georhermal Research 353 (55-67).

Uehara, D., Cas, R.A.F., Folkes, C., Takarada, S., Oda, H., Porreca, M. (2015). Using thermal remanent magnetisation (TRM) to distinguish block and ash flow and debris flow deposits, and to estimate their emplacement temperature: 1991–1995 lava dome eruption at Mt. Unzen Volcano, Japan. J. Volcanol. Geotherm. Res. 303, 92–111. http://dx.doi.org/10.1016/j.jvolgeores.2015.07.019.

Urrutia-Fucugauchi, J. (1983). Palaeomagnetic estimation of emplacement temperature of pyroclastic deposits – preliminary study of Caldera de Los Humeros and Alchichica Crater. Geofisica Internationale, 22–3, 277–292.

Urrutia-Fucugauchi, J., Alva-Valdivia, L.M., Gogichaishvili, A., Rivas, M.L., Morales, J. (2004). Paleomagnetic, rock-magnetic and microscopy studies of historic lava flows from the Paricutin volcano, Mexico: implication for the deflection of paleomagnetic directions. Geophys. J. Int. 156, 431–442. https://doi.org/10.1111/j.1365-246X.2004.02166

Urrutia-Fucugauchi, J., Goguitchaichvili, A., Pérez-Cruz, L., Morales, J. (2016). Archaeomagnetic dating of the eruption of Xitle Volcano, basin of Mexico: Implications for the mesoamerican centers of Cuicuilco and Teotihuacan. Arqueologia Iberoamericana, 30, 23-29.

Yang, S., Odah, H., Shaw, J. (2000). Variations in the geomagnetic dipole moment over the last 12000 years. Geophys. J. Int. 140, 158–162.

Yasuda, Y., Sato, E., Suzuki-Kamata, K. (2020). Paleomagnetic constraints on a time-stratigraphic framework for the evolution of Ohachidaira volcano and the summit caldera, central Hokkaido, Japan. Bulletin of Volcanology, 82(11), 1-24.

Valet, J. P., Soler, V. (1999). Magnetic anomalies of lava fields in the Canary Islands. Possible consequences for paleomagnetic records. Phys. Earth Planet In., 115(2), 109-118.

Valet, J.-P., Herrero-Bervera, E., LeMoüel, J.-L., Plenier, G. (2008). Secular variation of the geomagnetic dipole during the past 2000 years. Geochem. Geophys. Geosys. 9, Q01008. https://doi.org/10.1029/2007GC001728.

van Otterloo, J., Cas, R.A.F. (2016). Low-temperature emplacement of phreatomagmatic pyroclastic flow deposits at the monogenetic Mt Gambier Volcanic Complex, South Australia, and their relevance for understanding some deposits in diatremes. J. Geol. Soc. Lond.173. http://dx.doi.org/10.1144/jgs2015-122.

Vashakidze, G., Goguitchaichvili, A., García-Redondo, N., Calvo-Rathert, M., Carrancho, Á., Cejudo, R., et al. (2019). Magnetic dating of the Holocene monogenetic Tkarsheti volcano in the Kazbeki region (Great Caucasus). Earth, Planets and Space, 71(1), 1-7.

Verosub, K. L., Mehringer, P. J., Waterstraat, P. (1986). Holocene secular variation in western North America: Paleomagnetic record from Fish Lake, Harney County, Oregon. J. Geoph. Res.: Solid Earth, 91(B3), 3609–3623. https://doi.org/10.1029/jb091ib03p03609

Veselovskiy, R.V., Konstantinov, K.M., Latyshev, A.V., and Fetisova, A.M. (2012), Paleomagnetism of the trap intrusive bodies in arctic Siberia: Geological and methodical implications: Izvestiya, Physics of the Solid Earth, v.48, no. 9–10, p. 738–750

Vezzoli, L., Principe, C., Malfatti, J., Arrighi, S., Tanguy, J.-C., Le Goff, M. (2009). Modes and times of caldera resurgence: the <10 ka evolution of Ischia caldera, Italy, from high-precision archaeomagnetic dating. J. Volcanol. Geoth. Res., 186(3-4), 305–319. Doi:10.1016/J.Jvolgeores.2009.07.008

Villasante-Marcos, V., Pavón-Carrasco, F. J. (2014). Palaeomagnetic constraints on the age of Lomo Negro volcanic eruption (El Hierro, Canary Islands). Geophys. J. Intern., 199(3), 1497-1514.

Voight, B., Davis, M.J. (2000). Emplacement temperatures of the November 22, 1994 nuée ardente deposits, Merapi Volcano, Java. J. Volcanol. Geotherm. Res. 100:371–377. doi:10.1016/S0377-0273(00)00146-3

Watanabe, N. (1958). Secular variation in the direction of geomagnetism as the standard scale for geomagnetochronology in Japan. Nature 182, 383–384.

Winkler, A., Caricchi, C., Guidotti, M., Owczarek, M., Macrì, P., Nazzari, M., Amoroso, A., Di Giosa, A., Listrani, S. (2019). Combined magnetic, chemical and morphoscopic analyses on lichens from a complex anthropic context in Rome, Italy. Science of the Total Environment, v. 690, pp. 1355-1368.

Wright, J. (1978) Remanent magnetism of poorly sorted deposits from the Minoan eruption of Santorini. Bull. Volcanol. 41:131–135. doi:10.1007/BF02597026

Yamazaki, T., Kato, I., Muroi, I., Abe, M. (1973) Textural analysis and flow mechanism of the Donzurubo subaqueous pyroclastic flow deposits. Bull Volcanol 37:231–244. doi:10.1007/BF02597132

Zananiri, I., Batt, C. M., Lanos, P., Tarling, D. H., Linford, P. (2007), Archaeomagnetic secular variation in the UK during the past 4000 years and its application to archaeomagnetic dating, Phys. Earth Planet. Inter., 160, 97– 107.

Zanella, F., De Astis, G., Lanza, R. (2001). Paleomagnetism of welded, pyroclastic-fall scoriae at Vulcano, Aeolian archipelago. J. Volcanol. Geotherm. Res. 207, 71–86

Zanella, E., Gurioli, L., Lanza, R., Sulpizio, R., Bontempi, M. (2008). Deposition temperature of the AD 472 Pollena pyroclastic density current deposits, Somma-Vesuvius, Italy. Bull. Volcanol.70,

1237–1248. http://dx.doi.org/10.1007/s00445-008-0199-9.

Zanella, E., Sulpizio, R., Gurioli, L., Lanza, R. (2015). Temperatures of the pyroclastic density currents deposits emplaced in the last 22 kyr at Somma-Vesuvius (Italy). Geol. Soc. (Lond.) Spec. Publ.396, 13–33. http://dx.doi.org/10.1144/sp396.4.

Zijderveld, J.D.A. (1967). AC Demagnetization of Rocks: Analysis of Results. In: Runcorn, S.K., Creer, K.M. and Collinson, D.W., Eds., Methods in Palaeomagnetism, Elsevier, Amsterdam, 254-286.

Zlotnicki, J., Pozzi, J.P., Boudon, G., Moreau, M.G. (1984). A new method for the determination of the setting temperature of pyroclastic deposits (example of Guadeloupe–French-West-Indies). J. Volcanol. Geotherm. Res. 21:297–312.doi:10.1016/0377-0273(84)90027-1.

PART II

4 Palaeomagnetic dating of Holocene eruptions from the Canary Islands

4.1 Geological setting of the Canary Islands

The Canary Islands form a volcanic archipelago located in the northern Atlantic Ocean, between N27.5° and N29.5° latitudes, and W13.2° and W18.2° longitudes, approximately 100 km away from the closest point of Morocco. They belong to the Macaronesia, a region including also the Azores, Madeira, Cape Verde and Savage archipelagos (Fig. 4.1a). The Canary Islands are constituted by seven main volcanic islands (Fig. 4.1b): Fuerteventura, Lanzarote, Gran Canaria, Tenerife, La Gomera, La Palma and El Hierro; and four smaller islets, i.e. La Graciosa, Alegranza, Isla de Lobos and Montaña (hereinafter Mña) Clara.

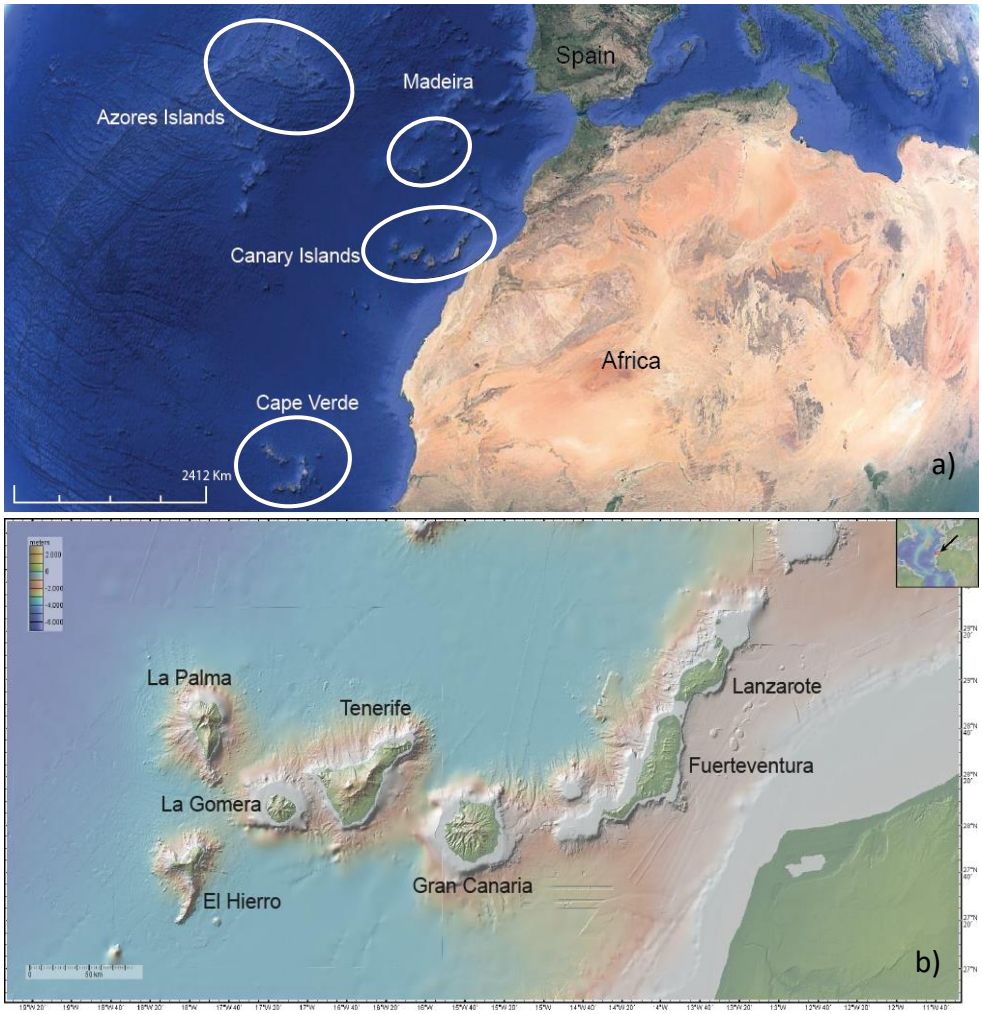

Fig. 4.1 a) Satellite image (from Google Earth), with the main islands of the Macaronesian region; b) the seven main islands of the Canary archipelago (image from GeoMapApp 3.6.1 version).

The archipelago is constituted by a larger system of volcanic islands, commonly subdivided in PalaeoCanaries (from 68 to 25 Ma), representing the now-subemerged older islands, and the Neo or Present Canaries (from 25 Ma to date), characterizing the presently emerged islands (Fig. 4.2, *Geldmacher et al., 2005*; *van den Bogaard, 2013*).

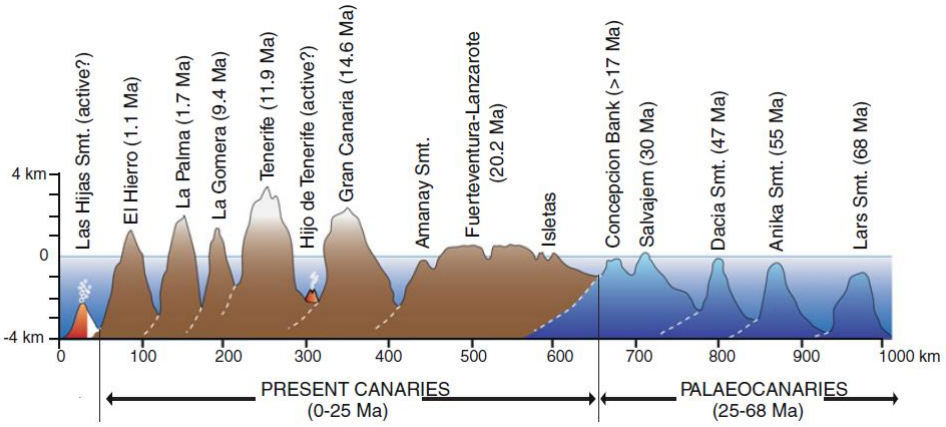

Fig. 4.2 Diagram showing Palaeo and NeoCanaries and ages (from *Geldmacher et al., 2001, Guillou et al., 2004)*.

The origin and the development of these islands have been debated for a long time. The earlier interpretation (*Rothe and Schmincke, 1968; Dietz and Sproll, 1979*) supposed a basement of continental crust for the islands (or at least for the earliest ones), suggesting a block of the African continent detached in the initial stage of continental rifting. Subsequent studies assumed as basement a cold and dense oceanic crust, covered with a thick sedimentary sequence, instead (*Bosshard and MacFarlane, 1970; Martinez del Olmo and Buitrago, 2002*). Nowadays, the second hypothesis is most widely accepted, also confirmed by the magnetic anomalies of the eastern Central Atlantic; the Canary Islands rest on an oceanic crust formed between the magnetic anomalies S1 (175 Ma) and M25 (158 Ma) (*Troll and Carracedo, 2016* and reference therein).

Since 1975, different hypotheses have been proposed to explain the origin of the magmatism of the archipelago. *Anguita and Hernán (1975, 2000)* justified the volcanic activity of this area due to the propagating fracture from the Atlas Mountains (northern Africa), which cut through the lithosphere and generate decompression and fusion. *Carracedo et al. (1998)* supposed an upwelling mantle plume, completely disconnected from the lithosphere, instead. The hypothesis of hotspot-generated islands is supported also by the lack of evidence of any major fault connecting the Atlas Mountains with the archipelago or in the Atlantic around the

Canarian archipelago (*Watts, 1994; Funck et al., 1996; Watts et al., 1997; Urgeles et al., 1998; Krastel et al., 2001; Krastel and Schmincke, 2002, Martínez and Buitrago, 2002*) and the evident systematic age progression of the islands (Fig. 4.3a; *Guillou et al., 2004*). However, to explain the long volcanic activity of the Canary Islands and the large volume of magma produced, *Geldmacher et al. (2005)*, supported also by *Gurenko et al. (2006),* proposed the interaction between the plume and the edge-driven convection at the edge of the African craton (Fig. 4.3b).

Tomographic images from seismic wave velocities confirmed the occurrence of a deep mantle plume below the Canaries, down to >1000 km depth (Fig. 4.4; *Montelli et al., 2004, 2006*).

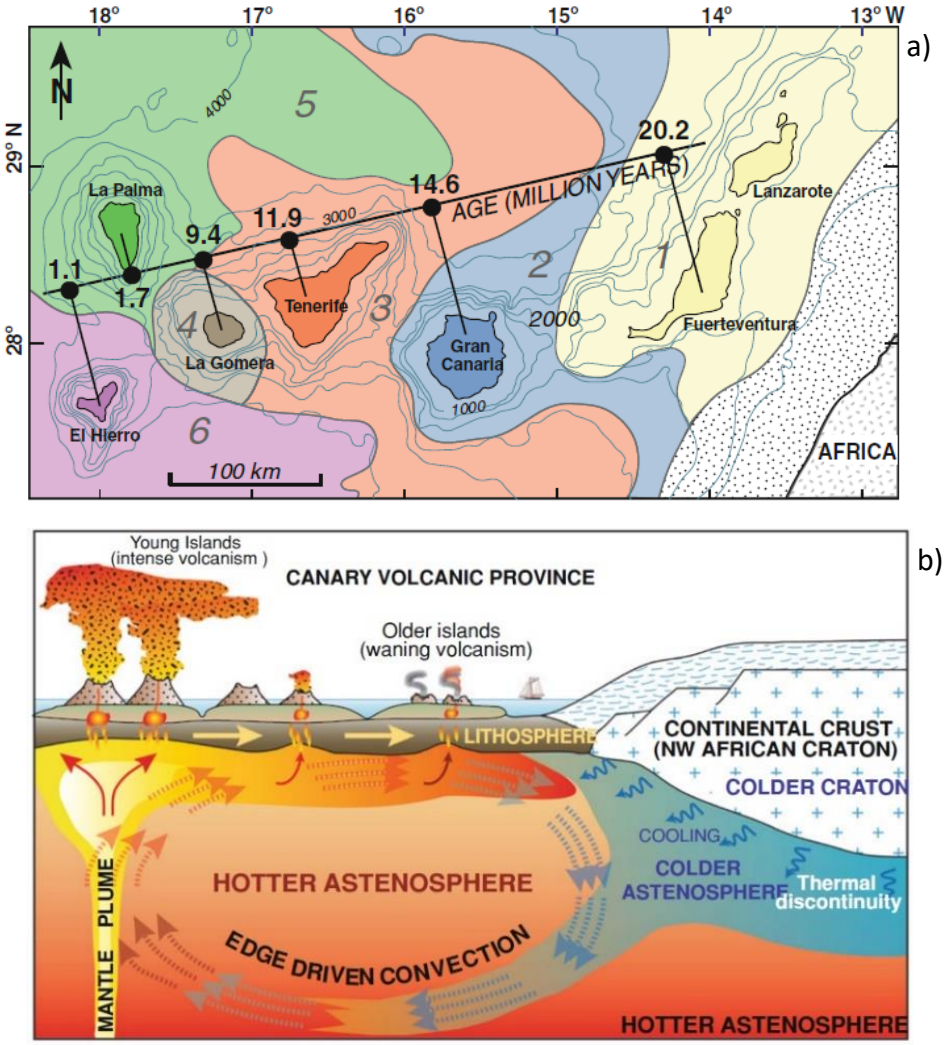

Fig. 4.3 a) Ages of the Canary Islands. Colours represent the progressive overlap oceanwards of the islands' aprons, starting at Fuerteventura-Lanzarote. Ages and aprons from *Guillou et al. (2004), and Urgeles et al. (1998),* respectively. b) Hot spot and upper mantle convection model (*Carracedo, 1999; Geldmacher et al., 2005*).

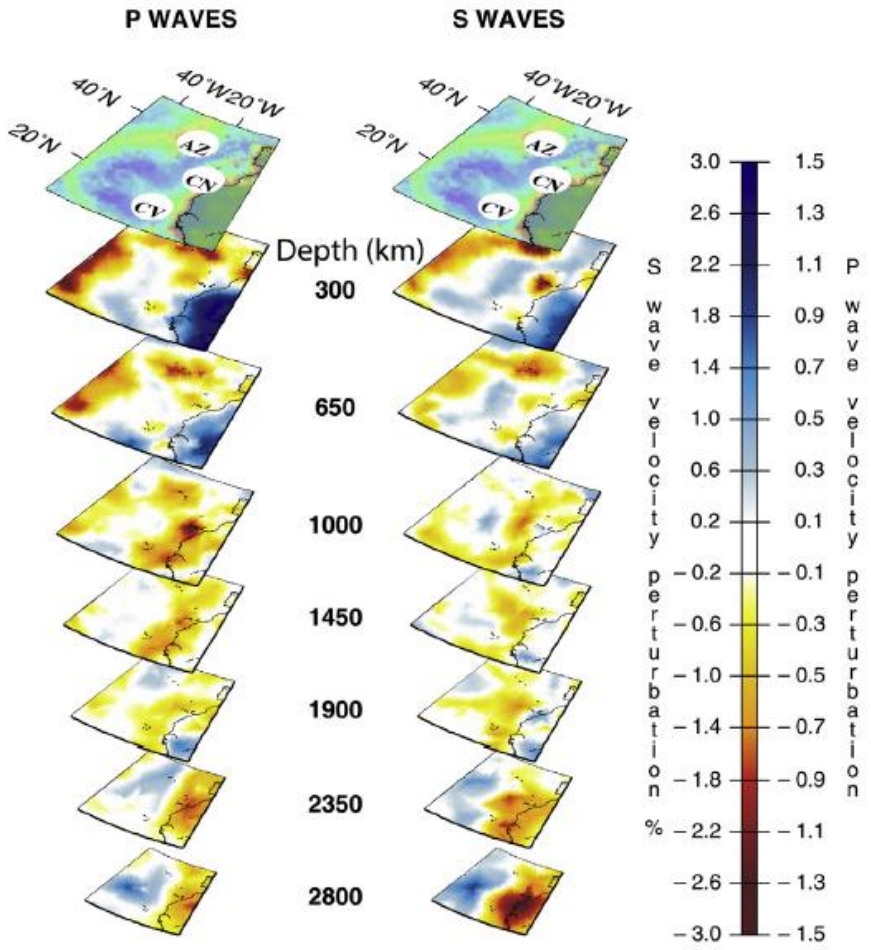

Fig. 4.4 3D view of P and S wave anomalies, beneath the Azores, Canary and Cape Verde Islands (AZ, CN and CV, respectively), from *Montelli et al. (2004)*.

The Canary Islands, like other ocean islands, are the results of several phases: they start with a juvenile seamount stage and a subsequently subaerial phase that form the greater part of the volume of the islands; then, the continuous volcanic activity leads to the shield stage with the very fast growth of the island, after which a period of repose starts. Finally, the combined action of erosion and subsidence causes the formation of atolls.

However, a peculiar characteristic of this archipelago (compared with the other ocean islands as the Hawaiian Islands) is the absence of subsidence. It is developed on a slow-moving old plate, with a very slow rate of subsidence, and for this reason, also the oldest islands (Lanzarote and Fuerteventura) remain above sea level for a long time (*Carracedo et al., 1998)*. Moreover, the subsequent post-erosive rejuvenation stage produces much lower volcanic emission with highly alkaline or more evolved magmas (for example as at Mount Teide on

Tenerife and Roque Nublo on Gran Canaria), which in some cases causes an increase in height of silicic volcanoes (*Carracedo et al., 2007; Pérez-Torrado et al., 1995*).

Based on the evolution and ages of the islands, the Canaries are divided into three main groups: the eastern and oldest islands (Lanzarote and Fuerteventura), in the erosive and decreasing growth phase; the central islands (Gran Canaria and Tenerife), which represent the present evolutionary peak, and the western younger islands (La Palma and El Hierro), which are still in a juvenile stage of shield growth (*Carracedo et al., 1998*).

An important feature of the oceanic islands are rift zones. Rifts represent the surface expression of initial plume-related fracturing in response to vertical upward loading (*MacFarlane and Ridley, 1968; Wyss, 1980; Luongo et al., 1991; Carracedo, 1994, 1996*) and/or extensional fissures caused by the volcano instability and spread, which develop once a volcano has grown to a certain height and instability (*Walter and Troll, 2003; Walter et al., 2005; Delcamp et al., 2010, 2012*). Rifts control the construction of edifices from the initial stages, contribute to form the shape and topography, and are characterized by a high concentration of eruptive vents, that frequently play a key role in the generation of flank collapses (*Carracedo et al., 2011*). In the Canary Islands, rifts are long-lasting; this has been interpreted as probably due to the lower magmatic activity of the mantle hot spot, which resulted in lower eruptive rates with short flows and favoured the higher aspect ratio of rift zones (*Troll and Carracedo, 2016*).

El Hierro, Tenerife and especially La Palma (within the Taburiente volcano) are the best islands in which to inspect rift zones. Two models have been suggested to describe the formation of rifts at the Canaries that have different initiation but similar results. The first (Fig. 4.5A) was proposed by *Carracedo (1994, 1996)*, in which rifts are the result of a magmatic doming and the slight upward bending of the crust. They are arranged according to the least-effort fracturing of the brittle crust at a 120° angle. This model allows the explanation of the concentrations of eruptive vents, their longevity, and the genesis of sector collapses within rifts arms, because the intrusion of dikes takes place in those areas of the rifts in which flanks are free to move apart. The second (Fig. 4.5B) hypothesizes that when a volcano becomes unstable due to dyke intrusions, flank deformations occur (*McGuire et al., 1990; Elsworth and Voight, 1995; Iverson, 1995; Elsworth and Voight, 1996; Walter and Troll, 2003; Walter et al., 2005; Delcamp et al., 2010*). Both types of rift zones are present at the Canary Islands: a

plausible assumption is that the triple-armed rift zones can be ascribed at the first stages of development of the island, while the second can be prevalent in the latter stages of rift development when volcano edifice stability is subject to modifications (*Carracedo and Troll, 2013*).

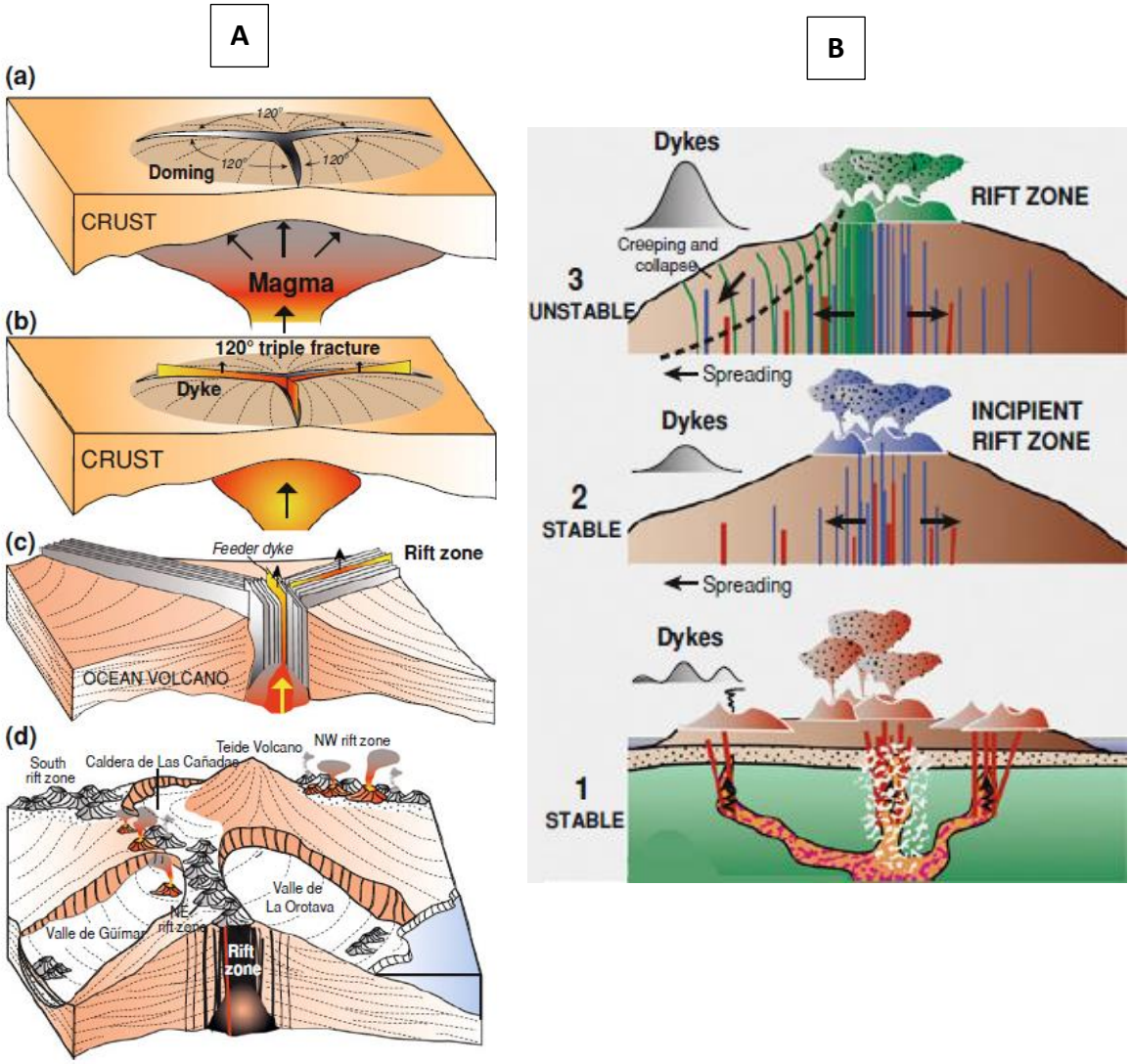

Fig. 4.5 A) Rifting model based on plume-derived updoming and fracturing (from *Carracedo 1994, 1996*); B) rifting model with creeping and spreading of flanks (modified from *Carracedo and Troll, 2013*).

A common characteristic of all islands of the archipelago is the cyclic pattern of growth, instability, flank collapse, nested volcanism and eruptive decline and dispersion (*Carracedo et al., 2011)*. Lateral collapses seem to cause variations in magma composition, probably due to the disruption of the feeding system of the rift (*Manconi et al., 2009*). This results in centralized eruptions within the landslide basin that fill up the collapse scar (*Carracedo et al.,*

2007, 2011; Longpré et al., 2009). Then, the magma emplaced at shallower depths within the volcanic edifice becomes more differentiated, reaching felsic compositions.

The Canary Islands were all active during the Holocene epoch, apart from La Gomera; this widespread volcanic activity has been recorded also in historic period with several eruption in Lanzarote (Nuevo del Fuego-1824; Montañas del Fuego-1736), Tenerife (Siete Fuente-Fasnia and Arafo-1705/06, Garachico-1706; Chahorra-1798; Chinyero-1909), La Palma (Teneguia-1971; San Juan Hoyo Negro-1949; El Charco-1712; Fuentecaliente-1677; Martin Tigalate-1646; Tahuya-1585; Mña Quemada-1480), and El Hierro (submarine eruption south of La Restinga-2011).

References

Anguita, F., Hernán, F. (1975). A propagating fracture model versus a hot spot origin for the Canary Islands. Earth Planet. Sci. Lett. 27, 11-19.

Anguita, F., Hernán, F. (2000). The Canary Islands origin: a unifying model. J. Volcanol. Geoth. Res. 103, 1-26.

Bosshard, E., MacFarlane, D.J. (1970). Crustal structure of the Western Canary Islands from seismic refraction and gravity data. J. Geophys. Res. 75, 4901-4918.

Carracedo, J.C. (1994). The Canary-Islands—an example of structural control on the growth of large oceanic island volcanoes. J. Volcanol. Geotherm. Res. 60:225–241

Carracedo, J.C. (1996). A simple model for the genesis of large gravitational landslide hazards in the Canary Islands. Geol. Soc. Spec. Publ. 110:125–135.

Carracedo, J.C., Troll, V. R. (2013). Teide Volcano - Geology and Eruptions of a Highly Differentiated Oceanic Stratovolcano. Springer-Verlag, Berlin Heidelberg, p. 234.

Carracedo, J.C., Day, S., Guillou, H., Rodríguez-Badiola, E., Canas, J.A., Pérez-Torrado, F.J. (1998). Hotspot volcanism close to a passive continental margin: the Canary Islands. Geol. Mag. 135:591–604.

Carracedo, J.C., Rodríguez-Badiola, E., Guillou, H., Paterne, M., Scaillet, S., Pérez-Torrado, F.J., Paris, R., Fra-Paleo, U., Hansen, A. (2007). Eruptive and structural history of Teide Volcano and Rift Zones of Tenerife, Canary Islands. Geol. Soc. Am. Bull. 119:1027–1051.

Carracedo, J.C., Guillou, H., Nomade, S., Rodríguez-Badiola, E., Pérez-Torrado, F.J., Rodriguez-González, A., Paris, R., Troll, V.R., Wiesmaier, S., Delcamp, A., Fernández-Turiel, J.L. (2011). Evolution of ocean-island rifts: the northeast rift zone of Tenerife, Canary Islands. Geol. Soc. Am. Bull. 123:562–584.

Delcamp, A., Petronis, M.S., Troll, V.R., Carracedo, J.C., de Vries, Bv.W., Pérez-Torrado, F.J. (2010). Vertical axis rotation of the upper portions of the north-east rift of Tenerife Island inferred from paleomagnetic data. Tectonophysics 492:40–59.

Delcamp, A., Troll, V.R., de Vries, Bv.W., Carracedo, J.C., Petronis, M.S., Pérez-Torrado, F.J., Deegan, F.M. (2012). Dykes and structures of the NE rift of Tenerife, Canary Islands: a record of stabilisation and destabilisation of ocean island rift zones. Bull. Volcanol. 74(5):963–980.

Dietz, R.S., Sproll, W.P. (1979). East Canary Islands as a microcontinent within the Africa-North America continental drift fit. Nature, 226, 1043-1045.

Elsworth, D., Voight, B. (1995). Dike intrusion as a trigger for large earthquakes and the failure of volcano flanks. J, Geophys. Res.-Solid Earth. 100:6005–6024.

Elsworth, D., Voight, B. (1996). Evaluation of volcano flank instability triggered by dyke intrusion. In: McGuire, WJJAPNJ (ed) Volcano instability on the Earth and other planets. Geological Society Special Publications, vol 110, pp 45–53.

Funck, T., Dickmann, T., Rihm, R., Krastel, S., Lykke-Andersen, H., Schmincke, H.U. (1996). Reflection seismic investigations in the volcaniclastic apron of Gran Canaria and implications for its volcanic evolution. Geophys. J. Int. 125:519–536.

Geldmacher, J., Hoernle, K., Van den Bogaard, P., Zankl, G., Garbe-Schönberg, D. (2001). Earlier history of the C70-Ma-old Canary hotspot based on the temporal and geochemical evolution of the Selvagen archipelago and neighbouring seamounts in the eastern north Atlantic. J. Volcanol. Geoth. Res. 111, 55-87.

Geldmacher, J., Hoernle, K., Van der Bogaard, P., Duggen, S., Werner, R., (2005). New Ar-40/Ar-39 age and geochemical data from seamounts in the Canary and Madeira

volcanic provinces: support for the mantle plume hypothesis. Earth Planet. Sc. Lett. 237:85–101.

Guillou, H., Carracedo, J.C., Paris, R., Pérèz-Torrado, F.J. (2004). Implications for the early shield-stage evolution of Tenerife from K/Ar ages and magnetic stratigraphy. Earth Planet. Sc. Lett. 222:599–614.

Gurenko, A.A., Hoernle, K.A., Hauff, F., Schmincke, H.U., Han, D., Miura, Y.N., Kaneoka, I. (2006). Major, trace element and Nd-Sr-Pb-O-He-Ar isotope signatures of shield stage lavas from the central and western Canary Islands: Insights into mantle and crustal processes. Chem. Geol. 233:75–112.

Iverson, R.M. (1995). Can magma-injection and groundwater forces cause massive landslides on Hawaiian volcanoes? J. Volcanol. Geotherm. Res. 66:295–308.

Krastel, S., Schmincke, H.U. (2002) Crustal structure of northern Gran Canaria, Canary Islands, deduced from active seismic tomography. J. Volcanol. Geotherm. Res. 115:153–177.

Krastel, S., Schmincke, H.U., Jacobs, G.L., Rihm, R., Le Bas, T.P., Alibés, B. (2001) Submarine landslides around the Canary Islands. J. Geophys. Res. Solid Earth. 106:3977–3997.

Longpré, M-A., Troll, V.R., Walter, T.R., Hansteen, T.H. (2009). Volcanic and geochemical evolution of the Teno massif, Tenerife, Canary Islands: some repercussions of giant landslides on ocean island magmatism. Geochem. Geophys. Geosyst. 10:Q12017. doi: 10.1029/2009gc002892.

Luongo, G., Cubellis, E., Obrizzo, F., Petrazzuoli, S.M. (1991). A physical model for the origin of volcanism of the Tyrrhenian margin: the case of the Neapolitan area. J. Volcanol. Geotherm. Res. 48:173–185.

MacFarlane, D.J., Ridley, W.I. (1968). An interpretation of gravity data for Tenerife, Canary Islands. Earth Planet. Sci. Lett. 4:481–486.

Manconi, A., Longpré, M.A., Walter, T.R., Troll, V.R.,Hansteen, T.H. (2009). The effects of flank collapses on volcano plumbing systems. Geology, 37:1099–1102.

Martínez del Olmo, W., Buitrago, J. (2002). Sedimentación y volcanismo al este de las islas de Fuerteventura y Lanzarote (Surco de Fúster Casas). Geogaceta 32, 51-54.

McGuire, W.J., Pullen, A.D., Saunders, S.J. (1990). Recent dyke-induced large-scale block movement at Mount Etna and potential slope failure. Nature. 343:357–359

Montelli, R., Nolet, G., Dahlen, F.A., Masters, G., Engdahl, E.R., Hung, S.H. (2004). Finite-frequency tomography reveals a variety of plumes in the mantle. Science 303, 338-343.

Montelli, R., Nolet, G., Dahlen, F.A., Masters, G., (2006). A catalogue of deep mantle plumes: new results from finite-frequency tomography. Geochem. Geophys. Geosyst. 7, Q11007.

Pérez-Torrado, F.J., Carracedo, J.C., Mangas, J. (1995). Geochronology and stratigraphy of the Roque Nublo Cycle, Gran Canaria, Canary Islands. J. Geol. Soc. 152:807–818

Rothe, P., Schmincke, H.U. (1968). Contrasting origins of the eastern and western islands of the Canarian Archipelago. Nature 218, 1152-1154.

Troll, V.R., Carracedo, J.C. (2016). The Geology of Tenerife, The Geology of the Canary Islands. https://doi.org/10.1016/b978-0-12-809663-5.00005-0

Urgeles, R., Canals, M., Baraza, J., Alonso, B. (1998). Seismostratigraphy of the western flanks of El Hierro and La Palma (Canary Islands): a record of Canary Islands volcanism. Mar. Geol. 146:225–241

van den Bogaard, P. (2013). The origin of the Canary Island seamount province - new ages of old seamounts. Sci. Rep. 3 (2107), 1-7.

Walter, T.R., Troll, V.R. (2003). Experiments on rift zone evolution in unstable volcanic edifices. J. Volcanol. Geotherm. Res. 127:107–120.

Walter, T.R., Troll, V.R., Cailleau, B., Belousov, A., Schmincke, H-U., Amelung, F., Bogaard, P.V.D. (2005). Rift zone reorganization through flank instability in ocean island volcanoes: an example from Tenerife, Canary Islands. Bull. Volcanol. 67:281–291.

Watts, A.B. (1994) Crustal structure, gravity-anomalies and flexure of the lithosphere in the vicinity of the Canary-islands. Geophys J Int 119:648–666

Watts, A.B., Peirce, C., Collier, J., Dalwood, R., Canales, J.P., Henstock, T.J. (1997). A seismic study of lithospheric flexure in the vicinity of Tenerife, Canary Islands. Earth Planet Sc Lett 146:431–447.

Wyss, M. (1980). Hawaiian rifts and recent Icelandic volcanism—expressions of plume generated radial stress-fields. J. Geophys. 47:19–22

4.2 Tenerife Island

4.2.1 Geological setting

Tenerife (Fig. 4.6) is the largest, most populated, and urbanized island of the Canary archipelago, with >908,000 residents, on a surface of 2.034,38 km^2 and a maximum altitude of 3.718 m a.s.l, corresponding to the Teide summit, the highest peak in Spain. Tenerife rises nearly 8,000 m above the top of the Miocene oceanic crust (*Watts et al., 1997*).

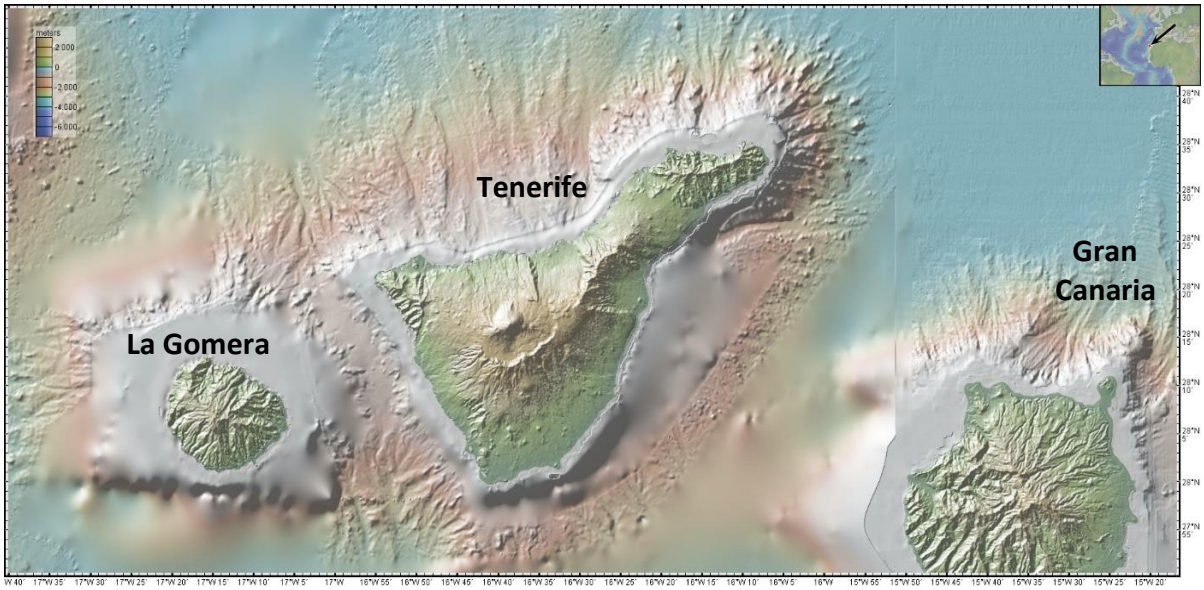

Fig. 4.6 Tenerife Island (from GeoMapApp 3.6.1). Colours represent meters above and below sea level.

The island has been extensively studied (*Hausen, 1955; Fúster et al., 1968; Ridley, 1970, 1971; Abdel-Monem et al., 1971; Carracedo, 1975, 1979; Schmincke, 1982; Wolff, 1983, 1987; Ancochea et al., 1990, 1999; Watts and Masson, 1995; Bryan et al., 1998, 2002; Thirlwall et al., 2000; Wolff et al., 2000; Edgar et al., 2002; Walter and Schmincke, 2002; Guillou et al., 2004; Pittari et al., 2005; Walter et al., 2005; Bryan, 2006; Pittari et al., 2006; Carracedo et al., 2007, 2011; Longpré et al., 2009*). The triangular shape is the result of a long-lasting volcanic activity of three main large shield volcanoes and periods of eruptive quiescence, followed by rejuvenation volcanism (Fig. 4.7; see 4.1 paragraph). Flanks of the island are marked by three main landslides scars triggered either by seismic shaking associated with caldera collapse (*Martí et al., 1997; Hürlimann et al., 1999, 2001*), or to lateral overpressure (*Carracedo, 1994; Carracedo et al., 2011*) and gravitational spreading of the Tenerife volcanic edifice (*Walter, 2003; Walter et al., 2005*): 1) the Icod landslide, occurred between ~0.165–0.179 Ma (*Martí et al., 1994, 1997; Boulesteix et al., 2012*); 2) Güímar landslide, between 0.86 and 0.83 Ma

(*Ancochea et al., 1990; Carracedo et al., 2011*), due to a flank instability; 3) La Orotava landslide, between 0.69 and 0.56 Ma (*Ibarrola et al., 1993; Carracedo et al., 2011*).

The first shield volcano, called *Central Shield*, developed in the central part of the island. *Guillou et al. (2004)* dated the oldest outcropping rocks (Roque del Conde) by $^{40}Ar/^{39}Ar$ and K/Ar between 11.9 to 8.9 Ma. A second shield volcano, called *Teno volcano*, grew in a short period, in the western sector of the Central shield, from 6.11 to 5.15 Ma (*Guillou et al., 2004; Longpré et al., 2009*). Then, in the north-eastern area of the island the third volcano, *Anaga Shield,* developed between 4.89 to 3.95 Ma (*Guillou et al., 2004; Walter et al., 2005*). At the end of the Anaga volcano, after an important erosive period (>3.5 Ma), volcanism resumed at the centre of the island and formed the *Las Cañadas Volcano* (*Ancochea et al., 1990, 1999; Martí et al., 1994; Huertas et al., 2002),* of which the Teide Volcanic Complex (TVC) represents the latest stage of growth.

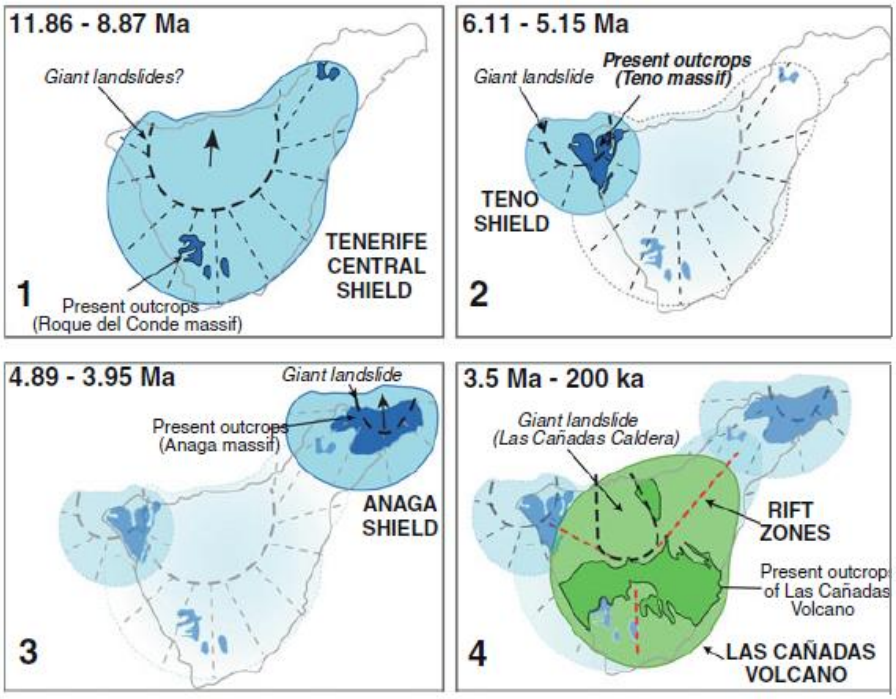

Fig. 4.7 Subsequent stages on Tenerife shield volcanoes (from *Carracedo and Troll, 2013*).

The Las Cañadas Volcano has been extensively studied (e.g., *Booth, 1973; Wolff, 1983, 1987; Martí et al., 1990, 1994; Bryan et al., 1998; Ancochea et al., 1999; Cantagrel et al., 1999; Edgar et al., 2002, 2007; Huertas et al., 2002; Brown et al., 2003; Brown and Branney, 2004; Pittari et al., 2005, 2006*): it developed in three phases separated by three large scale flank

collapses. The activity of this volcano can be divided into three phases: the first was characterized by effusive eruptions and basaltic magma compositions, while the last two phases were prevalently explosive and characterized by more differentiated magmas. *Martí et al. (1997)* proposed three principal basaltic-to-phonolitic cycles, starting with mafic or intermediate eruptions and evolving towards phonolitic products. Afterward, the combined action of several caldera-forming eruptions and large landslides formed Las Cañadas Caldera (0.8-0.2 Ma), an asymmetrical horseshoe-shaped depression 15 km wide and open to the north, occupying the central part of the island (*Martí, 2019* and reference therein).

4.2.2 Teide-Pico Viejo volcanic complex

The TVC (Fig. 4.8) grew nested into Las Cañadas caldera, filling the Icod embayment and is considered the volcanic renewal of the Las Cañadas Volcano. Five main volcano-stratigraphic units can be identified: 1) *Teide* stratovolcano (124-30 ka); 2) *Pico Viejo* stratovolcano (27-17 ka); 2) *peripheral domes* with associated lava flows (PLD) within the Las Cañadas caldera and around the Teide-Pico Viejo stratocones; 3) the *NW Rift Zone* (NWRZ), already active before the 200-ka lateral collapse and during the past 30 ka; 5) the *NE rift zone* (NERZ) with three main periods of activity, from Miocene to Holocene, interacting with the development of the Las Cañadas Volcano (*Carracedo et al., 2007, 2011*).

The eruptive activity of Teide stratocone was coeval with eruptions from the NE and NW rift zones. The oldest formations, reached with the *galerías* (tunnels excavated for groundwater), were dated at 124–32 ka (*Carracedo and Troll, 2013* and reference therein). The old phase of the construction of Teide stratocone (Old Teide) was completed at about 30 ka, and since then only one eruption has been observed, i.e. the Lavas Negras eruption at 1150 ± 140 yr BP (cal 645- 1168 AD, *Carracedo et al., 2007*).

The Pico Viejo volcano developed on the western flank of Teide and was active between 27 and 17 ka, even if minor Holocene eruptions at the rim and inside the crater occurred, producing from basaltic to phonolitic eruptions (*Carracedo and Troll, 2013* and reference therein). If its position and the fitting between the ages of its early basaltic eruptions with those of the final phonolitic eruptions of Teide is considered, Pico Viejo can be considered as an adventive eruptive centre of Teide volcano, that originated from the westward migration

of magmas. Moreover, this westward migration of the TVC eruptive activity seems to be corroborated by the abundant Holocene activity of the NWRZ of the last 30 ky.

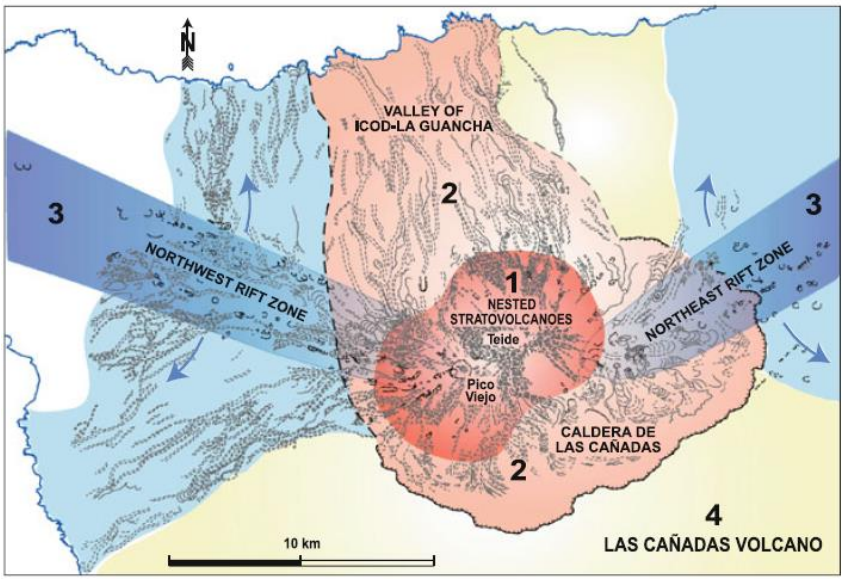

Fig. 4.8 Main volcanic units of Teide Volcanic complex. 1. Teide and Pico Viejo stratocone, 2. Icod- La Guancha landslide, 3. North-west and Northeast rift zones, 4. Pre-collapse Las Cañadas Volcano (from *Carracedo and Troll, 2013*).

The PLD unit is constituted by Holocene volcanic eruptions inside the Las Cañadas Caldera, in the eastern and southern Teide flanks or sub-horizontal areas of the caldera. They are mainly phonolitic domes, roughly circular, with thick and short lava flows around the vents inside the Las Cañadas Caldera (*Troll and Carracedo, 2016*). Conversely, eruptions that occurred along the northern slope of Teide formed lava flows of extraordinary length (>15 km) that reached the northern coast (e.g., Roques Blancos eruption, Abejera Alta and Pico Cabras lava domes). Some of them (for example the case of Roques Blancos eruption) show coulées, with levees and pressure ridges. Some of these eruptions also produced fallout deposits (for example Mña Blanca, Roques Blancos, Pico Cabras and Abejera), indicating explosive phases (*García et al., 2014*).

The NERZ extends from the base of Teide towards the Anaga shield. This rift hosts ~14 vents aligned along the Izaña and Fasnia volcanic chains, especially condensed in the SW end of the rift (near the central cone) and dispersed in a fan distribution in the SE termination. This rift had three cycles of activity, i.e. Miocene, Pliocene and Pleistocene. Three principal lateral collapses took place here: the first (Micheque) happened at ca. 830 ka, the second was the

Güímar lateral collapse, occurred at 860 ± 18 ka, which produced a depression 10 x 10 km wide. Finally, the Orotava collapse occurred, dated with a minimum age of 566 ± 13 ka and 690 ± 10 ka (*Abdel-Monem et al., 1971; Carracedo et al., 2011*). After such collapses, the activity progressively decreased. The most recent eruption in this rift is the 1704-1705 AD Arafo-Fasnia-Siete Fuentes eruption.

The NWRZ extends from the Teno Massif to Las Cañadas Caldera rim, along Chío (southward) and Garachico (northward) volcanic chains, and counts ~30 cones (*Carracedo et al., 2007*) clustered at the crest of the rift. The older cones are located near Teno Massif, whereas the younger edifices are in the central part and near the Teide stratocone. Compared to the NERZ, this rift was very active during the Holocene epoch, but many eruptions are not yet dated. In the historic period (since 1492 AD), four volcanic eruptions occurred in the NWRZ: Boca Cangrejo (1492 AD), Garachico (1706 AD), Chahorra (1789 AD), and Chinyero (1909 AD). A peculiar feature of this rift is the occurrence of magma mixing/mingling in the proximal end of the NWRZ, near the Teide volcano: basaltic and phonolitic magmas are contemporaneously erupted during a single eruption, as in the case of Mña Reventada eruption (*Ablay and Martì, 2000; Ablay et al., 1998; Araña et al., 1989a, b; Carracedo et al., 2007; Rodríguez-Badiola et al., 2006; Wiesmaier et al., 2011, 2013*).

As described above, rifts and central volcanoes in Tenerife acted as a continuous and interconnected system, in which basaltic rift and phonolitic eruptions represent the extreme ends of a bimodal compositional system. While fissure basaltic volcanism was active along the ridges, with reservoirs placed at a depth between 5 and 14 km b.s.l (*Araña et al., 2000; Almendros et al., 2007; Blanco-Montenegro et al., 2011*), explosive eruptions were fed by more evolved magmas located in several coexisting isolated reservoirs in the centre of the island (*Mitjavila and Villa, 1993; Martí et al., 1994; Ablay et al., 1998; Bryan et al., 1998; Marti and Gudmundsson, 2000; Wolf et al., 2000; Edgar, 2003; Martí et al., 2008; Martí and Geyer, 2009; Andújar and Scaillet, 2012; De Barros et al., 2012; Andújar et al., 2013*). According to several authors (*Ablay and Martí, 2000; Andújar 2007; Andújar et al., 2010*), the Teide-Pico Viejo phonolites were stored at about 1-2 km in depth below sea level (b.s.l.).

The TVC activity has been interpreted as the result of a volcanic cycle (Fig. 4.9): after the formation and the growth of Teide, the activity of both the NW and NE rifts zones declined and restarted only when Teide reached the critical elevation of 3,500 m above sea level (a.s.l.)

at about 30 ky. Then, Pico Viejo development started in the western flank of Teide, together with the renewal of eruptions at NERZ; when Pico Viejo reached a critical elevation, eruptions occurred both as peripheral lava domes and as basaltic fissures on both rift zones (*Carracedo and Troll, 2013*). According to *Walter et al. (2005)* and *Delcamp et al. (2010),* this regime may persist as long as the volcanic activity ceases or the rifts become unstable and collapse: when a collapse occurs, the ascent and eruption of mafic and crystal-rich magma are eased (*Longpré et al., 2009; Manconi et al., 2009*), and the plumbing destruction makes the emplacement of magma at shallower depths easier, allowing magmatic differentiation and felsic eruptions that can lead to the formation of a central volcano (*Carracedo et al., 2011*). If volcanism continues, the cycle might begin again. According to *Carracedo et al. (2011),* the TVC may have reached a terminal stage in the Holocene epoch.

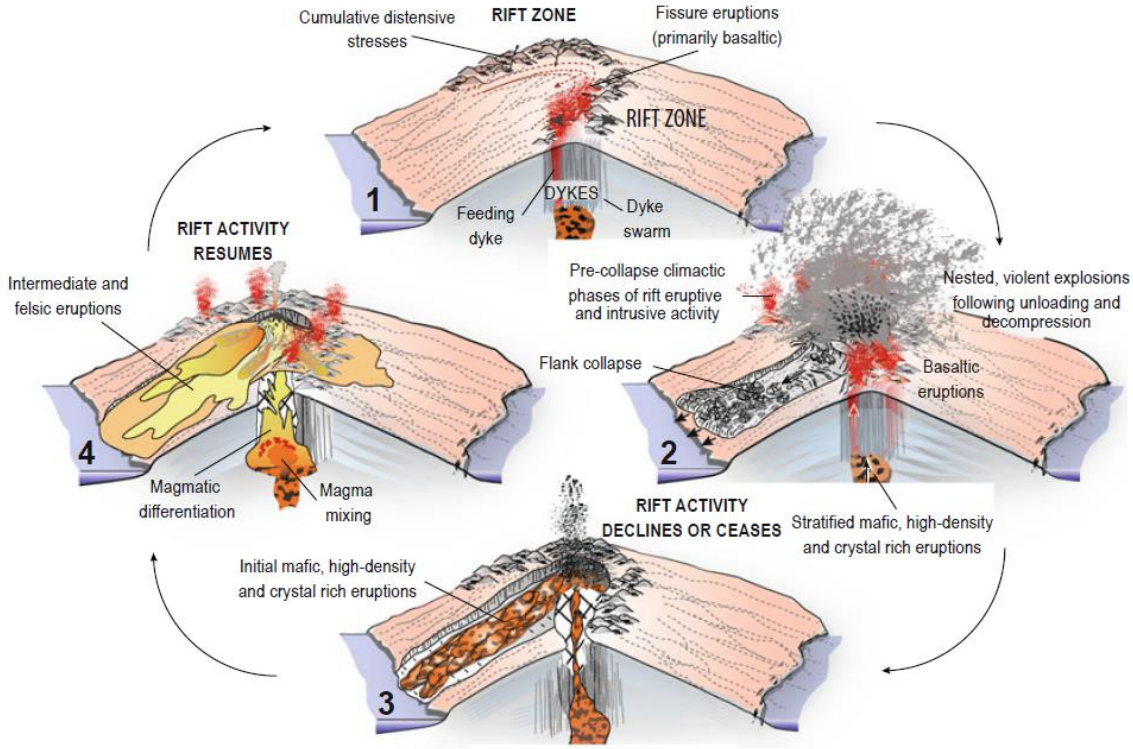

Fig. 4.9 Simplified model displaying the cycle of activity between rifts and central volcanism (from *Carracedo and Troll, 2013* and reference therein).

4.2.3 Studied eruptions

Many Holocene eruptions in the central area of Teide and Pico Viejo cones and along the two rifts, especially in the NWRZ, have taken place. Despite the volcanic activity having been very intense, the most recent period of TVC volcanic activity is still insufficiently investigated.

Nonetheless it is fundamental for a correct evaluation of volcanic hazard to forecast future eruptions. In Fig. 4.10, all Holocene eruptions are displayed. If historic eruptions are not considered, only 40% of them are dated, whereas the remaining part is undated or only stratigraphically constrained. Therefore, it is a crucial point to fill this gap to reconstruct correctly the evolution of the recent magmatic system of Tenerife.

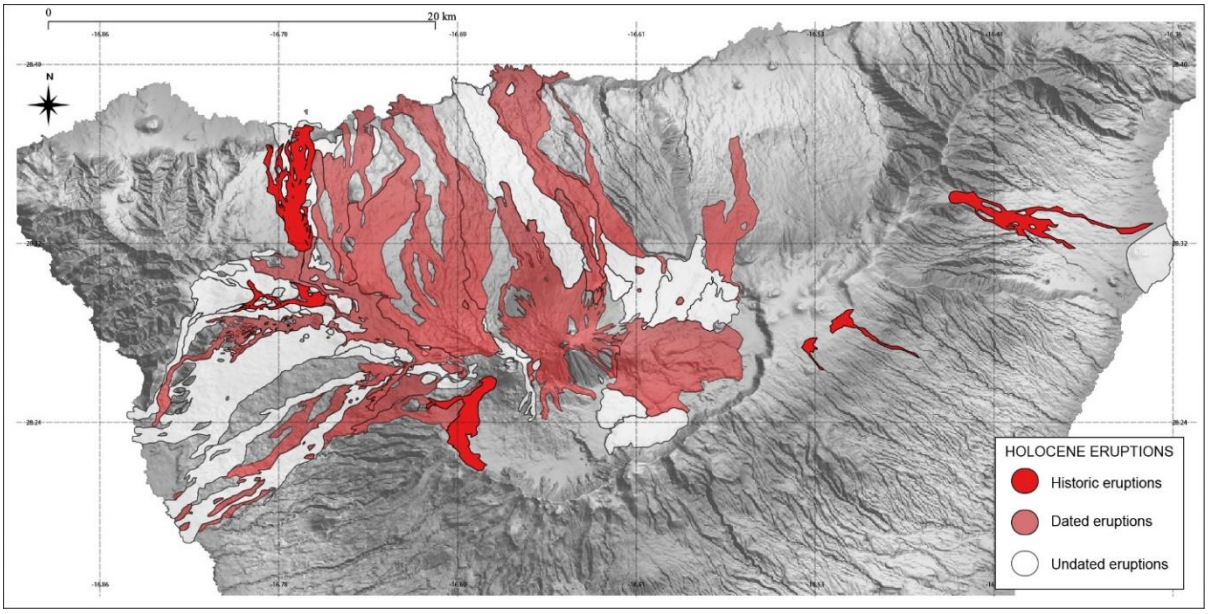

Fig. 4.10 Map of Tenerife (from a DEM-shaded relief image courtesy of Instituto Geográfico Nacional - IGN) showing Holocene eruptions.

For this study, large mostly effusive Holocene eruptions have been selected. Nine lava flows based on volumes, length and width of involved sectors have been chosen, giving preference to those that have affected inhabited areas. The studied eruptions (Fig. 4.11) include Pico Cabras, Roques Blancos and Abejera Alta from the PLD unit, Boca Cangrejo, Mña Reventada, Mña Cascajo, Mña Botija and Mña Bilma from the NWRZ and Mña Grande, located on the east coast in the Güímar Valley. Some of these eruptions (Abejera Alta, Roques Blancos, Mña Reventada and Boca Cangrejo) were already palaeomagnetically investigated by *Kissel et al. (2015b),* and dated with ^{14}C by *Carracedo et al. (2007).*

Results were compared with those obtained previously on the same lava flows with the ^{14}C method (*Carracedo et al., 2007*), to estimate methods' consistency and accuracies.

In Table 1, the location of each sampling site and independent age constraints are listed.

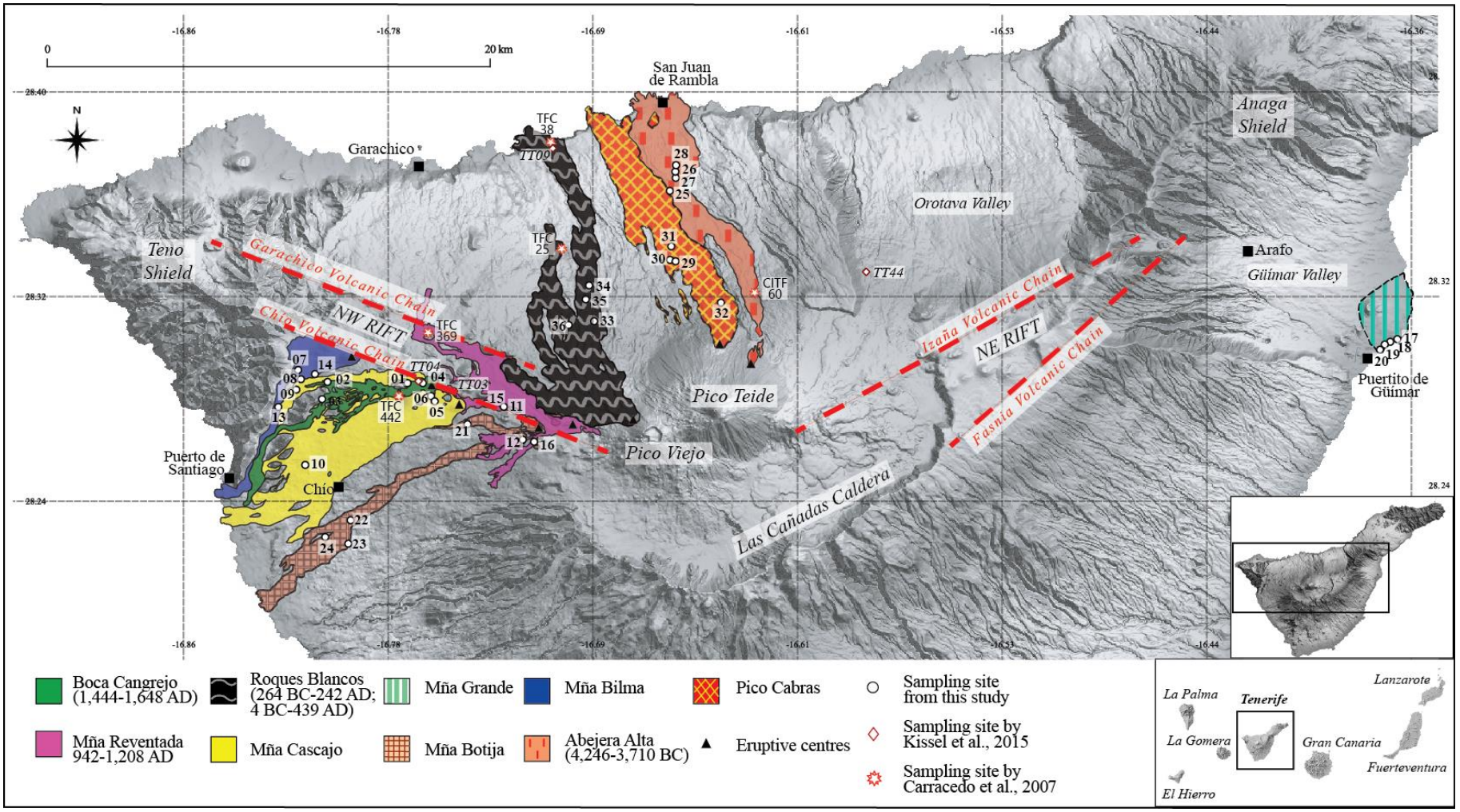

Fig. 4.11 Simplified map of Tenerife (from a DEM-shaded relief image courtesy of Instituto Geográfico Nacional - IGN) showing the studied lava flows and the sites of palaeomagnetic sampling. Reported flow ages are according to *Carracedo et al. (2007)*. For each site is implied TEN. Black circles reproduce palaeomagnetic sites of this study. Red rhombus and red stars represent sampling sites by *Kissel et al. (2015b)*, and *Carracedo et al. (2007)*, respectively.

Table 1. Location of the sampling sites at Tenerife and independent age constraints from geochronologic or geologic evidence.

Volcanic Unit	Area	Code	Locality	Latitude, °N	Longitude, °W	Alt. (m a.s.l.)	Method	Age Constraint (BP)	Calendar-Calibrated Ages (2σ error level)
Boca Cangrejo	NWRZ	TEN01	TF-38	28°16'59.18''	16°46'2.03''	1,446	^{14}C	350±60	1,444-1,648 AD
		TEN02	Las Manchas; TF-375	28°17'2.47''	16°47'58.22''	1,025			
		TEN03	Las Manchas; TF-375	28°16'38.51''	16°48'6.58''	1,057			
		TEN04	TF-38	28°16'59.98''	16°45'38.70''	1,479			
Montaña Reventada	NWRZ	TEN11	TF-38	28°16'22.40''	16°43'43.60''	1,816	^{14}C	990±70	942-1,208 AD
		TEN12	TF-38	28°15'34.34''	16°43'13.29''	1,931			
		TEN15	TF-38	28°16'26.14''	16°44'9.67''	1,749			
		TEN16	TF-38	28°15'29.55''	16°43'0.15''	1,950			
Montaña Grande	Extra NERZ	TEN17	Puertito de Güímar	28°18'5.22''	16°21'53.67''	0			
		TEN18	Puertito de Güímar	28°18'2.34''	16°22'4.33''	0			
		TEN19	Puertito de Güímar	28°17'59.28''	16°22'11.17''	0			
		TEN20	Puertito de Güímar	28°17'52.65''	16°22'22''	15			
Roques Blancos	PLD	TEN33	Pista del Agujero ("Pista 1600")	28°18'31.14''	16°41'38.75''	1,567	^{14}C	Early Roques Blancos (2,010±120) Roques Blancos (1,790 ±120)	Early Roques Blancos: 264 BC-242 AD Roques Blancos: 4 BC-439 AD
		TEN34	Pista Barranco de la Arena	28°19'22.29''	16°41'34.80''	1,286			
		TEN35	Pista del Agujero ("Pista 1600")	28°19'3.18''	16°41'39.44''	1,392			
		TEN36	Pista del Agujero ("Pista 1600")	28°18'26.42''	16°42'2.70''	1,609			
Montaña Cascajo	NWRZ	TEN05	TF-38	28°16'33.31''	16°45'22.39	1,531		Between Montaña de Chío (^{14}C: 3,620 ± 140)	Montaña de Chío: 2,350-1,630 BC Volcán El Ciego:
		TEN06	TF-38	28°16'42.31''	16°45'27.75''	1,516			
		TEN09	El Retamar; TF-82	28°16'50.23''	16°48'41.86''	817			

		TEN10	Camino Finca Chigora; TF-82	28°15'0.68''	16°48'30.96''	698		and Volcán El Ciego (^{14}C: 2,600 ±160)	1,128-367 BC
Montaña Botija	NWRZ	TEN21	TF-38	28°15'57.78''	16°44'35.01''	1,636		Between Montaña de Chío (^{14}C: 3,620 ± 140) and Volcán El Ciego (^{14}C: 2,600 ±160)	Montaña de Chío: 2,350-1,630 BC; Volcán El Ciego: 1,128-367 BC
		TEN22	Chiguergue; TF-82	28°13'40.26''	16°47'25.65''	650			
		TEN23	Guía de Isora; TF-463	28°13'6.77''	16°47'27.49''	511			
		TEN24	Pista de Alzola; TF463	28°13'16.10''	16°48'3.22''	429			
Montaña Bilma	NWRZ	TEN07	El Molledo; TF-375	28°17'21.15''	16°48'40.50''	912		Younger than Cuevas del Ratón (^{14}C: 5,370±50)	Cuevas del Ratón: 4,332-4,146 BC
		TEN08	El Molledo; TF-82	28°17'6.93''	16°48'37.90''	864			
		TEN13	Tamaimo; TF-82	28°16'25.45''	16°49'10.19''	623			
		TEN14	Las Manchas; TF-375	28°17'13.63''	16°48'14.79''	974			
Abejera Alta	PLD	TEN25	La Guancha; TF-344	28°21'42.87''	16°39'39.81''	696	^{14}C	5,170±110	4,246-3,710 BC
		TEN26	La Guancha; TF-344	28°22'9.48''	16°39'30.42''	580			
		TEN27	La Guancha; TF-344	28°22'0.12''	16°39'33.61''	608			
		TEN28	La Guancha; soccer field	28°22'17.83''	16°39'31.10''	545			
Pico Cabras	PLD	TEN29	Pista del Agujero ("Pista 1600")	28°20'0.81''	16°39'32.61''	1,103		Between Montaña Negra (^{14}C: 8,220±120) and Abejera Alta (^{14}C: 5,170±110)	Montaña Negra: 7,540-7,019 BC Abejera Alta: 4,246-3,710 BC
		TEN30	Pista del Agujero ("Pista 1600")	28°20'1.75''	16°39'40.75''	1,114			
		TEN31	Pista del Agujero ("Pista 1600")	28°20'21.01''	16°39'37.87''	1,015			
		TEN32	Pista del Agujero ("Pista 1600")	28°18'58.21''	16°38'25.08''	1,614			

Site coordinates were gathered by a Garmin GPS, using the WGS84 datum. All radiocarbon ages were retrieved from *Carracedo et al. (2007)* and *Carracedo et al. (2008).* The conversion of ^{14}C conventional ages (yr BP) into calendar-calibrates ages (cal yr AD-BC) was obtained using INTCAL13 *(Reimer et al., 2013*) terrestrial radiocarbon age calibration, with the Radiocarbon Calibration Program CALIB REV 7.1.0. (*Stuiver et al., 2020*). All ages are reported with corresponding uncertainties at the 2σ level. TF-38: Carretera Boca Tauce-Chío; TF-375: Carretera Santiago del Teide a Chio (Arguayo); TF-82: Carrettera Icod de Los Vinos a Armeñime; TF-463: Carretera Guía de Isora a Playa de San Juan. NWRZ, North-West rift zone; NERZ, North-East rift zone; PLD, peripheral Lava Dome.

4.2.3.1 NWRZ and extra-rift areas

On the NWRZ, five eruptions were sampled, including *Boca Cangrejo, Mña Cascajo, Mña Bilma, Mña Reventada* and *Mña Botija*. The *Mña Grande (Volcán de Güímar)* eruption is located completely off rift, along the east coast of Tenerife.

The **Boca Cangrejo** (Fig. 4.12) is considered one of the historical eruptions that occurred in Tenerife and is commonly associated with the eruption witnessed by Christopher Columbus during his voyage to the New World (1492 AD). During the eruption, lava flows with tephritic/basanitic composition (*Rodríguez-Badiola et al., 2006*) were emitted from multiple vents consisting of small spatter cones and fractures. Lavas are aa-type, a few meters thick and characterized by dark grey colour and sub-aphyric texture. Charcoal allowed dating the eruption at 1,444-1,648 AD (TFC-442, *Carracedo et al., 2007).* The Boca Cangrejo flows were also investigated by *Kissel et al. (2015b)* in TT04 site. Four sites were collected on this lava flow: TEN01, 02, 03 and TEN04.

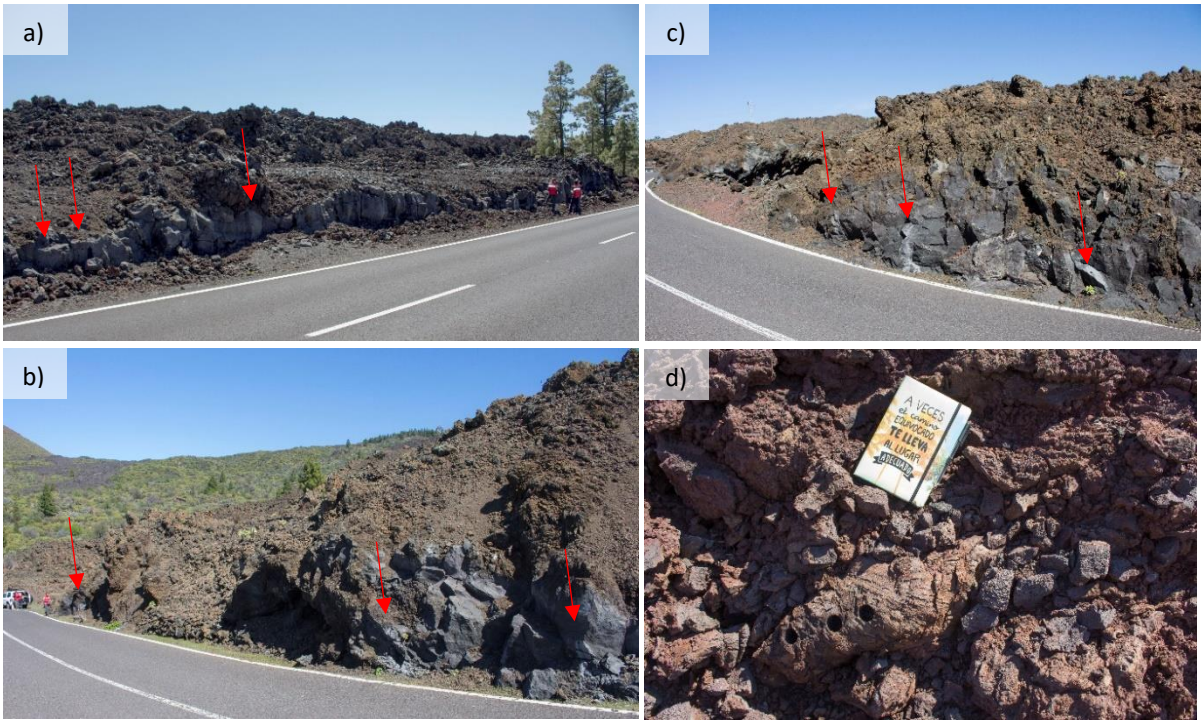

Fig. 4.12 Sampling sites of Boca Cangrejo: a) TEN01; b) TEN02; c) TEN03; d) TEN04. Red arrows indicate sampling points.

Mña Cascajo eruption (Fig. 4.13) produced several strombolian cones aligned along two NW-SE trending eruptive fissures (Mña Cascajo and El Espárrago). The Mña Cascajo lava complex is one of the biggest lava fields of Tenerife; flows covered 27.6 km^2 and reached the

west coast of the island ~10 km away from the vents, with an estimated total volume of 0.138 km^3 (*Carracedo and Troll, 2013*). The lava flow has a basanitic composition (*Rodríguez-Badiola et al., 2006*), with porphyritic texture and abundant crystals of olivine, mafic minerals, and few plagioclases. The eruption has not been dated, but the age is only stratigraphically constrained between Volcán El Ciego (1,128-367 BC) and Mña de Chío (2,350-1,630 BC) eruptions, possibly with an age closer to the Volcán El Ciego eruption (*Carracedo et al., 2008*). Four sites were sampled: TEN05, 06, 09 and TEN10.

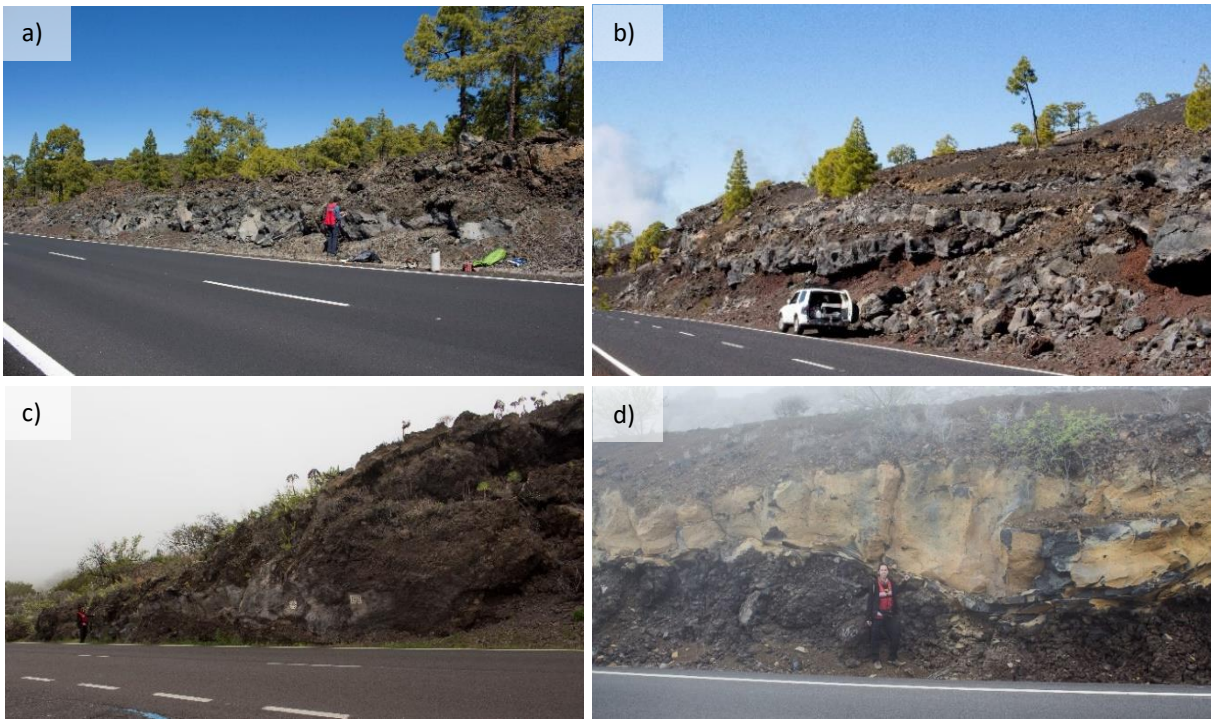

Fig. 4.13 Sampling sites of Mña Cascajo: a) TEN05; b) TEN06; c) TEN09; d) TEN10.

Mña Bilma (Fig. 4.14) is a ~180 m-high scoria cone located in the westernmost sector of the Chío volcanic chain, next to the Teno massif. A lava flow was emitted from a breach of the northwest base of the cone, which reached the western coast of the island. Lavas are basanites (*Rodríguez-Badiola et al., 2006*), with porphyritic texture and crystals of olivine and femic minerals, from millimetric to sub-centimetric size. The age of the eruption has not been yet determined, but only stratigraphically constrained as younger than Cuevas del Ratón eruption (*Carracedo et al., 2008*), which was dated by ^{14}C at 4,332-4,146 BC. In this lava flow four sites TEN07, 08, 13 and TEN14 were sampled.

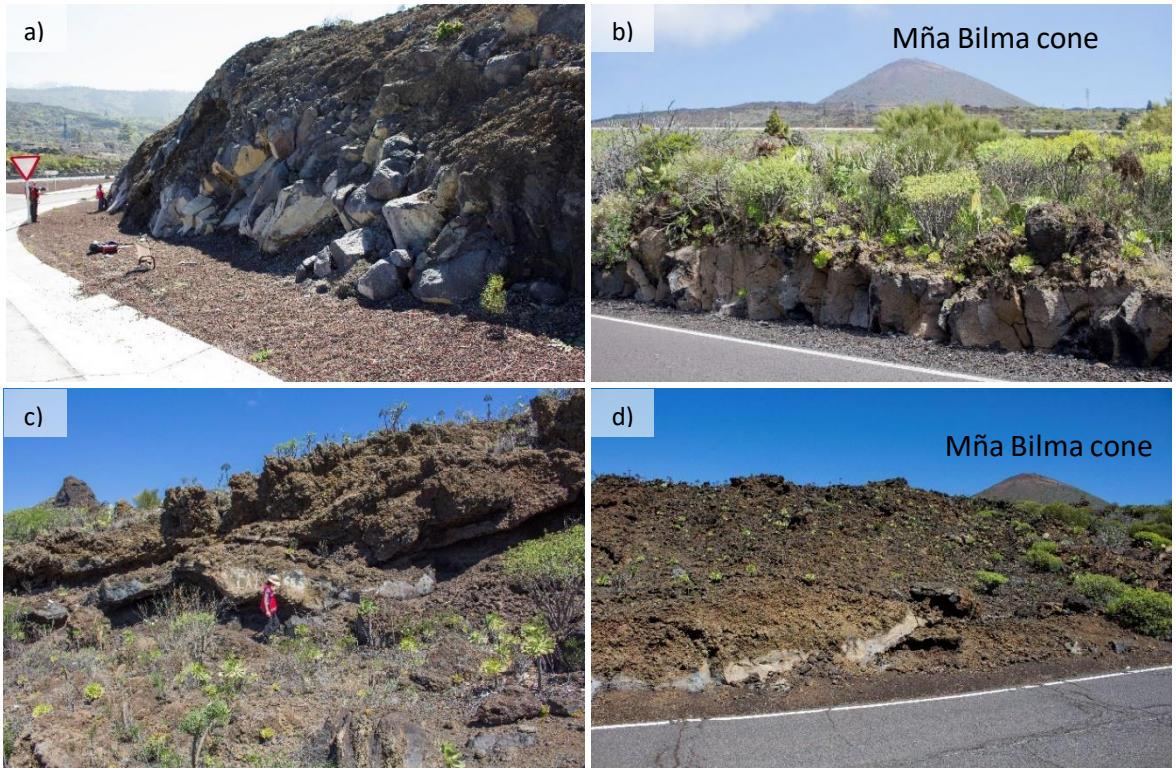

Fig. 4.14 Sampling sites of Mña Bilma: a) TEN07; b) TEN08; c) TEN13; d) TEN14.

The **Mña Reventada** (Fig. 4.15) is one of the eruptions that occurred in the easternmost sector of the Chío volcanic chain, in an interconnection zone between the NWRZ and the central complex of Teide. The eruption comprises multiple vents aligned on a NW-SE eruptive fissure from which two main lava flows of ~9 km to the northwest and ~4 km to the southwest were erupted respectively (*Carracedo and Troll, 2013*). The flows have a 20-200 cm thick base with basanite composition, with dark colour and aphyric lava, overlaid by massive up to 12 m-thick phonolite flow, light-coloured and porphyritic. The two parts are separated by a sharp and clear horizontal interface (Fig. 4.15a). According to *Wiesmaier et al. (2011)*, the process driving the Mña Reventada eruption was related to the partial mixing and mingling of the two different magmas. A hotter basanite dyke intruded the cooler phonolite magma chamber, and the thermal contrast allowed the partial mixing and hybridisation. *Carracedo et al. (2007)* dated it with the ^{14}C at 942-1,208 AD (TFC-369 site). The Mña Reventada lava was also sampled by *Kissel et al. (2015b)* in TT03 site. Four sites, TEN11, 12, 15 and TEN16, with a total of 20 and 22 basalt and phonolite cores, respectively, were collected.

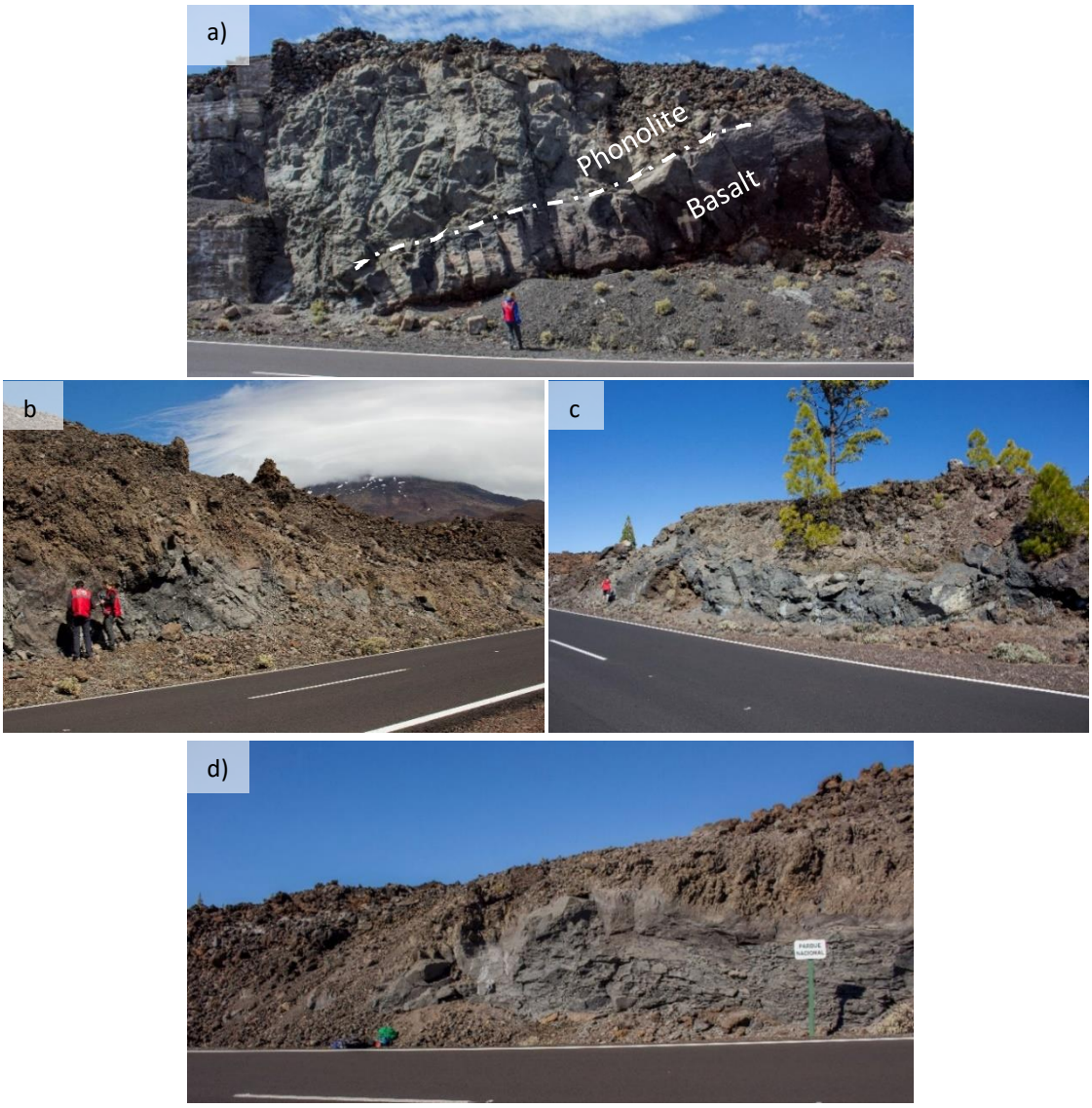

Fig. 4.15 Sampling sites of Mña Reventada: a) TEN11; b) TEN12; c) TEN15; d) TEN16.

The **Mña Grande** (Fig. 4.16) eruption was never studied previously, and only recently a detailed volcanological study has been provided by *Di Roberto et al. (2020).* The eruption occurred close to the south-eastern coast of the Güímar Valley, near the village of Puertito de Güímar, out the main rifts. It produced a ~180 m-high, slightly ellipsoidal scoria cone, elongated in a NNE-SSW direction, composed of unwelded deposits of coarse-grained scoriaceous lapilli, which vary in colour, thickness, and lithological features. These lie in angular unconformity on stratified lapilli deposits, deriving from the pre-Late Quaternary-Diego Hernandez Formation (DHF) (600 – ca. 180 ka; *Edgar et al., 2007; Martí, 2019*) basaltic volcanic activity (*Di Roberto et al., 2020*). Medial and distal deposits are partially removed and/or eroded, and they are recognized only within 2 km from the crater. The eruption

produced also a fan-shaped composite lava delta of 3.3 x 2.2 km, covering a total surface >4.5 km^2, which increased the coastline more than 100 m in some points (*Dóniz-Páez et al., 2013*). The lava flow shows differences in thickness and aspect from north to south (*Di Roberto et al., 2020*). In the northern part of the lava field, flow units are thicker and show the classical "aa" morphology; in contrast, in the southern part, lava flows emitted by an emission vent located southeast to the cone are more pellicular and often create flat, smooth surfaces or ropey pahoehoe. Generally, lavas are rich in vesicles with variable sizes, and porphyritic with olivine and pyroxene crystals.

Fig. 4.16 Sampling sites of Mña Grande: a) TEN17; b) TEN18; c) TEN19; d) TEN20; e) particular with fossils shell. Red arrows indicate sampling points.

A peculiar feature of the Mña Grande lavas is that, at several locations, they flowed over palaeobeaches and incorporated lava beach pebbles of various sizes, and fossil gastropod

shells (e.g., Stramonita haemastoma and Patella, Fig. 4.16e). No age constraint exists for this eruption. Only a general indication of Quaternary age was provided by *Dóniz-Páez et al. (2013)* based on geomorphologic features. However, the lava flow shows mostly unvegetated surfaces, lack of significant erosion and alteration, suggesting a very young Holocene age. Moreover, lava delta gently slopes into the sea forming a coastal platform, which according to *Carracedo et al. (2001)* is evidence of an age younger than the last glacial maximum (<18 ka). Four palaeomagnetic sites were sampled, TEN17, 18, 19 and TEN20, together with fossils shells to obtain also a ^{14}C dating.

Mña Botija (Fig. 4.17) is a fissural strombolian eruption, including several cones and a ~13 km-long lava flow that reached the western coast of Tenerife. Nowadays, the lava is partially covered by the products of the Mña Reventada eruption. The lava has a basanite composition (*Rodríguez-Badiola et al., 2006)* with sub-aphyric texture. This eruption is stratigraphically bracketed between the Volcán El Ciego (1,128-367 BC, ^{14}C age) and Mña de Chío (2,350-1,630 BC, ^{14}C age) eruptions and, according to *Carracedo et al. (2008)*, closer to the latter eruption age. TEN21, 22 23 and TEN24 sites were palaeomagnetically sampled.

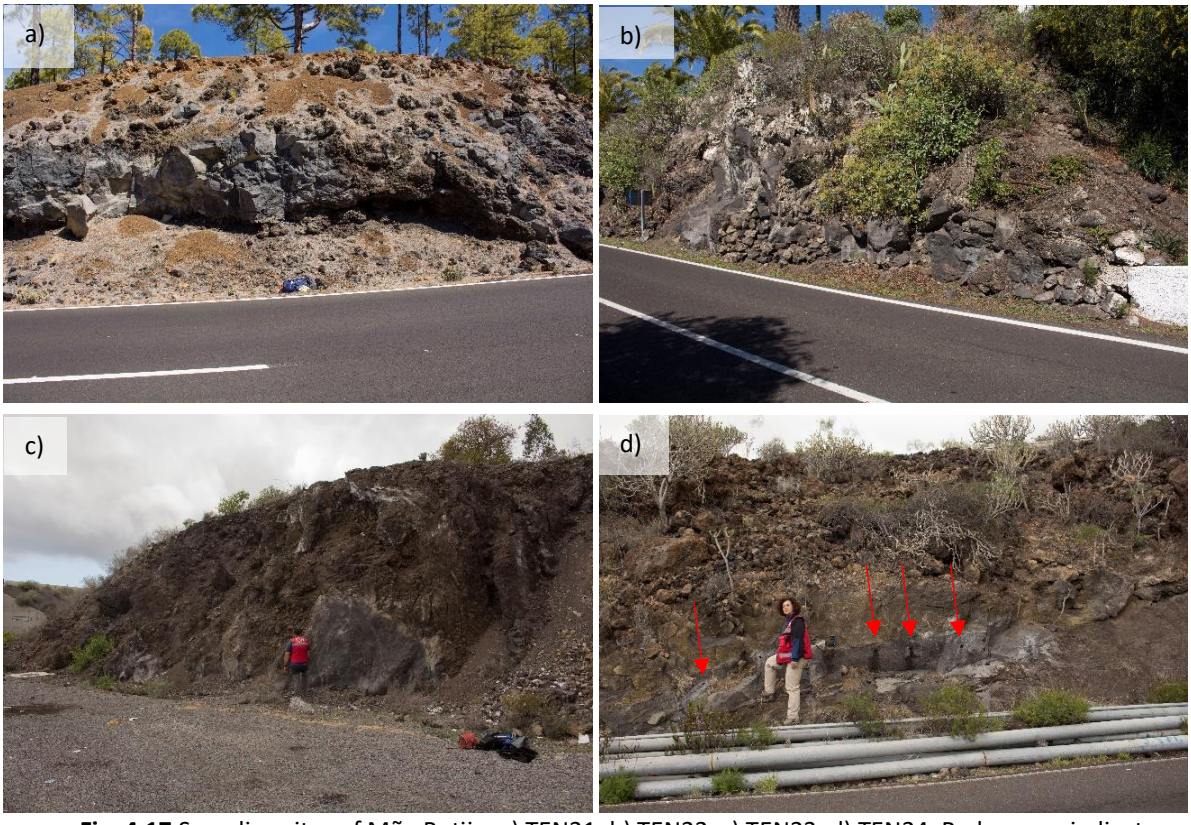

Fig. 4.17 Sampling sites of Mña Botija: a) TEN21; b) TEN22; c) TEN23; d) TEN24. Red arrows indicate sampling points.

4.2.3.2 Peripheral Lava Domes

The lava flows generated by peripheral domes have a blocky structure, with an appreciable thickness (>30 m and up to 160 m in Roques Blancos flows) and are usually channelled in well-developed lateral levees (*Carracedo and Troll, 2013).*

Pico Cabras (Fig. 4.18) is a volumetrically significant eruption (0.28 km^3; *García et al., 2014*) produced from a vent developed by a radial fissure on the Teide northern flank. The eruption produced phonolitic obsidian lavas (*Rodríguez-Badiola et al., 2006*), with laminar texture and strips with different colours and crystallinity. Lava is characterized by light grey colour, sub-aphyric texture, with feldspar (from few mm to cm) and femic crystals. Lava flows flowed downhill into the Icod Valley reaching the northern coast of Tenerife ~15 km away. Few well-preserved stratified outcrops of pumiceous lapilli are associated with the eruption, indicating that it also had a final explosive phase (*García et al., 2014*). The age of the eruption is stratigraphically constrained between 4,246-3,710 BC and 7,540-7,019 BC, the age of Abejera Alta and Mña Negra eruptions, respectively. In this lava flow four sites were selected: TEN29, 30, 31 and TEN32.

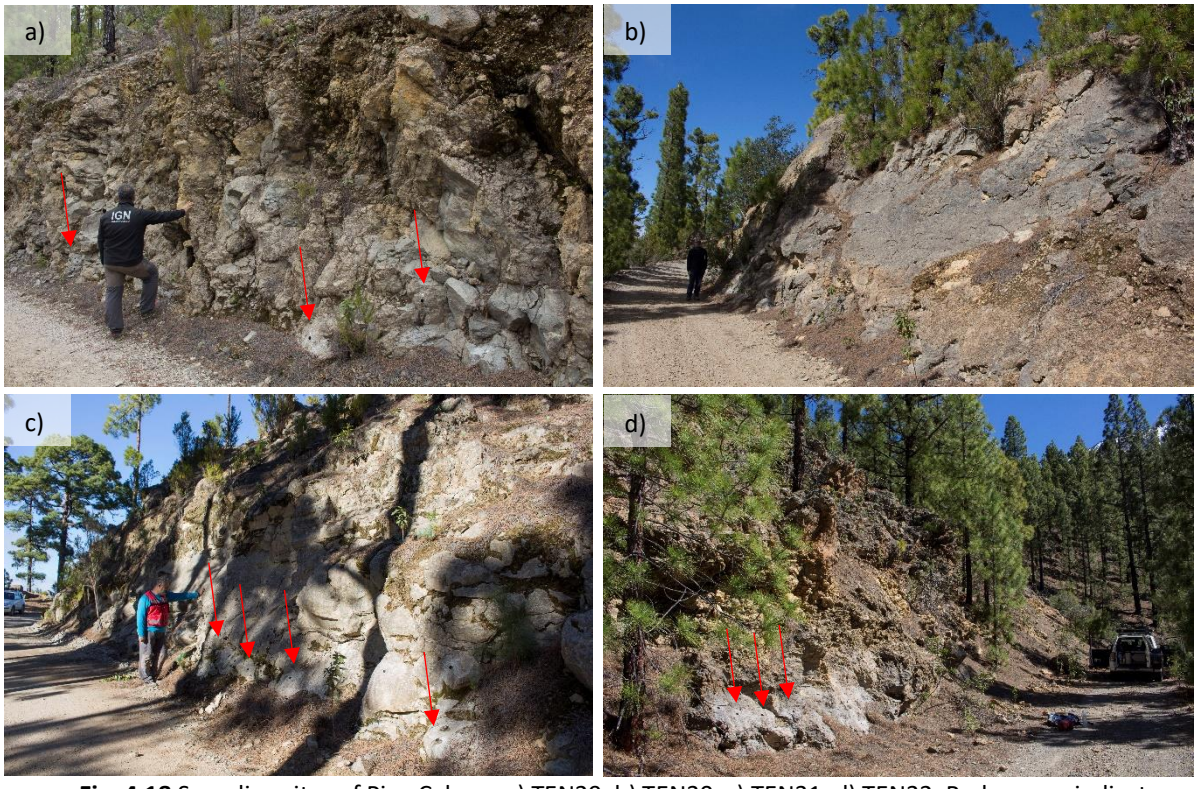

Fig. 4.18 Sampling sites of Pico Cabras: a) TEN29, b) TEN30, c) TEN31, d) TEN32. Red arrows indicate sampling points.

The **Abejera Alta** eruption (Fig. 4.19) is located east of the Pico Cabras vent complex. This strombolian eruption developed along a radial eruptive fissure of Teide and includes two lava domes and three phonolitic blocky lava flows (~0.36 km^3) erupted from two vents (*Ablay and Martí, 2000; García et al., 2014*). Lava is light grey in colour, aphyric and has a phonolitic composition (*Rodríguez-Badiola et al., 2006).* The vent complex is almost totally covered by the Abejera Baja volcanic products. The Abejera Alta eruption comprises pyroclastic fallout deposits, mostly formed by pumiceous lapilli, and lava flows that reached the northern island coast. Abejera Alta has been dated with ^{14}C method at 4,246-3,710 BC (CITF-60 site of *Carracedo et al., 2007*, Fig. 4.11 and Table 1), and has been sampled by *Kissel et al. (2015b)* in the TT44 site. Four sites were selected: TEN25, 26 27 and TEN28.

Fig. 4.19 Sampling sites of Abejera Alta: a) TEN25, b) TEN26, c) TEN27, d) TEN28. Red arrows indicate sampling points.

The **Roques Blancos** eruption (Fig. 4.20) occurred on the NW flank of Pico Viejo cone, and consists of a complex phonolitic coulées system generated by a summit dome. Lava flows are thick and anastomosed, with margins up to tens of metres high, and display layered structures and folding with steep and blocky levees. Lava has light grey colour, a porphyritic to sub-aphyric texture, with feldspar crystals. Despite their high viscosity, the obsidian flows of Roques Blancos reached the northern coast of the island (*Carracedo and Troll, 2013*).

According to the two ^{14}C datings provided by *Carracedo et al. (2007),* it is the youngest lava dome, with an age of 4 BC-439 AD (TFC-25 site), and 264 BC-242 AD (TFC-38 site, also called "Early Roques Blancos"). The discrepancy between ages was interpreted by authors assuming a long eruptive activity lasting ~200 yrs. *Kissel et al. (2015b)* palaeomagnetically sampled the Early Roques Blancos (TT09 in Fig. 4.11) near the TFC-38 site of *Carracedo et al. (2007).*

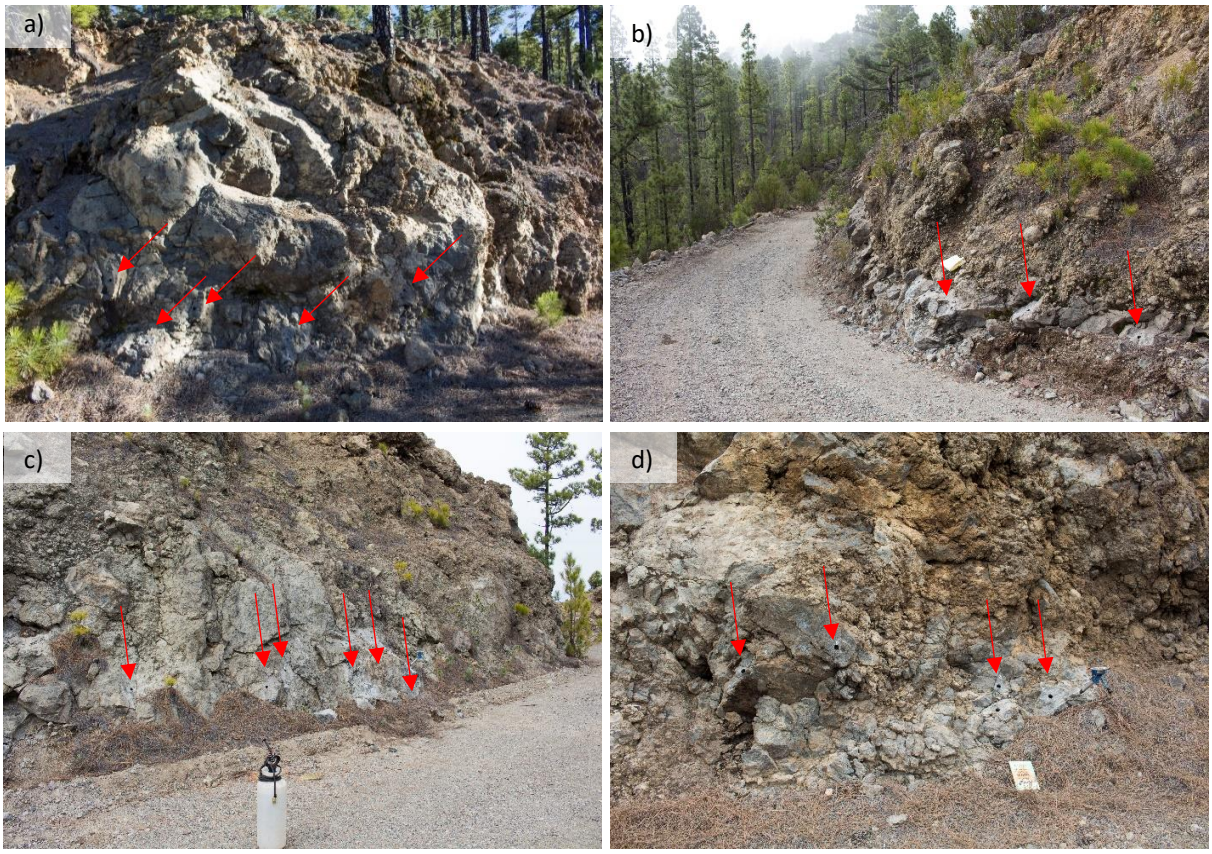

Fig. 4.20 Sampling sites of Roques Blancos: a) TEN33, b) TEN34, c) TEN35, d) TEN36. Red arrows indicate sampling points.

4.2.4 Sampling and Methods

During March 2018, fieldwork was carried out during which a total of 36 sites (363 oriented cores, of which 142 and 221 cores with phonolitic and basaltic composition, respectively) were sampled. At each site, 10-12 cores have been drilled. The regional magnetic field declinations at Tenerife (D=-4°, by the International Geomagnetic Reference Field model - IGRF (https://www.ngdc.noaa.gov/geomag/calculators/magcalc.shtml#igrfwmm) has been compared with the sun and magnetic compass readings, and the local magnetic field declinations varying from -22.1° to 13.8° (-4.1° on average), showing the absence of significant magnetic anomalies.

For each specimen, ten AF demagnetization steps, up to a maximum peak of 120 mT, were selected. In addition, for one specimen per site and for all samples from TEN29 and TEN34 sites (because they did not demagnetize with the AF cleaning), thermal demagnetization (TH) was also performed: also in this case, ten demagnetization steps were selected, up to a maximum temperature of 680°C. Site-mean (mean direction of samples belonging to the same site) and flow-mean (mean direction of samples belonging to the same volcanic eruption) palaeomagnetic directions were computed using *Fisher's* (1953) statistics. The flow-mean palaeomagnetic directions were obtained by averaging both all four sites (site mean) and all individual characteristic directions (ChRMs), as the number of samples from each site is the same. Thermal and AF demagnetization data were represented on orthogonal demagnetization diagrams (*Zijderveld, 1967*) and equal-area projections and the magnetization components were isolated by principal component analysis (*Kirschvink, 1980*).

For one specimen per site, the hysteresis properties were measured, and the hysteresis ratios were plotted in a Day plot (*Dunlop, 2002*).

For each sample, the Q Königsberger ratio (*Kono, 2015*), i.e. the ratio between NRM and induced magnetization intensity, was also calculated. The induced magnetization intensity is the product of k (bulk volume susceptibility measured with an MFK1- Multifunction Kappabridge) and B. At Tenerife, the Earth's magnetic field total intensity was 38,580 nT in March 2018 (according to the IGRF model).

On crushed powders from one specimen per site (13 with phonolitic and 23 with basaltic composition), the variation of the low-field magnetic susceptibility during heating and cooling cycles performed in air, from room temperature up to 700°C has been measured.

For one sample per site, the petrographic features were also evaluated to control and check the selected sites with petrographic data from *Rodríguez-Badiola et al. (2006).*

The mollusc shells embedded at the base of the Mña Grande lava flow were sampled for a radiocarbon dating, and samples were analysed by Beta Analytic Inc., Miami, USA. The dates were converted to calendar years before present (cal. yrs BP, where present refers to AD 1950), based on calibration BetaCal3.21, HPD method: MARINE13 *(Reimer et al., 2013)*.

Finally, the palaeomagnetic ages were evaluated using input age windows both on stratigraphic evidence and, when available, on ^{14}C age constraints. All original ^{14}C conventional

ages-yr BP from *Carracedo et al. (2007)* were recalibrated into calendar-calibrates ages -cal yr AD/BC, with corresponding uncertainties at the 2σ level, using INTCAL13 terrestrial radiocarbon age calibration with the Radiocarbon Calibration Program CALIB REV 7.1.0.; *Reimer et al., 2013, Stuiver et al., 2020*).

4.2.5 Results

4.2.5.1 Magnetic Properties

The k-T curves (or susceptibility vs temperature curves, Fig. 4.22) show a wide range of behaviours: ~70% of the samples display T_c between 500°-580°C, about 30% of samples show an inflection on the heating curve between 200° and 400°C, and ~70% of the samples show also the occurrence of T_c> 580°C. The first range of temperatures are typical of magnetites and low-Ti magnetites, the second may indicate the presence of titanomagnetites and/or maghemite and the T_c above 580 °C is probably due to a limited amount of hematite. In most cases, the remanence is not annulled at 680 °C, indicating the non-negligible contribution of paramagnetic fraction on total susceptibility values at room temperature. Finally, about half of the samples yield an irreversible behaviour, with the formation of further magnetite during heating.

The hysteresis properties (Fig. 4.23) reported on the Day-plot diagram (*Dunlop, 2002*) show M_{rs}/M_s comprise between 0.3 e 0.04 and B_{cr}/B_c values between 1.7 and 10.8. Samples are mainly clustered in the field of PSD magnetite field; some of them are aligned on the SD-MD mixing curve of the magnetite, others along the titanomagnetite (TM60) curve, while few samples are spread around the SP-MD of 10 nm magnetite mixing curve. This diagram shows also that hysteresis properties cannot be used to correlate samples from the same lava flow: both coercivity and saturation magnetization ratios from the same flow vary greatly and are in overlap with values from other flows.

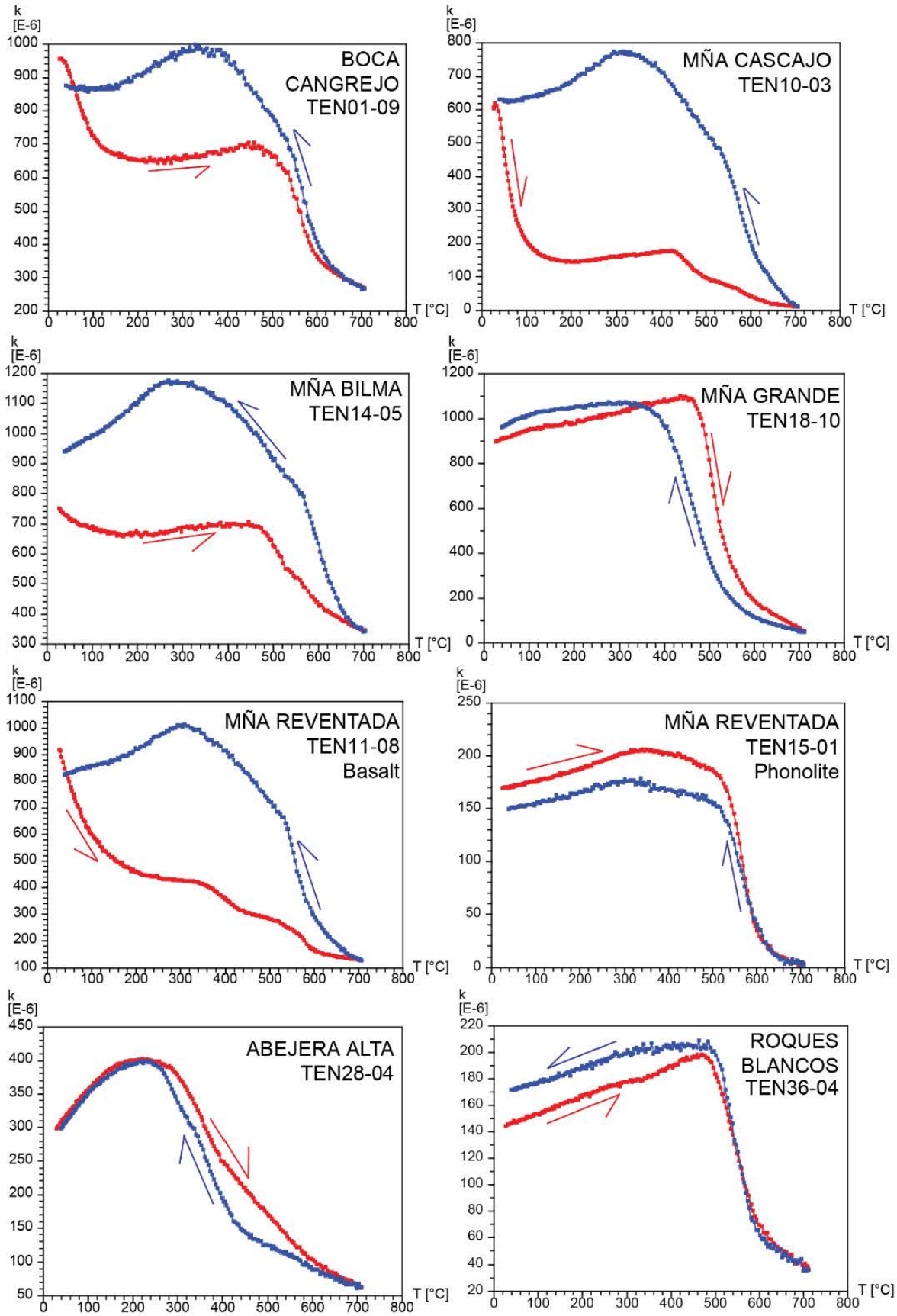

Fig. 4.22 Representative k-T curves. k is the magnetic susceptibility and T is the temperature (°C). Curves represent the heating (red curve) and cooling (blue curve) cycles.

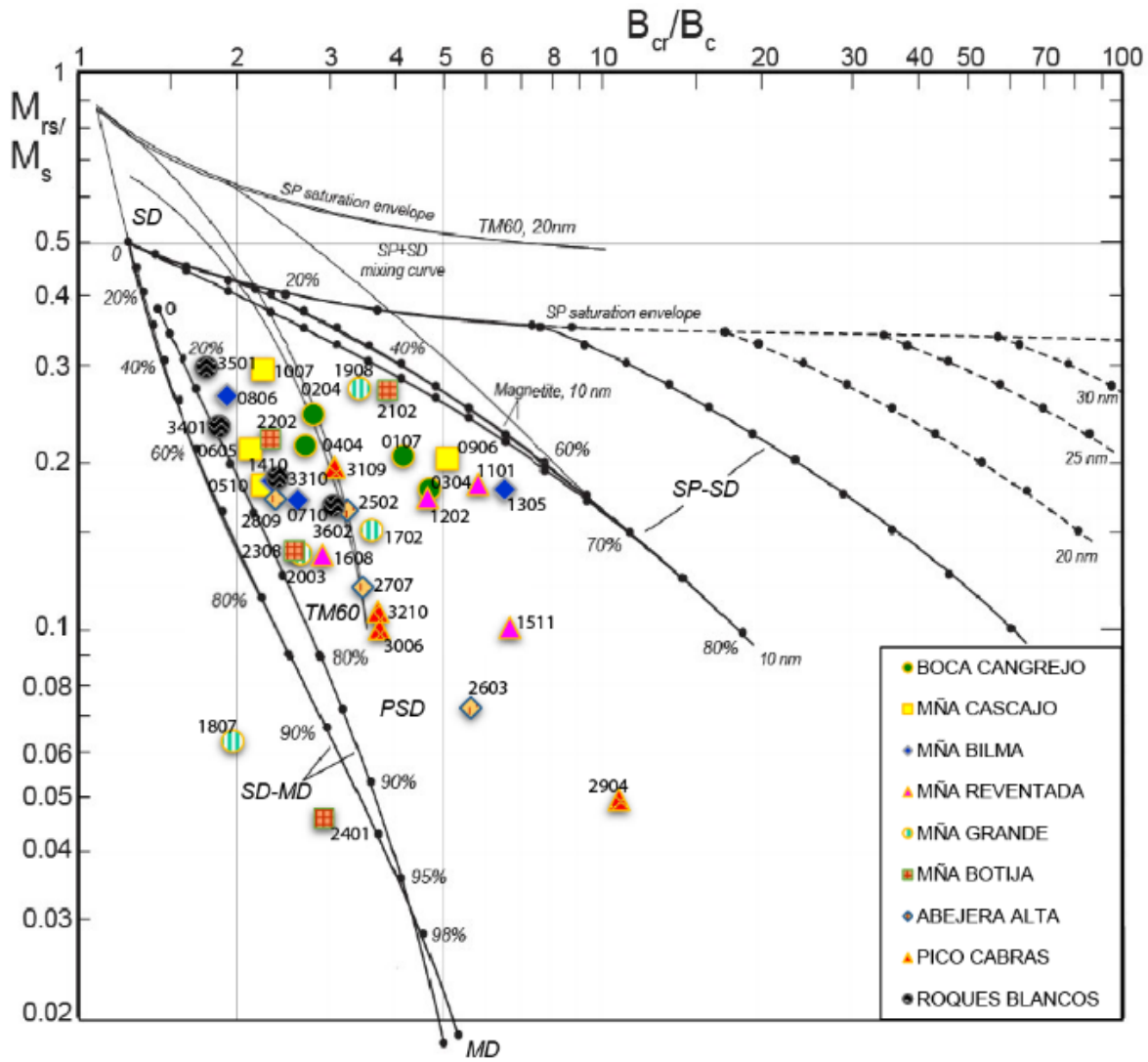

Fig. 4.23 Mrs/Ms versus Bcr/Bc (modified by *Dunlop, 2002*). SD, single domain; MD, multidomain; PSD, pseudo-single domain; SP, super-paramagnetic. TM60, titanomagnetite ($Fe_3 - xTixO_4$) with composition x=0.6.

Samples show NRM values ranging between 1 and 30 A/m, 9.7 A/m on average, except for samples from one site of the Pico Cabras flow (TEN29) that yield lower values. For most samples, k values are comprised between 4 x 10^{-3} and 6 x 10^{-2}, 2 x 10^{-2} on average. Therefore, samples fall on Q slope lines (Fig. 4.24) between 10 and 50, except samples from TEN29 site, yielding Q values as low as 0.05-0.1. The difference between magnetic properties of TEN29 site and others belonging to the same unit can be explained due to the hydrothermal alteration, which occurred after lava emplacement and produced the transformation of magnetite into hematite at TEN29 site. The magnetic remanence of samples belonging to the TEN29 site is much lower than that of other sites from the same flow (and this data set in

general). This suggests the loss of SD domain magnetite, transformed into hematite. Consequently, TEN29 site was discarded and excluded from further consideration.

The Königsberger diagram allows the correlation of samples from the same flow thanks to the similar NRM and k values. Moreover, phonolitic samples yield lower NRM and k values than basaltic samples (Fig. 4.24b), although both rock groups share similar Q values (again except for site TEN29).

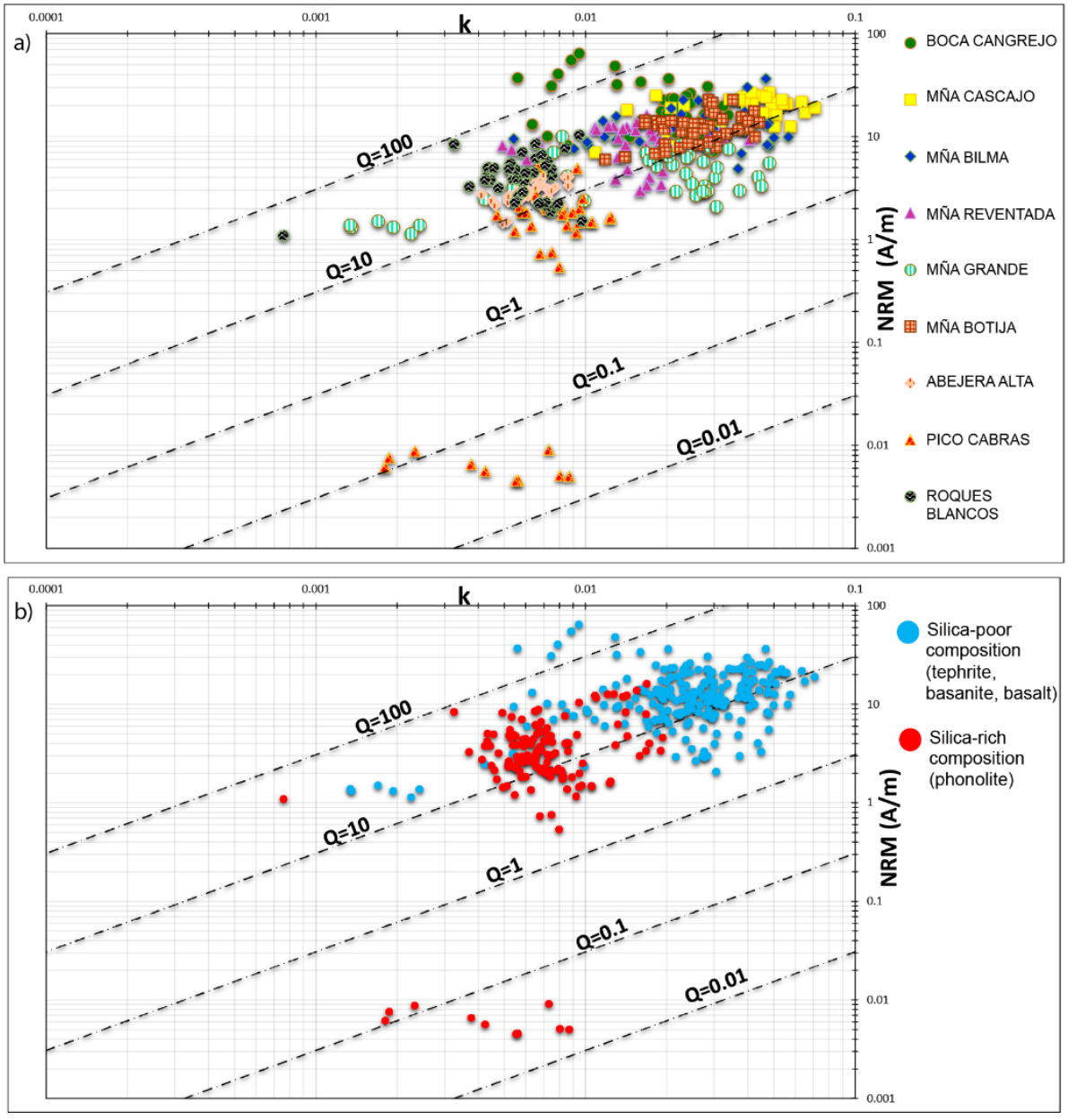

Fig. 4.24 a) NRM intensity vs. magnetic susceptibility values for all samples from Tenerife; sloping Q (Königsberger ratio) lines are calculated for a local geomagnetic field intensity of 38,580 nT; b) same plot as in a) but separating the samples according to their basaltic or phonolitic composition.

4.2.5.2 Palaeomagnetic directions

A viscous magnetic component has been eliminated at 20 mT, and the ChRM direction was isolated for almost all samples in the 30-120 mT AF interval, and 350-680°C TH interval for the TEN34 site from Roques Blancos flow. In Figure 4.25, two Zijderveld diagrams for each lava flow are shown (AF and TH demagnetization diagram for the same sample, except for Mña Reventada in which samples with the different composition are shown). Less than 10% of the samples show high coercivities (except for TEN34 site, in which only 70-80% of the NRM is removed at 120 mT), and for all thermally cleaned samples, a total demagnetization occurs at 600°C (again apart from samples of TEN34 site).

The magnetic mineralogy and the palaeomagnetic results show that Holocene lavas are mostly characterized by a variable mixture of low-coercivity titanomagnetite and magnetite, predominantly in the PSD size range, with subordinate SP and MD grains and hematite occurrence. Conversely, phonolite sites from Pico Cabras and Roques Blancos flows (TEN29 and TEN34) show a mixture of magnetite and hematite.

Lava flow-mean and site mean directions for each flow were calculated; an extra plot for Boca Cangrejo, Mña Reventada, Abejera Alta and Roques Blancos has been added to compare data of this work and *Kissel et al. (2015b)* data (Fig. 4.26). Mña Botija, Abejera Alta and Pico Cabras flows data are also shown excluding discarded sites TEN21, TEN25 and TEN31. TEN21 and TEN25 sites directions are not consistent with those of the other sites from the same flow; moreover, the removal of TEN25 site is also supported by its petrological and textural characteristics (as is visible in Table 3) that are clearly different than those of the other sites belonging to the same flow. TEN31 has been considered as a scattered site (with α_{95} =14°).

Site-mean declinations (Table 2 and Figs. 4.26 and 4.27) vary from 347.4° to 43.4° (TEN13-Mña Bilma, and TEN17-Mña Grande, respectively), while inclinations are comprised between 19.6° and 63.5° (TEN28-Abejera Alta and TEN20-Mña Grande, respectively). Finally, the α_{95} values (calculated averaging all the individual ChRMs from the same flow) vary from 2.2° to 6.0° (TEN33-Roques Blancos and TEN04-Boca Cangrejo, respectively), 4.2° on average.

The comparison between data of this work and *Kissel et al. (2015b)* data for Boca Cangrejo and Mña Reventada shows palaeomagnetic directions perfectly comparable; otherwise, the

direction of TT44 site in the Abejera Alta flow (at a locality that has not been found) is similar to that of TEN25 site (however discarded).

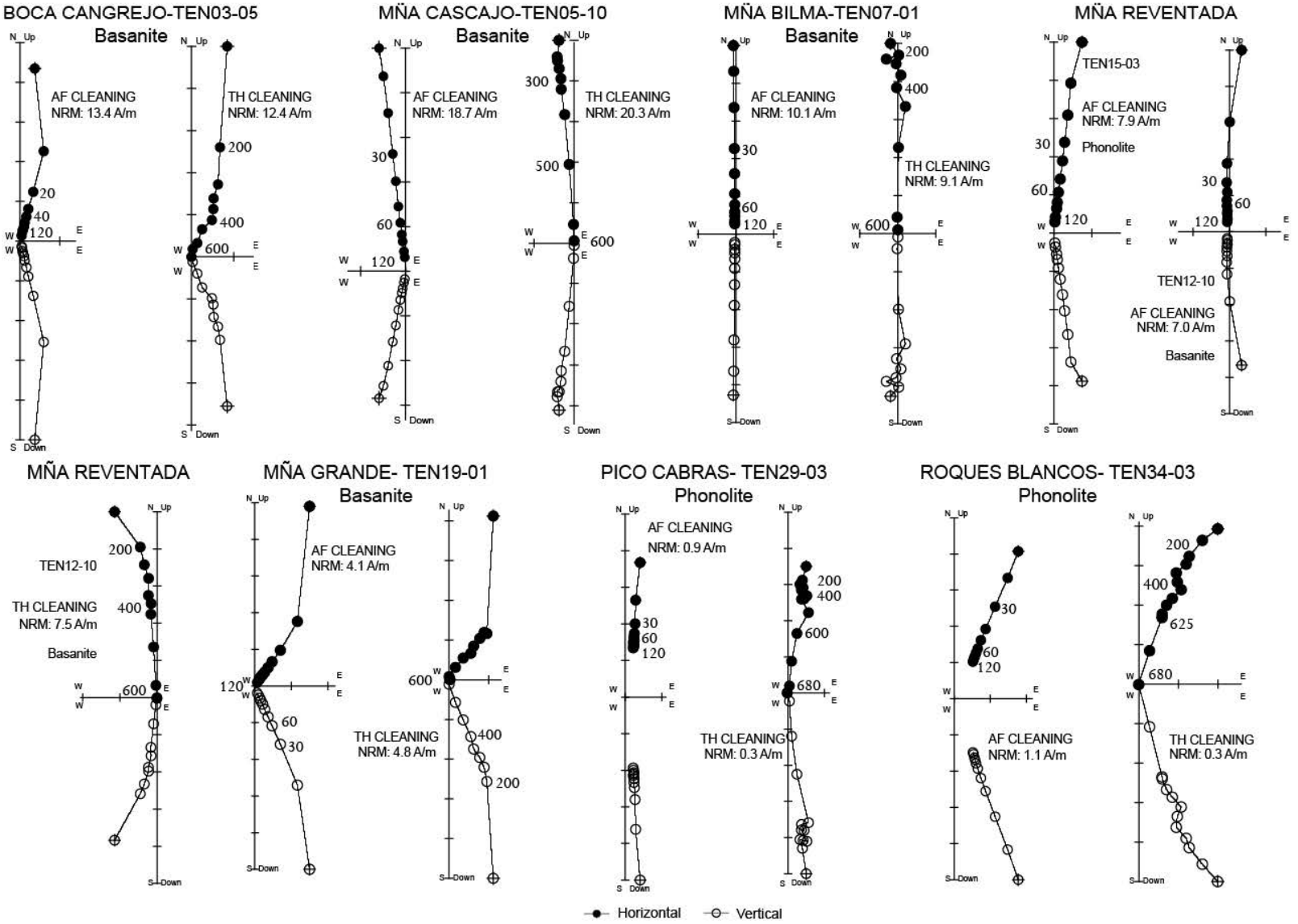

Fig. 4.25 Representative Zijderveld diagrams of typical demagnetization data, in situ coordinates. White and black dots represent projections on the vertical and horizontal planes, respectively. Demagnetization step values are in mT for the AF cleaned samples and °C for TH cleaned samples.

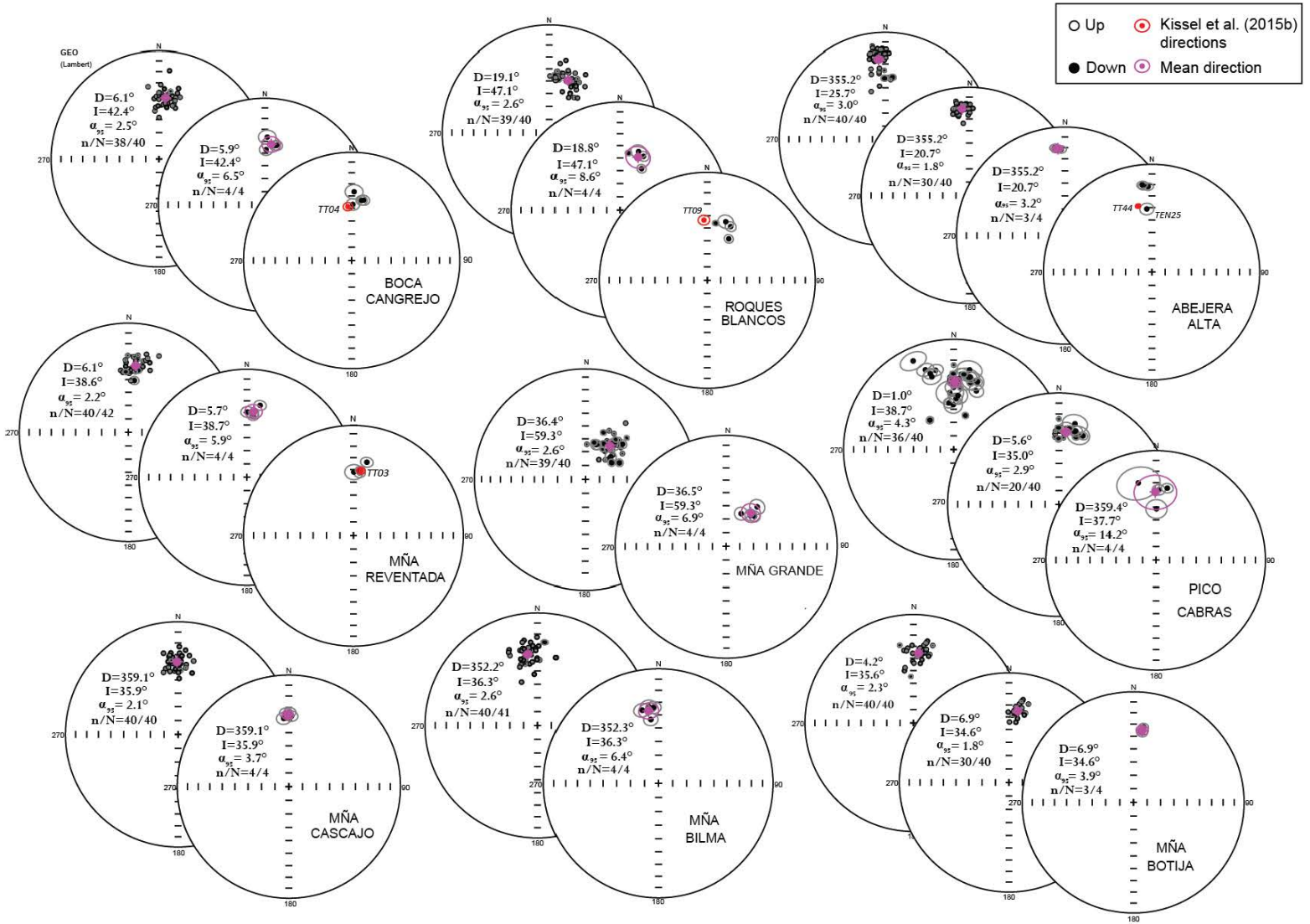

Fig. 4.26 Equal-area projection (lower hemisphere) of ChRMs, site-mean and flow-mean palaeomagnetic directions for all studied eruptions. The ellipses around the palaeomagnetic directions are the projections of the relative α_{95} cones. D, declination; I, inclination, α_{95}; statistical parameter. Red dots indicate the palaeomagnetic directions sampled by *Kissel et al. (2015b).*

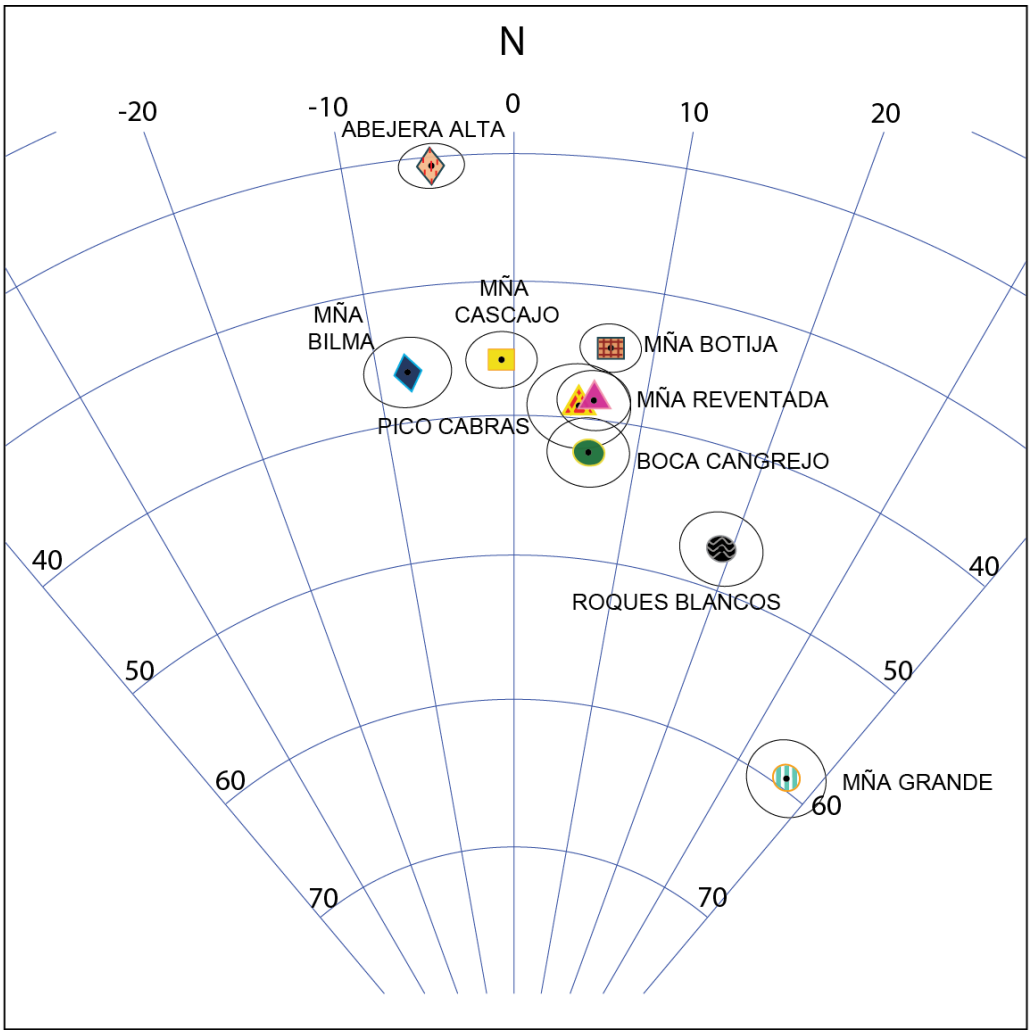

Fig. 4.27 Equal-area projection (lower hemisphere) of lava flow-mean palaeomagnetic directions from Tenerife. The ellipses around the palaeomagnetic directions are the projections of the relative α_{95} cones.

Table 2. Mean Palaeomagnetic Directions from Tenerife and Palaeomagnetically Inferred Ages.

Volcanic Unit	Code	n/N	D°	I°	k	α_{95}°	Inferred Age (BC-AD)
Boca Cangrejo	TEN01	9/10	1.2	47.0	119	4.7	
	TEN02	10/10	9.3	43.1	165	3.8	
	TEN03	10/10	11.2	42.6	138	4.1	
	TEN04	9/10	2.0	36.6	73	6.0	
Boca Cangrejo (site mean)	TEN01+TEN02+TEN03+TEN04	4/4	5.9	42.4	203	6.5	
Boca Cangrejo (sample mean)		38/40	6.1	42.4	86	2.5	1,484-1,536 AD
Montaña Reventada	TEN11	10/10	5.6	42.2	157	3.9	
	TEN12	8/10	0.5	39.4	155	4.5	
	TEN15	11/11	6.0	40.3	188	3.3	
	TEN16	11/11	10.4	32.8	125	4.1	
Montaña Reventada (site mean)	TEN11+TEN12+TEN15+TEN16	4/4	5.7	38.7	243	5.9	
Montaña Reventada (sample mean)		40/42	6.1	38.6	108	2.2	(842-876 AD) 899-974 AD
Montaña Grande	TEN17	9/10	43.4	59.5	163	4.0	
	TEN18	10/10	38.2	60.8	136	4.2	
	TEN19	10/10	38.2	52.7	78	5.5	
	TEN20	10/10	24.6	63.5	100	4.8	
Montaña Grande (site mean)	TEN17+TEN18+TEN19+TEN20	4/4	36.5	59.3	180	6.9	
Montaña Grande (sample mean)		39/40	36.4	59.3	78	2.6	790-723 BC

Roques Blancos	TEN33	9/10	8.4	45.6	563	2.2	
	TEN34	10/10	23.5	44.9	152	3.9	
	TEN35	10/10	27.4	54.4	211	3.3	
	TEN36	10/10	17.5	42.6	80	5.4	
Roques Blancos (site mean)	TEN33+TEN34+TEN35+TEN36	4/4	18.8	47.1	114	8.6	
Roques Blancos (sample mean)		39/40	19.1	47.1	79	2.6	686-596 BC
Montaña Cascajo	TEN05	10/10	0.8	33.7	164	3.8	
	TEN06	10/10	2.1	36.9	133	4.2	
	TEN09	10/10	357.7	34.3	138	4.1	
	TEN10	10/10	355.7	38.6	104	4.8	
Montaña Cascajo (site mean)	TEN05+TEN06+TEN09+TEN10	4/4	359.1	35.9	614	3.7	
Montaña Cascajo (sample mean)		40/40	359.1	35.9	121	2.1	2,159-1,981 BC 1,879-1,516 BC
Montaña Botija	TEN21*	10/10	355.5	38.2	63	6.1	
	TEN22	10/10	7.7	31.8	246	3.1	
	TEN23	10/10	7.0	36.5	196	3.5	
	TEN24	10/10	5.9	35.5	296	2.8	
Montaña Botija (site mean)	TEN22+TEN23+TEN24	3/4	6.9	34.6	981	3.9	
Montaña Botija (sample mean)		30/40	6.9	34.6	218	1.8	2,267-2,109 BC 1,777-1,550 BC
Montaña Bilma	TEN07	10/10	353.1	43.3	107	4.7	
	TEN08	10/11	352.5	32.8	91	5.1	

	TEN13	10/10	347.4	34.9	81	5.4	
	TEN14	10/10	356.1	34.1	102	4.8	
Montaña Bilma (site mean)	TEN07+TEN08+TEN13+TEN14	4/4	352.3	36.3	210	6.4	
Montaña Bilma (sample mean)		40/41	352.2	36.3	75	2.6	(4,641-4,630 BC) 4,352-4,031 BC 3,473-2,928 BC 2,707-2,588 BC (1,871-1,836 BC)
Abejera Alta	TEN25*	10/10	355.3	40.9	103	4.8	
	TEN26	10/10	354.6	20.9	193	3.5	
	TEN27	10/10	357.4	21.7	221	3.3	
	TEN28	10/10	353.6	19.6	217	3.3	
Abejera Alta (site mean)	TEN26+TEN27+TEN28	3/4	355.2	20.7	1456	3.2	
Abejera Alta (sample mean)		30/40	355.2	20.7	204	1.8	4,500-4,356 BC 3,382-3,279 BC
Pico Cabras	TEN29*	9/10	0.1	49.9	90	5.5	
	TEN30	10/10	2.2	36.0	129	4.3	
	TEN31*	6/10	347.0	28.5	24	14.0	
	TEN32	10/10	8.9	33.9	157	3.9	
Pico Cabras (site mean)	TEN30+TEN32	2/4	5.6	35.0			
Pico Cabras (sample mean)		20/40	5.6	35.0	124	2.9	6,753-6,571 BC 6,540-6,228 BC 5,368-5,241 BC

n/N is number of characteristic remanent magnetization directions used to calculate the site-sample mean direction/total number of cores drilled at a site, or number of sites/samples used to calculate a volcanic unit-mean direction/total number of sites/samples from the volcanic unit. Asterisks indicate the discarded sites. Inferred ages are gathered by comparing samples-mean palaeomagnetic directions with 14 ka global Palaeosecular Variation (PSV) model by *Pavón-Carrasco et al. (2014).* Inferred ages by parenthesis are discarded by geochronologic and/or stratigraphic evidence, and on the base of the probability density (see the text).

Table 3. Characteristics of the studied eruptions, petrographic features and composition.

Eruption	Location	Area km²	Volume km³	Code	Texture	Pheno/Microphenо*	Groundmass*	Composition
Boca Cangrejo	NWR	5.8	0.029	TEN01	SAP	Pl, Cpx, Ox, rare Amp	Pl, Ox, Cpx, Ol	Basanite(1)
				TEN02	SAP	Pl, Cpx, Ox, rare Amp	Pl, Ox, Cpx, Ol	
				TEN03	SAP	Pl, Cpx, Ox, rare Amp	Pl, Ox, Cpx, Ol	
				TEN04	SAP	Pl, Cpx, Ox, rare Amp	Pl, Ox, Cpx, Ol	
Montaña Reventada	NWR	21.8	0.1308	TEN11	AP		Pl, Ox, Cpx, Ol,	Basanite-Phonolite(1)
				TEN12	PO	Pl=Sa, Amp, Cpx	Fsp, Ox, Cpx	
				TEN15	PO	Pl=Sa, Amp, Cpx	Fsp, Ox, Cpx	
				TEN16	PO	Pl=Sa, Amp, Cpx	Fsp, Ox, Cpx	
Montaña Grande	GV	>4.5		TEN17	PO	Ol, Cpx, Pl, Ox	Pl, Ox, Ol, Cpx	Basanite(2)
				TEN18	PO	Ol, Cpx, Pl, Ox	Pl, Ox, Ol, Cpx	
				TEN19	PO	Ol, Cpx, Pl, Ox	Pl, Ox, Ol, Cpx	
				TEN20	PO	Ol, Cpx, Pl, Ox	Pl, Ox, Ol, Cpx	
Roques Blancos	PLD	27.8	1.39	TEN33	PO	Sa, Pl, Cpx, Amp, Ox	Fsp, Ox	Phonolite(1)
				TEN34	SAP	Sa	Fsp, Ox	
				TEN35	SAP	Sa, Cpx, Amp	Fsp, Ox	
				TEN36	SAP	Sa, Cpx	Fsp, Ox	
Montaña Cascajo	NWR	18.4+9.2 (El Esparrago)	0.092+0.046 (El Esparrago)	TEN05	PO	Ol=Cpx, Pl, Ox	Ox, Cpx, Ol, Pl	Basanite(1)
				TEN06	PO	Ol, Cpx. Pl	Pl, Ox, Cpx, Ol	
				TEN09	PO	Cpx, Ol, Pl, Ox	Pl, Ox, Cpx, Ol	
				TEN10	SAP	Cpx, Ol, Pl	Pl, Cpx, Ol, Ox	
Montaña Botija	NWR	10.5	0.0525	TEN21	SAP	Ol, Pl, Cpx	Pl, Ox, Cpx, Ol	Basanite(1)
				TEN22	SAP	Pl, Cpx, Ox	Pl, Ox, Cpx, Ol	

				TEN23	SAP	Pl, Cpx, Ox	Pl, Ox, Cpx, Ol	
				TEN24	SAP	Pl, Cpx, Ox	Pl, Ox, Cpx, Ol	
Montaña Bilma	NWR	5.8	0.029	TEN07	PO	Ol, Cpx, Pl, Ox	Pl, Ox, Cpx, Ol	Basanite(1)
				TEN08	PO	Ol, Cpx, Pl, Ox	Pl, Ox, Cpx, Ol	
				TEN13	PO	Ol, Cpx, Pl, Ox	Pl, Ox, Cpx, Ol	
				TEN14	PO	Ol, Cpx, Pl, Ox	Pl, Ox, Cpx, Ol	
Abejera Alta	PLD	16.5	0.495	TEN25	PO	Sa, Pl, Cpx, Amp, Ox	Fsp, Ox	Phonolite(1)
				TEN26	AP	rare Sa, Amp, Cpx	Fsp, Ox	
				TEN27	AP	rare Sa, Amp	Fsp, Ox	
				TEN28	AP	rare Ox	Fsp, Ox	
Pico Cabras	PLD	15.5	0.775	TEN29	SAP	Sa, Cpx, Ox	Fsp, Ox	Phonolite(1)
				TEN30	SAP	Sa, Cpx, Ox	Fsp, Ox	
				TEN31	SAP	Sa, Ox	Fsp, Ox	
				TEN32	SAP	Pl, Sa, Amp, Ox, Cpx	Fsp, Ox	

Note: NW = North-West Rift; GV = Güímar Valley; PLD = Peripheral Lava Domes. AP = Aphyric (<5% of phenocrysts); SAP=Sub-APhyric (5-10% of phenocrysts); PO = Porphyritic (>10% phenocrysts). *Mineral phases in order of decreasing abundance: Amp = Amphibole; Cpx = Clinopyroxene; Fsp = Feldspar; Ol = Olivine; Pl = Plagioclase; Ox = Oxides, Sa = Sanidine. Composition after: (1) *Rodríguez-Badiola et al. (2006)* and (2) this work.

4.2.5.3 Palaeomagnetic Dating

One or more possible ages were determined for the studied eruptions (Table 2). Age constraints for each eruption are listed in Table 1. In Fig. 4.28, Boca Cangrejo, Mña Reventada, Mña Bilma and Mña Grande dating results are shown (the other results are displayed in Appendix I).

Based on the stratigraphic contacts (i.e. between Mña Negra, 7,540-7,019 BC, and Abejera Alta, 4,246-3,710 BC; Table 1) for the Pico Cabras flow, an 8,000-4,000 BC input age window has been considered, and three possible age spans between 6,753 and 5,241 BC were obtained.

For Abejera Alta (dated with ^{14}C at 4,246-3,710 BC), no possible palaeomagnetic age was found in the same input age window. Therefore, a larger 4,500-3,000 BC input age window has been evaluated, and two age intervals between 4,500 and 3,279 BC were obtained.

For the Mña Cascajo eruption, a 3,000 BC - 0 AD time interval (i.e. between Mña de Chío -2,350-1,630 BC- and Volcán El Ciego -1,128-367 BC- eruptions) was used, and two possible ages - 2,159-1,981 BC and 1,879-1,516 BC- were found.

The Mña Bilma eruption, according to *Carracedo et al. (2008)*, relies on the Cuevas del Ratón age, i.e. 4,332-4,146 BC) and for this reason, a 5,000 BC lower bound age has been considered. Moreover, based on the geological map of *Carracedo et al. (2006*), Mña Cascajo eruption is younger than Mña Bilma; consequently, an upper bound age of 1,500 BC (that is the younger inferred age of Mña Cascajo) has been assumed, and five possible ages for Mña Bilma, between 4,641 and 1,836 BC, were found.

For the Mña Botija eruption, the same input age interval of Mña Cascajo (3,000 BC-0 AD) has been considered (according to its comparable stratigraphic position suggested by *Carracedo et al. (2007)*, and two possible ages 2,267-2,109 BC and 1,777-1,550 BC were obtained.

For the Mña Grande eruption, the only geomorphologic constraint has been provided by *Dóniz-Páez et al. (2013),* suggesting a Quaternary age. Since the lava flows are not modified significantly by the action of waves and covered by beach deposits, a Holocene age has been supposed. Moreover, the radiocarbon dating of marine shells yielded an age of 2,316-2,030

cal BC (4,265-3,979 cal BP, in Appendix I). Consequently, a temporal window from 2,400 BC to 1,900 AD was considered, and a unique and very narrow 790-723 BC age interval was found.

No possible age was found for the Roques Blancos eruption using the radiocarbon age given by *Carracedo et al. (2007)* (i.e. 264 BC-439 AD). If, conversely, a wider 1,000 BC to 500 AD age range is assumed, a 686-596 BC age is obtained.

Finally, for Mña Reventada eruption, an 800-1300 AD age window was considered (based on the 942-1,208 AD ^{14}C age of *Carracedo et al., 2007*); accordingly, 842-876 AD and 899-974 AD ages were obtained (Fig. 4.28).

Finally, for the Boca Cangrejo lava flow, a 1,300-1,700 AD input age window was used, and a 1,484-1,536 AD age was inferred (Fig. 4.28).

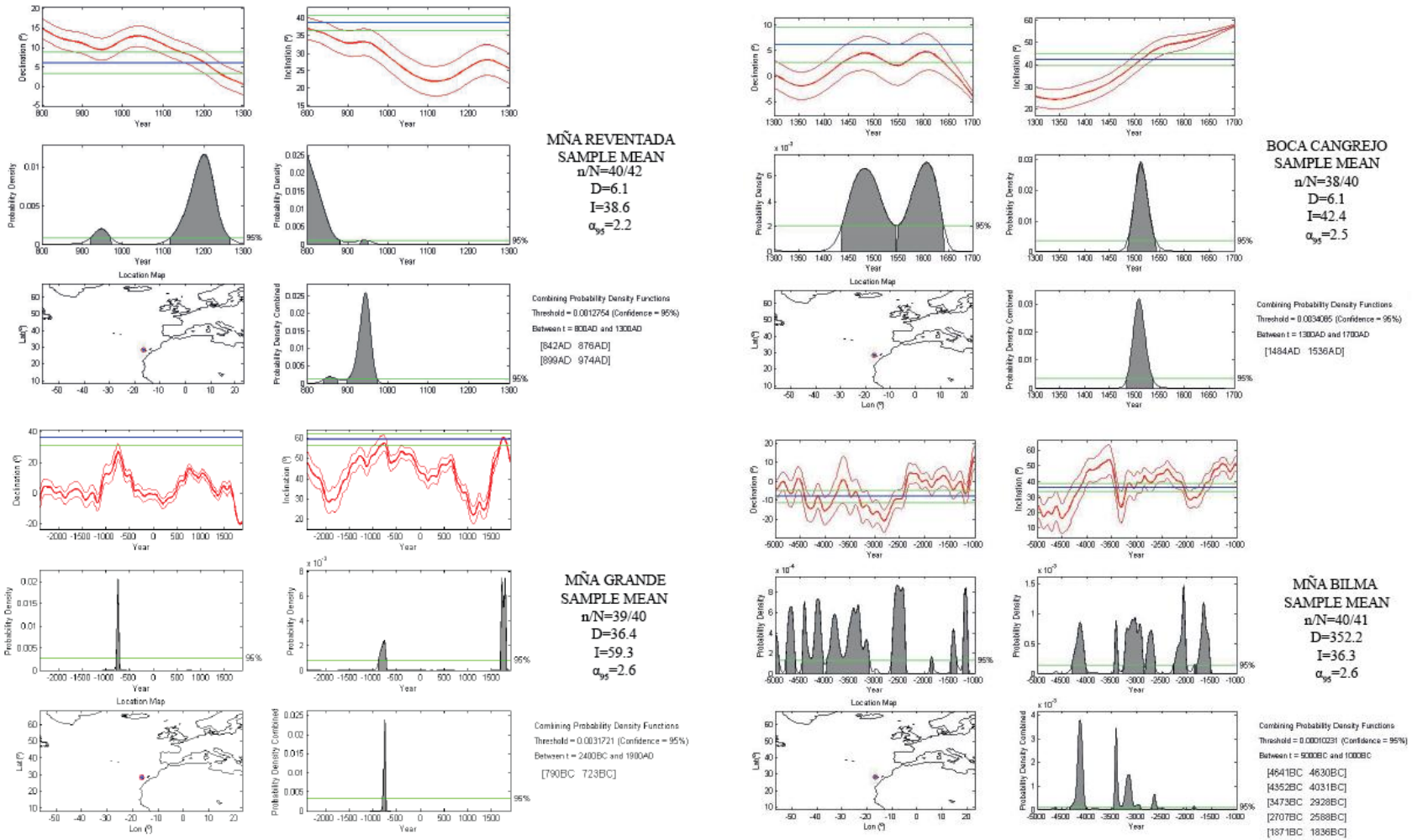

Fig. 4.28 Palaeomagnetic dating of Boca Cangrejo, Mña Reventada, Mña Bilma and Mña Grande eruptions, according to the method and software by *Pavón-Carrasco et al. (2011*), and the PSV reference model by *Pavón-Carrasco et al. (2014).* Left-hand panel shows the PSV curves (red lines) for the declination and right-hand panel for the inclination (thin red lines for the associated errors, 95% confidence level), together with the probability density curves (in grey-shade). Palaeomagnetic declination and inclination values are shown in blue straight lines; the 95% associated errors are in green straight lines. In the probability density graphs the 95% confidence level is shown as a green line.

4.2.6 Discussion

4.2.6.1 Age ranges for the undated eruptions

The ages of Mña Bilma, Pico Cabras Mña Cascajo, Mña Botija and Mña Grande eruptions, which had been previously constrained only by relative stratigraphy, were determined.

Five possible ages for Mña Bilma eruption within the 5,000-1000 BC time window were found. Ages older than 4,300 BC were excluded, according to the ^{14}C age of Cuevas del Ratón lava flow, which underlies the Mña Bilma eruption; in addition, the youngest age has also been discarded relying on the low probability density peak. Thus, three possible age intervals, between 4,352 BC and 2,588 BC, have been proposed, with a significantly narrower age span than the one previously available.

For Pico Cabras lava flow, the previous age range (between Abejera Alta, 4,246-3,710 BC, and Mña Negra, 7,540-7,019 BC) has been restricted to ~6,800-5,200 BC.

Finally, Mña Botija and Mña Cascajo, roughly sharing the same stratigraphic interval (between Mña de Chío and Volcán El Ciego), have both been dated by more than 1,000 yrs more precisely, than the previous evidence.

The eruption of Mña Grande has been added for the first time to the list of the Holocene volcanic activity. Palaeomagnetism, coupled with the radiocarbon dating of shells found below the lava flow, revealed that the eruption is much younger than previously thought and occurred in a well-constrained age window, from 790 BC to 723 BC. However, the magnetic inclination obtained for Mña Grande (59.3°±2.6°) could be considered very steep for such a low latitude; the declination (36.4°±5.2°) is on the edge of the SHA.DIF.14K reference curve (Fig. 4.23). Nevertheless, the dataset is robust and consistent: four independent sites (ca. 40 samples) yield very similar palaeomagnetic data, and another lava flow from Tenerife (Volcán El Ciego, dated with ^{14}C at 1,128-367 BC; TFC-138 in *Carracedo et al., 2007* and TF-4 in *de Groot et al., 2015*), and further three eruptions from Gran Canaria with similar ages (Sima de Jinàjar, El Lentiscal and Doramas, *Kissel et al., 2015b*) show similarly high declination and inclination values, testifying that, around 700-800 BC, the geomagnetic field at the Canary Islands was characterized by such peculiar magnetic direction.

4.2.6.2 Comparison between ^{14}C method and palaeomagnetism

Four of the nine studied eruptions, i.e. Boca Cangrejo, Mña Reventada, Roques Blancos and Abejera Alta, had been already dated by *Carracedo et al. (2007)* using the radiocarbon method. This method is routinely considered the best tool to date recent volcanic products, although it has some limits. In recent years, palaeomagnetism has been increasingly used to date Holocene volcanic rocks. Thus, Tenerife is a key site to compare and combine these two different techniques. In this paragraph, the principal pro and cons of these two methods will be analysed.

The ^{14}C dating method is based on measuring the age of organic or carbonate phases in radiocarbon years, determining the level of the nuclide ^{14}C remaining in the sample. Carbon-14 is formed in the upper part of the atmosphere by the action of cosmic ray-induced radiation on nitrogen in the atmosphere, and it is in equilibrium in the atmosphere and the biosphere on a time scale of <1 year. The ^{14}C remains integrated into the living organic systems; after death, the organism ceases acquiring ^{14}C and the isotope starts to decay. The limit of the technique is around 50,000 years, and for this reason, it is one of the most used techniques to date recent products (*Jull and Burr, 2015*). The traditional measurements are based on counting the radioactive decay of the ^{14}C isotope (*Cook and van der Plicht, 2007*), which is counted either by the decays of ^{14}C (β particles) or the atoms themselves. This method is still used, both for liquid and gas samples, especially when sufficient material is available (*Longin, 1971; Cook and van der Plicht, 2007*), but in recent decades, another method, accelerator mass spectrometry (AMS), has been developed and is commonly used (*Burr and Jull, 2009*).

In volcanology, carbonized woods and/or humus-rich soils are usually dated; in fact, the first materials can be found within the volcanic deposit and provides an age of the eruption, the second is embedded between the deposits and provides a minimum or maximum limiting age for the eruption. The formation of soil needs some conditions: a suitable climate, favourable topography, biological factors, and timing. Tenerife is a big island characterized by a large difference in altitude (the peak of Teide is 3718 m a.s.l.), in which the environmental conditions change considerably on short distances, and they are not always favourable for pedogenesis and formation of humic-rich soils. Some areas (as the NE areas) receive more rainfall than the dry and desertic southern ones.

In addition, the radiocarbon dating may suffer major accuracy flaws due to contamination by carbon having a different radiocarbon signature. In volcanic areas, plants capture volcanic carbon dioxide, which is devoid of ^{14}C as well as atmospheric CO_2. This can cause a lower radiocarbon concentration in the organic materials and may yield misleading ages, up to several thousand years older. In Tenerife, this resulted in radiocarbon ages up to some kyr older than those obtained from the same flows by Ar/Ar and K/Ar methods (*Carracedo et al., 2007; Guillou et al., 2011*). Other studies in different areas, as in Eifel province, Germany (*Bruns et al., 1980*), Grosseto and Siena, Italy (*Saupè et al., 1980*), and in the Azores Islands (*Pasquier-Cardin et al., 1999*) show bias in the ^{14}C dating.

Nevertheless, palaeomagnetism has also several possible sources of bias (see 2.2 paragraph) as has been shown by *Valet and Soler (1999)*, *Urrutia-Fucugauchi et al. (2004)*, *Lanza et al. (2005)*, *Lanza and Zanella (2006), Speranza et al. (2006, 2008, 2012)* among many others. According to such works, the principal sources of biased palaeomagnetic directions from volcanic rocks that translate to incorrect dating can be: 1) local magnetic anomalies, caused by magnetized underlying terrain and regional magnetic sources and, 2) outcrop tilting occurred after lava flow emplacement, due to tectonics or local landslide instability. Moreover, the palaeomagnetic dating is based on the comparison between the palaeomagnetic direction recorded by the lava flows and the PSV master curves. The quality of the palaeomagnetic dating is, therefore, correlated with the availability and quality of archaeo- and palaeomagnetic reference PSV.

In this study, the SHA.DIF.14K model, which was successfully applied in the last few years to get eruption ages at several volcanoes of Italy and around the world (*Alva-Valdivia et al., 2019; Risica et al., 2019; Vashakidze et al., 2019,* among many others), has been used. However, it is important to clarify that the SHA.DIF14k model predictions have higher resolution for the last 3 kyr than for older ages (see 2.2.1 paragraph). In addition, the advantages of the palaeomagnetic dating technique are the possibility to get whole-rock samples (it allows avoiding having to isolate crystals) and the application of this method on lavas of nearly all compositions. Combining different dating methods is highly desirable to provide a more robust geochronological framework for Holocene volcanic activity.

Carracedo et al. (2007) obtained by radiocarbon dating a 1,444-1,648 AD age for Boca Cangrejo, a 942-1,208 AD age for Mña Reventada, 264 BC-242 AD and 4 BC-439 AD ages for Roques Blancos, and finally a 4,246-3,710 BC age for Abejera Alta.

The palaeomagnetic age of 1,484-1,536 AD determined for the Boca Cangrejo eruption matches well with the ^{14}C age of *Carracedo et al. (2007)* and confirms that this eruption is that witnessed by Christopher Columbus in 1492 AD (*Carracedo and Troll, 2013* and references therein).

For the other eruptions, palaeomagnetic dating yielded much narrower age intervals than those obtained by ^{14}C method (Fig. 4.29). For the Mña Reventada eruption, the two possible age intervals obtained (842-876 AD and 899-974 AD) are narrower than the ^{14}C age. Relying on the low probability density peak, the 842-876 AD age can be excluded, and the 899-974 AD inferred age indicates that the eruption could be slightly older.

For the Abejera Alta eruption, different ages than those provided by ^{14}C were found. The two inferred ages are ~250 yrs older and ~300 yrs younger than those obtained by *Carracedo et al. (2007).*

Finally, the inferred age for Roques Blancos eruption is 685-596 BC age, which is ~400 yrs older than the lower bound of the radiocarbon age range.

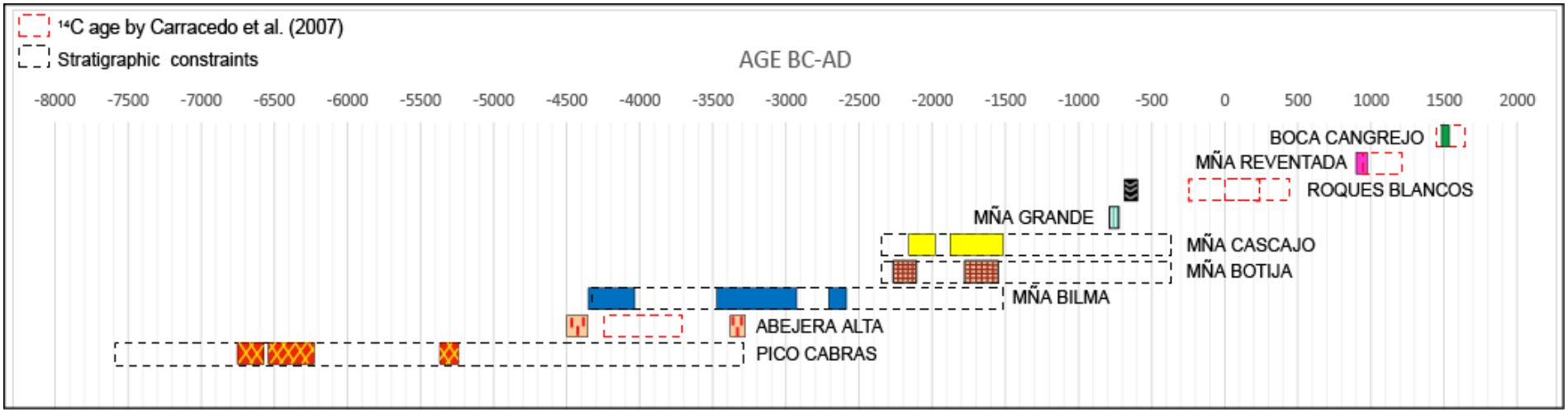

Fig. 4.29 Comparison of palaeomagnetically-inferred ages vs. literature stratigraphic/radiometric ages relative to the studied eruptions. Dashed black and red boxes indicate stratigraphically and ^{14}C-constrained ages by *Carracedo et al. (2007)*, respectively.

4.2.6.3 Implications for volcanic hazard

One of the most relevant objectives of volcanological studies is to provide information to better identify and assess volcanic hazards, i.e. every potentially dangerous volcanic process that may cause loss of life, health impacts, damage, social and economic disruption or environmental devastation. This is extremely important, especially in densely inhabited, touristic and industrial areas as Tenerife, which has been considered the area with the highest volcanic risk in Spain (*Scandone et al., 2016*).

To accomplish this, it is fundamental to study the volcanic history, documenting the past behaviour through geological and geochronological investigations and calculating the frequency and magnitude of eruptions, monitoring and analysing the volcanic activity, running models and generating hazard maps. To obtain significant statistics and trends of the temporal evolution of TVC and to figure out how the rifts and Teide-Pico Viejo system operated, it is necessary to have a complete overview of the entire Holocene activity.

As already shown by *Carracedo et al. (2007),* volcanic activity in Tenerife has been characterized by phases with frequent eruptions and period of inactivity, with an average of few eruptions per millennium. They occurred as flank and central vent eruptions, with basaltic, mainly effusive activity along the rifts, and more felsic explosive events near the central volcanoes, but without any apparent structural or petrological pattern that could explain such random eruption behaviour (*Martí et al., 2008*). Effusive eruptions fed by basaltic magmas are closely linked with the NE and, especially, the NW rift zones. The emitted lava flows during the last 12 ky by the NWRZ covered the 95% of its areal extent (with approximately 1 km^3 of lava released), whereas the NERZ had much fewer eruptions, with a resurfaced area <10% (*Carracedo and Troll, 2013*). In contrast, eruptions in the central edifices (both from Teide and peripheral lava domes) have been less frequent but much more voluminous than basaltic eruptions, producing ca. 4 km^3 of lava flows (*Martí et al., 2008; Carracedo and Troll, 2013)*. While felsic volcanism seems to have had two main pulses, at ~5000 and 1800-1200 BP, basaltic eruptions were more continuous, with a rate of 66 x 10^6 m^3/ky (*Carracedo and Troll, 2013*).

According to *Carracedo et al. (2003, 2007)*, future eruptive activity on Tenerife should be basaltic, generating short lava flows and small cinder cones; however, the possibility of an

eruption from Teide-Pico Viejo cannot be excluded, because petrological, geochronological and volcanological data suggest that Teide-Pico Viejo cannot be considered extinct volcanoes at all (*Ablay and Martí, 2000; Martí et al., 2008*). The implications for the volcanic hazard are, therefore, of dual nature.

Several works on the volcanic risk and hazard in Tenerife were carried out in the last years. *Gómez-Fernandez (1970, 2000)* simulated lava flows in three areas of Tenerife; *Araña et al. (2002)* tested different volcanic hazard levels by simulating ash fall and lava flows. *Marrero et al. (2012)* assessed the number of potential fatalities caused by pyroclastic density currents from the central volcanic complex. A comprehensive volcanic risk assessment was performed by *Scaini et al. (2014)* but was limited to restricted areas (Icod de los Vinos, San Juan de la Rambla and La Guancha). Recently, *Liu et al. (2020)* elaborated a more comprehensive volcanic risk assessment for the whole island, considering two main scenarios: 1) sub-Plinian eruption at the central edifice, ash fall dispersion and PDCs from column collapse; 2) Strombolian eruptions and basaltic lava flows in the NE-SW and NW-SE rift zones. According to the two different scenarios, the inferred vent susceptibility maps show different vent locations (Fig. 4.30a and b); if basaltic eruptions along rifts zones are considered as more probable (*Carracedo et al., 2003, 2007*), the affected sectors in the NW area would be very vast and would involve several municipalities (Fig. 4.30c).

In the light of the new information provided by this work, the chronological framework for the Holocene volcanic eruptions of Tenerife previously published by *Carracedo et al. (2007)* and *Carracedo and Troll (2013)* has been integrated with the new inferred ages (Fig. 4.31). The updated high-resolution chronology confirms that there is no chronological clustering of the eruptions, but they occurred randomly along the rifts and in the central area.

Furthermore, the suggestions of *Carracedo et al. (2007)* and *Carracedo and Troll (2013)*, who proposed periods with low eruptive frequencies, during which one/two eruptions per 1,000 yrs occurred, and periods with higher eruptive frequencies, with six/seven eruptions per 1,000 yrs, are also confirmed. In particular, the last 3 ka are characterized mainly by basaltic eruptions that occurred in the NW and NE rift zones.

However, it is necessary to add particular emphasis to the eruption of Mña Grande. This eruption, never considered before, occurred very recently in an unusual context, outside the

principal rifts (NWRZ and NERZ) and Las Cañadas Caldera, which are the most active geological structures of Tenerife where the Holocene volcanic activity was concentrated. It built a large scoria cone in the presently highly inhabited Güímar Valley, with an estimated volume of 0.09 km^3 for the cone, 0.013 km^3 for the lava fan, and from 0.315 to 0.81 km^3 for the pyroclastic deposits (*Di Roberto et al., 2020*). The petrographic and geochemical analyses of the Mña Grande deposits show also that the magma feeding the eruption originated from a distinct source and followed a path that is independent and different from the central feeding system of the TVC.

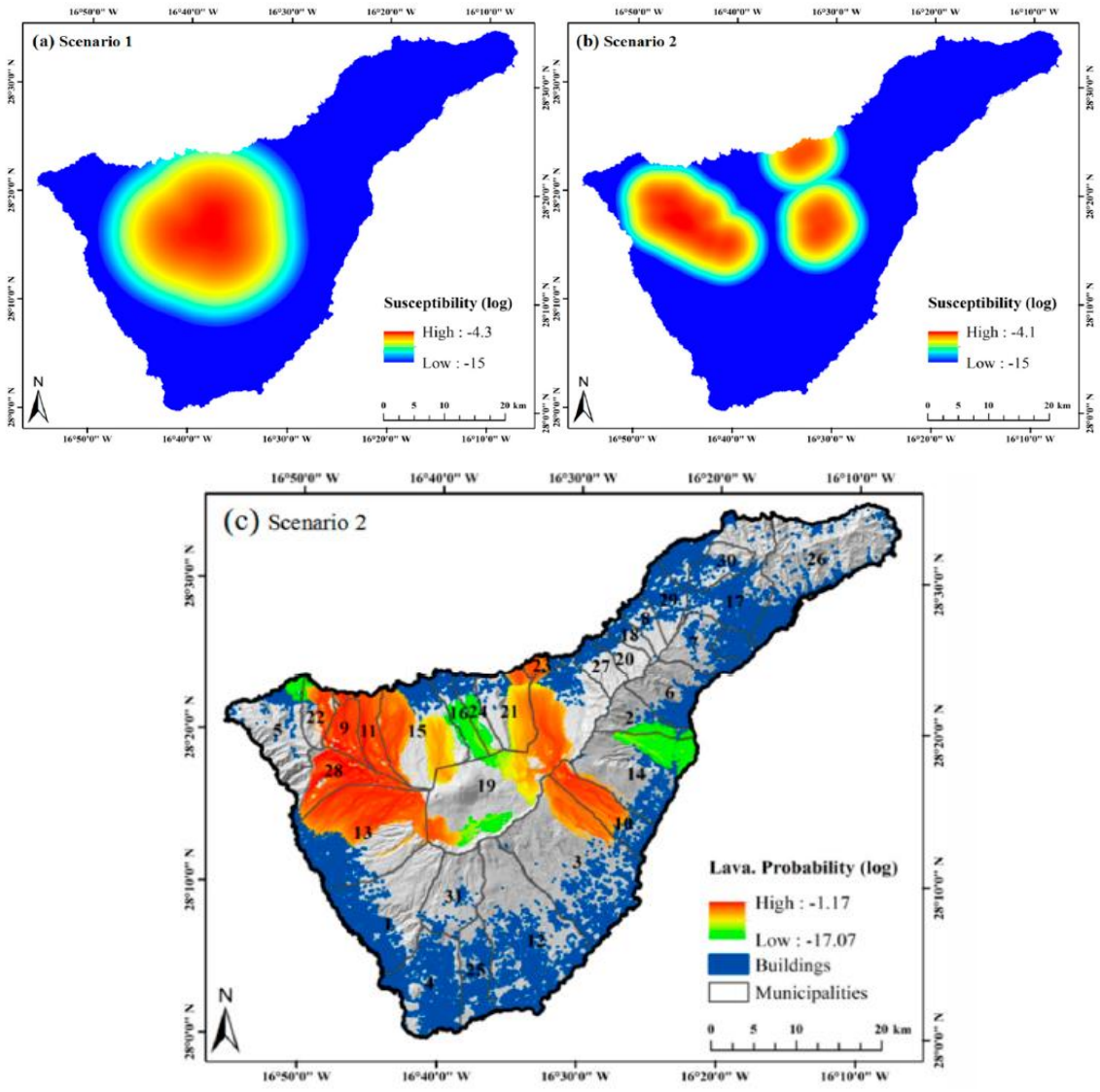

Fig. 4.30 a) and b) Vent susceptibility maps indicating the probabilities of future vent locations for the two scenarios elaborated with the Susceptibility module in the VORIS tool (*Felpeto, 2007; Liu et al., 2020*); c) distribution of simulated lava flows according to the scenario 2 *(Liu et al., 2020).*

The Güímar Valley was also the site of one of the historical eruptions, the Arafo eruption, that took place from February 2nd to March 27th, 1705. This eruption, less than 9 km from Mña Grande vent, produced a 100 m high cinder cone and a composite > 9 km-long lava flow, that stopped less than 500 m from the coast. This eruption is the final episode of a complex fissural eruption that started on 24th December 1704 with the Siete-Fuentes eruptive fracture and continued from 6 to 14 January 1705 with the Fasnia eruption, both producing small cinder cones and short lava flows channeled into gorges of the SE flank of Tenerife.

The occurrence of two large eruptions in the same highly inhabited area during a relatively short time (<3,000 yrs) is of great interest and force for the assessment of volcanic hazard. As is visible in Fig. 4.30, this sector of the island is not taken into account as a probable location for future vents. Nevertheless, if an eruption similar to Mña Grande occurred today, the infrastructure potentially affected by the fallout of lapilli and ash, estimated to be within 10 km from the source, would include ca. 40,000 inhabitants, industries and the TF-1 highway, one of the main transportation networks of the island. Moreover, the urban zone of Santa Cruz de Tenerife (ca. 500,000 inhabitants) and several other smaller centres would be involved, for a total population of ca. 700,000, if the fallout of volcanic ash extends farther. Finally, considering the hazard of lava flows, the island could be cut into two parts, with major problems due to the disruption of essential services (*Di Roberto et al., 2020*).

Finally, it is important to point out that all considerations treated above do not take into account submarine volcanism: although the occurrence of an eruption near the coastline may lead to an interaction between magma and water, and therefore produce phreatomagmatic explosions, it is not considered in the actual hazard assessments.

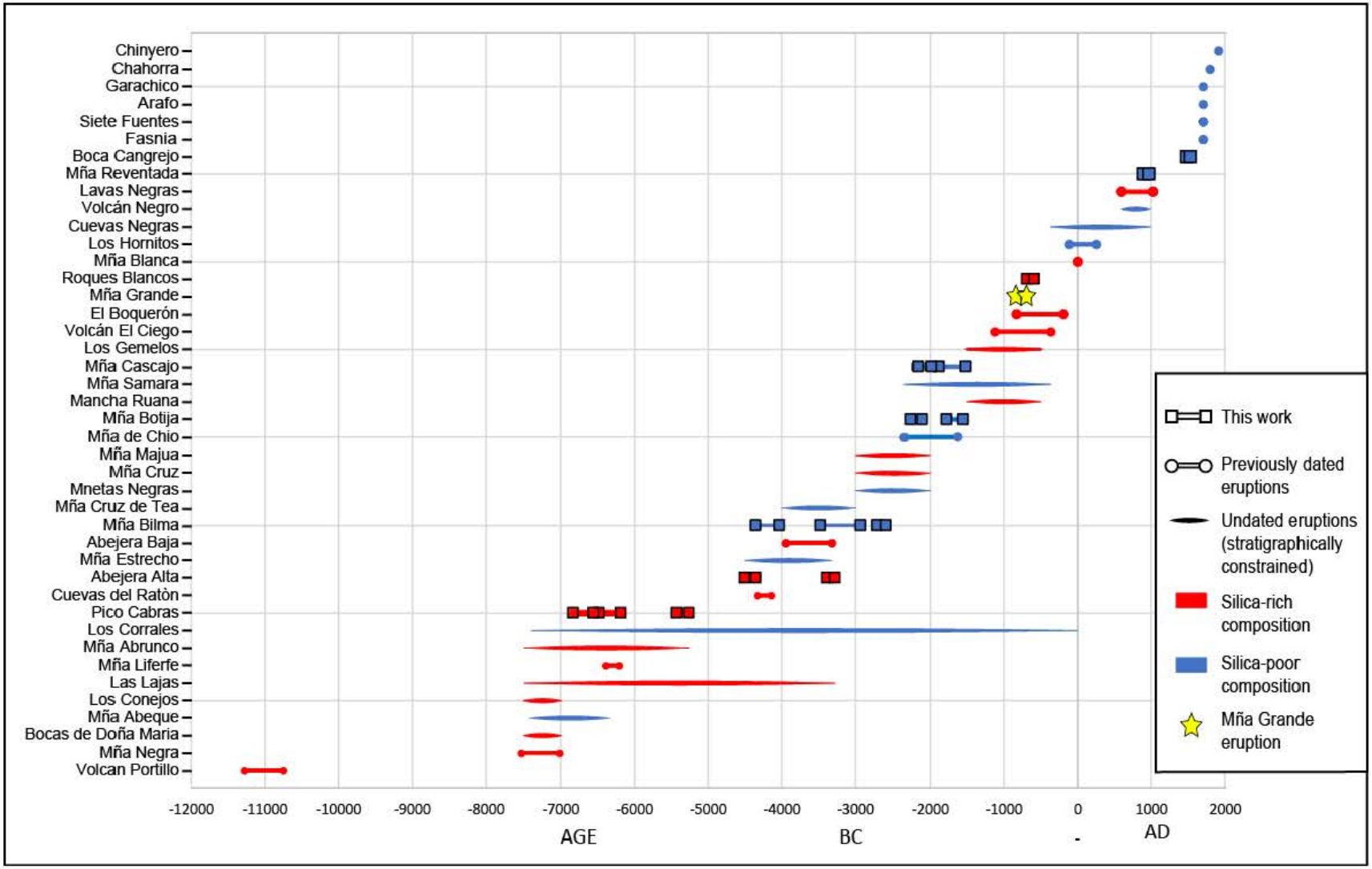

Fig. 4.31 Synthesis of Holocene volcanic eruptions from Tenerife. Squares represent the palaeomagnetically dated eruptions (this work); circles are historical and previously radiometrically dated eruptions (*Carracedo et al., 2007; Carracedo and Troll, 2013*). Lines are undated eruptions; red and blue colours represent volcanic eruptions with phonolitic and basaltic compositions, respectively (*Carracedo and Troll, 2013* and references therein).

4.2.6 Conclusions

New palaeomagnetic data obtained from Tenerife allow better constraint of the ages of nine volcanic eruptions that occurred in the last 9 ka: four of them (Pico Cabras, Mña Bilma, Mña Botija and Mña Cascajo) had been only stratigraphically constrained, four (Abejera Alta, Roques Blancos, Mña Reventada, Boca Cangrejo) had been previously dated with ^{14}C method, while one (Mña Grande) was undated so far.

The age ranges obtained for the first four lava flows are much narrower than the time windows given by stratigraphic evidence, whereas the comparison between ^{14}C and palaeomagnetic dating for the other three eruptions shows that the palaeomagnetic technique yields notably higher age resolution than the former method. Finally, the Mña Grande eruption, for which no age was previously available, was dated with very high accuracy (67 yrs time interval) at the VIII century BC. This work shows that radiocarbon surely represents a fundamental pillar for dating Holocene lava flows, but palaeomagnetism can yield higher dating accuracy, and in some cases, with very small errors (~70 years), at least on volcanoes for which reliable reference PSV data are available (i.e. Europe, circum-Europe areas, and Hawaii). Therefore, the use of palaeomagnetic dating, especially for Holocene volcanic rocks, should be highly encouraged, together with other isotopic/radiometric methods.

Our dataset, when integrated with the previously available chronological framework, strengthens the suggestion that the Holocene eruptive activity of TVC was characterized by alternating periods with different eruptive frequencies. In particular, the last 3 ka were characterized by high eruptive frequency, producing almost twice as many basaltic eruptions as felsic ones, predominantly in the NW and NE rifts. Nevertheless, although the new dating obtained with this work significantly improves the chronology of the recent volcanism of the TVC, many dating investigations, at least for onshore eruptions, need to be done before a complete overview of the recent volcanic activity and the definition of how the volcanic system worked. Finally, the very young age of Mña Grande (790-723 BC) and eruptions producing the ~180-m-high scoria cone and a large lava delta, requires a re-assessment of the volcanic hazard, especially along the east coast of Tenerife, which is not currently considered a probable location for future vents opening.

References

Abdel-Monem, A., Watkins, N.D., Gast, P.W. (1971). Potassium-argon ages, volcanic stratigraphy, and geomagnetic polarity history of the Canary Islands; Lanzarote, Fuerteventura, Gran Canaria, and La Gomera. Am J Sci 271:490–521

Ablay, G.J., Martí, J. (2000). Stratigraphy, structure, and volcanic evolution of the Pico Teide-Pico Viejo formation, Tenerife, Canary Islands. J. Volcanol. Geotherm. Res., 103: 175-208.

Ablay, G.J., Carroll, M.R., Palmer, M.R., Martí, J., Sparks, R.S.J. (1998). Basanite-Phonolite Lineages of the Teide-Pico Viejo Volcanic Complex, Tenerife, Canary Islands. J. Petrol., 39, (5): 905-936.

Almendros, J., Ibáñez, J.M., Carmona, E., Zandomeneghi, D. (2007). Array analyses of volcanic earthquakes and tremor recorded at Las Cañadas caldera (Tenerife Island, Spain) during the 2004 seismic activation of Teide volcano. J. Volcanol. Geotherm. Res. 160(3–4):285–299. https://doi.org/10.1016/j.jvolgeores.2006.10.002.

Alva-Valdivia, L. M., Rodríguez-Trejo, A., Vidal-Solano, J. R., Paz-Moreno, F., Agarwal, A. (2019). Emplacement temperature resolution and age determination of Cerro Colorado tuff ring by paleomagnetic analysis, El Pinacate Volcanic Field, Sonora, Mexico. Journal of Volcanology and Geothermal Research, 369, 145-154.

Ancochea, E., Fúster, J., Ibarrola, E., Cendrero, A., Coello, J., Hernan, F., Cantagrel, J.M., Jamond, C. (1990). Volcanic evolution of the island of Tenerife (Canary Islands) in the light of new K-Ar data. J Volcanol Geotherm Res 44:231–249.

Ancochea, E., Huertas, M., Cantagrel, J.M., Coello, J., Fúster, J.M., Arnaud, N., et al. (1999). Evolution of the Cañadas edifice and its implications for the origin of the Las Cañadas Caldera (Tenerife, Canary Islands). J. Volcanol. Geoth. Res. 88 (3), 177-199.

Andújar, J. (2007). Application of experimental petrology to the characterization of phonolitic magmas from Tenerife, Canary Islands. Ph.D. thesis, Universitat de Barcelona, p 183

Andújar, J., Scaillet, B. (2012). Experimental constraints on parameters controlling the difference in the eruptive dynamics of phonolitic magmas: the case of Tenerife (Canary Islands). J. Pet., 53(9):1777–1806. https://doi.org/10.1093/petrology/egs033.

Andújar, J., Costa, F., Martí, J. (2010). Magma storage conditions of the last eruption of Teide volcano (Canary Islands, Spain). Bull. Volcanol., 72(4):381–395. https://doi.org/10.1007/s00445-009-0325-3

Andújar, J., Costa, F., Scaillet, B. (2013). Storage conditions and eruptive dynamics of central versus flank eruptions in volcanic islands: the case of Tenerife (Canary Islands, Spain). J. Volcanol. Geotherm. Res., 260:62–79.

Araña, V., Barberi, F., Ferrara, G. (1989a). El complejo volcánico del Teide-Pico Viejo. En: Los Volcanes y la Caldera del Parque Nacional del Teide (Tenerife, Islas Canarias). V. Araña y J. Coello (eds.), Serie Técnica, ICONA: 85-101.

Araña, V., Aparicio, A., García Cacho, L., García García, R. (1989b). Mezcla de magmas en la región central de Tenerife. En: Los Volcanes y la Caldera del Parque Nacional del Teide (Tenerife, Islas Canarias). V. Araña y J. Coello (eds.), Serie Técnica, ICONA: 269-298.

Araña, V., Camacho, A. G., Garcia, A., Montesinos, F. G., Blanco, I., Vieira, R., Felpeto, A. (2000). Internal structure of Tenerife (Canary Islands) based on gravity, aeromagnetic and volcanological data. J. Volcanol. Geotherm. Res., 103(1-4), 43-64.

Araña, V., García, A., Astiz, M., Felpeto, A., Abella, R., Ortiz, R. (2002). Zonation of the main volcanic hazards (lava flows and ash fall) in Tenerife, Canary Islands. A proposal for a surveillance network. J. Volcanol. Geotherm. Res., 103, 377–391.

Blanco-Montenegro, I., Nicolosi, I., Pignatelli, A., García, A., Chiappini, M. (2011). New evidence about the structure and growth of ocean island volcanoes from aeromagnetic data: the case of Tenerife, Canary Islands. J. Geophys, Res. Solid Earth. 116(B3):B03102. https://doi.org/10.1029/2010jb007646.

Booth, B. (1973). The Granadilla pumice deposits of southern Tenerife, Canary Islands. Proc Geol Assoc 84:353–370

Boulesteix, T., Hildenbrand, A., Soler, V., Gillot, P.Y. (2012). Eruptive response of oceanic islands to giant landslides: new insights from the geomorphologic evolution of the Teide-Pico Viejo volcanic complex (Tenerife, Canary). Geomorphol 138:61–73

Branca, S., D'Ajello Caracciolo, F., Malaguti, A. B., Speranza, F. (2019). Constraining age and volume of lava flow invasions of the Alcantara valley, Etna volcano (Italy). New insights from paleomagnetic dating and 3D magnetic modeling. Journal of Volcanology and Geothermal Research, 374, 13–25. https://doi.org/10.1016/j.jvolgeores.2019.02.009

Brown, R.J., Branney, M.J. (2004). Event-stratigraphy of a caldera-forming ignimbrite eruption on Tenerife: the 273 ka Poris formation. Bull Volcanol 66:392–416.

Brown, R.J., Barry, T.L., Branney, J.J., Pringle, M.S., Bryan, S.E. (2003). The Quaternary pyroclastic succession of southeast Tenerife, Canary Islands; explosive eruptions, related caldera subsidence, and sector collapse. Geol Mag 140:265–288.

Bruns, M., Ingeborg, L., Münnich, K.O., Hubberten, H.W., Fillipakis, S. (1980). Regional sources of volcanic carbon dioxide and their influence on 14C content of present-day plant material. Radiocarbon 2:532–536.

Bryan, S.E. (2006). Petrology and geochemistry of the Quaternary caldera-forming, phonolitic Granadilla eruption, Tenerife (Canary Islands). J Petrol 47:1557–1589

Bryan, S.E., Marti, J., Cas, R.A.F. (1998). Stratigraphy of the Bandas del Sur formation: an extracaldera record of quaternary phonolitic explosive eruptions from the Las Cañadas edifice, Tenerife (Canary Islands). Geol Mag 135:605–636.

Bryan, S.E., Martí J, Leosson, M. (2002). Petrology and geochemistry of the bandas del sur formation, Las Cañadas edifice, Tenerife (Canary Islands). J Petrol 43:1815–1856.

Burr, G.S., Jull, A.J.T. (2009). Accelerator mass spectrometry for radiocarbon research. Encyclopedia of mass spectrometry, 5, 656-669.

Calvo-Rathert, M., Morales-Contreras, J., Carrancho, A., Goguitchaichvili, A. (2016). A comparison of Thellier-type and multispecimen paleointensity determinations on Pleistocene and historical lava flows from Lanzarote (Canary Islands, Spain), Geochem. Geophys. Geosyst., 17, 3638–3654.

Cantagrel, J.M., Arnaud, N.O., Ancochea, E., Fúster, J.M., Huertas, M.J. (1999). Repeated debris avalanches on Tenerife and genesis of Las Cañadas Caldera wall (Canary Islands). Geology 27:739–742.

Carracedo, J.C. (1975). Estudio paleomagnético de la isla de Tenerife. Ph.D. thesis, Universidad Complutense, Madrid.

Carracedo, J.C. (1979). Paleomagnetismo e historia volcánica de Tenerife. Aula Cultura Cabildo Insular de Tenerife, Santa Cruz de Tenerife, p 81

Carracedo, J.C. (1994). The Canary Islands: an example of structural control on the growth of large oceanic-island volcanoes. J. Volcanol. Geotherm. Res. 60, 225–241.

Carracedo, J.C., Troll, V. R. (2013). Teide Volcano - Geology and Eruptions of a Highly Differentiated Oceanic Stratovolcano. Springer-Verlag, Berlin Heidelberg, p. 234.

Carracedo, J.C., Rodríguez Badiola, E., Guillou, H., de la Nuez, J., Perez Torrado, F.J. (2001). "Geology and volcanology of La Palma and El Hierro, Western Canaries." Estudios Geologicos-madrid, 57: 175-273.

Carracedo, J.C., Paterne, M., Guillou, H., Pérez-Torrado, F.J., Paris, R., Rodríguez-Badiola, E., Hansen, A. (2003). Dataciones radiométricas (C14 y K-Ar) del Teide y el Rift NO, Tenerife, Islas Canarias. Estud. Geol. 59:15–29.

Carracedo, J.C. Guillou, H., Paterne, M., Scaillet, S., Rodríguez Badiola, E., Pérez Torrado, F. J., Paris, R., Hansen Machín, A. (2006). Los Volcanes del Parque Nacional del Teide: El Teide, Pico Viejo y las dorsales activas de Tenerife. mapas geológicos 1/50.000. Organismo Autónomo Parques Nacionales (España)

Carracedo, J.C., Rodríguez-Badiola, E., Guillou, H., Paterne, M., Scaillet, S., Pérez Torrado, F.J., et al. (2007). Eruptive and structural history of Teide volcano and rift zones of Tenerife, Canary Islands. Geol. Soc. Am. Bull. 19, 10271051.

Carracedo, J C., Rodríguez Badiola, E., Guillou, H., Paterne, M., Scaillet, S., Pérez Torrado, F.J., Paris, R., Rodríguez González, A., Socorro, S. (2008). El volcán Teide; volcanología, interpretación de paisajes e itinerarios comentados. Tomos 3: Análisis de las erupciones y excursiones comentadas (199 p.). Ediciones y Promociones Saquiro.

Carracedo, J.C., Guillou, H., Nomade, S., Rodríguez-Badiola, E., Pérez-Torrado, F.J., Rodríguez-González, A., Paris, R., Troll, V.R., Wiesmaier, S., Delcamp, A., Fernández- Turiel, J.L. (2011). Evolution of ocean-island rifts: the northeast rift zone of Tenerife, Canary Islands. Geol. Soc. Am. Bull. 123:562–584.

Cook, G.T., van der Plicht, J. (2007). Radiocarbon dating. In: Elias, SA, editor. Encyclopedia of Quaternary Science. Amsterdam: Elsevier. p 2899–911

De Barros., L., Martini, F., Bean, C.J., Garcia-Yeguas, A., Ibáñez, J. (2012). Imaging magma storage below Teide volcano (Tenerife) using scattered seismic wavefields. Geophys J Int 191(2):695–706. https://doi.org/10.1111/j.1365-246X.2012.05637.x.

de Groot, L.V. *et al.* (2015). High paleointensities for the Canary Islands constrain the Levant geomagnetic high, Earth planet. Sci. Lett., 419, 154–167.

Delcamp, A., Petronis, M.S., Troll, V.R., Carracedo, J.C., de Vries, Bv.W, Pérez-Torrado, F.J. (2010). Vertical axis rotation of the upper portions of the north-east rift of Tenerife Island inferred from paleomagnetic data. Tectonophysics 492:40–59.

Di Chiara, A., Speranza, F., Porreca, M. (2012). Paleomagnetic secular variation at the Azores during the last 3 ka. J. Geophys. Res. 117, B07101. https://doi.org/10.1029/2012JB009285.

Di Chiara, A., Speranza, F., Porreca, M., Pimentel, A., D'Ajello Caracciolo, F., Pacheco, J. (2014). Constraining chronology and time-space evolution of Holocene volcanic activity on the Capelo Peninsula (Faial Island, Azores): the paleomagnetic contribution. Geol. Soc. Am. Bull. 126, 1164–1180. https://doi.org/10.1130/B30933.1.

Di Roberto, A., Risica, G., Del Carlo, P., Pompilio, M., Speranza, F., Meletlidis, S. (2020). The forgotten eruption: the basaltic scoria cone of Montaña Grande, Tenerife. Journal of Volcanology and Geothermal Research. https://doi.org/10.1016/j.jvolgeores.2020.106918

Dóniz-Páez, J., De Jesús-Rojas, J.C., Zamorano-Orozco, J.J., Becerra-Ramírez, R. (2013). El Patrimonio Geomorfológico De Los Volcanes De El Malpaís De Güímar (Tenerife, España) Y Parícutin (Michoacán, México): Implicaciones Geoturísticas.

Dunlop, D.J. (2002). Theory and application of the Day plot (Mrs/Ms versus Hcr/Hc): 1. Theoretical curves and tests using titanomagnetite data. J. Geophys. Res., 107(B3), 2056, doi:10.1029/2001JB000486.

Edgar, C.J. (2003). Stratigraphy, eruption dynamics and pyroclastic flow emplacement of quaternary phonolitic plinian eruption. The Fasnia member of Diego Hernández formation, Tenerife, Canary Islands (Spain) Ph.D. thesis. Universidad de Monash, Australia, p 258

Edgar, C.J., Wolff, J.A., Nichols, H.J., Cas, R.A.F., Martí, J. (2002). A complex Quaternary ignimbrite-forming phonolitic eruption: the Poris member of the Diego Hernández formation (Tenerife, Canary Islands). J Volcanol Geotherm Res 118:99–130

Edgar, C.J., Wolff, J.A., Olin, P.H., Nichols, H.J., Pittari, A., Cas, R.A.F., Reiners, P.W., Spell, T.L., Martí, J. (2007). The late Quaternary Diego Hernandez formation, Tenerife: volcanology of a complex cycle of voluminous explosive phonolitic eruptions. J Volcanol Geotherm Res 160:59–85

Felpeto, A. (2007). A GIS-Based Tool for Volcanic Hazard Assessment User's Guide. Available online: http://www.gvb-csic.es/GVB/VORIS/VORIS_2_0_1_guide.pdf

Fisher, R. A. (1953). Dispersion on a sphere, Proc.R.Soc.Ser.A and Ser.B, 217, 195-305.

Fúster, J.M., Araña, V., Brandle, J.L., Navarro, J.M., Alonso, V., Aparicio, A. (1968). Geology and volcanology of the Canary Islands: Tenerife. Instituto Lucas Mallada, CSIC, Madrid.

García, O., Guzman, S., Martí, J. (2014). Stratigraphic correlation of Holocene phonolitic explosive episodes of the Teide–Pico Viejo Volcanic Complex, Tenerife. J. Geolog. Soc, London. http://dx.doi.org/10.1144/jgs2013-086.

Gómez-Fernandez, F. (1970). Development of a Volcanic Risk Assessment Information System for the Prevention And Management Of Volcanic Crisis: Stating The Fundamentals. WIT Trans. Inf. Commun. Technol., 21.

Gómez-Fernández, F. (2000) Application of a GIS algorithm to delimit the areas protected against basic lava flow invasion on Tenerife Island. J. Volcanol. Geotherm. Res., 103, 409–423.

Greve, A., Turner, G. M. (2017). New and revised palaeomagnetic secular variation records from post-glacial volcanic materials in New Zealand. Phys. Earth Planet. Inter. 269, 1–17.

Greve, A., Turner, G. M., Conway, C.E., Townsend, D.B., Gamble, J.A., Leonard, G.S. (2016). Palaeomagnetic refinement of the eruption ages of Holocene lava flows, and implications for the eruptive history of the Tongariro Volcanic Centre, New Zealand. Geophys. J. Int. 207 (2), 702–718. https://doi.org/10.1093/gji/ggw296.

Guillou, H., Carracedo, J. C., Paris, R., Torrado, F. J. P. (2004). Implications for the early shield-stage evolution of Tenerife from K/Ar ages and magnetic stratigraphy. Earth and Planetary Science Letters, 222(2), 599-614.

Guillou, H., Nomade, S., Carracedo, J.C., Kissel, C., Laj, C., Wandres, C. (2011). Effectiveness of combined unspiked K-Ar and 40Ar/39Ar dating methods in the 14C age range. Quat. Geochronol. 6:530–538.

Hausen, H. (1955). Contributions to the geology of Tenerife (Canary Islands). Societas scientiarum fennica, commentationes physico-mathematicae, geologic results of the Finnish expedition to the Canary Islands 1947–1951, vol 18, Issue no 1. Centraltryckeriet, Helsingfors.

Huertas, M.J., Arnaud, N.O., Ancochea, E., Cantagrel, J.M., Fúster, J.M. (2002). Ar-40/Ar-39 stratigraphy of pyroclastic units from the Cañadas Volcanic Edifice (Tenerife, Canary

Islands) and their bearing on the structural evolution. J. Volcanol. Geoth. Res. 115 (34), 351365.

Hürlimann, M., Turon, E., Martí, J. (1999). Large landslides triggered by caldera collapse events in Tenerife, Canary Islands. Phys. Chem. Earth 24 (10A), 921–924.

Hürlimann, M., Ledesma, A., Martí, J. (2001). Characterisation of a volcanic residual soil and its implications for large landslide phenomena: application to Tenerife, Canary Islands. Eng. Geol. 59, 115–132.

Ibarrola, E., Ancochea, E., Fuster, J.M., Cantagrel, J.M., Coello, J., Snelling, N.J., Huertas, M.J. (1993). Cronoestratigrafía del Macizo de Tigaiga: evolución de un sector del edificio Cañadas (Tenerife, Islas Canarias). Boletín de la Real Sociedad Española de Historia Natural (Sec Geol) 88(1–4):57–72

Juárez-Arriaga, E., Böhnel, H., Carrasco-Núñez, G., Mahgoub, A. N. (2018). Paleomagnetism of Holocene lava flows from Los Humeros caldera, eastern Mexico: Discrimination of volcanic eruptions and their age dating. Journal of South American Earth Sciences, 88, 736-748.

Jull, A.J.T., Burr, G.S. (2015). Radiocarbon Dating. In: Jack Rink W., Thompson J.W. (eds) Encyclopedia of Scientific Dating Methods. Encyclopedia of Earth Sciences Series. Springer, Dordrecht

Kirschvink, J. L. (1980). The least-square line and plane and the analysis of paleomagnetic data, Geophys. J., 62, 699-718.

Kissel, C., Laj, C., Rodriguez-Gonzalez, A., Perez-Torrado, F., Carracedo, J.C., Wandres, C. (2015a). Holocene geomagnetic field intensity variations: contribution from the low latitude Canary Islands site, Earth planet. Sci. Lett., 430, 178–190.

Kissel, C., Gonzalez, A., Laj, C., Perez-Torrado, F., Carracedo, J., Wandres, C., Guillou, H. (2015b). Paleosecular variation of the earth magnetic field at the Canary Islands over the last 15 ka. Earth and Planetary Science Letters. 412. 10.1016/j.epsl.2014.12.031.

Kono, M. (2015). Geomagnetism: An Introduction and Overview. Chapter 5 in Schubert, G. (2015), Treatise on Geophysics. Elsevier.

Lanza, R., Zanella, E. (2006). Comments on “Chronology of Vesuvius’ activity from A.D. 79 to 1631 based on archeomagnetism of lavas and historical sources” by C. Principe et al.. Bulletin of Volcanology, 68, 394–396.

Lanza, R., A. Meloni, Tema, E. (2005). Historical measurement of the Earth’s magnetic field compared with the remanence directions from lava flows in Italy over the last four centuries, Phys. Earth Planet. Inter., 148, 97–107, doi:10.1016/j.pepi.2004.08.005.

Liu, W., Li, L., Chen, L., Wen, M., Wang, J., Yuan, L., et al. (2020). Testing a Comprehensive Volcanic Risk Assessment of Tenerife by Volcanic Hazard Simulations and Social Vulnerability Analysis. ISPRS International Journal of Geo-Information, 9(4), 273.

Longin, R. (1971). New method of collagen extraction for radiocarbon dating. Nature, 230 (5291), 241-242.

Longpré, M.A., Troll, V.R., Walter, T.R., Hansteen, T.H. (2009). Volcanic and geochemical evolution of the Teno massif, Tenerife, Canary Islands: some repercussions of giant landslides on ocean island magmatism.Geochem Geophys Geosyst 10:Q12017. doi:10.1029/2009gc002892.

Manconi, A., Longpré, M.A., Walter, T.R., Troll, V.R., Hansteen, T.H. (2009). The effects of flank collapses on volcano plumbing systems. Geology, 37:1099–1102.

Marrero, J.M., García, A., Llinares, A., Rodriguez-Losada, J.A., Ortiz, R. (2012). A direct approach to estimating the number of potential fatalities from an eruption: Application

to the Central Volcanic Complex of Tenerife Island. J. Volcanol. Geotherm. Res., 219–220, 33–40.

Martí, J. (2019). Las Cañadas caldera, Tenerife, Canary Islands: a review, or the end of a long volcanological controversy. Earth-Science Reviews, 196, 102889. https://doi.org/10.1016/j.earscirev.2019.102889

Martí, J., Geyer, A. (2009). Central vs flank eruptions at Teide–Pico Viejo twin stratovolcanoes (Tenerife, Canary Islands). J. Volcanol. Geotherm. Res. 181(1–2):47–60. https://doi.org/10.1016/j.jvolgeores.2008.12.010.

Martí, J., Gudmundsson, A. (2000). The Las Cañadas caldera (Tenerife, Canary Islands): an overlapping collapse caldera generated by magma-chamber migration. J. Volcanol. Geotherm. Res., 103(1–4):161–173. https://doi.org/10.1016/S0377-0273(00)00221-3.

Martí, J., Mitjavila, J., Villa, I.M. (1990). Stratigraphy and K-Ar ages of the Diego Hernández wall and their significance on the Las Cañadas Caldera formation (Tenerife, Canary Islands). Terra Nova 2:148–153

Martí, J., Mitjavila, J., Araña, V. (1994). Stratigraphy, structure and geochronology of the Las Cañadas Caldera (Tenerife, Canary Islands). Geol Mag 131: 715–727

Martí, J., Hurlimann, M., Ablay, G.J., Gudmundsson, A. (1997). Vertical and lateral collapses on Tenerife (Canary Islands) and other volcanic ocean islands. Geology 25:879–882

Martí J., Geyer A., Andujar J., Teixido F., Costa F. Assessing the potential for future explosive activity from Teide-Pico Viejo stratovolcanoes (Tenerife, Canary Islands) J. Volcanol. Geotherm. Res., 178 (2008), pp. 529-542,

Mitjavila, J.M., Villa, I.M. (1993). Temporal evolution of Diego Hernández formation (Las Cañadas, Tenerife) and confirmation of the age of the Caldera using the 40Ar/39Ar method. Rev la Soc Geológica España 1–2:1–10

Nasser-Mahgouba, A., Böhnela, H., Siebeb, C., Oryaëlle Chevrelc, M. (2017). Paleomagnetic study of El Metate shield volcano (Michoacán, Mexico) confirms its monogenetic nature and young age (~1250 CE). J. Volcanol. Geotherm. Res. 336, 209–218.

Pasquier-Cardin, A., Allard, P., Ferreira, T., Hatte, C., Coutinho, R., Fontugne, M., Jaudon, M. (1999). Magma derived CO^2 emissions recorded in ^{14}C and ^{13}C contents of plants growing in Furnas caldera, Azores. J Volcanol Geotherm Res 92:195–207.

Pavón-Carrasco, F. J., Villasante-Marcos, V. (2010). Geomagnetic Secular Variation in the Canary Islands: paleomagnetic data, models and application to paleomagnetic dating. Física de la Tierra, 22 59-80.

Pavón-Carrasco, F.J., Rodríguez-González, J., Osete, M.L., Torta, J.M. (2011). A Matlab tool for archaeomagnetic dating. Journal of Archaeological Science 38, 408-419.

Pavón-Carrasco, F.J., Osete, M.L., Torta, J.M., De Santis, A. (2014). A geomagnetic field model for the Holocene based on archaeomagnetic and lava flow data. Earth and Planetary Science Letters vol. 388, pp. 98–109.

Pinton, A., Giordano, G., Speranza, F., Þórðarson, Þ. (2018). Paleomagnetism of Holocene lava flows from the Reykjanes Peninsula and the Tungnaà lava sequence (Iceland): implications for flow correlation and ages. Bull. Volcanol. 80, 10. https://doi.org/ 10.1007/s00445-017-1187-8.

Pittari, A., Cas, R.A.F, Martí, J. (2005). The occurrence and origin of prominent massive, pumice-rich ignimbrite lobes within the late Pleistocene Abrigo ignimbrite, Tenerife, Canary Islands. J Volcanol Geotherm Res 139:271–293

Pittari, A., Cas, R.A.F., Edgar, C.J., Nichols, H.J., Wolff, J.A., Martí, J. (2006). The influence of palaeotopography on facies architecture and pyroclastic flow processes of a lithic-rich

ignimbrite in a high gradient setting: the Abrigo Ignimbrite, Tenerife, Canary Islands. J Volcanol Geotherm Res 152:273–315

Reimer, P.J., Bard, E., Bayliss, A., Beck, J.W., Blackwell, P.G., Bronk Ramsey, C., Buck, C.E., Cheng, H., Edwards, R.L., Friedrich, M., Grootes, P.M., Guilderson, T.P., Haflidason, H., Hajdas, I., Hatté, C., Heaton, T.J., Hogg, A.G., Hughen, K.A., Kaiser, K.F., Kromer, B., Manning, S.W., Niu, M., Reimer, R.W., Richards, D.A., Scott, E.M., Southon, J.R., Turney, C.S.M., van der Plicht, J. (2013). IntCal13 and MARINE13 radiocarbon age calibration curves 0-50000 years cal BP Radiocarbon 55(4). DOI: 10.2458/azu_js_rc.55.16947.

Ridley, W.I. (1970). The abundance of rock types on Tenerife, Canary Islands, and its petrogenetic significance. Bull Volcanol 34196–204

Ridley, W.I. (1971). The field relations of the Las Cañadas volcanoes, Tenerife, Canary Islands. Bull Volcanol 35:318–334

Risica, G., Speranza, F., Giordano, G., De Astis, G., Lucchi, F. (2019). Palaeomagnetic dating of the Neostromboli succession, Journal of Volcanology and Geothermal Research, 371, 229–244. https://doi.org/10.1016/j.jvolgeores.2018.12.009.

Rodríguez-Badiola, E., Pérez-Torrado, F.J., Carracedo, J. C., Guillou, H. (2006). Petrografía y Geoquíca del edificio volcánico Teide-Pico Viejo y las dorsales noreste y noroeste de Tenerife. In: Carraedo, J.C. (ed) Los volcanes del Parque Nacional del Teide/El Teide, Pico Viejo y las dorsales activas del Tenerife. Naturaleza y Pasques Nacionales - Serie Técnica. Organismo Autónomo Parques acionales Ministerio de Medio Ambiente, Madrid, pp. 129-186.

Saupé, F., Strappa, O., Coppens, R., Guillet, B., Jaegy, R. (1980). A possible source of error in ^{14}C dates: volcanic emanations (examples from the Monte Amiata district, provinces of Grosseto and Sienna, Italy). Radiocarbon 22:525–531.

Scaini, C., Felpeto, A., Martí, J., Carniel, R. (2014). A GIS-based methodology for the estimation of potential volcanic damage and its application to Tenerife Island, Spain. J. Volcanol. Geotherm. Res. 278–279, 40–58

Scandone, R., Bartolini, S., Martí, J. (2016). A scale for ranking volcanoes by risk. Bull. Volcanol., 78, 1–8.

Schmincke, H.U. (1982). Volcanic and chemical evolution of the Canary Islands. In: Von Rad, U., Hinz, K., Sarntheim, M., Seibold, E. (eds). Geology of the northwest African continental margin. Springer, Berlin, pp 273–276.

Sigurdsson, H., Houghton, B., McNutt, S., Rymer, H., Stix, J. (Eds.) (2015). The encyclopedia of volcanoes. Elsevier.

Sobradelo, R., Martí, J., Mendoza-Rosas, A. T., Gómez, G. (2011). Volcanic hazard assessment for the Canary Islands (Spain) using extreme value theory. Natural Hazards and Earth System Sciences, 11(10), 2741-2753.

Soler, V., Carracedo, J.C., Heller, F. (1984). Geomagnetic secular variation in historical lavas from the Canary-Islands, Geophys. J. R. astr. Soc., 78, 313–318.

Speranza, F., Branca, S., Coltelli, M., D'ajello Caracciolo, F., Vigliotti, L. (2006). How accurate is “paleomagnetic dating”? New evidence from historical lavas from Mount Etna. J. Geophys. Res. 111 (B12). https://doi.org/10.1029/2006JB004496.

Speranza, F., Pompilio, M., D'Ajello Caracciolo, F., Sagnotti, L. (2008). Holocene Eruptive history of the Stromboli volcano: constraints paleomagnetic dating. J. Geophys. Res. 113 (B9). https://doi.org/10.1029/2007JB005139.

Speranza, F., Di Chiara, A., Rotolo, S.G. (2012). Correlation of welded ignimbrites on Pantelleria (Strait of Sicily) using paleomagnetism. Bull. Volcanol. 74, 341–357. https://doi.org/10.1007/s00445-011-0521-9.

Stuiver, M., Reimer, P.J., and Reimer, R.W. (2020). CALIB 7.1 [WWW program]

Thirlwall, M.F., Singer, B.S., Marriner, G.F. (2000). 39Ar-40Ar ages and geochemistry of the basaltic shield stage of Tenerife, Canary Islands, Spain. J Volcanol Geotherm Res 103:247–297

Troll, R. V., Carracedo, J. C. (2016). The Geology of Tenerife, in Editor(s): Troll, R. V., Carracedo, J. C., The Geology of the Canary Islands, Elsevier, 227-355. https://doi.org/10.1016/B978-0-12-809663-5.00005-0

Urrutia-Fucugauchi, J., Alva-Valdivia, L.M., Gogichaishvili, A., Rivas, M.L., Morales, J. (2004). Paleomagnetic, rock-magnetic and microscopy studies of historic lava flows from the Paricutin volcano, Mexico: implication for the deflection of paleomagnetic directions. Geophys. J. Int. 156, 431–442. https://doi.org/10.1111/j.1365-246X.2004.02166

Valet, J. P., Soler, V. (1999). Magnetic anomalies of lava fields in the Canary Islands. Possible consequences for paleomagnetic records. Physics of the earth and planetary interiors, 115(2), 109-118.

Vashakidze, G., Goguitchaichvili, A., García-Redondo, N. et al. (2019). Magnetic dating of the Holocene monogenetic Tkarsheti volcano in the Kazbeki region (Great Caucasus). Earth Planets Space 71, 133. https://doi.org/10.1186/s40623-019-1109-4

Walter, T.R. (2003). Buttressing and fractional spreading of Tenerife, an experimental approach on the formation of rift zones. Geophys. Res. Lett. 30 (6), 1296.

Walter, T.R., Schmincke, H.U. (2002). Rifting, recurrent landsliding and Miocene structural reorganization on NW-Tenerife (Canary Islands). Int J Earth Sci 91:615–628

Walter, T.R., Troll, V.R., Cailleau, B., Belousov, A., Schmincke, H.U., Amelung, F., Bogaard, P.V.D. (2005). Rift zone reorganization through flank instability in ocean island volcanoes: an example from Tenerife, Canary Islands. Bull Volcanol 67:281–291. https://doi.org/10.1007/s00445-004-0352-z.

Watts, A.B., Masson, D.G. (1995). A giant landslide on the north flank of Tenerife, Canary Islands. J Geophys Res 100:24487–24498.

Wiesmaier, S., Deegan, F. M., Troll, V. R., Carracedo, J.C., Chadwick, J.P., Chew, D.M. (2011). Magma mixing in the 1100 AD Montaña Reventada composite eruption, Tenerife, Canary Islands: interaction between rift zone and central volcano plumbing systems. Contrib. Mineral. Petrol. 162, 651-669.

Wiesmaier, S., Troll, V.R., Wolff, J. A., Carracedo, J.C. (2013). Open-system processes in the differentiation of mafic magma in the Teide-Pico Viejo succession, Tenerife. J. Geol. Soc. London. 170, 557-570.

Wolff, J.A. (1983). Petrology of Quaternary pyroclastic deposits from Tenerife, Canary Islands. Ph.D. Thesis, University of London, London

Wolff, J.A. (1987). Crystallisation of nepheline syenite in a subvolcanic magma system: Tenerife, Canary Islands. Lithos 20:207–223

Wolff, J.A., Grandy, J.S., Larson, P.B. (2000) Interaction of mantle-derived magma with island crust? Trace element and oxygen isotope data from the Diego Hernández formation, Las Cañadas, Tenerife. J Volcanol Geotherm Res 103:343–366.

Zijderveld, J. D. A. (1967). AC demagnetization of rocks: Analysis of results, in Methods in Palaeomagnetism, edited by S. K. Runcorn, K. M. Creer, and D. W. Collinson, pp. 254–286, Elsevier, Amsterdam.

4.3 El Hierro Island

4.3.1 Geological setting

El Hierro is the smallest (with only 268 km^2), the westernmost and the youngest (<1.12 Ma) island of the Canarian archipelago (Fig. 4.32). It is also the least populated, with ca. 10,500 inhabitants, half of whom are concentrated in the capital, Valverde.

The island is the emergent part of a volcanic shield 1,501 m a.s.l. (Pico de Malpaso), which rises from 3700-4000 m b.s.l. the deep oceanic seafloor (*Carracedo et al., 2001*). It has a truncated trihedral shape, with three main convergent ridges separated by a horseshoe-shaped embayment, generated by multiple sector collapses.

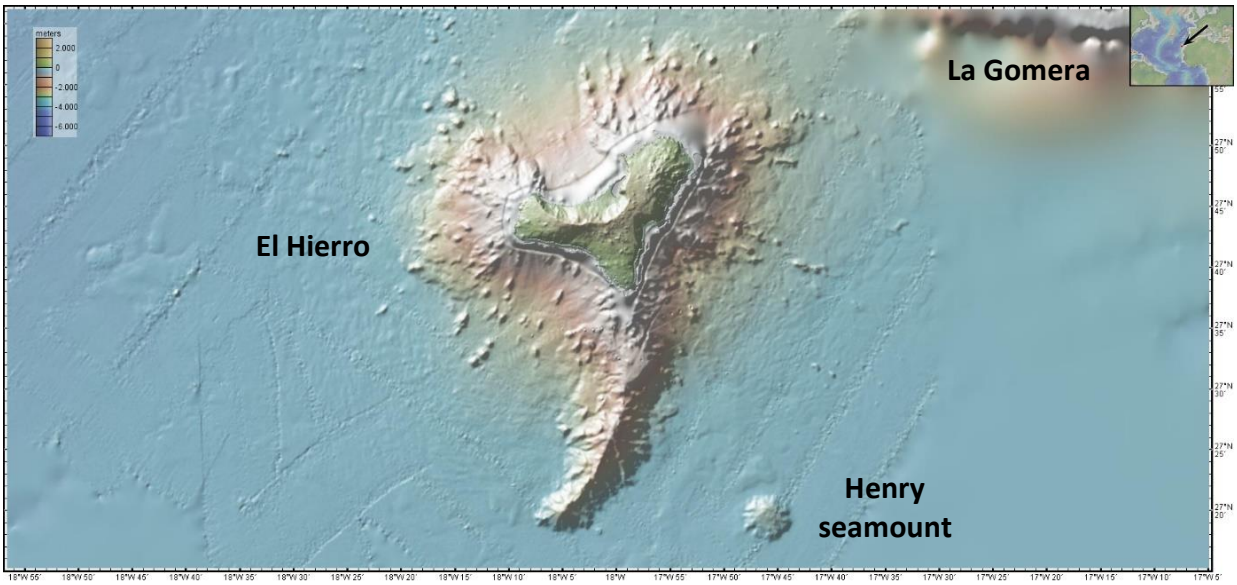

Fig.4.32 El Hierro Island (from GeoMapApp 3.6.1). Colours represent meters above and below sea level.

One of the most peculiar characteristics of El Hierro is its "Mercedes star" geometry controlled by a three-armed rift system that gives rise to three ridges extending from the centre of the island (*Carracedo, 1994*), and the associated large gravitational landslides *(Carracedo, 1996a, b; Masson, 1996; Urgeles et al., 1996, 1997; Carracedo et al., 1999, 2001; Masson et al., 2002; Walter and Troll, 2003; Manconi et al., 2009; Longpré et al., 2011*). The rift zones host the larger part of subaerial eruptions; one of the submarine propagations (the 20 km-long and curved prolongation of the South rift, visible in Fig. 4.32) was the site of the last eruption occurred on the island between 2011 to 2012 AD.

Similar to Tenerife, three main hypotheses have been proposed to explain the triple-armed rift: 1) it is the result of local stresses generated by the up-pushing action of upcoming magma

(*Carracedo, 1996a*); 2) it is related to gravitational spreading that controls rift zones and flank instability (*Münn et al., 2006*); or 3) the evolution and origin have been strongly controlled by regional tectonic structures (*Geyer and Martí, 2010*).

Several works have been carried out to study the older part of the island: radiometric ages coupled with geomagnetic reversal analysis (*Abdel Monem et al., 1971; Guillou et al., 1996; Szérémata et al., 1999; Pèrez-Torrado et al., 2011*) place the formation of El Hierro island within the Quaternary period. The construction of the island mainly took place during two magnetic polarity chrons: the R1 *Matuyama* reverse polarity chron (including the Jaramillo event, 0.97-0.9 Ma), and the normal N1 *Brunhes* chron (<0.78 Ma, *Carracedo et al., 2001*).

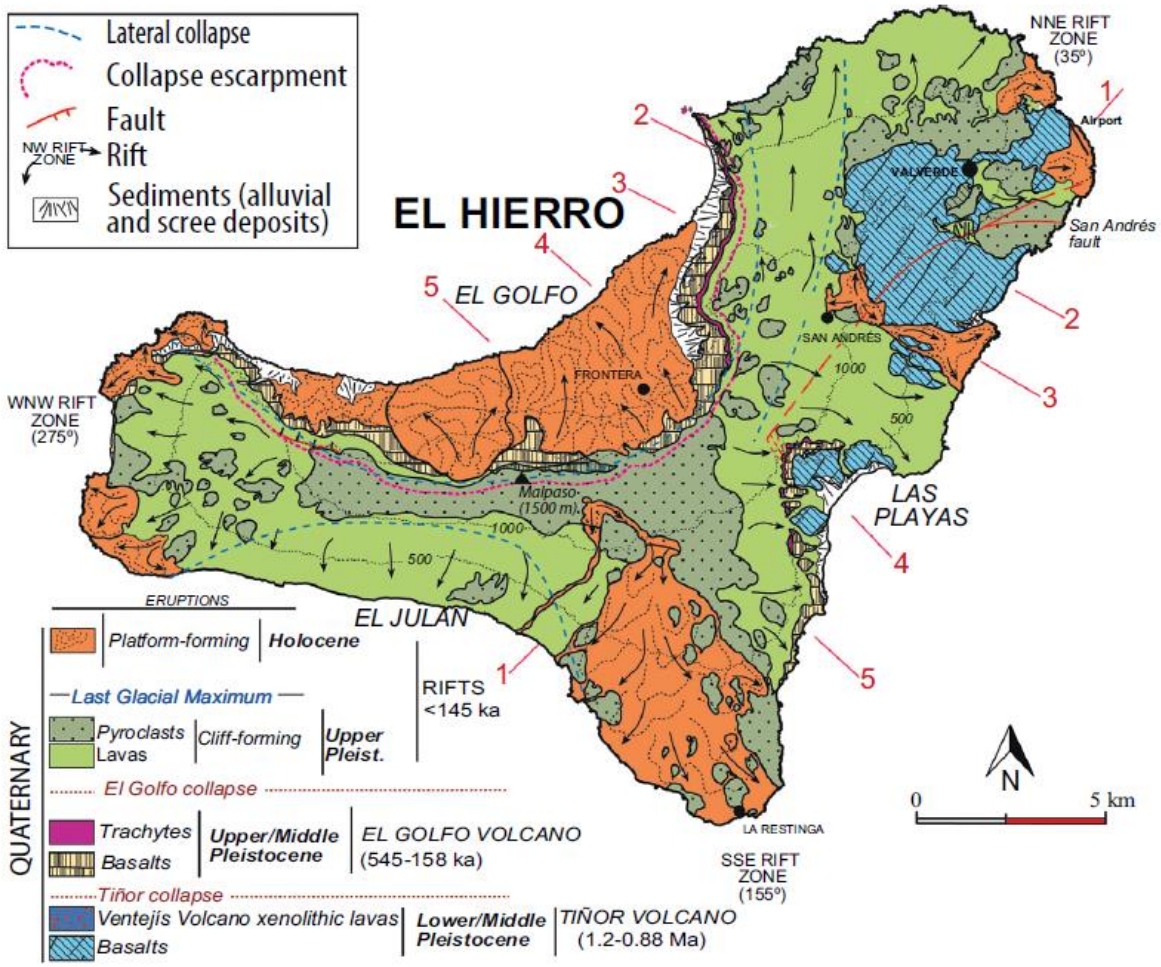

Fig. 4.33 Simplified map of El Hierro island (from *Troll and Carracedo, 2016; Carracedo et al., 2001*).

Three large superimposed volcanoes have been recognized: the *Tiñor*, the *El Golfo* and the *Recent Rift* volcano (Fig. 4.33).

The *Tiñor volcano* represents the first stage of the subaerial growth of El Hierro and developed on the northeast flank of the island, between 1.12 and 1.03 Ma. Outcrops of this stage, confined to the northeast flank and the interior part of the Las Playas embayment, show homogeneous compositions with time, in which it is possible to recognize three principal units: 1) a basal level, corresponding to the initial stages of subaerial growth; 2) a unit with thicker lavas that progressively tend to sub-horizontal flows toward the center of the edifice; and 3) a group of emission vents and associated lavas (the Ventejís volcano group), with abundant content of peridotite mantle xenoliths (*Carracedo et al., 2001; Troll and Carracedo, 2016*). The first volcanic stage ende with a collapse (Tiñor lateral collapse) at approximately 0.88 Ma. This giant collapse is the oldest found in El Hierro and probably removed half or more of the volcanic edifice.

El Golfo volcano developed filling the NW-facing collapse embayment and towards the east coast. The second volcanic stage occurred entirely during the Brunhes polarity chron. Two units have been identified: 1) a basal unit composed of strombolian and surtseyan pyroclastic deposits, with minor lava flows, and 2) an upper unit composed of lava flows. One of the characteristics of the lower unit is the presence of dikes cutting the sequences, indicating the activity of the triple-arm rift system. The upper unit is characterized by several differentiated lava flows and trachybasalt deposits, representing the final stages of activity of this volcano. El Golfo volcano lasted approximately from 545 ka to 176 ka (according to the age of trachytic lavas in the collapse scars section, *Troll and Carracedo, 2016* and reference therein). This volcanic edifice ended its activity with a giant collapse (El Golfo giant collapse).

The last phase is represented by the *Recent Rift volcanism*, developed with three arms of the simultaneously active rifts. Lavas produced by rifts lie conformably on the El Golfo sequence, covering much of the island and filling the El Julan collapse embayment. The rift eruptions started after the final differentiated products of El Golfo volcano (*Guillou et al., 1996; Troll and Carracedo, 2016*). More than 220 monogenetic cones belong to this stage (*Becerril et al., 2015*).

Generally, the Total Alkali-Silica (TAS) diagram of El Hierro lavas (Fig. 4.34) shows silica-saturated rocks with high alkali contents, corresponding to the Canarian ocean island alkaline trend (Oceanic Island Basalts-OIB series). However, El Golfo volcano lavas show Hawaiian tendency, merging into the Hawaiian-type Tholeiites (OIT) series (*Carracedo et al., 2001*).

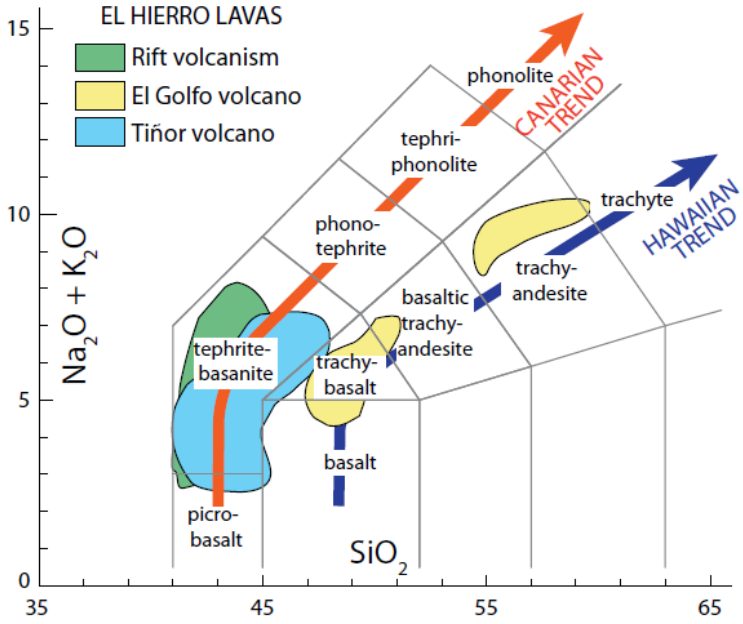

Fig. 4.34 Total alkali versus silica diagram, comparing lavas from the three main stages of El Hierro island with the general Canary magmatic evolutionary trend (*Carracedo et al., 2001; Troll and Carracedo, 2016).*

The concentration of eruptions in the center of the island due to the triple rift system increased the gravitational instability, triggering lateral collapses. The three principal landslides are (Fig. 4.35): the *Tiñor lateral collapse*, the *El Julan* and *Las Playas landslides* and *El Golfo giant collapse*.

The first, as described above, occurred at the end of Tiñor volcano.

The second, based on the thickness of the sediments covering the El Julan avalanche, occurred probably before 0.6 Ma, pre-dating the El Golfo landslide. Las Playas collapse is more complex and involved a larger landslide (*Masson et al., 2002*). Part of this collapse remained anchored, and the scar of this aborted collapse can be observed as a fault in the southeast flank of the island, near La Caleta and the San Andrès village.

Finally, the largest and most recent collapse in El Hierro is El Golfo giant collapse: the age of this huge landslide is still debated, due to the conflicting information obtained from onshore and offshore observations. The marine investigations indicate an age between 13 ka and 17 ka *(Masson et al., 2002*), coinciding with the end of the last glaciation. Onshore observations indicate a much longer period to take place, instead (*Carracedo and Day, 2002*). According to *Longpré et al. (2011),* the main El Golfo landslide has been constrained with radiometric ages between 87±8 ka and 39±13 ka.

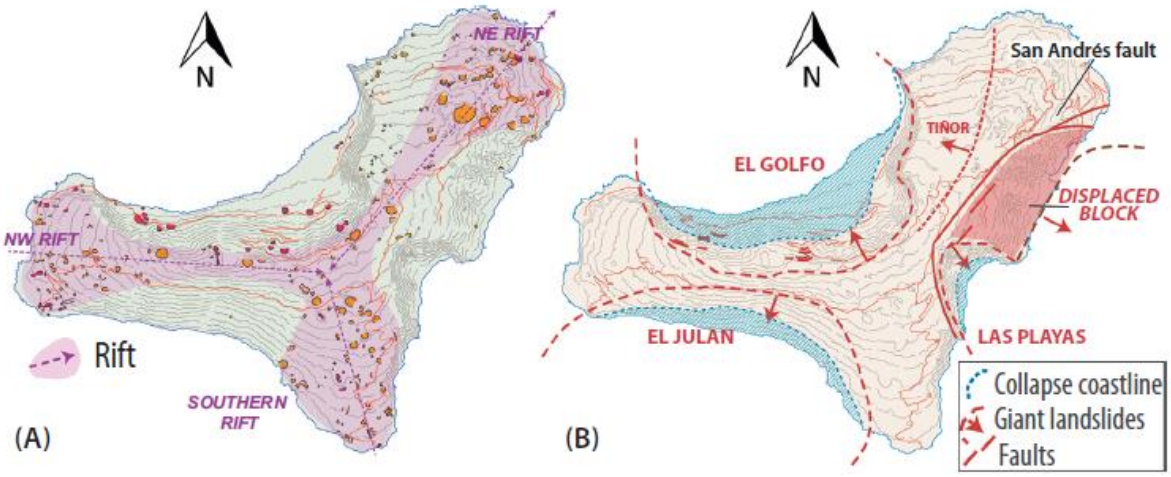

Fig. 4.35 Recent rift zones of El Hierro. Geometry and disposition of the rifts (a) and giant landslides of El Hierro (B) (from *Troll and Carracedo, 2016*).

4.3.2 Recent Rift Volcanism

Although the island shows a recent well-developed volcanic activity, it is still poorly known.

One of the main problems for the construction of a complete stratigraphy of the recent volcanism is the scattered location of the vents. This activity is mainly monogenetic and mostly characterized by mafic magmas as well as the intrusion of subvolcanic bodies generally erupted along the three rift zones, ranging in composition from picrobasalts to basanites (*Pellicer, 1977; Stroncik et al., 2009*). Eruptions typically produce proximal fallout, ballistic ejecta, and lava flows, with an erupted volume of magma between 0.0001 to 0.1 km^3 (DRE; *Sobradelo et al., 2011*), often without any direct contact between deposits belonging of the different eruptions.

According to *Becerril et al. (2016)*, about 31 eruptions occurred during the last 33 ka, of which nineteen are located along the rifts, and twelve within El Golfo embayment. Only seven of them were dated; for the others, only lower bound ages are available. An approximate geomorphologic constraint to recognize Holocene eruptions is given by the formation of coastal platforms. As on La Palma island (*Carracedo et al., 2001*), the recent eruptions form coastal platforms that have not been significantly eroded or dismantled and thus are considered as formed after sea level rise following the last glacial maximum (ca. 10-12 ka).

The island was conquered by Spaniards in the XV century and no records before this period are available. Aboriginal (*Bimbache)* communities occupied El Hierro for many centuries and

left seafood remains in some cavities and lava tunnels where they lived around the island. The oldest radiocarbon date for the Bimbache presence on the island indicates a 120 ± 60 AD age (*Ordóñez et al., 2017; Velasco-Vázquez et al., 2005).*

The two youngest prehistoric eruptions, located in the ENE rift, are Mña Los Cascajos and Mña Chamuscada: the first has been dated by *Becerril et al. (2016)* with a ^{14}C at 2280 ± 30 BP (401- 351 and 295- 208 cal BC; recalibrated ages as described in 4.2.4 paragraph) and the second has been dated at 2500 ±70 years BP (794-428 cal BC; *Guillou et al., 1996*).

An older eruption is Tanganasoga, a large volcano emplaced on the scarp of El Golfo depression, which has been dated with ^{14}C age both by *Pellicer (1977)* at 4200 ± 100 BC and 6740 ± 150 BC, and *Pérez-Torrado et al. (2011)* at 3900 ± 70 BP and 8100 ± 60 BP (i.e. 2502 BC–2198 cal BC and 7199-6904 cal BC). Recently, *Pedrazzi et al. (2014)* discussed the ages provided by *Pérez-Torrado et al. (2011),* due to stratigraphic discrepancy. *Pérez-Torrado et al. (2011)* also dated another eruption with ^{14}C method, Mña Humilladeros, at 5100 ± 40 BP (3977- 3794 cal BC). Finally, Mña del Tesoro has been dated at 9 ka, with K/Ar isotopic method by *Rodriguez-Gonzalez et al. (2012).*

In 18th century, as reported by *Bory de St. Vincent (1803), von Humboldt (1814),* and *Darias y Padrón (1929),* strong earthquakes shook the island from March 27th to June 15th, 1793, damaging buildings and raising public alarm. However, no mention of manifestations of subaerial volcanic activity were reported. *Hernandez-Pacheco (1982*) linked the seismic activity with the Lomo Negro eruption in the NW rift, which produced a small cone and a thin lava field in the NW rift zone. Recently, this was refuted by palaeomagnetic dating (*Villasante-Marcos and Pavón-Carrasco, 2014*) and the eruption has been constrained in the XVI century.

The last eruption occurred in 2011. It was submarine, with vents located ~2 km offshore of La Restinga village (Fig. 4.36). It was preceded by an unrest period of three months during which more than 10,000 earthquakes were registered along with a vertical ground deformation up to 6 cm on the whole island (*Domínguez Cerdeña et* al., 2014*; Meletlidis et al., 2015).* The eruption started on October 10th, 2011, and lasted about five months, ending on March 5th, 2012 *(Rivera et al., 2013).* A discoloured and bubbling area appeared on the sea surface, under which a submarine cone formed, with a final accumulated volume of pyroclastic material of ca. 329×10^6 NDRE m^3. The cone summit reached the depth of 89 m b.s.l. (*Rivera et al., 2013*). A variety of volcanic materials were erupted, including the peculiar

floating “restingolites” (*Troll et al., 2012*) or “xenopumice” bombs (Fig. 4.36 a, b; *Del Moro et al., 2015*; *Meletlidis et al., 2015*), i.e. eject a consisting of an outer black to greenish, vesicular crust (1-2 cm in thickness) with basanite bulk rock composition embedding grey to white, pumiceous xenoliths with trachytic to alkali rhyolitic bulk rock composition (*Troll et al., 2012; Del Modo et al., 2015; Meletlidis et al., 2015*). The origin of these products is highly debated. According to *Troll et al. (2012),* xenolithic material came from pre-island sedimentary layers that were picked up and heated by the ascending magma. According to the interpretation of other authors, xenopumices result from the interaction (heating) between the basanite magma feeding the eruption, a stagnant trachytic magma pocket/s and an associated hydrothermally altered halo with rhyolitic composition (*Sigmarsson et al. 2012, Meletlidis et al., 2015; Del Moro et al. 2015*). *Meletlidis et al. (2015)* suggested the eruption was driven by a stepwise migration of a batch of magma from a deep reservoir to two superficial reservoirs (a crustal reservoir and a shallow conduit). Initially, the ascending magma tried to reach the surface through a low fractured zone located below the central-northern part of the island; later, it erupted off the coast of La Restinga village, 350 m b.s.l.

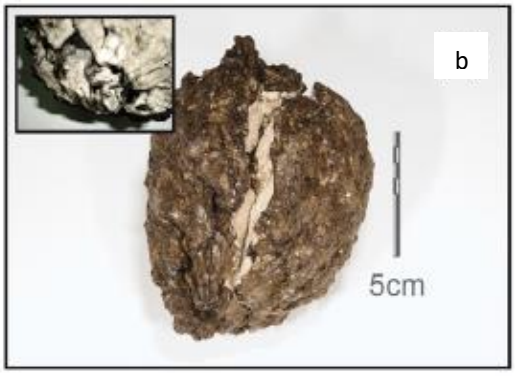

c)

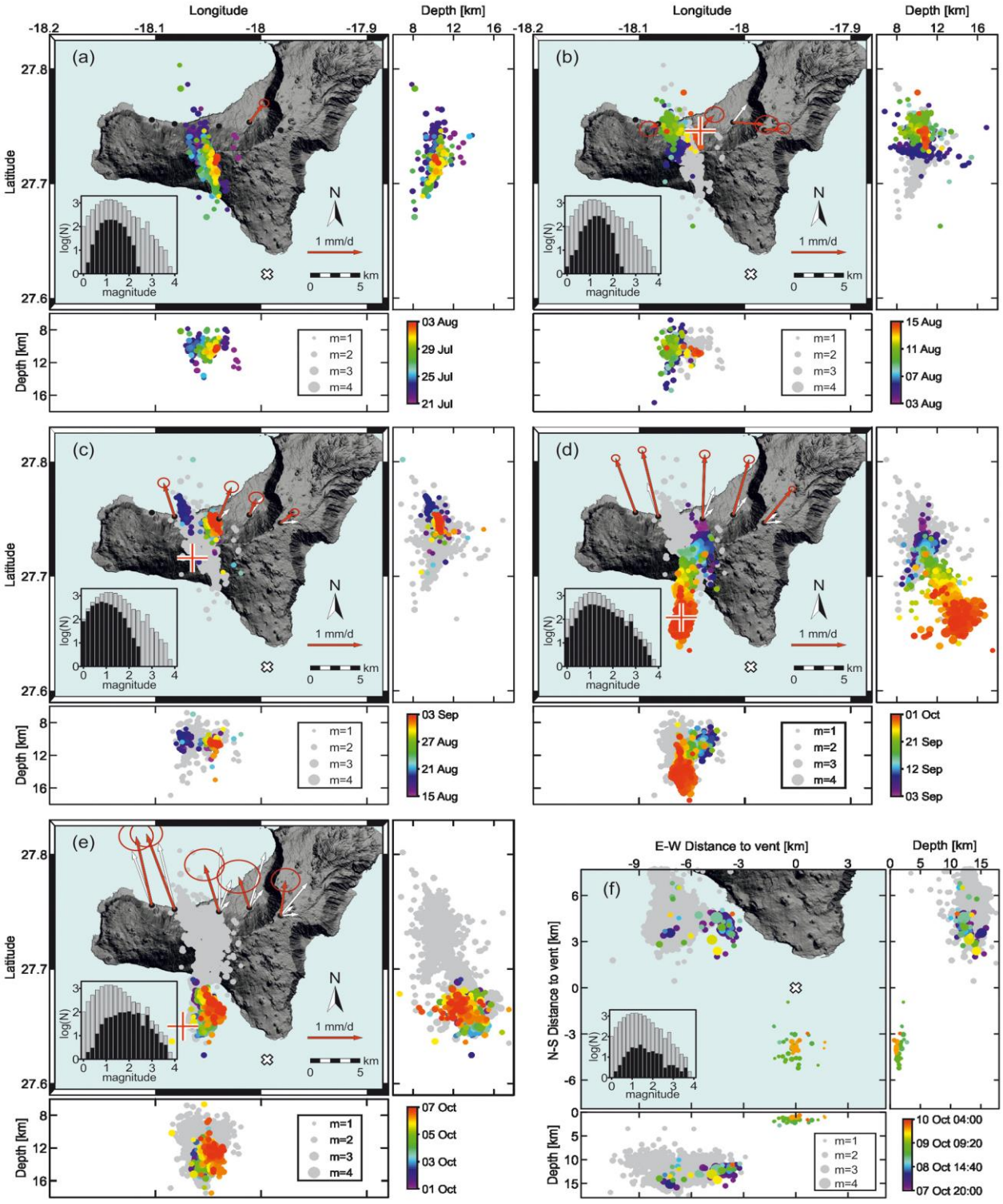

Fig. 4.36 a) Hot scoriaceous blocks and "lava balloons" floating on the sea surface emitted during the 2011-2012 eruption (from *Meletlidis et al., 2015*). (b) "coconut-like" bomb (from *Meletlidis et al., 2015*). (c) Temporal evolution of the earthquakes with magnitude >1.5 along with the evolution of the horizontal deformation registered by GPS stations during the pre-eruptive phase of 2011-2012 eruption of El Hierro Island (*Meletlidis et al., 2015 and reference therein*).

4.3.3 Studied eruptions

As described above, the monogenetic and scattered nature, as well as the poor dispersion of the deposits, of the recent eruptions in El Hierro, makes it impossible to use a relative chronology, taking advantage of dated eruptions, and the only way to obtain a chronological framework is to date one by one all the eruptions. Therefore, one of the main goals of this work is to provide new dating to fill this gap, using palaeomagnetism as a fundamental dating method.

Nine Holocene eruptions (Fig. 4.37) located along the three rifts were selected based upon on the observation of coastal platform formation and their unaltered and fresh aspect (see 4.3.2 paragraph). Furthermore, the selected eruptions are those that affected widespread sectors of the island and currently inhabited areas.

The studied eruptions were divided into three groups, according to their location in the three rift zones (Fig. 4.37): 1) El Lajal, in the SSE rift; 2) Mña Chamuscada and Mña del Tesoro in the NNE rift; 3) Orchilla, Las Calcosas and Mña Negra south of the WNW rift, and Lomo Negro, a lava flow below Lomo Negro lavas (Below Lomo Negro eruption hereinafter), and Cuchillo del Roque north to the WNW rift. For five of them (i.e. Orchilla, Las Calcosas, Mña Negra, Below Lomo Negro and Cuchillo del Roque), no ages have been determined and no other geological constraints are available (apart from the coastal platform-forming geomorphologic feature). Conversely, for four eruptions, previous age data are available. For Lajal eruption, a lower bound age is given by an Ar/Ar dating of the underlying lavas belonging to the Irama-La Restinga eruption (7±2 ka determined by *Becerril et al., 2016)*. The age of Mña Chamuscada eruption was determined by ^{14}C at 2500±70 BP by *Guillou et al. (1996)*. Mña del Tesoro has been also previously dated at 9 ka, with K/Ar isotopic method by *Rodriguez-Gonzalez et al. (2012).* Finally, Lomo Negro eruption has been considered for a long time as having occurred in 1793 AD. Recently, *Villasante-Marcos and Pavón-Carrasco (2014)* have palaeomagnetically dated the eruption, suggesting a sixteenth-century age. In addition to the palaeomagnetic dating, ^{14}C ages for two eruptions, Mña Chamuscada and Lomo Negro, are also provided in this study. Results are compared with those obtained previously on the same lava flows.

In Table 4, the location of each sampling site and independent age constraints are listed.

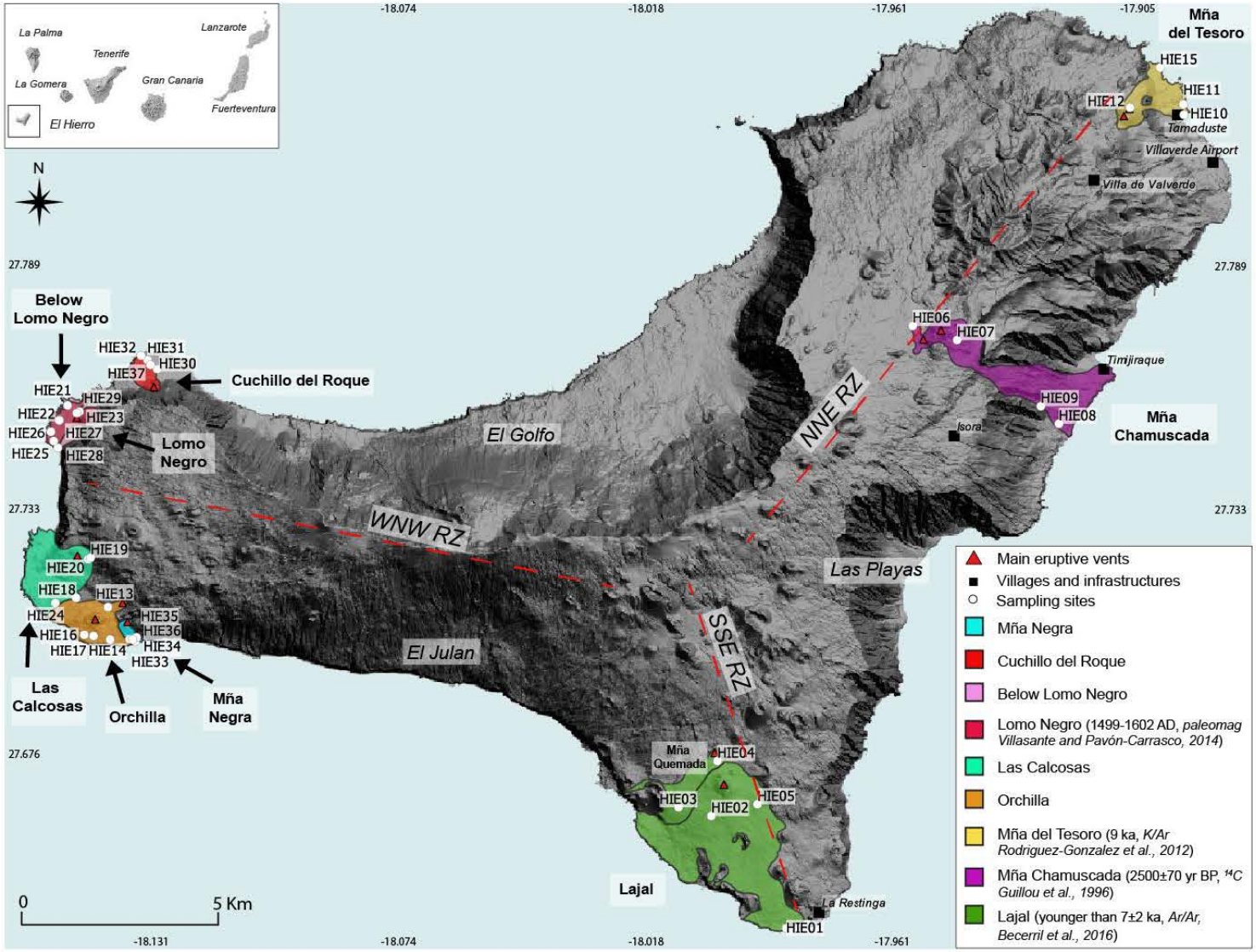

Fig. 4.37 Simplified map of El Hierro (from a DEM-shaded relief image courtesy of Instituto Geográfico Nacional - IGN) showing the studied lava flows and the sites of palaeomagnetic sampling.

Table 4. Location of the Sampling Sites at El Hierro and Independent Age Constraints from Geochronologic or Geologic Evidence.

Volcanic Unit	Code	Locality	Latitude, °N	Longitude, °W	Alt. (m a.s.l.)	Age Constraint
Lajal	HIE01	La Restinga	27°38'18.80''	17°59'7.10''	5	Younger than 7±2 ka (Ar/Ar, *Becerril et al., 2016)*
	HIE02	HI-410	27°39'51.4''	18°00'09.0''	279	
	HIE03	HI-410	27°39'58.5''	18°00'36.1''	233	
	HIE04	Mña Quemada	27°40'36.7''	18°00'04.0''	414	
Mña Chamuscada	HIE05	HI-4	27°40'01.0''	17°59'30.9''	350	794-428 cal BC (recalibrated ^{14}C age*, Guillou et al., 1996*)
	HIE06	HI-10	27°46'36.8''	17°57'21.8''	1036	
	HIE07	HI-1	27°46'25.1''	17°56'45.1''	1017	
	HIE08	HI-30	27°45'16.1''	17°55'21.0'	75	
	HIE09	Calle Jirdana	27°45'30.5''	17°55'35.9''	209	
Mña Del Tesoro	HIE10	near El Picacho (Tamaduste)	27°49'31.2''	17°53'37.7''	1	9 ka (K/Ar*, Rodriguez-Gonzalez et al., 2012)*
	HIE11	Playa del Salto	27°49'39.7''	17°53'38.1''	1	
	HIE12	pit crater	27°49'37.6''	17°54'22.21''	369	
	HIE15	Playas de las Puentes	27°50'10.1''	17°53'57.4''	0	
Orchilla	HIE13	fissural eruption	27°42'43.8''	18°08'27.6''	146	
	HIE14	HI-503	27°42'17.0''	18°08'25.8''	66	
	HIE16	near Orchilla Lighthosue	27°42'20.9''	18°08'47.2''	123	
	HIE17	HI-503	27°42'20.0''	18°08'39.5''	107	

Las Calcosas	HIE18	unpaved road near HI-503	27°42'51.4''	18°08'53.9''	101	1499-1602 AD (palaeomagnetism, *Villasante-Marcos and Pavón-Carrasco, 2014*)
	HIE19	HI-503	27°43'24.6''	18°08'41.9''	246	
	HIE20	near HI-503	27°43'23.4''	18°08'44.0''	274	
Lomo Negro	HIE24	near Monumento Meridiano Cero	27°42'47.2''	18°09'11.1''	39	
	HIE21	near the coast	27°45'31.1''	18°09'01.0''	20	
	HIE22	lava field	27°45'18.9''	18°09'07.9''	44	
	HIE23	HI-502	27°45'24.8''	18°08'53.3''	55	
	HIE25	near La Punta del Berodal	27°45'01.7''	18°09'12.4''	22	
Below Lomo Negro	HIE26	near La Playa de Cueva Honda	27°45'09.4''	18°09'14.8''	12	
	HIE27	lava field	27°45'18.8''	18°09'07.8''	40	
	HIE28	near La Punta del Rancho	27°44'56.1''	18°09'09.0''	7	
Cuchillo Del Roque	HIE29	HI-502	27°45'26.0''	18°08'51.1''	54	
	HIE30	near HI-500	27°46'01.2''	18°07'47.0''	20	
	HIE31	lava field	27°46'08.7''	18°07'54.9''	10	
	HIE32	near El Veril	27°46'12.2''	18°08'00.2''	10	
	HIE37	lava field	27°46'04.6''	18°07'52.5''	6	
Mña Negra	HIE33	HI-503	27°42'17.4''	18°08'09.8''	33	
	HIE34	HI-503	27°42'17.1''	18°08'07.1''	34	
	HIE35	near El Varadero de Juan Baltasar	27°42'15.7''	18°08'05.00''	11	

HIE36	near the Recreational area of Muelle de Orchilla	27°42'18.8''	18°08'04.0''	16

Site coordinates were gathered by a Garmin GPS, using the WGS84 datum. The conversion of ^{14}C conventional ages (yr BP) into calendar-calibrates ages (cal yr AD-BC) was obtained by means of INTCAL13 (*Reimer et al., 2013*) terrestrial radiocarbon age calibration, with the Radiocarbon Calibration Program CALIB REV 7.1.0. (*Stuiver et al., 2020*), with corresponding uncertainties at the 2σ level. HI-4, Carrettera General La Restinga; HI-30, Carrettera Las Playas; HI-503, Carrettera La Montaña.

4.3.3.1 SSE rift zone

Lajal volcano is a Quaternary complex (*Dóniz-Páez et al., 2011*), younger than 20 ka (*Carracedo, 2008*), developed in the south rift of the island, near La Restinga village (Fig. 4.37). It comprises several cinder and scoria cones roughly aligned on a 1.2 km-long eruptive fissure. Products erupted include small scoria cones (as Mña Quemada) cinder cones and hornitos, and pyroclastic deposits (lapilli and bombs) produced by explosive activity and a large lava field showing mixed morphological features (*Dóniz-Páez et al., 2011*). In particular, the long (ca. 4,7 km from north to south) and thin lava field has both pahoehoe (Fig. 4.38a) and "aa" morphology, with several lava ponds, cascade lavas, ropy lavas (Fig.4.38e), levees, channels, tumuli and lava tubes. Lava is characterized by dark colour, abundant vesicles, and is sub-aphyric with few millimetric olivine phenocrysts. In some points near the coast, under the Lajal lava flows, older and very thick lavas occur, attributed to the Irama-La Restinga eruption, dated at 7±2 ka by *Becerril et al. (2016)*.

Five sites were sampled in Lajal lava field: HIE01, 02, 03, 04 and HIE05 (Table 4 and Fig. 4.38). HIE03 and HIE04 were sampled in the proximal and distal lava emitted by Mña Quemada vent, respectively.

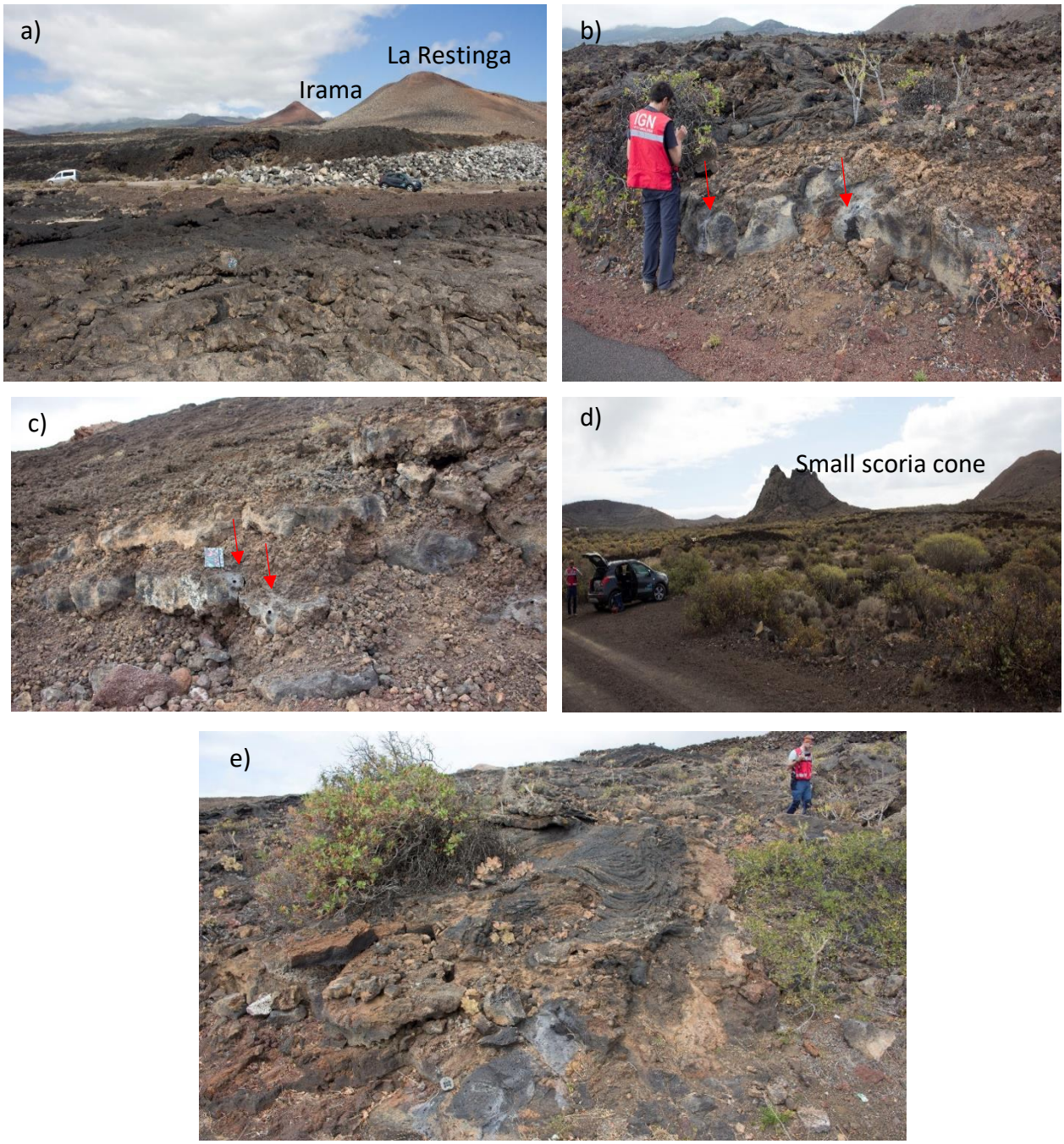

Fig. 4.38 Sampling sites of Lajal eruption. a) HIE01; b) HIE02; c) HIE03; d) HIE04; e) HIE05. Red arrows indicate sampling points.

4.4.2.2 NNE rift zone

Along the NNE rift, two lava flows, Mña Chamuscada and Mña del Tesoro, were sampled.

Mña Chamuscada eruption occurred northeast of the San Andrés village (Fig. 4.37) and consists of multiple vents from which several lava flows were emitted in different directions. West of the cones, lavas preserve lava casts of the tree trunks that were formed when a small

lava flow swept through a forested area. The main lava flow was emitted from the base of the Mña Chamuscada cone, which breached to the east, and from a spatter cone southeast of the main cone. These lavas reached the eastern coast 3,7 km away, near the Punta de Timijiraque. The eruption started with a main explosive phase, producing Mña Chamuscada cone and lapilli deposits some meters thick, above which clastogenic lavas, produced by the spatter cone southeast to the Mña Chamuscada cone, were emplaced. The lava flow shows variable degrees of welding and molten margins are still clearly visible, dark in colour, moderately vesiculated, with crystals of pyroxene and olivine. This activity continued with a large lava flow issued from the base of the breached cone. This eruption has been previously dated by *Guillou et al. (1996)* with ^{14}C at 2500 ± 70 BP (794-428 cal BC; see 4.2.4 paragraph).

Four sites were sampled: HIE06, 07, 08 and 09 (Table 4 and Fig. 4.39). In addition, two charcoals, one under a lapilli outcrop and one within the lava flow, were dated with the ^{14}C dating method.

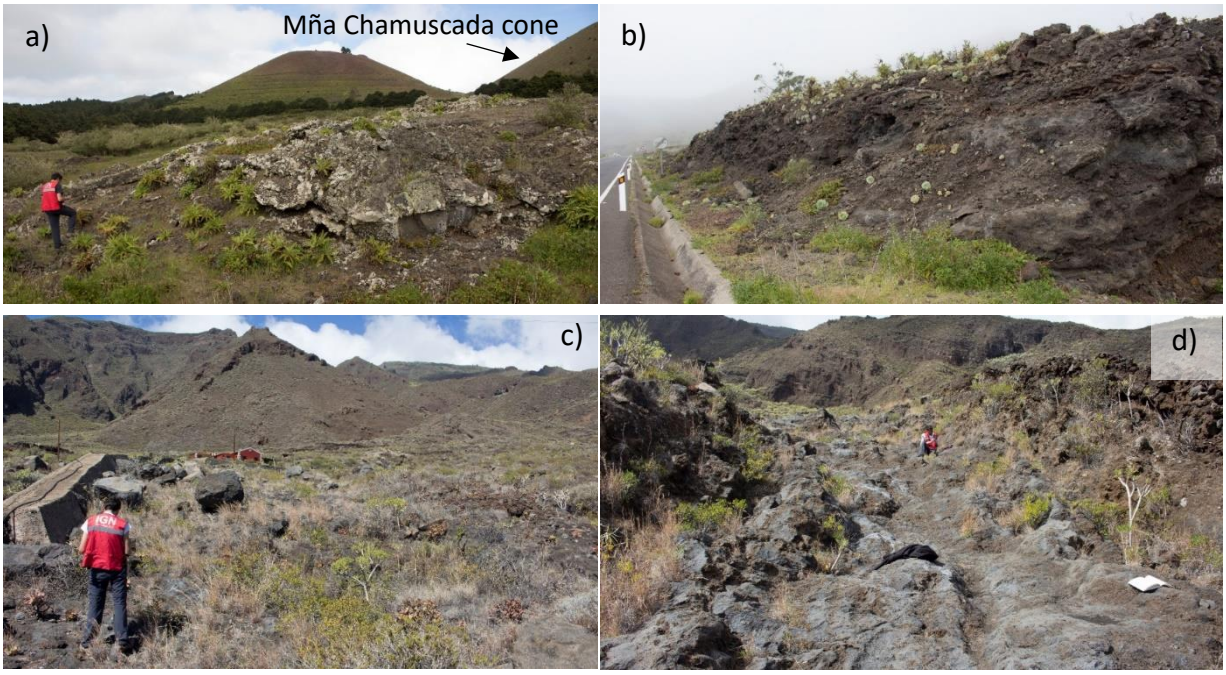

Fig. 4.39 Sampling sites of Mña Chamuscada eruption. a) HIE06; b) HIE07; c) HIE08; d) HIE09.

Mña del Tesoro edifice is located in the easternmost part of the NNE rift near the east coast (Fig. 4.37), and rests on an inclined surface near to the pre-littoral 200 m-high scarp formed by old volcanic edifices as Roque Colorado, Mña Charneta and Mña del Pico (*Dóniz-Páez et al, 2005*). The eruption produced a main scoria and ash cone formed during the explosive activity and composed of spatter and lapilli. At the base of the cone, the propagation towards the

north of the dike feeding the eruption formed a complex system of multiple and super-imposed lava flow units (*Dóniz-Páez et al., 2005*); the discharge of magma probably caused the formation of a pit crater near the cone. Lavas flowed down the palaeo-cliff, producing lava falls, chaotic surfaces with "aa" morphology and spherical boulders, in some cases 2-3 m in diameter (*Dóniz-Páez et al., 2005; Rodriguez-Gonzalez et al., 2012*). Lava is almost aphyric and non-vesicular, with a few small crystals of olivine. Pumiceous xenoliths similar to "restingolites" or "xenopumices" are recurrent. This eruption has been dated at 9 ka, using the K/Ar isotopic method, by *Rodriguez-Gonzalez et al. (2012)*.

The sites HIE10, 11 and 15 were sampled in Mña del Tesoro lava flows close to the coast, whereas HIE12 was sampled within the pit crater (Table 4 and Fig. 4.40).

Fig.4.40 Sampling sites of Mña del Tesoro. a) HIE10; b) HIE11; c) HIE12; d) HIE15. Red arrows indicate sampling points.

4.4.2.3 WNW rift zone

In the westernmost propagation of the WNW rift, six eruptions were sampled (Fig. 4.37). Three eruptions, i.e. Orchilla, Las Calcosas and Mña Negra, occurred in the southern area, while three eruptions, i.e. Lomo Negro, "Below Lomo Negro" and Cuchillo del Roque, on the north-western coast.

Orchilla eruption developed on top of the palaeo-cliff built by lavas and pyroclastic deposits of older eruptions (Mña Quemada, Mña Toscones and Mña Banco). The eruption is characterized by two eruptive fissures, the larger developed in NNE-SSW direction and the smaller in NNW-SSE direction (*Becerra-Ramírez et al., 2010*). During the eruption, two large scoria cones were built juxtaposed, with associated smaller vents and several hornitos and an NNE-SSW eruptive fracture (*Becerra et al., 2007*). The main volcanic edifice, 190 m high, is the result of multiple explosive events: it has subcircular morphology, with two craters of 576 m and 379 m in diameter. The cones are composed mainly of lapilli, bombs, ash and spatter (*Becerra-Ramírez et al., 2010*). The associated small vents produced principally spatter deposits and lava flows with pahoehoe morphology, characterized by lava channels, tubes and ropy lava. Based on their position, they can be subdivided into two groups: 1) those located south of the main cone, with larger size, generated by an NNW-SSE trend eruptive fissure; 2) those located in the NNE flank of the Orchilla cone, produced by an NNE-SSW fracture, principally constituted of hornitos and small cones. The NE trend eruptive fissure produced 25 small eruptive vents and 16 hornitos and occurred before the formation of the main cone, due to the presence of Orchilla tephra above some lavas emitted by hornitos (*Becerra-Ramírez et al., 2010*). Lava is moderately vesiculated, with few olivine and pyroxene crystals of small size (in some cases of 5 mm). This eruption has never been dated, and only a generic Holocene indication has been provided (*Carracedo, 2008).* At some sites, seafood remains left by aboriginal occur inside natural cavities like lava caves and tunnels.

Four sites were sampled in this lava field: HIE13 was sampled near the NE eruptive fissure; HIE14 and HIE17 along roadcuts and, finally, HIE16 was sampled in a spatter sequence within a hornito (Table 4 and Fig. 4.41).

Just north of the Orchilla flow, another volcanic eruption, ***Las Calcosas***, was produced by a NE-SW eruptive fissure. The explosive activity produced a ca. 300 m high scoria cone with a double crater: the larger crater is ca. 170 m wide and the smaller is ca. 50 m in diameter. Lava flows with pahoehoe morphology were emitted both from the base of the main cone breached to the east and by several hornitos located along the eruptive fissure. The lava flow thickness varies from 1 to 3 m in the sampled sites. It is moderately vesiculated, with bubbles of 4-5 mm in diameters, and it is sub-aphyric, bearing few visible crystals of olivine and pyroxene. Above the lava flows some seafood remains left by aboriginal people were found.

Orchilla and Las Calcosas do not show strong differences in the degree of erosion or vegetation and their contact is not visible: the stratigraphic contact occurs in a channel cut between the two eruptions and is covered by alluvial deposits.

In this eruption, four sites were sampled (Table 4 and Fig. 4.42), of which HIE19 and HIE20 were collected in lavas produced by hornitos east of the cone, whereas HIE18 and HIE24 in the lateral propagation of lava flow toward the south.

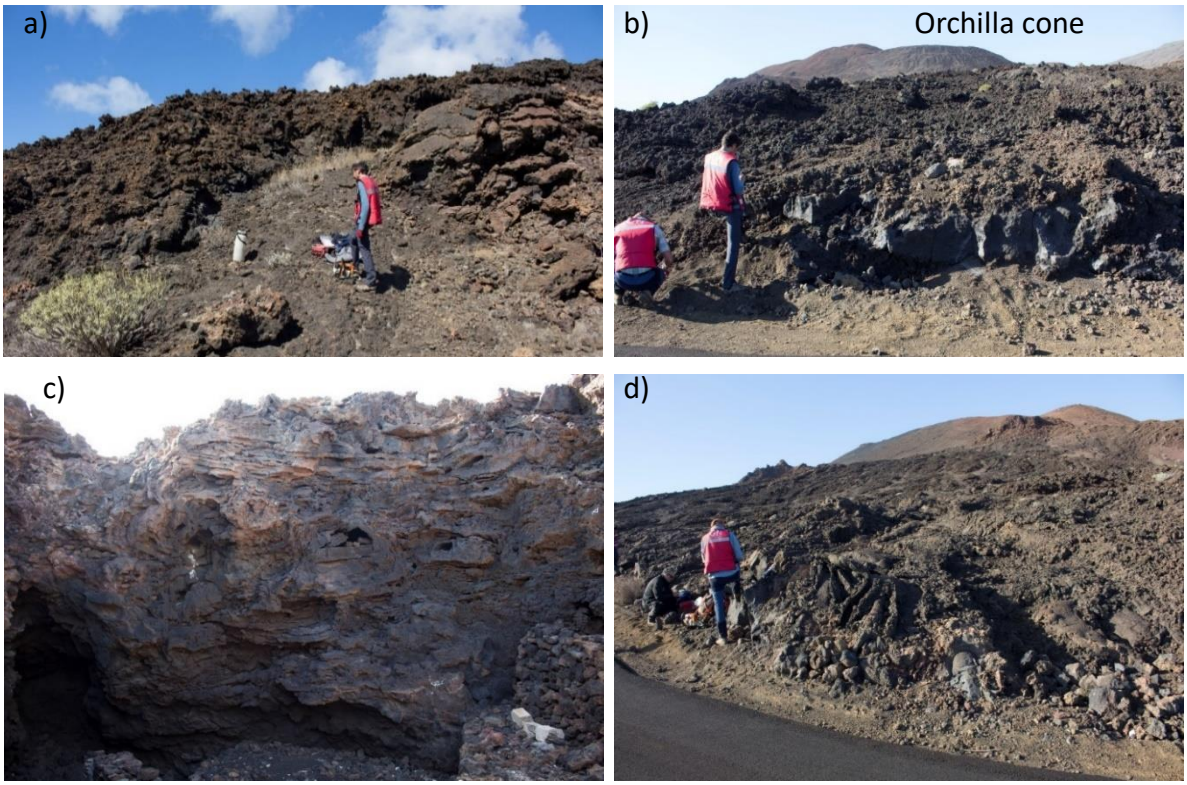

Fig. 4.41 Sampling sites of Orchilla. a) HIE13; b) HIE14; c) HIE16; d) HIE17.

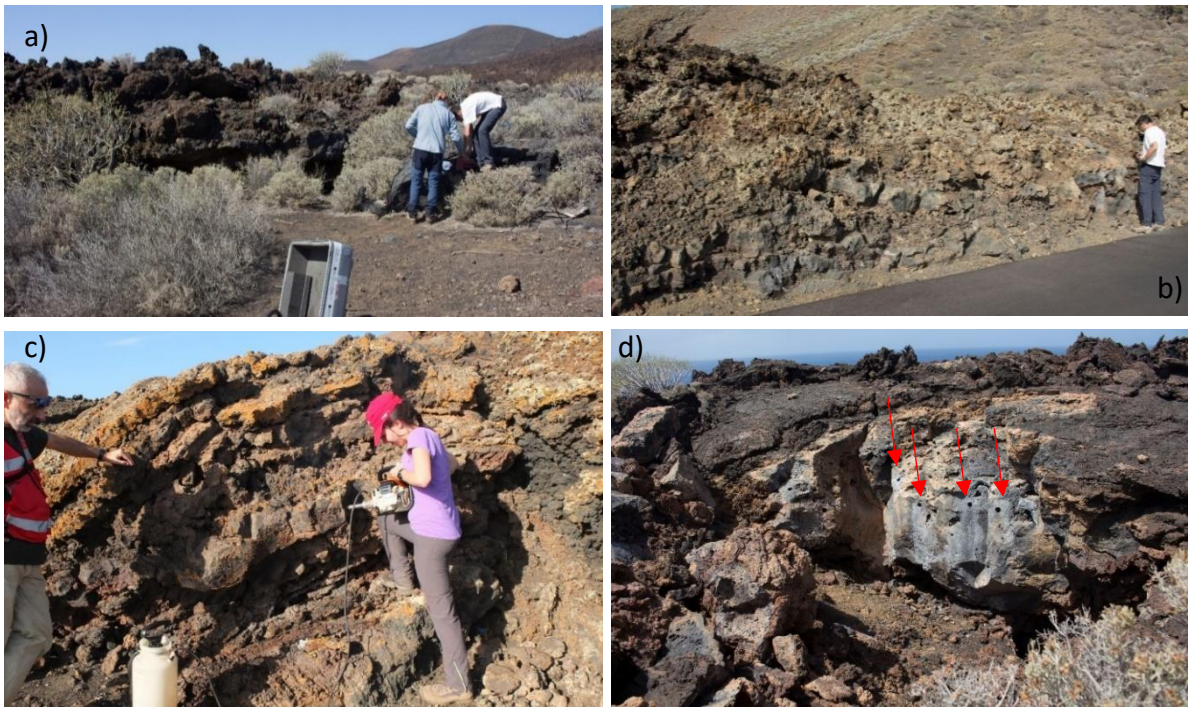

Fig. **4.42** Sampling sites of Las Calcosas. a) HIE18; b) HIE19; c) HIE20; d) HIE24. Red arrows indicate sampling points.

Mña Negra produced a small monogenic eruption south of the old eruptive fissure of Calderotón de la Higuera and east to the Orchilla cone. The volcanic edifice consists of a small cone of ca. 60 m in diameter, open to the south, and two thin and short lava flows, one emitted southwestward and one southward, both reached the south coast 550 m away. Small crystals of olivine are visible. Lava flows show freshness of the outcrops, without erosion and/or alteration as well as vegetation, suggesting a very young age. Between Mña Negra and Orchilla, a small gorge, El Estancadero, is filled by alluvial deposits; therefore, the contact between the two flows is not clear. No ages are available for this eruption.

Four sites were selected (Table 4 and Fig. 4.43), two sites (HIE33 and HEI34) along roadcuts, one near the coast (HIE35) and one (HIE36) in the recreational area of Muelle de Orchilla.

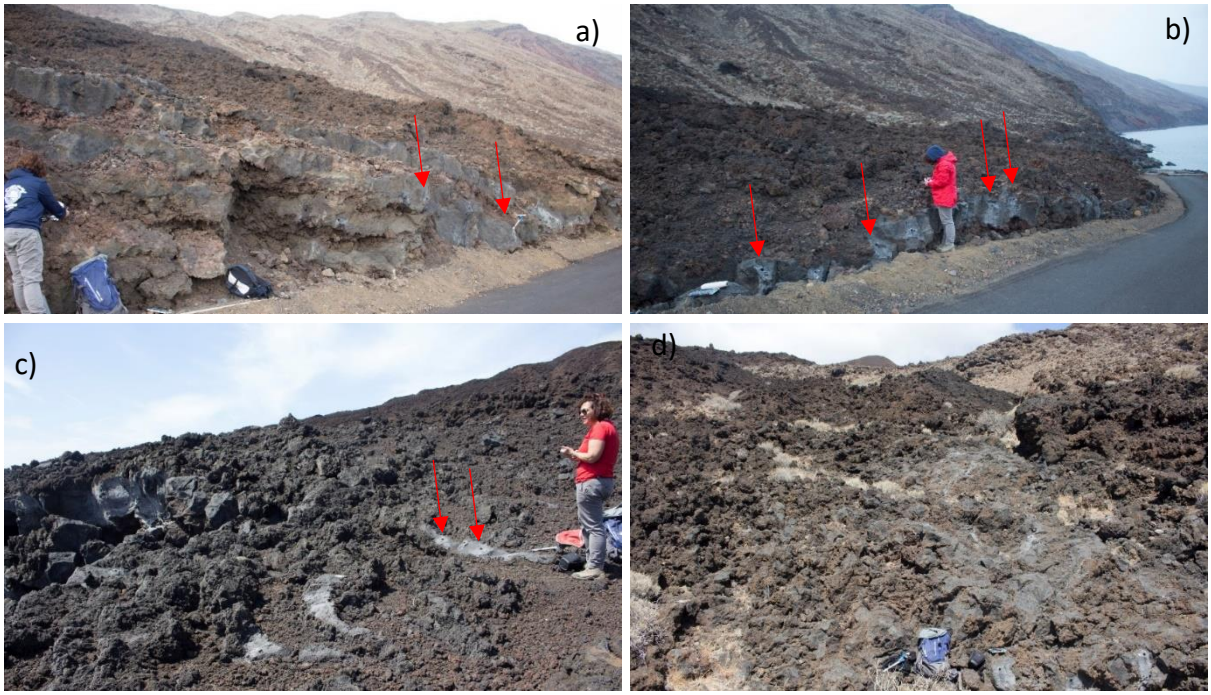

Fig. 4.43 Sampling sites of Mña Negra. a) HIE33; b) HIE34; c) HIE35; d) HIE36. Red arrows indicate sampling points.

The **Lomo negro** eruption (Fig. 4.44) occurred on the northwest termination of the NW rift, close to the older Mña Los Charcos cone. The edifice of Lomo Negro is not well preserved and was partially dismantled during the construction of the HI-500 road. The eruption includes the pyroclastic cone built along the cliff wall and a short eruptive fissure with NW-SE trend, from which abundant lava flows were emitted from a hornito. Lava flows, dark in colour and moderately vesiculated, are a few decimetres thick and have pahoehoe flow features. Lavas are also rich in olivine and pyroxene crystals several millimetres in size. Before entering the sea, at some points, lava flows from Lomo Negro created lava falls. The eruption produced 2 million m^3 of lava, with an extension of 0.54 km^2 (*Martín et al., 1987*). Initially, this eruption was related to the seismic crisis in 1793 AD reported by historical documents (*Darias y Padrón, 1929*). *Hernandez-Pacheco (1982)* dated it at ~1800 AD, both with ^{14}C dating of organic matter (it was chemically altered by volcanic gasses) found below Lomo Negro products and with the presence of aboriginal seafood remains in natural cavities underlying the Lomo Negro lava flows and not in Lomo Negro products. However, other authors, such as *Bravo (1968)* and *Carracedo et al. (2001),* proposed that this seismic crisis ended in a submarine eruption. Recently, *Villasante-Marcos and Pavón-Carrasco (2014*) palaeomagnetically sampled the eruption in six outcrops for a total of 30 cores, obtaining a palaeomagnetic direction: D= 4.1°,

I=44.4° and α_{95}= 2.8°. The palaeomagnetic direction provided three possible palaeomagnetic ages: 115 BC-7 AD, 410-626 AD, and 1499-1602 AD. Moreover, they recalibrated the ^{14}C age of *Hernandez-Pacheco (1982),* obtaining an age of 1625 AD. Therefore, they suggested that the Lomo Negro eruption occurred in the XVI century AD.

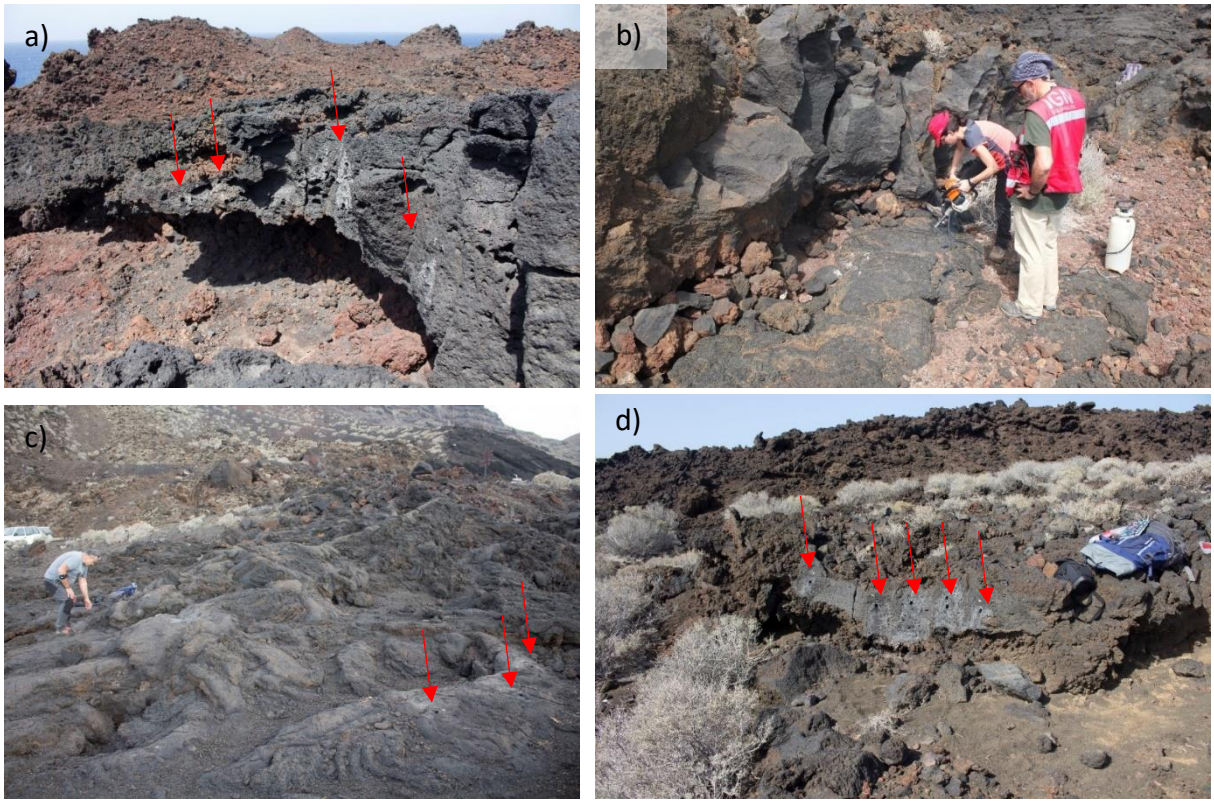

Fig. 4.44 Sampling sites of Lomo Negro. a) HIE21; b) HIE22; c) HIE23; d) HIE25. Red arrows indicate sampling points.

"Below Lomo Negro" products are distinguished from Lomo Negro lavas in colour, thickness, and morphological aspect. Lava is reddish, with scarce vesicles and generally aphyric texture except for some outcrops in which rare small crystals of pyroxene and feldspar occur. The emission point for these lavas is difficult to recognize because they are covered by the products of the Lomo Negro eruption. Below Lomo Negro, lavas form a very thick sequence, which near the coast is ca. 20 m in thickness, with characteristic columnar jointing. These lavas form a coastal platform, on which the following Lomo Negro eruption lies.

No previous studies are available for this eruption. The only datum is given by *Hernandez-Pacheco (1982),* who noted the presence of aboriginal seafood remains in natural cavities. According to *Carracedo et al. (2001)* and *Carracedo (2008)*, it can be considered as occurred,

due to the formation of the coastal platform, so therefore after the last glacial maximum termination (<12 ka).

Four sites were sampled in these lavas: HIE26, 27, 28 and HIE29 (Table 4 and Fig. 4.45).

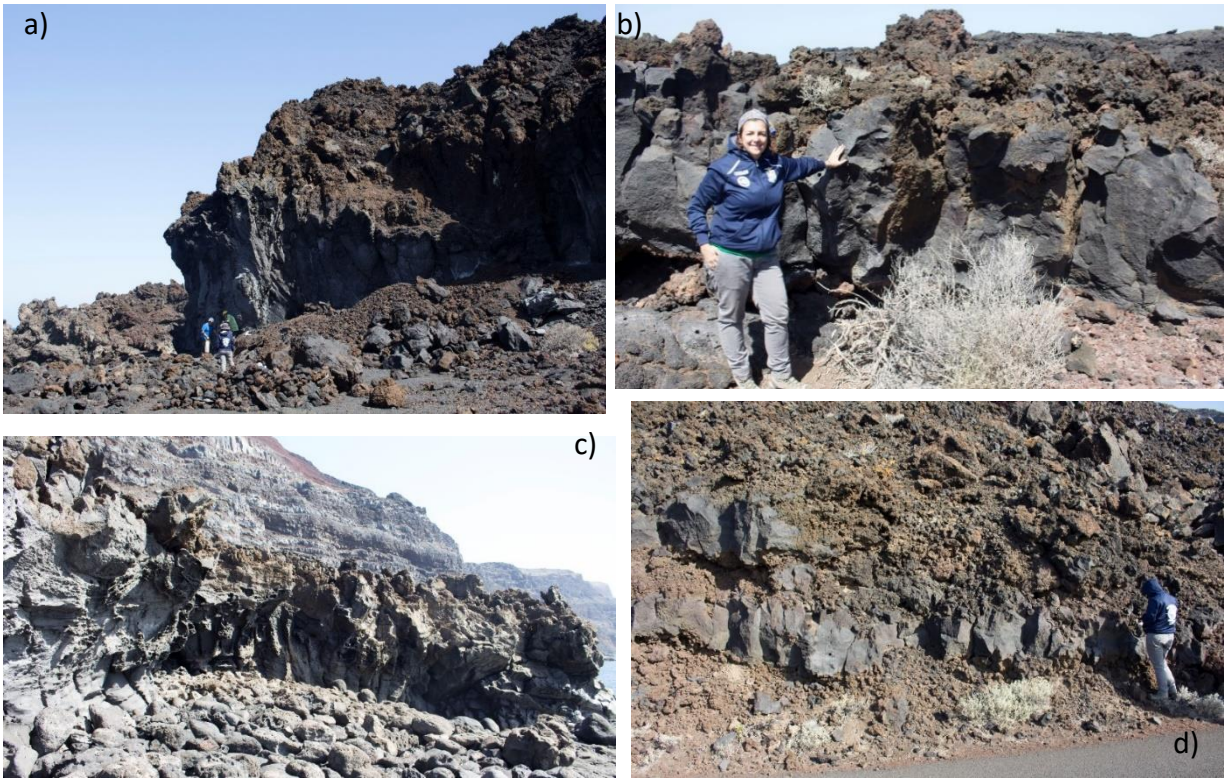

Fig.4.45 Sampling sites of Below Lomo Negro. a) HIE26; b) HIE27; c) HIE28; d) HIE29.

The last sampled eruption is **Cuchillo del Roque**, a small eruption that occurred 1.5 km northeast of the Lomo Negro site. The eruption produced an irregular scoria cone of ca. 160 m in diameter, slightly elongated toward the northwest and from which a main lava flow, ca. 600 m long and 600 m wide, was emitted. Lava is reddish in colour, aphyric, with "aa" morphology, and 2-3 m thick. No previous age data are available but, based on *Carracedo et al. (2001)* and *Carracedo (2008),* it can be considered a Holocene eruption.

Four sites were sampled: HIE30, 31, 32, and HIE37 (Table 4 and Fig. 4.46).

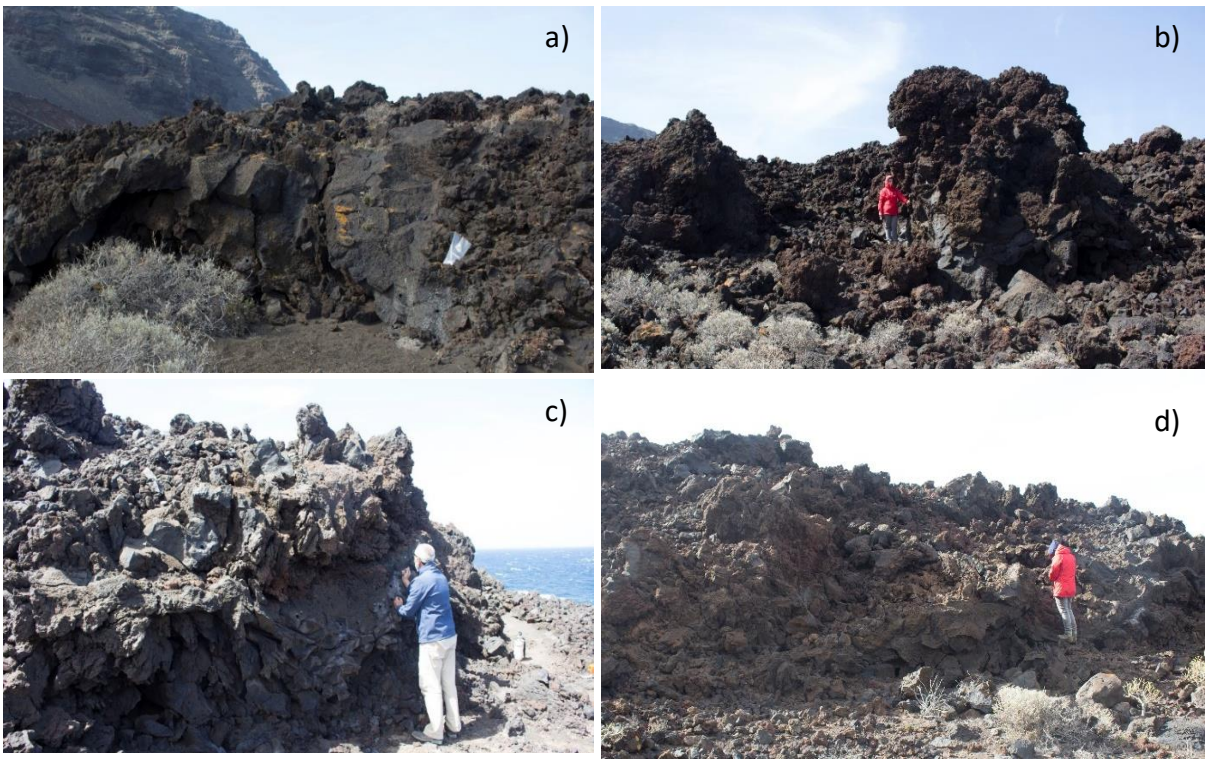

Fig. 4.46 Sampling sites of Cuchillo del Roque. a) HIE30; b) HIE31; c) HIE32; d) HIE37.

4.3.4 Sampling and Methods

Field work was carried out during March 2019, sampling 4 sites per flow (except for the Lajal eruption, in which 5 sites were collected), for a total of 37 sites (369 oriented cores). At each site, 9-10 cores have been drilled. The local magnetic field declination at El Hierro (D=-5°, extrapolated by the International Geomagnetic Reference Field model - IGRF (https://www.ngdc.noaa.gov/geomag/calculators/magcalc.shtml#igrfwmm) has been compared with the sun and magnetic compass readings, yielding declinations varying at the sampling points from -18.6° to 7.9° (-4.5° on average), suggesting the lack of significant regional magnetic anomalies.

For each specimen, demagnetization steps, experimental measurements, site and flow-mean directions, data diagrams and projections and principal component analysis procedure are the same as described in 4.2.4 paragraph.

For each sample, the Q Königsberger ratio (*Kono, 2015*) was also calculated. At El Hierro, the Earth's magnetic field total intensity was 38,258 nT in March 2019 (according to the IGRF model).

The charcoals sampled in Lomo Negro and in Mña Chamuscada lava flows were analysed by Beta Analytic Inc., Miami, USA. The dates were converted to calendar years BP as described in 4.2.4 paragraph.

Finally, the palaeomagnetic ages were evaluated using input age windows relying both on stratigraphic evidence and, when available, on ^{14}C age constraints.

4.3.5 Results

4.3.5.1 Magnetic Properties

The k-T curves (Fig. 4.47) show three principal behaviours: 1) four specimens (HIE0401, HIE0701, HIE1706 and HIE3406) display in the heating curves T_c of 580°C; 2) two specimens - HIE1210 and HIE2005- show an inflection at 150 °C and 350°C, respectively, and a drop at 580 °C; 3) three samples (HIE2303, HIE2607 and HIE3208) show two main drops, one at 150-200 °C and one at 580 °C. The T_c recorded by the first group is typical of magnetites and Ti-magnetites with low-Ti content; the second may indicate the presence of titanomagnetites with different amount of titanium; finally, the third group is likely formed by a mix of titanomagnetites rich in titanium and magnetites. Finally, all sampled (except for HIE1210) yield an irreversible behaviour with a substantial enhancement of magnetic susceptibility in the cooling curve, except for HIE0701 in which there is a reduction of magnetic susceptibility.

The hysteresis properties (Fig. 4.48) reported on the Day-plot diagram (*Dunlop, 2002*) show M_{rs}/M_s comprised between 0.4 e 0.08 and B_{cr}/B_c values between 1.0 and 5.8. Samples are mainly clustered on the SD-MD mixing curve of the magnetite, and few samples in the PSD domain along the titanomagnetite (TM60) curve.

Samples show NRM values ranging between 2 and 101 A/m, 15.6 A/m on average; k values are comprised between 1×10^{-3} and 7×10^{-2}, 2×10^{-2} on average. Therefore, samples fall on Q slope lines (Fig. 4.49) between 1 and 100, mainly clustered between 10 and 100 Q slope lines.

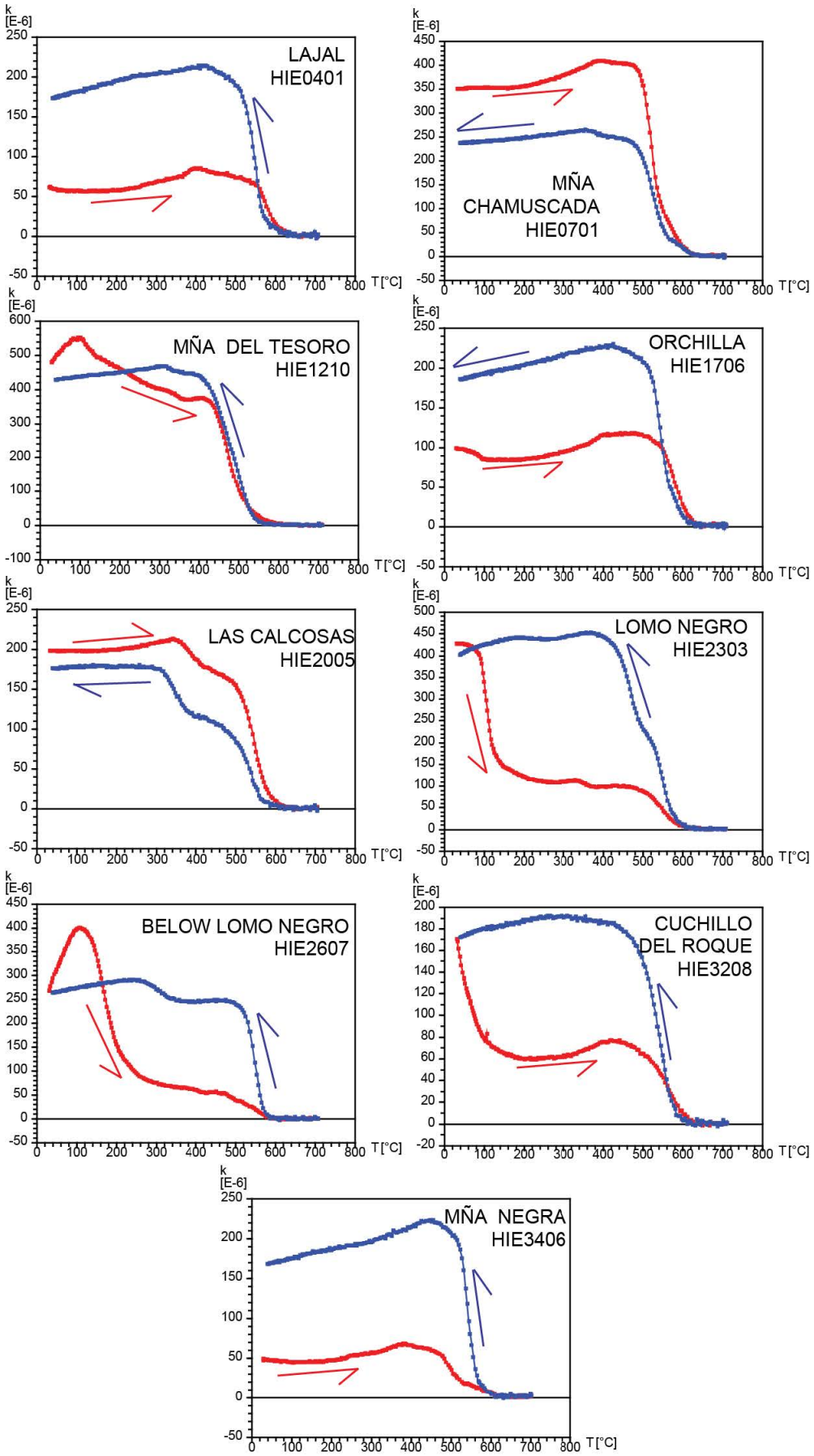

Fig. 4.47 Representative k-T curves. k is the magnetic susceptibility and T is the temperature (°C). Curves represent the heating (red curve) and cooling (blue curve) cycles.

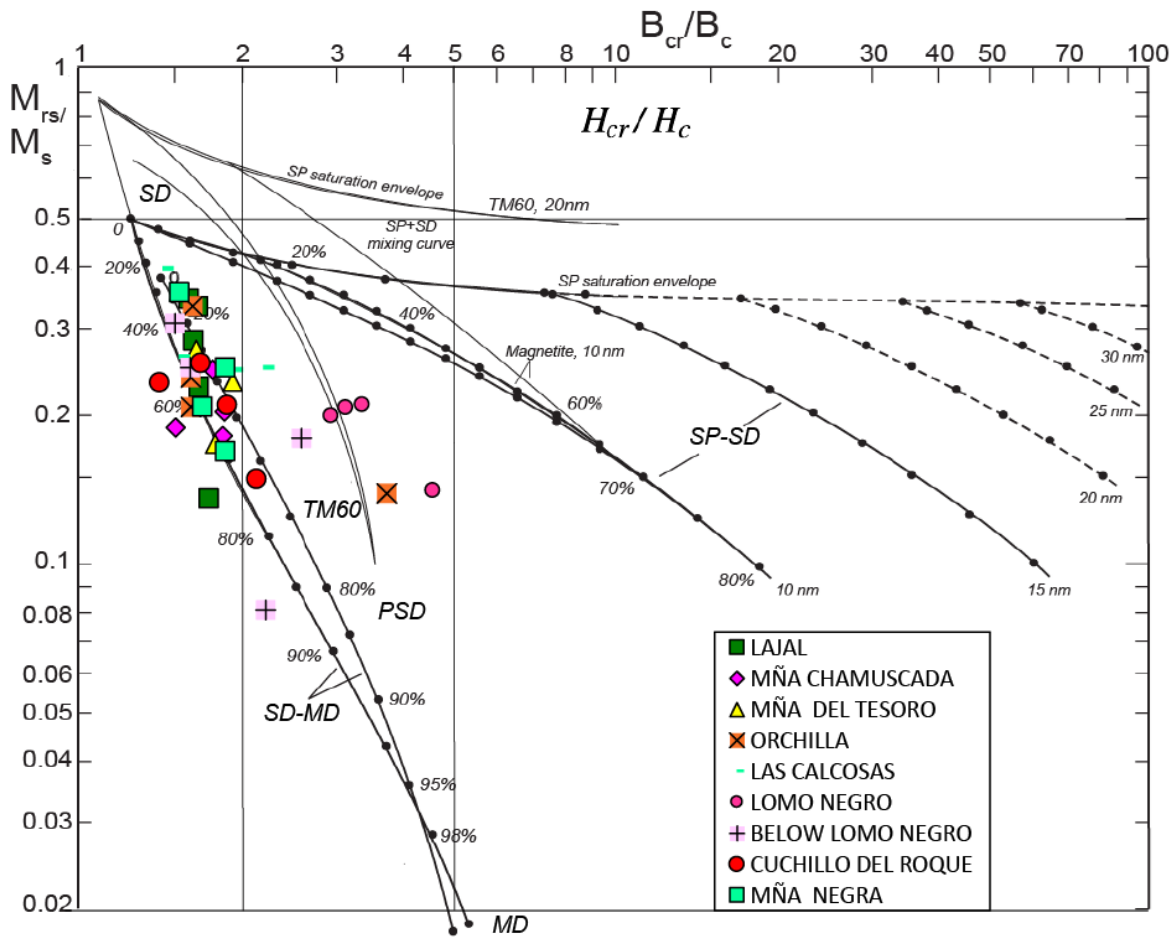

Fig. 4.48 Mrs/Ms versus Bcr/Bc (modified by *Dunlop, 2002*). SD, single domain; MD, multidomain; PSD, pseudo-single domain; SP, super-paramagnetic. TM60, titanomagnetite ($Fe_3 - xTi_xO_4$) with composition x=0.6.

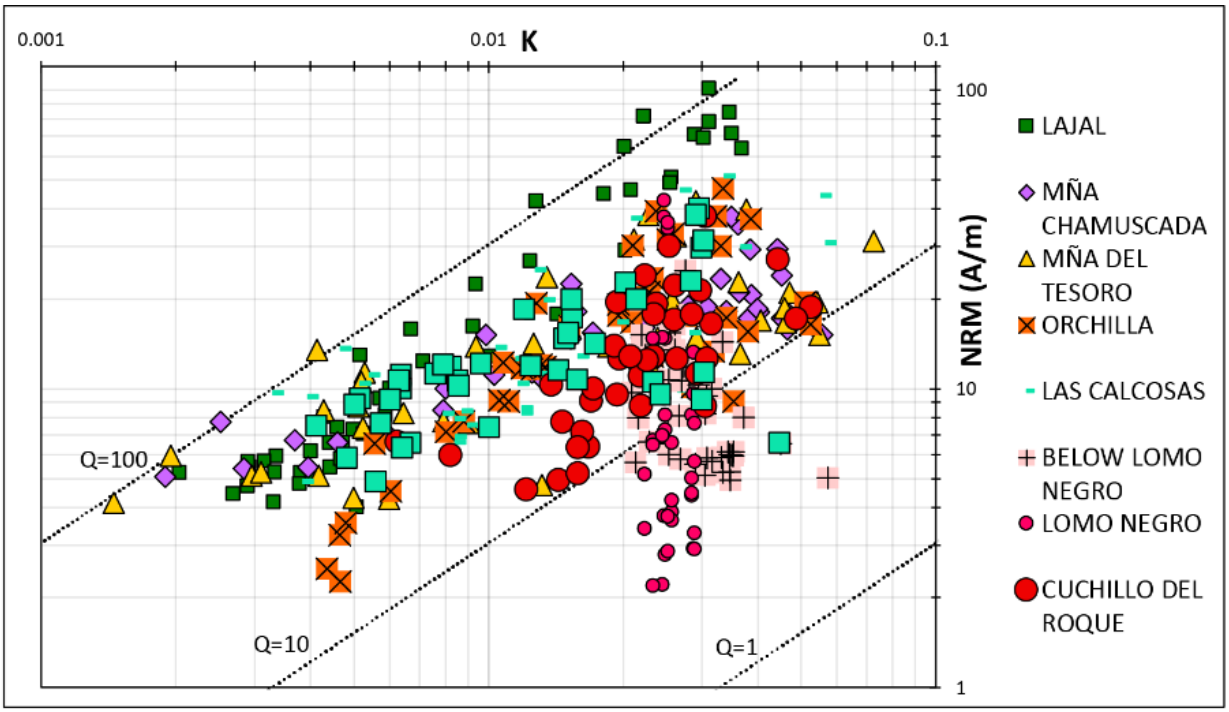

Fig. 4.49 NRM intensity vs. magnetic susceptibility values for all samples from El Hierro; sloping Q (Königsberger ratio) lines are calculated for a local geomagnetic field intensity of 38,2580 nT.

4.3.5.2 Palaeomagnetic directions

A viscous magnetic component was eliminated at 20-30 mT, and the ChRM direction was isolated for almost all samples in the 40-120 mT AF interval. In Fig. 4.50, one orthogonal diagram for each lava flow is shown. Generally, samples are characterized by low coercivities, and 90% of the demagnetization occurs between 70-100 mT. In Fig. 4.51a sample-mean and site-mean directions from each flow are shown.

Three sites (i.e. one for Orchilla -HIE13 site, one for Lomo Negro -HIE23 site, and one for Mña Negra -HIE33 site) have been discarded because their palaeomagnetic directions are far (angular distance >8°) from the others of the same flow. For Lomo Negro eruption, two comparisons were carried out: the first was gained comparing sample-mean palaeomagnetic directions obtained in this work and the site-mean palaeomagnetic direction of *Villasante-Marcos and Pavón-Carrasco (2014*) (Fig. 4.51a), and the second between site-mean palaeomagnetic directions of this work and each *Villasante-Marcos and Pavón-Carrasco (2014*) site (Fig. 4.51b). Figures show that the palaeomagnetic directions overlap and consistent among them.

Site-mean declinations (Table 5 and Fig. 4.52) vary from 345.7° to 19.6° (HIE28-Below Lomo Negro, and HIE11-Mña del Tesoro, respectively), while inclinations are comprised between 21.4° and 50.0° (HIE27-Below Lomo Negro and HIE23-Lomo Negro, respectively); α_{95} values vary from 2.5° to 8.3° (HIE05-Lajal and HIE15- Mña del Tesoro, respectively), 4.3° on average. As is clear in Fig. 4.52, four eruptions (Orchilla, Las Calcosas, Mña Negra and Mña Chamuscada) show overlapping mean palaeomagnetic directions, whereas for the others five yield distinctive declination and inclination values.

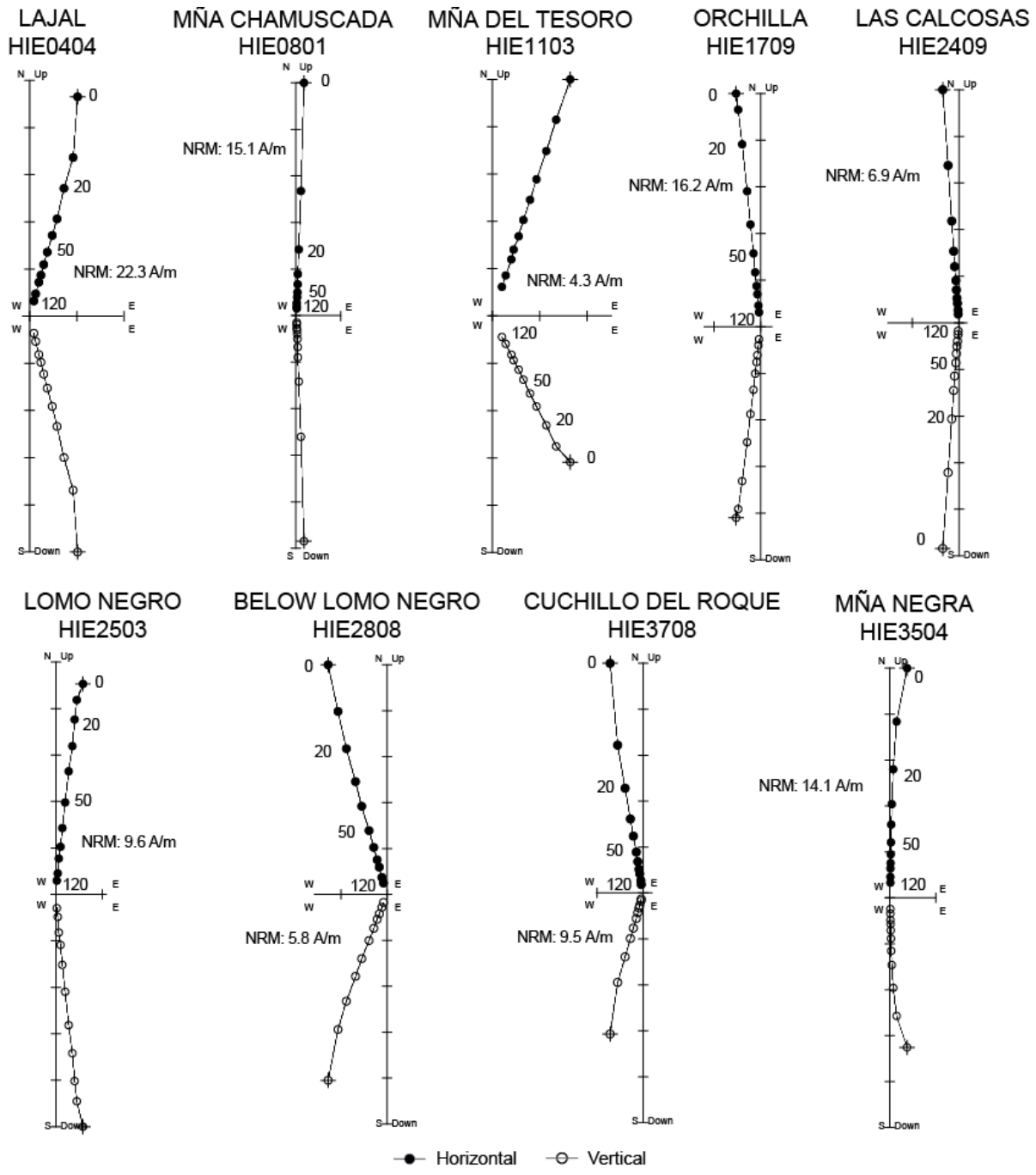

Fig. 4.50 Representative Zijderveld diagrams of typical demagnetization data, in situ coordinates. White and black dots represent projections on the vertical and horizontal planes, respectively. AF Demagnetization step values are in mT.

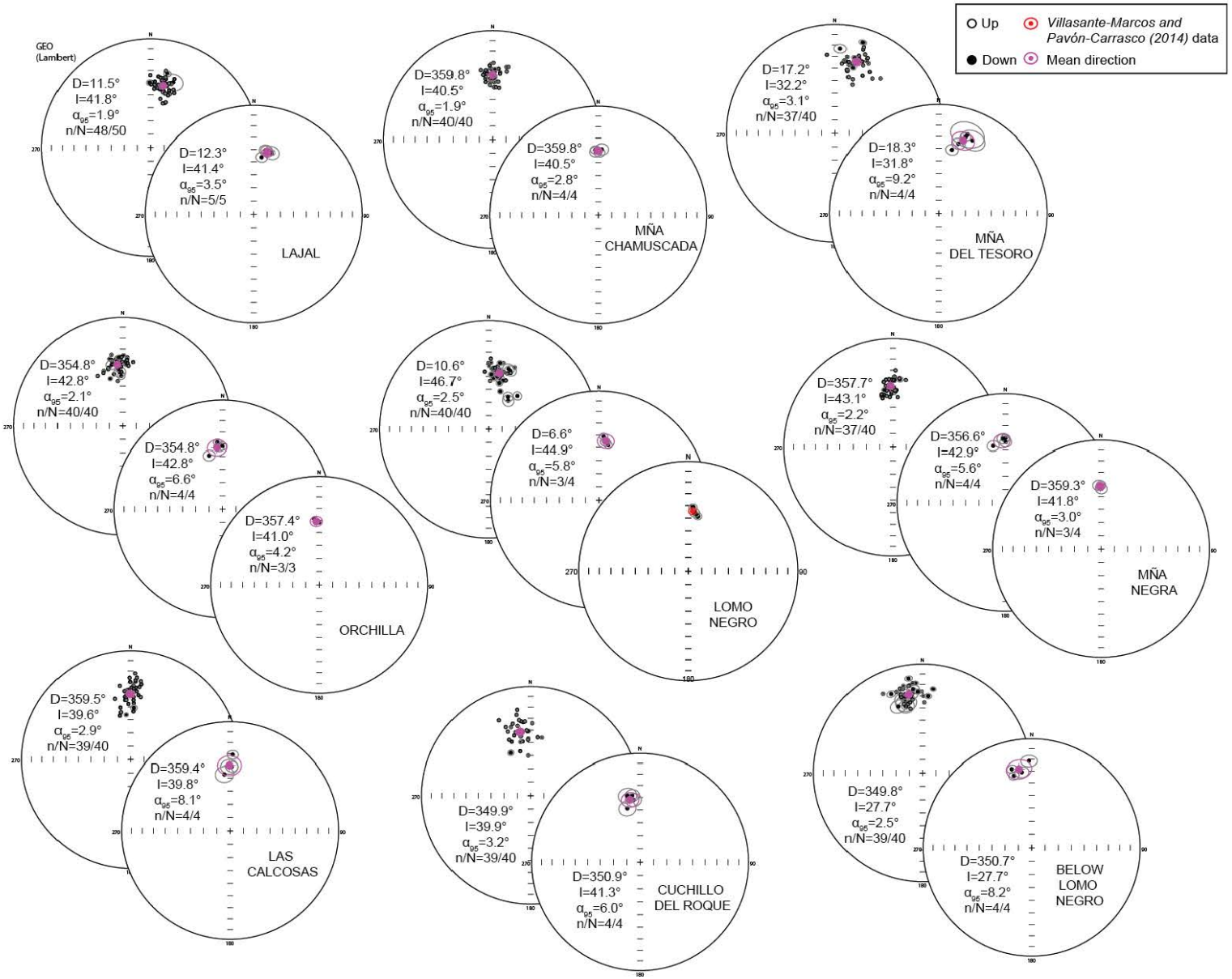
Up
Down
Villasante-Marcos and Pavón-Carrasco (2014) data
Mean direction
GEO (Lambert)
D=11.5° I=41.8° α95=1.9° n/N=48/50
D=12.3° I=41.4° α95=3.5° n/N=5/5
LAJAL
D=359.8° I=40.5° α95=1.9° n/N=40/40
D=359.8° I=40.5° α95=2.8° n/N=4/4
MÑA CHAMUSCADA
D=17.2° I=32.2° α95=3.1° n/N=37/40
D=18.3° I=31.8° α95=9.2° n/N=4/4
MÑA DEL TESORO
D=354.8° I=42.8° α95=2.1° n/N=40/40
D=354.8° I=42.8° α95=6.6° n/N=4/4
D=357.4° I=41.0° α95=4.2° n/N=3/3
ORCHILLA
D=10.6° I=46.7° α95=2.5° n/N=40/40
D=6.6° I=44.9° α95=5.8° n/N=3/4
LOMO NEGRO
D=357.7° I=43.1° α95=2.2° n/N=37/40
D=356.6° I=42.9° α95=5.6° n/N=4/4
D=359.3° I=41.8° α95=3.0° n/N=3/4
MÑA NEGRA
D=359.5° I=39.6° α95=2.9° n/N=39/40
D=359.4° I=39.8° α95=8.1° n/N=4/4
LAS CALCOSAS
D=349.9° I=39.9° α95=3.2° n/N=39/40
D=350.9° I=41.3° α95=6.0° n/N=4/4
CUCHILLO DEL ROQUE
D=349.8° I=27.7° α95=2.5° n/N=39/40
D=350.7° I=27.7° α95=8.2° n/N=4/4
BELOW LOMO NEGRO

a)

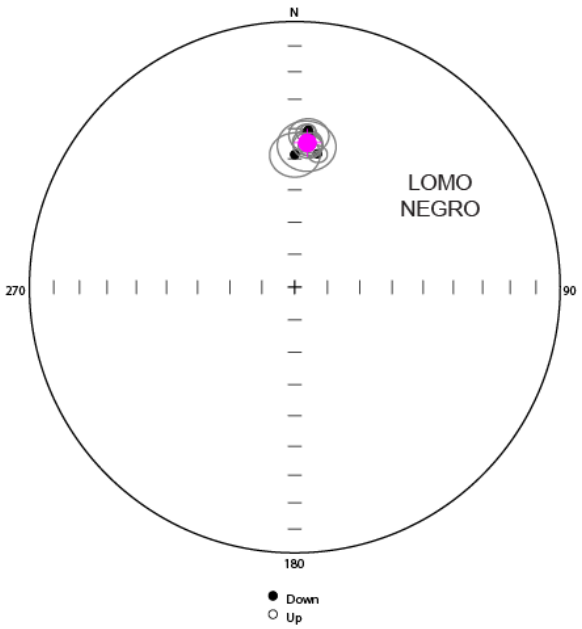

	Name	Dec	Inc	α_{95}
1	HIE21	4.2	41.3	2.8
2	HIE22	9.7	47.8	2.8
3	HIE25	6.3	45.5	3.4
4	VPLN1	5.0	44.5	4.2
5	VPLN2	4.9	40.4	2.0
6	VPLN3	5.3	42.1	5.6
7	VPLN4	4.8	45.6	8.3
8	VPLN5	0.0	48.7	7.2
9	VPLN6	5.3	45.4	4.2
	site-mean	**5.1**	**44.4**	**2.1**

b)

Fig. 4.51 a) Equal-area projection (lower hemisphere) of ChRMs, site-mean and flow-mean palaeomagnetic directions for all studied eruptions. The ellipses around the palaeomagnetic directions are the projections of the relative α_{95} cones. D, declination; I, inclination, α_{95}; statistical parameter. Red dots indicate the palaeomagnetic directions sampled by *Villasante-Marcos and Pavón-Carrasco (2014).* b) Equal-area projection (lower hemisphere) of site-mean palaeomagnetic directions for Lomo Negro eruption, including palaeomagnetic sites of *Villasante-Marcos and Pavón-Carrasco (2014)* (VPLN). Site-mean represents the mean palaeomagnetic direction obtained averaging all sites.

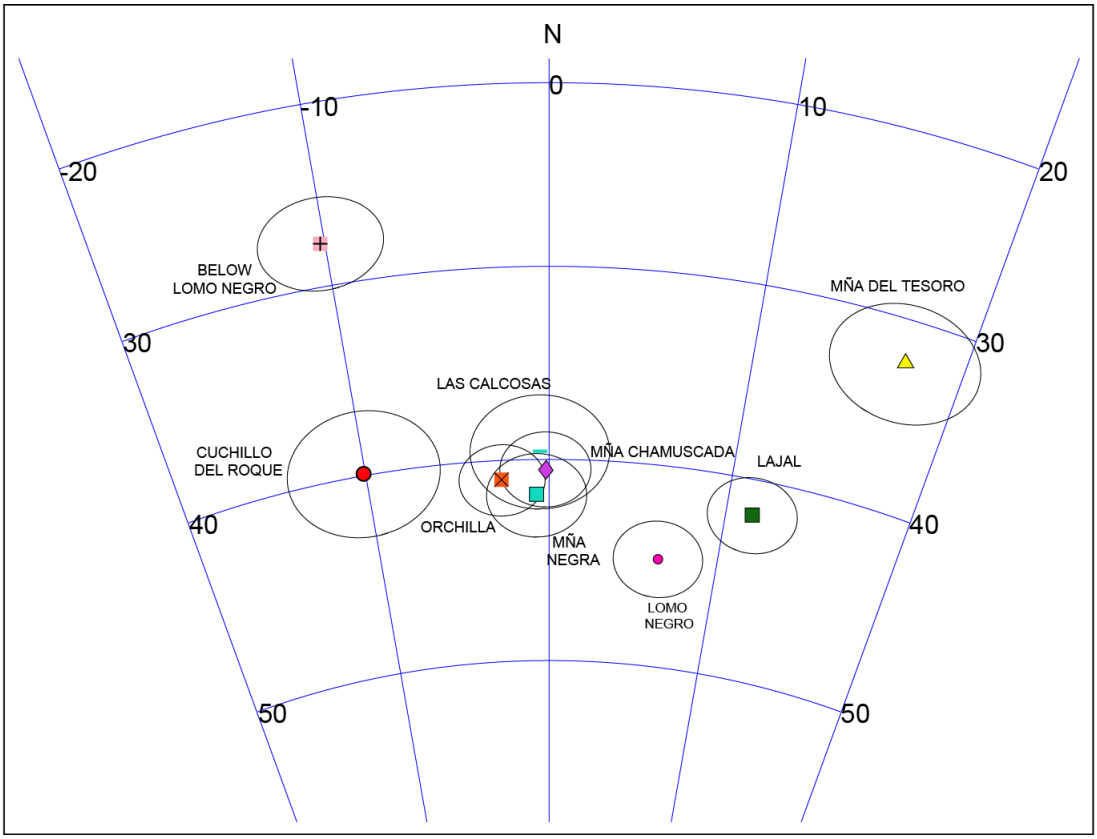

Fig. 4.52 Equal-area projection (lower hemisphere) of lava flow-mean palaeomagnetic directions from El Hierro. The ellipses around the palaeomagnetic directions are the projections of the relative α_{95} cones.

Table 5. Mean Palaeomagnetic Directions from El Hierro and Palaeomagnetically Inferred Ages.

Volcanic Unit	Code	n/N	D°	I°	k	α_{95}°	Inferred Age (BC-AD)
Lajal	HIE01	10/10	7.9	45.9	145.8	4.0	
	HIE02	7/10	16.2	40.8	131.5	5.3	
	HIE03	10/10	10.7	39.8	120.7	4.4	
	HIE04	9/10	10.8	39.7	222.7	3.5	
	HIE05	8/10	15.8	40.4	496.0	2.5	
Lajal (site mean)	HIE01+HIE02+HIE03+HIE04+HIE05	5/5	12.3	41.4	472.9	3.5	
Lajal (sample mean)		48/50	11.5	41.8	120.6	1.9	5437-5322 BC 3660-3614 BC 2330-2171 BC 1067-1048 BC 637-515 BC 522-605 AD 668-761 AD
Mña Chamuscada	HIE06	10/10	1.1	41.8	170.4	3.7	
	HIE07	10/10	357.4	39.6	210.9	3.3	
	HIE08	10/10	357.7	41.2	132.0	4.2	
	HIE09	10/10	3.1	39.2	113.4	4.6	
Mña Chamuscada (site mean)	HIE06+HIE07+HIE08+HIE09	4/4	359.8	40.5	1097.6	2.8	
Mña Chamuscada (sample Mean)		40/40	359.8	40.5	144.1	1.9	1665-1472 BC 67 BC-129 AD 272-412 AD 1496-1529 AD
Mña del Tesoro	HIE10	10/10	11.8	40.0	124.8	4.3	
	HIE11	9/9	19.6	26.1	253.1	3.2	
	HIE12	9/10	15.8	33.8	132.8	4.5	

	HIE15	9/10	24.9	26.9	39.5	8.3	
Mña del Tesoro (site mean)	HIE10+HIE11+HIE12+HIE15	4/4	18.3	31.8	101.7	9.2	
Mña del Tesoro (sample mean)		37/39	17.2	32.2	60.5	3.1	9351-9088 BC 745-909 AD 985-1009 AD
Orchilla	HIE13	10/10	346.0	48.0	131.2	4.2	
	HIE14	10/10	356.9	42.5	190.6	3.5	
	HIE16	10/10	355.6	38.5	311.0	2.7	
	HIE17	10/10	359.9	41.9	233.5	3.2	
Orchilla (site mean)	HIE14+HIE16+HIE17	3/4	357.4	41.0	883.1	4.2	
Orchilla (sample mean)		30/40	357.4	41.0	211.1	1.8	11775-11631 BC 11419-11194 BC 9063-8856 BC 8241-8157 BC 7261-6711 BC 6248-6185 BC 5462-5326 BC 4169-4092 BC 3807-3724 BC 3486-3396 BC 2424-2210 BC 2151-2057 BC 1656-1421 BC 1386-1375 BC 1157-1104 BC 81 BC- 434 AD
Las Calcosas	HIE18	10/10	359.2	40.8	67.6	5.9	
	HIE19	10/10	1.9	30.8	169.4	3.7	
	HIE20	10/10	1.5	40.7	124.4	4.3	
	HIE24	9/10	354.2	46.7	66.6	6.4	

Las Calcosas (site mean)	HIE18+HIE19+HIE20+HIE24	4/4	359.4	39.8	130.3	8.1	
Las Calcosas (sample mean)		39/40	359.5	39.6	63.7	2.9	11791-11610 BC 11471-11110 BC 9388-8898 BC 8217-8136 BC 7200-6535 BC 6313-6181 BC 5448-5295 BC 3457-3402 BC 2359-2035 BC 1707-1464 BC 1123-1116 BC 71 BC -168 AD 236-418 AD 1480-1532 AD
Lomo Negro	HIE21	10/10	4.2	41.3	298.3	2.8	
	HIE22	8/10	9.7	47.8	399.1	2.8	
	HIE23	9/10	20.9	50.0	69.8	6.2	
	HIE25	10/10	6.3	45.5	208.7	3.4	
Lomo Negro (site mean)	HIE21+HIE22+HIE25	3/4	6.6	44.9	446.6	5.8	
Lomo Negro (sample mean)		28/40	6.5	44.7	205.9	1.9	584-552 BC 468-677 AD 1507-1554 AD 1568-1585 AD
Below Lomo Negro	HIE26	8/10	346.1	32.3	272.8	3.4	
	HIE27	10/10	358.2	21.4	91.2	5.1	
	HIE28	10/10	345.7	26.3	209.1	3.3	
	HIE29	10/10	352.5	30.6	110.8	4.6	
Below Lomo Negro (site mean)	HIE26+HIE27+HIE28+HIE29	4/4	350.7	27.7	126.6	8.2	

Below Lomo Negro (sample mean)		39/40	349.8	27.7	84.0	2.5	5031-4958 BC 4764-4598 BC 4437-4120 BC 3420-3198 BC
Cuchillo del Roque	HIE30	9/10	353.3	38.0	114.5	4.8	
	HIE31	8/10	353.9	41.8	104.6	5.4	
	HIE32	8/10	346.7	47.7	86.4	6.0	
	HIE37	8/10	349.2	37.6	81.1	6.2	
Cuchillo del Roque (site mean)	HIE30+HIE31+HIE32+HIE37	4/4	350.9	41.3	232.2	6.0	
Cuchillo del Roque (sample mean)		39/40	349.9	39.9	52.7	3.2	123-281 AD
Mña Negra	HIE33	10/10	347.7	45.7	131.7	4.2	
	HIE34	10/10	359.9	40.6	248.0	3.1	
	HIE35	10/10	0.2	43.8	150.5	4.0	
	HIE36	10/10	357.9	40.9	134.0	4.5	
Mña Negra (site mean)	HIE34+HIE35+HIE36	3/4	359.3	41.8	1643.5	3.0	
Mña Negra (sample mean)		30/40	359.3	41.8	165.1	2.1	1628-1457 BC 1137-1102 BC 89 BC-129 AD 260-441AD 1505-1537 AD

n/N is number of characteristic remanent magnetization directions used to calculate the site-mean direction/total number of cores drilled at a site, or number of sites used to calculate a volcanic unit-mean direction/total number of sites from the volcanic unit. Inferred ages are gathered by comparing samples-mean palaeomagnetic directions with 14 ka global Palaeosecular Variation (PSV) model by *Pavón-Carrasco et al. (2014).* Inferred ages by parenthesis are discarded by geochronologic or stratigraphic evidence (see text).

4.3.5.3 Palaeomagnetic Dating

For the studied eruptions, one or more possible ages were determined (Table 5). In Fig. 4.53, the Lajal, Mña Chamuscada, Orchilla and Cuchillo del Roque eruptions dating diagrams are shown (the other results are available in Appendix II). In Fig. 4.54a, all inferred ages for each eruption are illustrated, whereas in Fig. 4.54b, only the most probably ages are shown.

For Lajal eruption, based on the Ar/Ar dating of 7±2 ka for the underlying Irama-La Restinga lavas (*Becerril et al., 2016*), a 7,000 BC-1900 AD input age window was considered; within this time interval, seven possible ages between 5,437 BC and 761 AD were found.

Mña Chamuscada was previously dated with ^{14}C at 794-428 cal BC-recalibrated age (*Guillou et al., 1996*). The charcoal found under the lapilli provided a lower bound age of 3410 ± 30 BP (1773 - 1627 cal BC, 2σ error; see Appendix II); therefore, an input time window from 2000 BC to 1900 AD was used. Four palaeomagnetic inferred ages, from 1665 BC to 1529 AD, were found; moreover, the charcoal found by us within the lava flow and dated with ^{14}C, provided a consistent age of 320 ± 30 BP (1518 - 1594 cal AD; see Appendix II).

For Mña del Tesoro eruption, a previous age of 9 ka was obtained by *Rodríguez-González et al., (2012)* using the K/Ar isotopic method. However, this result must be considered with caution, due to the poor trustworthiness of the K/Ar method to date young K-poor volcanic products (see 4.3.6 paragraph). Therefore, the whole-time range covered by the PSV curve (i.e. the last 12 ka) was considered, and only three possible ages were found: 9351-9088 BC, 745-909 AD and 985-1009 AD.

For Orchilla and Las Calcosas, no radiometric data were available, so again the whole Holocene period was considered to date them, and multiple ages for both eruptions were found (Table 5).

Lomo Negro eruption was palaeomagnetically dated by *Villasante-Marcos and Pavón-Carrasco (2014)*, who found three possible ages, 115 BC-7 AD, 410-626 AD, 1499-1602 AD. Therefore, an age range of 1000 BC- 1900 AD was considered, and four possible ages were found. Moreover, the charcoal found by us in the lava field was dated with the ^{14}C, obtaining an age of 380 ± 30 BP (1445 - 1524 cal AD; see Appendix II).

To date “Below Lomo Negro” eruption, the whole age range covered by the PSV curve (due to the lack of any age constraints) has been considered. Only four possible ages in restricted age ranges between 5031 BC and 3198 BC were found.

For Cuchillo del Roque, no previous data were available as well; therefore, as a first step, the last 12 ka as input age range were considered, and several possible ages were found (Appendix II). Subsequently, a smaller 1000 BC - 1900 AD age range was considered, due to the freshness of the lavas, in which no vegetation or alteration/erosion signs are present. In this case, only one possible age, i.e. 123-281 AD, was found (Fig. 4.53).

Finally, for Mña Negra eruption as well as for Cuchillo del Roque, no previous geological studies or age constraints exist. Also in this case, lavas show a very fresh aspect and with no evidence of alteration and/or erosion. Therefore, an input time range from 2000 BC to 1900 AD was considered, and five ages between 1628 BC and 1537 AD were found.

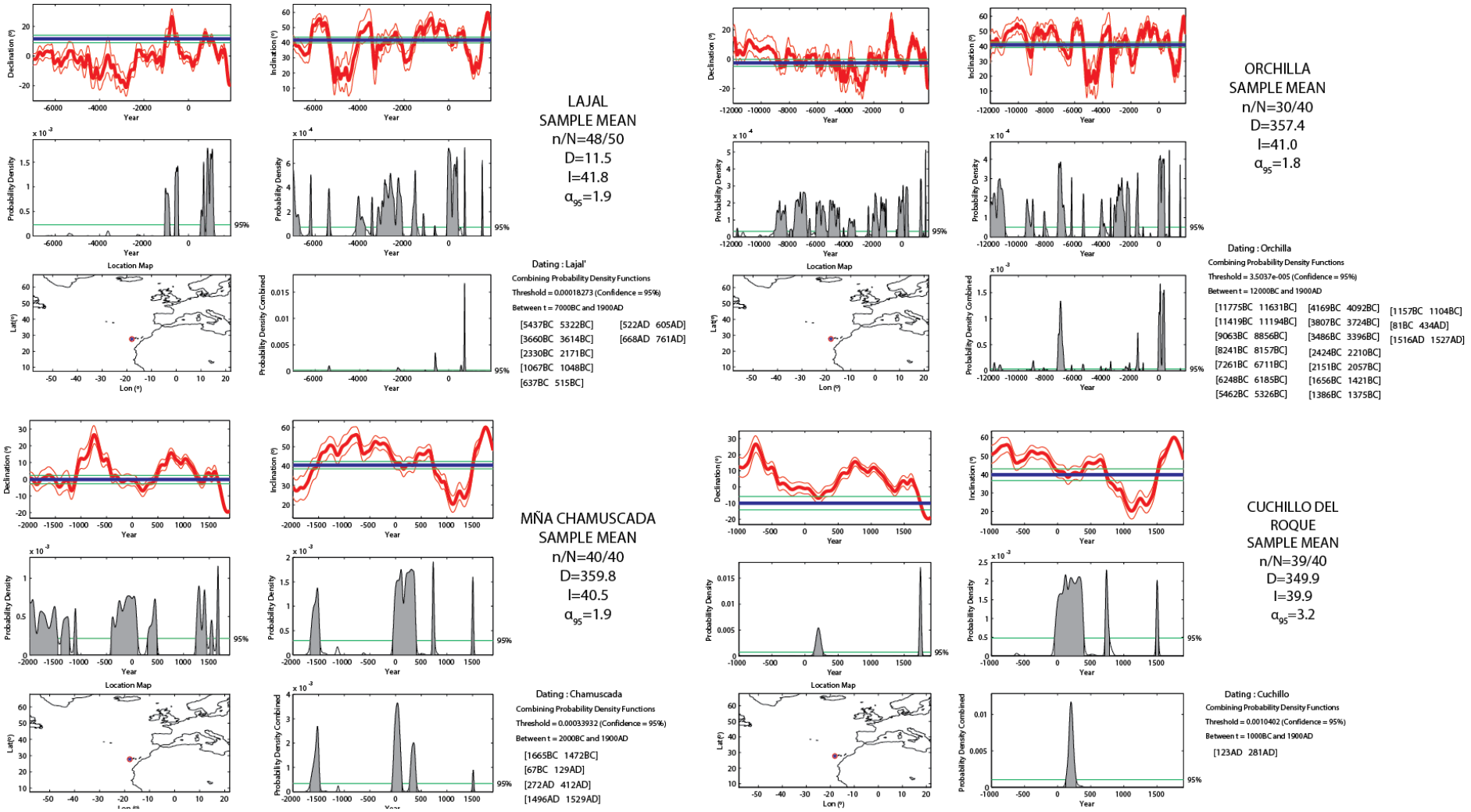

Fig. 4.53 Palaeomagnetic dating of Lajal, Mña Chamuscada, Orchilla and Cuchillo del Roque eruptions, according to the method and software by *Pavón-Carrasco et al. (2011*), and the PSV reference model by *Pavón-Carrasco et al. (2014).* Left-hand panel shows the PSV curves (red lines) for the declination and right-hand panel for the inclination (thin red lines for the associated errors, 95% confidence level), together with the probability density curves (in grey-shade). Palaeomagnetic declination and inclination values are shown in blue straight lines; the 95% associated errors are in green straight lines. In the probability density graphs the 95% confidence level is shown as a green line.

4.3.6 Discussion

El Hierro is the smallest, the westernmost and the least populated island of the Canarian archipelago. This is also the least studied island, although it is considered the youngest expression of the Canarian hot spot activity together with La Palma island (see 4.1 paragraph).

In particular, the Holocene epoch has been scarcely investigated; most of the principal works were focused on the big lateral collapses and the older volcanic stages (*Guillou et al., 1996; Carracedo et al., 2001; Masson et al., 2002; Longprè et al., 2011).* Conversely, for the last 12 ka, limited and uncertain data are available, including ages, location and magnitude of the eruptions.

During the fieldwork, the main problem was the almost complete absence of geological data, as detailed geological maps, dating and stratigraphic relations between eruptions. For four of the studied eruptions (i.e. Lomo Negro, Mña Chamuscada, Mña del Tesoro and Lajal), few and, in some cases, controversial ^{14}C and K/Ar dating data are available.

As already discussed for Tenerife island, the ^{14}C isotopic dating is the common method to date recent eruptions, using charcoals and organic materials; however, in some conditions, the finding of charcoals is difficult. Due to its location, El Hierro is characterized by warm, arid semi-desertic climatic conditions, especially in the south of the island, with 7-8 dry months (*Marzol, 2000*). These climatic characteristics imply that erosion processes and vegetal colonization are not very developed (*Dóniz-Páez et al., 2011*). Furthermore, radiocarbon dating may suffer major accuracy flaws due to contamination from carbon with a different radiocarbon signature, thus resulting in erroneous radiocarbon ages (*Bruns et al., 1980; Saupè et al., 1980; Pasquier-Cardin et al., 1999; Carracedo et al., 2007; Guillou et al., 2011*).

For a long time, the Lomo Negro eruption has been related to a seismic crisis in 1793 AD; recently, *Villasante-Marcos and Pavón-Carrasco (2014*) palaeomagnetically dated it, obtaining three possible ages: 115 BC-7 AD, 410-626 AD, 1499-1602 AD. *Villasante-Marcos* and co-authors also recalibrated the ^{14}C age (150±100 BP; 2σ) of *Hernández-Pacheco (1982),* obtaining an age of 1665 AD. The mean palaeomagnetic direction obtained in this work is consistent with that published by *Villasante-Marcos and Pavón-Carrasco (2014*) (Fig. 4.51a) and translates to two possible ages within the XVI century, i.e. 1507-1554 AD and 1568-1585 AD (Table 5). Furthermore, the site-mean palaeomagnetic direction of all sites, i.e. sites of this

work and those gathered by *Villasante-Marcos and Pavón-Carrasco (2014*), has been calculated (Fig. 4.51b). The inferred ages are: 92-57 BC, 443-649 AD and 1498-1595 AD (Appendix II). Finally, the ^{14}C dating of the charcoal found by us in the lava flow gives an age of 380 ± 30 BP (1445 - 1524 cal AD). Combined, these constrain the Lomo Negro eruption to the XVI century AD.

Mña Chamuscada was dated by *Guillou et al. (1996*) with ^{14}C at 2500 ± 70 BP (794-428 cal BC). The mean palaeomagnetic direction obtained from this lava flow translates to different ages than that provided by *Guillou et al. (1996*): older (1665-1472 BC) or younger (67 BC-129 AD, 272-412 AD, 1496-1529 AD) ages have been found for this eruption. The difference between the *Guillou et al. (1996)* age and ours, as described above, may be due to several sources of bias. *Guillou et al. (1996)* did not indicate where the charcoal was located (below the lava flow or incorporated within). The ^{14}C ages gained by us from charcoals lying below the flow indicate a lower bound age of 1773-1627 cal BC, whereas the charcoal from trunk remains incorporated in the lava flow itself provides a 1518 - 1594 cal AD eruption age. The youngest inferred palaeomagnetic age (1496-1529 AD) agrees with the charcoal found in trunk remains, setting the eruption within the XVI century AD. These data shift this eruption to a much more recent date than previously thought.

Mña del Tesoro has been dated by *Rodríguez-González et al. (2012),* at 9 ka, using the K/Ar isotopic method. However, this method can be problematic. To use the K-Ar method minerals must be K-rich (like K-feldspar, plagioclase, etc. *Lee, 2015)*, and for this reason, this dating method is not recommended to date K-poor volcanic rock. Furthermore, the ^{40}K half-life is 1,250 Ma, making the K–Ar dating method well suited for dating most old rocks (*Lee, 2015*); for rocks younger than 1 Ma (*Takaoka et al., 1989*), the influence of atmospheric Ar can magnify errors in the K-Ar dating (*Cox and Dalrymple, 1967*). The palaeomagnetic dating found for Mña del Tesoro yields an older age of 9351-9088 BC, and two much younger ages of 745-909 AD and 985-1009 AD. If the freshness of the lava flow and the absence of substantial alteration or erosion signs are considered, the recent date are more likely; therefore, I suggest that the Mña del Tesoro eruption occurred between 745 AD and 1009 AD.

To date the Lajal eruption, the Ar/Ar dating provided by *Becerril et al. (2016)* for the underlying Irama-La Restinga eruption was considered as the lower bound age. The Irama-La Restinga cones were produced by an eruptive fissure south of the Lajal volcanic complex.

These cones were partially covered by the Lajal lava flows. Considering an input time window between 7000 BC to 1900 AD, several possible ages, from ~5400 BC to ~760 AD, were found for this eruption. According to the probability density combined graph (Fig. 4.53) the most probable ages are 637-515 BC and 668-761 AD.

For the other five eruptions (Below Lomo Negro, Mña Negra, Cuchillo del Roque Orchilla, Las Calcosas), no age constraints were available.

For Below Lomo Negro eruption, even if the whole-time interval covered by the curve is considered, only a few possible ages between 5000 and 3200 BC was found. For Mña Negra and Cuchillo del Roque eruptions, the freshness of the lava flows and the lack of alteration or erosion signs, as well as the absence of vegetation, implies that they are very young, excluding older ages than 4000-5000 years BP. For Mña Negra, two possible ages between 2000 BC and 1000 BC, two between 0 AD and 600 AD, and a youngest possible age between 1505-1537 AD were found, whereas, only one possible age, 123-281 AD, was obtained for Cuchillo del Roque eruption.

Conversely, for the Orchilla and Las Calcosas eruptions, several possible ages have been obtained but none can be excluded. The many possible inferred ages are the consequence of the characteristics of the palaeosecular variation of the geomagnetic field: the field swings around the same directions and can yield similar palaeomagnetic directions several times during a few millennia (see 2.2 paragraph). At the latitude of El Hierro, according to the GAD model and the relations between the latitude and the inclination of the geomagnetic field ($2\tan\lambda = \tan I$, see 2.1 paragraph), the expected inclination value is I= ~45°, and this translates to many possible inferred ages within the last 12 ka. Moreover, the mean palaeomagnetic directions obtained for these two eruptions are statistically indistinguishable, therefore the inferred ages overlap in most cases. On the other side, the aboriginal seafood remains lying above the lava flows cannot provide an upper limit age. Even if the oldest aboriginal site was dated at 120±60 AD (*Velasco-Vázquez et al., 2005*), this age does not necessarily coincide with the first arrival of aboriginal people on the island. Therefore, the seafood remains simply means that the lava flows existed while they lived there, and the possibility that they have seen the eruptions and used it a few decades later cannot be excluded. The absence of geological constraints that could yield lower or upper bound ages and the lack of a stratigraphic relation between these two eruptions do not allow the exclusion of any possible

age ranges. However, the appearance of the outcrops (the limited erosion and alteration signs, scarce colonization of vegetation, etc.), support the exclusion of the oldest age ranges (older than 7 ka). Nevertheless, the degradation of monogenic volcanic edifices is a combination of various sediment transport mechanisms and erosion processes and their degree of transformation evolves independently of their age, often without a correlation between morphology and age (*Wood, 1980; Brady and Carroll, 1994; Hooper and Sheridan, 1998; Hooper, 1995; Hinsinger et al., 2001; Riebe et al., 2004; Rodríguez-González et al., 2011; Fornaciai et al., 2010, 2012; Kereszturi et al., 2012, 2013*, *Bemis and Ferencz, 2017,* among many other).

The updated chronological framework for El Hierro shows that at least 4-5 eruptions occurred in the last 2 ka, without a clear spatial distribution over time: vents opened on the NW and NE rifts randomly. Moreover, the several inferred ages found for each eruption do not allow calculation of a recurrence rate. Therefore, it would be advisable to carry out further fieldwork and detailed investigations to obtain a stratigraphy of the lava flows and further geological constraints.

4.3.7 Conclusion

For the first time, a chronological reconstruction of the Holocene eruptions for El Hierro island is provided using palaeomagnetic dating and ^{14}C ages.

For three previously dated eruptions (Mña del Tesoro, Mña Chamuscada and Lomo Negro), new palaeomagnetic ages show an inconsistency between the previous data (K/Ar and ^{14}C ages) and the new palaeomagnetic and ^{14}C ages in two cases (i.e. Mña del Tesoro and Mña Chamuscada), setting these eruptions in the last 2 ka. For Lomo Negro eruption, consistent palaeomagnetic and radiocarbon ages were obtained by this work and *Villasante-Marcos and Pavón-Carrasco (2014),* proving that it occurred in the XVI century AD.

For the previously undated six eruptions, different input age assumptions were used. For Orchilla and Las Calcosas, due to the lack of any geological constraints, the entire Holocene epoch was investigated and many possible ages within the last 12 ka were found; therefore, further investigations are needed to better constrain their age. For Below Lomo Negro eruption, a 5031 BC-3198 BC age range was obtained. Finally, the stratigraphic constraint of

the underlying Irama-La Restinga eruptive activity (7±2 ka) translated into two possible palaeomagnetic ages for Lajal eruption, whereas some possible ages younger than 4 ka were obtained for Mña Negra and one for Cuchillo del Roque. The younger age was preferred, due to the freshness of the surfaces and the absence of erosion and/or alteration of the lava flows.

Until now, La Palma and Tenerife were considered the most volcanically active islands during the Holocene epoch (*Carracedo et al., 2001*), but our new data show that many effusive eruptions occurred at El Hierro in the last few thousand years along the three rift zones of the island, with a cluster of five eruptions from ~2000 BC to ~1500 AD (Fig. 4.54). These data are significant for a correct assessment of the volcanic hazard, although of course further studies are needed to complete and better outline the most recent volcanic history of the island.

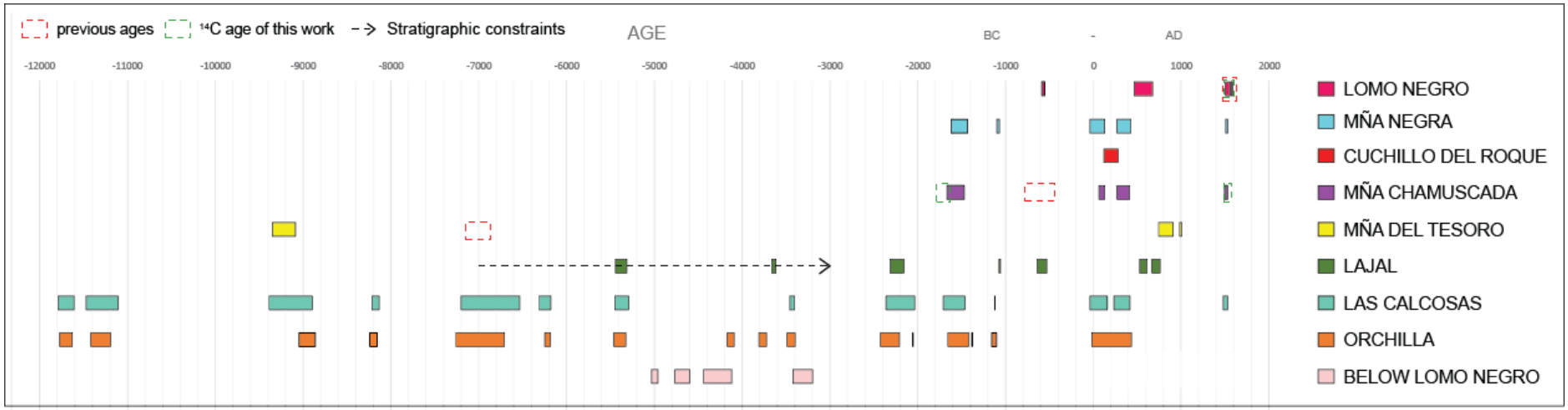

a)

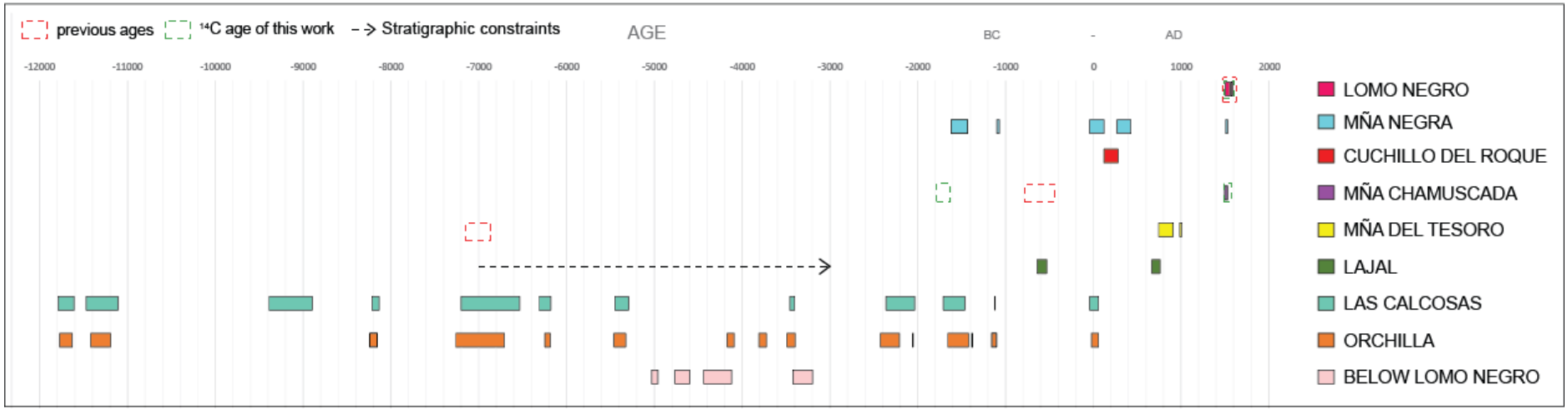

b)

Fig. 4.54 a) Comparison of palaeomagnetically-inferred ages vs. literature stratigraphic/isotopic ages relative to the studied eruptions. b) Same diagram as in A) but with only the most probable ages for each eruption. Dashed red boxes and black arrows indicate previous isotopic dating and stratigraphic constraints, respectively. Green boxes are ^{14}C ages from this work.

4.4 Volcanic activity and recurrence rates at the Canary Islands

To assess the volcanic hazard, it is necessary to know how volcanism has behaved in the past and determine the recurrence of volcanic eruptions. However, the recurrence or eruption frequency is based on the study of historical and prehistorical records, which in the Canary Islands are still poorly defined. The Canaries are an active volcanic region and Holocene volcanic eruptions occurred at almost all islands of the archipelago, with 15 eruptions during the last 600 years; however, only the recent activity is well known, whereas dated for the prehistoric eruptions are in most cases still imprecise and debated. The ages of many Holocene eruptions are not yet known and only a few eruptions are stratigraphically constrained, while large age errors are often associated with the dated eruptions.

In Fig. 4.55 all dated and stratigraphically constrained eruptions of the Canary Islands in the last 5 ka are reported to identify a recurrence rate for each island and the whole archipelago. Data are derived from this work and *Carracedo et al. (2007), Carracedo and Troll (2013), Becerrill et al. (2016), Rodriguez et al. (2018)* works and the *Global Volcanism Program (GVP, 2013)*.

Some qualifications are necessary before analysing diagrams.

First, in Fuerteventura, despite late Pleistocene and Holocene cinder cones and lava flows being mentioned (*GVP, 2013*), *Troll and Carracedo (2016)* indicate the youngest eruption is older than 100 ka. No dated eruptions (to the best of my research) have been found for this island. For the other islands, several Holocene eruptions have not been dated or constrained in other ways yet, and therefore they have not been reported; this is especially the case of El Hierro, where at least another twelve eruptions (beyond those discussed in this thesis) occurred within El Golfo embayment and others located along the three rifts are undated but indicated as <20 ka by *Becerril et al. (2016*). For the eruptions belonging to Tenerife and El Hierro dated in this work, higher resolution dating has been obtained in some cases, whereas in others more possible ages were found. This rules out the possibility of discarding some of them. Therefore, the following discussion and conclusions are mainly qualitative, and more investigations are necessary.

Lanzarote, which represents, together with Fuerteventura, the oldest island in a post-erosional phase, shows the lowest eruptive activity in the last 5 ka (Fig. 4.55); only four

eruptions, of which two were in the historic period (the Timanfaya eruption in 1730-36 AD and Tao eruption in 1824 AD), have been recorded, with a mean value of 2 eruptions/kyr.

Tenerife and Gran Canaria islands, considered in the mature phase of their evolution, had many eruptions, with different rates over time. Whereas Tenerife shows approximately 4-5 eruptions/kyr, with a higher concentration in the last 2-3 kyrs and several eruptions in the historic period, Gran Canaria recorded about 10 eruptions between 1500 BC and 500 BC, and 6 between 500 BC and 500 AD, with the last eruption (Pico Bandama eruption) occurring 2 kyr ago.

Fewer eruptions (but possibly due to the paucity of available data) have been recorded in El Hierro and La Palma. La Palma had about 9 eruptions in the last 2 kyrs, with 7 of them in the last 600 years (the last was the Teneguia eruption in 1971 AD); according to *Astiz et al. (2000),* the eruptive recurrence period has a range between 50 and 100 years. In El Hierro, at least three eruptions (La Restinga in 2011 AD, Lomo Negro 1568-1585 AD and Mña Chamuscada in 1496-1529 AD) occurred in the last 500 yrs. For previous periods, due to the several possible ages obtained for some eruptions, it is difficult to calculate a correct eruptive rate.

It is noteworthy that, if only historic eruptions are considered, there were 2 eruptions on two different islands, El Hierro and La Palma, in the XVI century; 2 eruptions on La Palma in the XVII century; 4 eruptions on Tenerife, 1 eruption on La Palma and 1 eruption, lasting six years, on Lanzarote in the XVIII century; 1 eruption on Tenerife and 2 on La Palma in the XX century; and 1 eruption on El Hierro during the XXI century. This shows that the Canary Islands can be active almost contemporaneously, and therefore it is important to assess and monitor the volcanic hazard to reduce and manage this potential risk, developing appropriate preparedness plans. Commonly, volcanic hazard assessments consider one island at a time (*Araña et al., 2002; Bartolini et al., 2013; Becerril et al., 2013, 2014*; *Carracedo et al., 2004a, b, 2005; Felpeto, 2002; Felpeto et al., 2001, 2007*; *Gómez-Fernandez, 1970, 1996, 2000; Liu et al., 2020; Marrero et al., 2012; Martí and Felpeto, 2010; Martí et al., 2012; Rodríguez-González, 2009; Scaini et al., 2014; Sobradelo and Martí, 2010;* among many others), but only one has been evaluated for the Canary Islands as a whole (*Sobradelo et al., 2011*).

It would be useful to evaluate this eruptive behaviour for previous periods, and palaeomagnetism can be of help to date them because this technique is faster and more broadly applicable than other dating methods. However, further geological and volcanological studies are required to correctly reconstruct the Holocene chronological framework of the whole Canary archipelago.

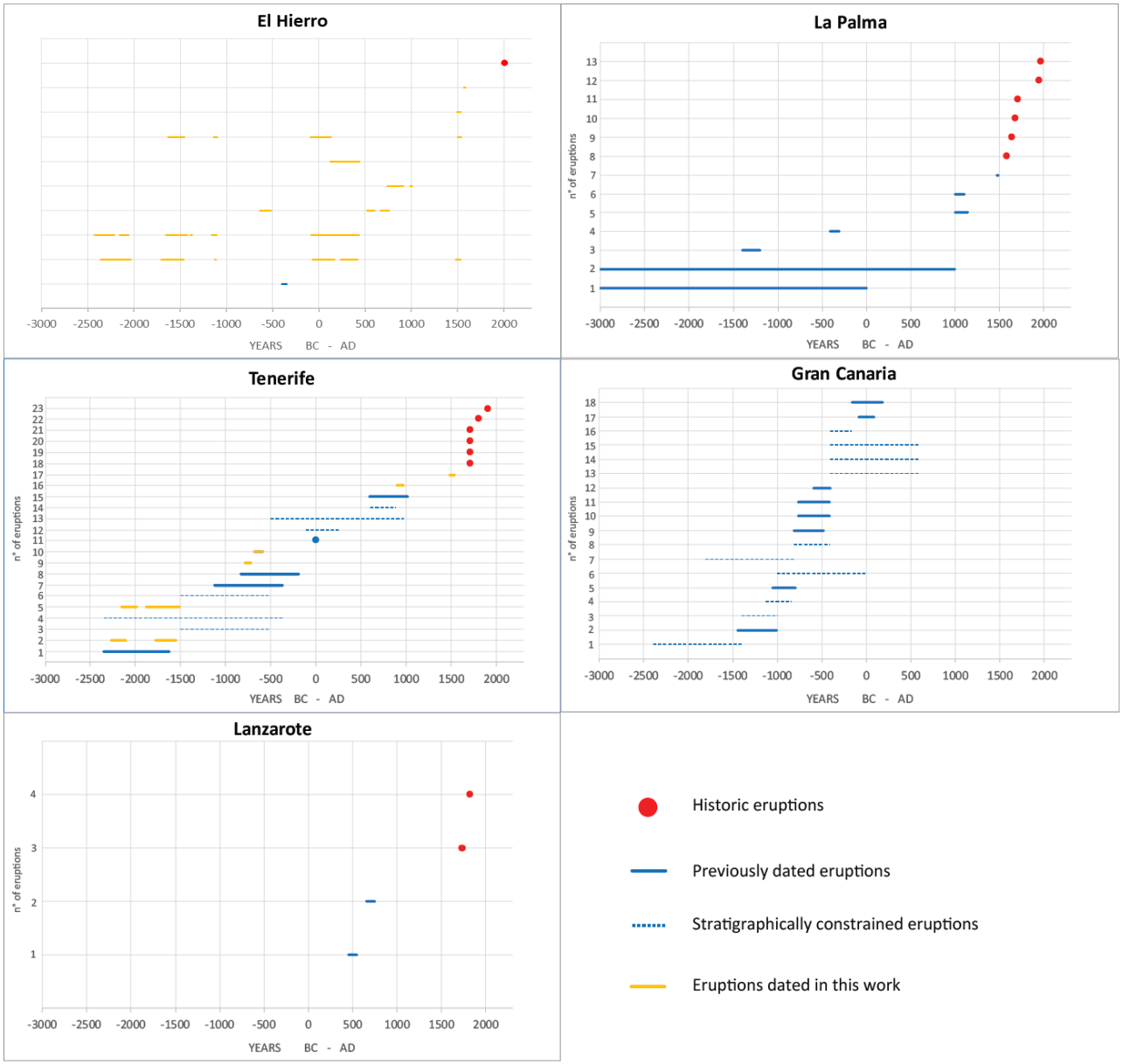

Fig. 4.55 Eruptions occurred in the last 5 ka at the Canary Islands (ages of previously dated eruptions are according to *Carracedo et al., 2007* and *Carracedo and Troll, 2013* for Tenerife; *Global Volcanism Program* and *Troll and Carracedo, 2016* for La Palma; *Rodriguez-Gonzales et al., 2018* for Gran Canaria; *Global Volcanism Program* for Lanzarote).

References

Abdel Monem, A., Watkins, N.D., Gast, P.W., (1971). Potassium-argon ages, volcanic stratigraphy, and geomagnetic polarity history of the Canary Islands: Lanzarote, Fuerteventura, Gran Canaria, and La Gomera. Am. J. Sci. 271, 490521.

Astiz, M., Tárraga, M., Sánchez, N. (2000). Curso Internacional de Volcanología y Geofísica Volcánica, Casa de los Volcanes, vol 7, Excmo. Cabildo Insular de Lanzarote. Servicio de Publicaciones. Lanzarote, chap Modelos estadísticos en volcanología, 5:401–10.

Araña, V., Felpeto, A., Astiz, M., García, A., Ortiz, R., Abella, R. (2002). Zonation of the main volcanic hazards (lava flows and ash fall) in Tenerife, Canary Islands. A proposal for a surveillance network, J. Volcanol. Geoth. Res., 103, 377–391.

Bartolini, S., Cappello, A., Martí, J., and Del Negro, C. (2013). QVAST: a new Quantum GIS plugin for estimating volcanic susceptibility, Nat. Hazards Earth Syst. Sci., 13, 3031–3042, doi:10.5194/nhess-13-3031-2013.

Becerra, R., Guillén, C., Dóniz, J. (2007). Erupción basáltica fisural al ne del volcán monogénico de Orchilla, El Hierro, Canarias. Caracteres geomorfológicos. In Lario, J., Silva, G. (eds) Contribuciones al estudio del perÍodo cuaternario, Aequa, Ávila, 133-134.

Becerra–Ramírez, R., Dóniz Páez, J., Guillén Martín C. (2010). Geomorfología de los volcanes de orchilla y de la erupción fisural del NE (El Hierro, Islas Canarias). In: González Cárdenas, E., Escobar Lahoz, E., Becerra Ramírez, R., Gosálvez Rey, R. U., Dóniz Páez, J. (2010) Aportaciones recientes en volcanología 2005-2008. Centro de Estudios Calatravos

Becerril, L., Cappello, A., Galindo, I., Neri, M., Del Negro, C. (2013). Spatial probability distribution of future volcanic eruptions at El Hierro Island (Canary Islands, Spain), J. Volcanol. Geoth. Res., 257, 21–30, doi:10.1016/j.jvolgeores.2013.03.005.

Becerril, L., Bartolini, S., Sobradelo, R., Martí Molist, J., Morales, J. M., Galindo, I. (2014). Long-term volcanic hazard assessment on El Hierro (Canary Islands). Nat. Hazards Earth Syst. Sci., 14, 1853–1870.

Becerril, L., Galindo, I., Martì, J., Gudmundsson, A. (2015). Three-armed rifts or masked radial pattern of eruptive fissures? The intriguing case of El Hierro volcano (Canary Islands). Tectonophysics, 674-648, 33-47.

Becerril, L., Ubide, T., Sudo, M., Martí, J., Galindo, I., Gale, C., et al. (2016). Geochronological constraints on the evolution of El Hierro (Canary Islands). Journal of African Earth Sciences, 113, 88-94.

Bemis, K. G., Ferencz, M. (2017). Morphometric analysis of scoria cones: the potential for inferring process from shape. Geological Society, London, Special Publications, 446(1), 61–100. doi:10.1144/sp446.9

Bory de St. Vincent, J.B.G.M. (1803). Essais sur les isles Fortunées et l'antique Atlantide, ou, Précis de l'histoire générale de l'archipel des Canaries. Baudouin, Paris, p. 522. an XI.

Brady, P. V., Carroll, S. A. (1994). Direct effects of CO2 and temperature on silicate weathering: Possible implications for climate control. Geochimica et Cosmochimica Acta, 58(7), 1853-1856.

Bravo, T. (1968). Hidrogeolog´ıa de la isla de El Hierro, Estudios Canarios, 11, 12, 13, 88–90.

Bruns, M., Ingeborg, L., Münnich, K.O., Hubberten, H.W., Fillipakis, S. (1980). Regional sources of volcanic carbon dioxide and their influence on 14C content of present-day plant material. Radiocarbon 2:532–536.

Carracedo, J.C. (1994) The Canary Islands: an example of structural control on the growth of large oceanic island volcanoes. J. Volcanol. Geoth. Res., 60, ¾, 225-242.

Carracedo, J.C., (1996a). Morphological and structural evolution of the western Canary Islands: hotspot-induced three-armed rifts or regional tectonic trends? J. Volcanol. Geoth. Res. 72, 151162.

Carracedo, J.C. (1996b). A simple model for the genesis of large gravitational landslide hazards in the Canary Islands. In: McGuire, W., Neuberg, J., Jones, A. (Eds.), Volcano Instability on the Earth and Other Planets, Geological Society of London, Special Publications, London, 110. pp. 125135.

Carracedo J.C. (2008). Los volcanes de las Islas Canarias, IV, La Palma, La Gomera, El Hierro, Ed. Rueda, Madrid.

Carracedo, J.C., Day, S.J. (2002). Canary Islands, Series Classic Geology in Europe, vol. 4. Terra Publishing, Harpenden, p. 249.

Carracedo, J.C., Day, S.J., Guillou, H., Gravestock, P. (1999). Later stages of volcanic evolution of La Palma, Canary Islands: rift evolution, giant landslides, and the genesis of the Caldera de Taburiente. Geol. Soc. Am. Bull. 111, 755768.

Carracedo, J.C., Rodríguez Badiola, E., Guillou, H., de la Nuez, J., Perez Torrado, F.J. (2001). Geology and volcanology of La Palma and El Hierro, Western Canaries." Estudios Geologicos-madrid, 57: 175-273.

Carracedo, J. C., Guillou, H., Paterne, M., Scaillet, S., Rodríguez Badiola, E., Paris, R., Pérez Torrado, F. J., Hansen Machín, A. (2004a). Análisis del riesgo volcánico asociado al flujo de lavas en Tenerife (Islas Canarias): escenarios previsibles para una futura erupción en la isla, Estud. Geol., 60, 63–93.

Carracedo, J. C., Guillou, H., Paterne, M., Scaillet, S., Rodríguez Badiola, E., Paris, R., Pérez Torrado, F. J.,Hansen, A. (2004b). Avance de un mapa de peligrosidad volcánica de Tenerife (escenarios previsibles para una futura erupción en la isla), Servicio de Publicaciones de la Caja General de Ahorros de Canarias (Caja Canarias), Tenerife, 46 pp.

Carracedo, J. C., Pérez Torrado, F. J., Rodríguez Badiola, E., Hansen, A., Paris, R., Guillou, H., Scaillet, S. (2005). Análisis de los riesgos geológicos en el Archipiélago Canario: Origen, características, probabilidades y tratamiento, Anuario de Estudios Atlánticos, 51, 513–574.

Carracedo, J.C., Rodríguez-Badiola, E., Guillou, H., Paterne, M., Scaillet, S., Pérez Torrado, F.J., et al. (2007). Eruptive and structural history of Teide volcano and rift zones of Tenerife, Canary Islands. Geol. Soc. Am. Bull. 19, 10271051.

Cox, A., Dalrymple, G. B. (1967). Statistical analysis of geomagnetic reversal data and the precision of potassium-argon dating. Journal of Geophysical Research, 72(10), 2603-2614.

Darias y Padrón, D.V., 1929. Noticias generales históricas sobre la Isla del Hierro, una de las Canarias. Imprenta Curbelo, San Cristo´bal de La Laguna, p. 407.

Del Moro, S., Di Roberto, A., Meletlidis, S., Pompilio, M., Bertagnini, A., Agostini, S., Ridolfi, F., Renzulli, A. (2015). Xenopumice erupted on 15 October 2011 offshore of El Hierro (Canary Islands): a subvolcanic snapshot of magmatic, hydrothermal and pyrometamorphic processes, B. Vulcanol., 77 (6), 53; doi:10.1007/s00445-015-0940-0.

Domínguez Cerdeña, I., C. del Fresno, Gomis Moreno, A. (2014). Seismicity patterns prior to the 2011 El Hierro Eruption, B. Seismol. Soc. Am., 104 (1), 567-575; doi:10.1785/0120130200.

Dóniz-Páez J., (2009), Patrimonio geomorfológico de los volcanes basálticos monogénicos de la Caldera de Gairía-Malpaís Chico y el malpaís grande en la isla de Fuerteventura (Canarias, España), Nimbus, 23-24, 89-103.

Dóniz Páez., J., Beltrán, E., Romero, C. (2005). Geomorphic and biogeographical diversity in volcanic coastal areas: Tamaduste (Hierro, Canary Islands). Forum. Unesco. 141-149.

Dóniz-Páez, J., Becerra-Ramírez, R., González-Cárdenas, E., Guillén-Martín, C., Escobar-Lahoz, E. (2011). Geomorphosites And Geotourism In Volcanic Landscape: The Example Of La Corona Del Lajial Cinder Cone (El Hierro, Canary Islands, Spain). Geojournal Of Tourism and Geosites, Iv No.2, Vol. 8, November 2011, Pp. 185-197.

Dunlop, D. J. (2002). Theory and application of the Day plot (Mrs/Ms versus Hcr/Hc): 1. Theoretical curves and tests using titanomagnetite data. J. Geophys. Res., 107(B3), 2056, doi:10.1029/2001JB000486.

Felpeto, A. (2002). Modelización física y simulación numérica de procesos eruptivos para la generación de mapas de peligrosidad volcánica, Ph.D. thesis, University of Madrid, Madrid, Spain, 250 pp.

Felpeto, A., Araña, V., Ortiz, R., Astiz, M., García, A. (2001). Assessment and modelling of lava flow hazard on Lanzarote (Canary Islands), Nat. Hazards, 23, 247–257.

Felpeto, A., Martí, J., Ortiz, R. (2007). Automatic GIS-based system for volcanic hazard assessment, J. Volcanol. Geoth. Res., 166, 106–116, doi:10.1016/j.jvolgeores.2007.07.008.

Fornaciai, A., Behncke, B., Favalli, M., Neri, M., Tarquini, S., Boschi, E. (2010). Detecting short-term evolution of Etnean scoria cones: a LIDAR-based approach. Bulletin of Volcanology, 72, 1209–1222.

Fornaciai, A., Behncke, B., Favalli, M., Neri, M., Tarquini, S., Boschi, E. (2012). Morphometry of scoria cones, and their relation to geodynamic setting: A DEM-based analysis. J. Volcanol. Geotherm. Res., 217-218, 56-72.

Geyer, A., Martí, J. (2011). The distribution of basaltic volcanism on Tenerife, Canary Islands: implications on the origin and dynamics of the rift system, reply to the comment by Carracedo et al. Tectonophysics, 503 (334), 234238.

Global Volcanism Program (2013). Volcanoes of the World, v. 4.9.2. Venzke, E (ed.). Smithsonian Institution. Downloaded 23 Jan 2021. https://doi.org/10.5479/si.GVP.VOTW4-2013.

Gómez-Fernandez, F. (1970). Development of a Volcanic Risk Assessment Information System for the Prevention And Management Of Volcanic Crisis: Stating The Fundamentals. WIT Trans. Inf. Commun. Technol., 21.

Gómez-Fernández, F. (1996). Desarrollo de una Metodología para el Análisis del Riesgo Volcánico en el marco de un Sistema de Información Geográfica, Ph.D. thesis, University of Madrid, Madrid, Spain, 255 pp.

Gómez-Fernández, F. (2000). Application of a GIS algorithm to delimit the areas protected against basic lava flow invasion on Tenerife Island. J. Volcanol. Geotherm. Res., 103, 409–423.

Guillén Martín, C., Becerra-Ramírez, R., J., Dóniz-Páez, J. (2010). Geomorfología de los volcanes de Orchilla y de la erupción fisural del NE (El Hierro, Islas Canarias).

Guillou, H., Carracedo, J.C., Pérez-Torrado, F.P., Badiola, E.R. (1996). K-Ar ages and magnetic stratigraphy of a hotspot-induced, fast grown oceanic island: El Hierro, Canary Islands. J. Volcanol. Geoth. Res. 73, 141-155.

Guillou, H., Nomade, S., Carracedo, J.C., Kissel, C., Laj, C., Wandres, C. (2011). Effectiveness of combined unspiked K-Ar and 40Ar/39Ar dating methods in the 14C age range. Quat. Geochronol. 6:530–538.

Hinsinger, P., Fernandes Barros, O., N., Benedetti, M., F., Noack, Y., Callot, G. (2001) Plant-induced weathering of a basaltic rock: experimental evidence. Geochim. Cosmochim. Acta, 65, 1, 137-52.

Hernández-Pacheco, A. (1982). Sobre una posible erupción en 1793 en la isla de El Hierro (Canarias), Estudios Geológicos, 38, 15–25.

Hooper, D. M., (1995). Computer-simulation models of scoria cone degradation in the Colima and Michoacán-Guanajuato volcanic fields, Mexico. Geofisica Internacional 34 3 321 40

Hooper, D. M., Sheridan, M., F., (1998). Computer-simulation models of scoria cone degradation. J. Volcanol. Geotherm. Res. 83, 3-4, 241 67.

Kereszturi, G., Németh, K. (2012). Monogenetic basaltic volcanoes: genetic classification, growth, geomorphology and degradation. In Updates in volcanology-new advances in understanding volcanic systems. IntechOpen.

Kereszturi, G., Geyer, A., Martí, J., Németh, K., Dóniz-Páez, F. J. (2013). Evaluation of morphometry-based dating of monogenetic volcanoes—a case study from Bandas del Sur, Tenerife (Canary Islands). Bulletin of Volcanology, 75(7), 1-19.

Kirschvink, J.L. (1980). The least-squares line and plane and the analysis of palaeomagnetic data. Geophys. J. R. Astron. Soc. https://doi.org/10.1111/j.1365-246X.1980.tb02601.x

Kono, M. (2015). Geomagnetism: an introduction and overview. Chapter 5. In: Schubert, G. (Ed.), Treatise on Geophysics. 2015. Elsevier.

Lee J.K.W. (2015) Ar–Ar and K–Ar Dating. In: Jack Rink W., Thompson J.W. (eds) Encyclopedia of Scientific Dating Methods. Encyclopedia of Earth Sciences Series. Springer, Dordrecht. https://doi.org/10.1007/978-94-007-6304-3_40

Liu, W., Li, L., Chen, L., Wen, M., Wang, J., Yuan, L., et al. (2020). Testing a Comprehensive Volcanic Risk Assessment of Tenerife by Volcanic Hazard Simulations and Social Vulnerability Analysis. ISPRS International Journal of Geo-Information, 9(4), 273.

Longpré, M.A., Chadwick, J.P., Wijbrans, J., Iping, R. (2011). Age of the El Golfo debris avalanche, El Hierro (Canary Islands): new constraints from laser and furnace 40Ar/39Ar dating. J. Volcanol. Geoth. Res. 203, 7680.

Manconi, A., Longpré, M.-A., Walter, T.R., Troll, V.R., Hansteen, T.H. (2009). The effects of flank collapses on volcano plumbing systems. Geology 37, 10991102.

Marrero, J.M., García, A., Llinares, A., Rodriguez-Losada, J.A., Ortiz, R. (2012). A direct approach to estimating the number of potential fatalities from an eruption: Application to the Central Volcanic Complex of Tenerife Island. J. Volcanol. Geotherm. Res., 219–220, 33–40.

Martí, J. Felpeto, A. (2010). Methodology for the computation of volcanic susceptibility. An example for mafic and felsic eruptions on Tenerife (Canary Islands), J. Volcanol. Geoth. Res. 195, 69–77, doi:10.1016/j.jvolgeores.2010.06.008, 2010.

Martí, J., Sobradelo, R., Felpeto, A., García, O. (2012): Eruptive scenarios of phonolitic volcanism at Teide-Pico Viejo volcanic complex (Tenerife, Canary Islands), Bull. Volcanol., 74, 767–782, doi:10.1007/s00445-011-0569-6.

Martín, J. L., Oromí, P., Izquierdo, I. (1987). El ecosistema eolico de la colada volcánica de Lomo Negro en la isla de El Hierro (isla Canarias). Vieraea, 17, 261-270.

Marzol, V., (2000). El clima, In: Morales G., Pérez R., (ed): Gran atlas temático de Canarias, S/C Tenerife: 87-106

Masson, D.G. (1996). Catastrophic collapse of the volcanic island of Hierro 15 ka ago and the history of landslides in the Canary Islands. Geology 24, 231234.

Masson, D.G., Watts, A.B., Gee, M.J.R., Urgelés, R., Mitchell, N.C., Le Bas, T.P., et al. (2002). Slope failures on the flanks of the western Canary Islands. Earth Sci. Rev. 57, 135.

Meletlidis, S., A. Di Roberto, M. Pompilio, A. Bertagnini, I. Iribarren, A. Felpeto, P.A. Torres and C. D'Oriano (2012). Xenopumices from the 2011-2012 submarine eruption of El Hierro (Canary Islands, Spain): Constraints on the plumbing system and magma ascent, Geophys. Res. Lett., 39, L17302; doi:10.1029/2012GL052675.

Meletlidis, S., Di Roberto, A., Cerdeña, I. D., Pompilio, M., García-Cañada, L., Bertagnini, A., et al. (2015). New insight into the 2011–2012 unrest and eruption of El Hierro Island (Canary Islands) based on integrated geophysical, geodetical and petrological data. Annals of Geophysics, 58(5), S0546.

Münn, S., Walter, T. R., Klügel, A. (2006) Gravitational spreading controls rift zones and flank instability on El Hierro, Canary Islands. Geological Magazine, 143.3: 257-268.

Ordóñez, A. C., Fregel, R., Trujillo-Mederos, A., Hervella, M., de-la-Rúa, C., Arnay-de-la-Rosa, M. (2017). Genetic studies on the prehispanic population buried in Punta Azul cave (El Hierro, Canary Islands). *J. Archaeolog. Sc.*, *78*, 20-28.

Pasquier-Cardin, A., Allard, P., Ferreira, T., Hatte, C., Coutinho, R., Fontugne, M., Jaudon, M. (1999). Magma derived CO2 emissions recorded in 14C and 13C contents of plants growing in Furnas caldera, Azores. J Volcanol Geotherm Res 92:195–207.

Pellicer, M.J. (1977). Estudio volcanológico de la Isla de El Hierro (Islas Canarias) (Volcanological study of the island of El Hierro (Canary Islands). Estud. Geol. 33, 181197.

Pérez-Torrado, F.J., Rodríguez-Gonzalez, A., Carracedo, J.C., Fernández-Turiel, J.L., Guillou, H., et al. (2011). Edades C-14 Del Rift ONO de El Hierro (Islas Canarias). In: Turu, V., Constante, A. (Eds.), El Cuaternario en España y A´ reas Afines, Avances en 2011. Asociación Española para el Estudio del Cuaternario (AEQUA), Andorra, pp. 101-104.

Reimer, P.J., Bard, E., Bayliss, A., Beck, J.W., Blackwell, P.G., Bronk Ramsey, C., Buck, C.E., Cheng, H., Edwards, R.L., Friedrich, M., Grootes, P.M., Guilderson, T.P., Haflidason, H., Hajdas, I., Hatté, C., Heaton, T.J., Hogg, A.G., Hughen, K.A., Kaiser, K.F., Kromer, B., Manning, S.W., Niu, M., Reimer, R.W., Richards, D.A., Scott, E.M., Southon, J.R., Turney, C.S.M., van der Plicht, J. (2013). IntCal13 and MARINE13 radiocarbon age calibration curves 0-50000 years cal BP Radiocarbon 55(4). DOI: 10.2458/azu_js_rc.55.16947.

Riebe, C., S., Kirchner, J., W., Finkel, R., C. (2004) Erosional and climatic effects on long-term chemical weathering rates in granitic landscapes spanning diverse climate regimes. Earth Planet. Sci. Lett., 224, 3-4, 547-62

Rivera, J., Lastras, G., Canals, M., Acosta, J., Arrese, B., Hermida, N., et al. (2013). Construction of an oceanic island: Insights from the El Hierro (Canary Islands) 2011–2012 submarine volcanic eruption. Geology, 41(3), 355-358.

Rodríguez-González, A. (2009). El Vulcanismo Holoceno de Gran Canaria: Aplicación de un sistema de Información Geográfica, Ph.D. thesis, University of Las Palmas de Gran Canaria, Las Palmas de Gran Canaria, Spain, 424 pp., 2009

Rodriguez-Gonzalez, A., Fernandez-Turiel, J.L., Perez-Torrado, F.J., Aulinas, M., Carracedo, J.C., Gimeno, D., Guillou, H., Paris, R. (2011). GIS methods applied to the degradation of

monogenetic volcanic fields: a case study of the Holocene volcanism of Gran Canaria (Canary Islands, Spain) Geomorphology, 134 (3–4), pp. 249-259

Rodríguez-González, A., Perez-Torrado, F. J., Fernández Turiel, J. L., Carracedo, J. C., Guillou, H. (2012). Modelado geomorfológico con técnicas SIG de erupciones volcánicas generadoras de plataformas costeras: el volcán de Montaña del Tesoro (El Hierro, Islas Canarias).

Rodríguez-González, A., Perez-Torrado, F. J., Fernandez-Turiel, J. L., Aulinas, M., Paris, R., Moreno-Medina, C. (2018). The Holocene volcanism of Gran Canaria (Canary Islands, Spain). Journal of Maps, 14(2), 620-629.

Saupé, F., Strappa, O., Coppens, R., Guillet, B., Jaegy, R. (1980). A possible source of error in ^{14}C dates: volcanic emanations (examples from the Monte Amiata district, provinces of Grosseto and Sienna, Italy). Radiocarbon 22:525–531.

Scaini, C., Felpeto, A., Martí, J., Carniel, R. (2014). A GIS-based methodology for the estimation of potential volcanic damage and its application to Tenerife Island, Spain. J. Volcanol. Geotherm. Res. 278–279, 40–58

Sigmarsson, O., Laporte, D., Devouard, B., Martí J., Devidal, J.L., Carpentier M. (2012). Formation of U-depleted rhyolite from a basanite at El Hierro, Canary Islands, Contrib. Min. Pet., 165, 601-622; doi:10.1007/s00410-012-0826-5.

Sobradelo, R., Martí, J. (2010). Bayesian event tree for long-term volcanic hazard assessment: Application to Teide-Pico Viejo stratovolcanoes, Tenerife, Canary Islands, J. Geophys. Res., 115, B05206, doi:10.1029/2009JB006566, 2010.

Sobradelo, R., Martí, J., Mendoza-Rosas, A. T., Gómez, G. (2011). Volcanic hazard assessment for the Canary Islands (Spain) using extreme value theory. Natural Hazards and Earth System Sciences, 11(10), 2741-2753.

Stroncik, N. A., Klügel, A., Hansteen, T. H. (2009). The magmatic plumbing system beneath El Hierro (Canary Islands): constraints from phenocrysts and naturally quenched basaltic glasses in submarine rocks. Contributions to Mineralogy and Petrology, 157(5), 593.

Stuiver, M., Reimer, P.J., Reimer, R.W. (2020). CALIB 7.1 [WWW program]

Széréméta, N., Laj, C., Guillou, H., Kissel, C., Mazaud, A., Carracedo, J. C. (1999). Geomagnetic paleosecular variation in the Brunhes period, from the island of El Hierro (Canary Islands). Earth and Planetary Science Letters, 165(3-4), 241-253.

Takaoka N. (1989) Problem in K–Ar dating of Quaternary volcanic rocks J. Mass Spectr. Soc. Japan, 37, pp. 343-351

Troll, V., Carracedo, J. C. (2016). The geology of El Hierro. In Editors(s): Troll, R. V., Carracedo, J. C., The geology of Canary Islands. Elsevier, Amsterdam, 43-99.

Troll, V.R., A. Klügel, M.-A. Longpré, S. Burchardt, S., F.M. Deegan, J.C. Carracedo, S. et al., (2012). Floating sandstones off El Hierro (Canary Islands, Spain): The peculiar case of the October 2011 eruption, Solid Earth Discussion, 3, 975-999; doi:10.5194/sed- 3-975-2011.

Urgelés, R., Canals, M., Baraza, J., Alonso, B. (1996). The submarine" El Golfo" debris avalanche and the Canary debris flow, West Hierro lsland: The last major slides in the Canary archipelago.

Urgelés, R., Canals, M., Baraza, J., Alonso, B., Masson, D.G. (1997). The last major megalandslides in the Canary Islands: the El Golfo debris avalanche and the Canary debris flow, west Hierro Island. J. Geophys. Res. 102, 305323

Velasco-Vazquez, F., Ruíz Gonzalez, T., Sanchez Perera, S. (2005). El lugar de los antepasados. La necropolis bimbape de Monta~na Lajura. El Hierro. Cabildo Insular de El Hierro.

von Humboldt, A. (1814). Voyage de Humboldt et Bonpland. Premie`re Partie. Relation Historique. Tome Premier. G. Dufour et Comp., Rue des Mathurins-Saint-Jaques 7, Paris.

Villasante-Marcos, V., Pavón-Carrasco, F. J. (2014). Palaeomagnetic constraints on the age of Lomo Negro volcanic eruption (El Hierro, Canary Islands). Geophysical Journal International, 199(3), 1497-1514.

Walter, T.R., Troll, V.R. (2003). Experiments on rift zone formation in unstable volcanic edifices. J. Volcanol. Geoth. Res. 127, 107120.

Wood C. A. (1980). Morphometric analysis of cinder cone degradation. J. Volcanol. Geotherm. Res. 8, 2-4, 137 60.

Zijderveld, J.D.A. (1967) AC Demagnetization of Rocks: Analysis of Results. In: Runcorn, S.K., Creer, K.M. and Collinson, D.W., Eds., Methods in Palaeomagnetism, Elsevier, Amsterdam, 254-286.

PART III

5 Palaeomagnetic estimate of emplacement temperature of pyroclastic flows from El Fuego eruption

5.1 Geological Setting of El Fuego volcano

El Fuego volcano (Guatemala) is a 3,763-m-high stratocone located in the basaltic-andesite Central American Volcanic Arc (CAVA). It is located close to the triple junction of the North American, Cocos, and Caribbean tectonic plates, where the Cocos plate subducts under the Caribbean plate (Fig. 5.1; *Rose et al., 1978; Carr et al., 2002; Álvarez-Gómez et al., 2008; Authemayou et al., 2011*).

The CAVA is controlled by a complex interaction between compressive and translational forces (*Álvarez- Gómez et al., 2008; Authemayou et al., 2011*) and is divided into seven segments of volcanic lineaments. Fuego volcano lies in the northern sector (*Stoiber and Carr, 1973; Burkart and Self, 1985)* and is part of Fuego-Acatenango massif, a volcanic complex also including Ancient Acatenango, Yepocapa, Pico Mayor de Acatenango and Meseta eruptive centres aligned along a north-south trend perpendicular to the CAVA trend (Fig. 5.2a; *Basset, 1996*; *Vallance et al., 2001*).

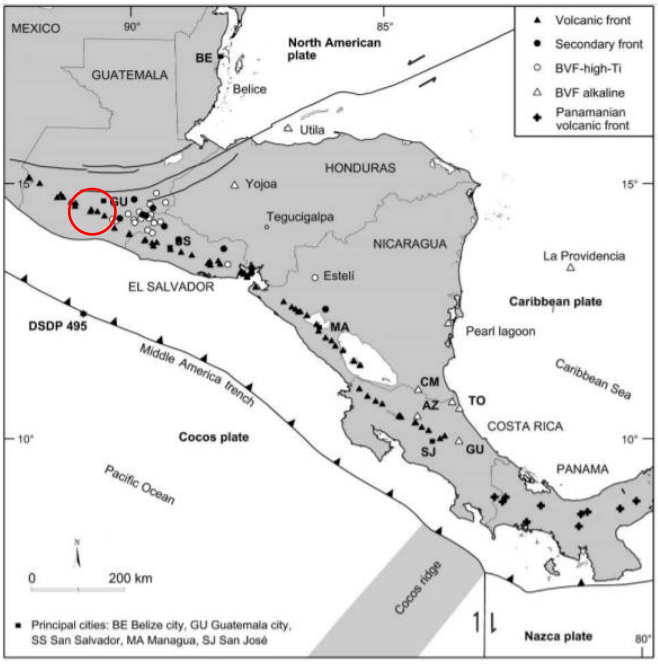

Fig. 5.1 Volcanological framework of Central America from *Carr et al. (2007).* CM is Cerro Mercedes, AZ is Aguas Zarcas, GU is Guayacán and TO is Tortugero. Red circle indicated the position of El Fuego volcano.

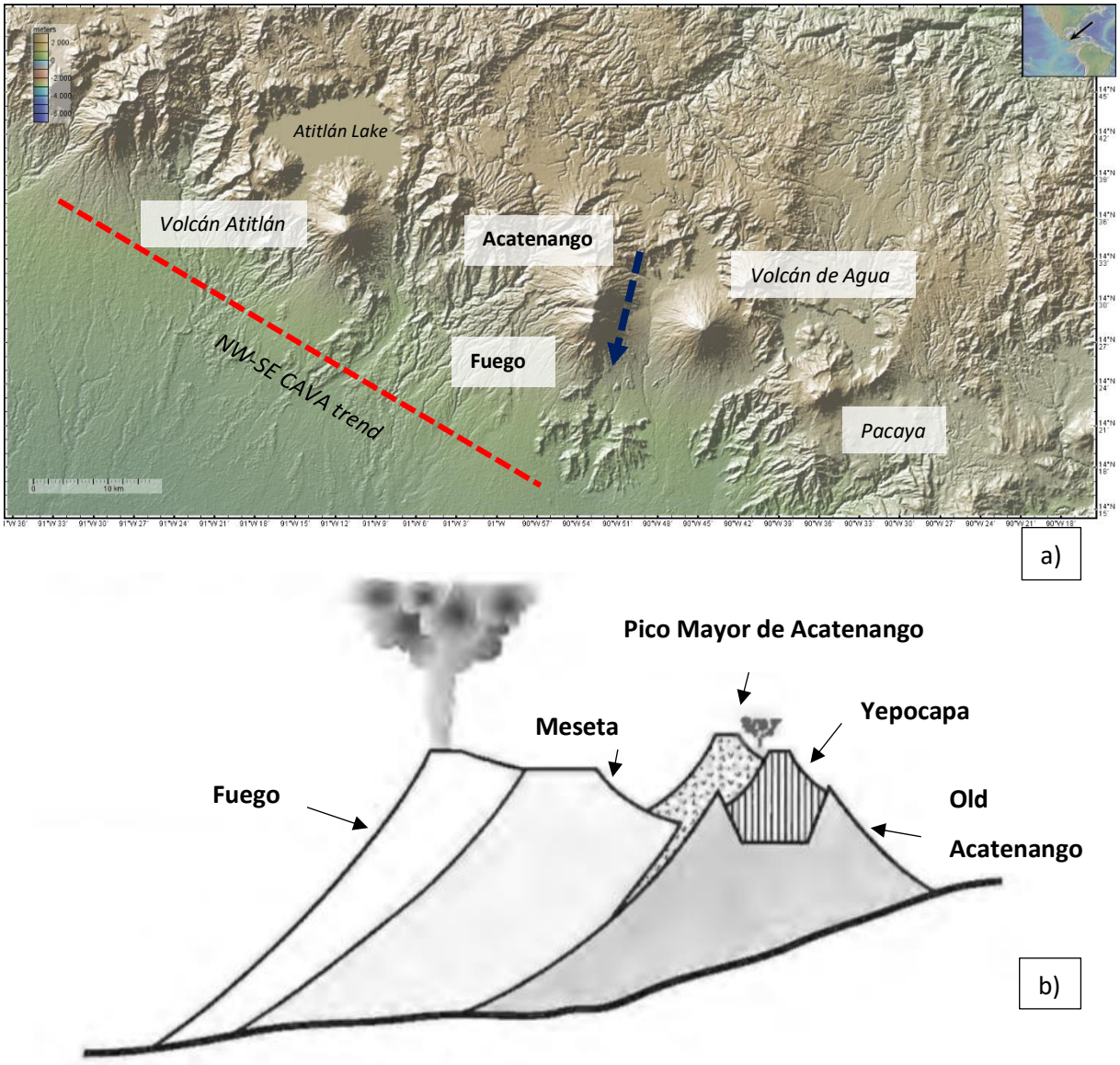

Fig. 5.2 a) Fuego and nearby volcanoes (from GeoMapApp 3.6.1). Colours represent meters above and under sea level. Red and blue lines indicate the Central American volcanic arc (CAVA) and Fuego-Acatenango trends, respectively. b) Schematic illustration of the Fuego-Acatenango massif showing the main vents. (modified from *Basset, 1996*). Plumes indicate vents active in historic time.

The oldest volcanic activity at this complex is given by a lava flow dated at 234 ± 31 ka, but most of the complex was built after the Los Chocoyos ash eruption from nearby Atitlán volcano (which hosts the modern Lake Atitlán), dated at 84 ka (*VanKirk and Bassett-VanKirk, 1996; Vallance et al., 2001*). At least two flank collapse events have occurred: the most recent is the collapse of La Meseta's eastern flank, between 30 and 8.5 ka (*Vallance et al., 1995*). This flank failure extinguished the activity of La Meseta volcano, allowing for the development of the Fuego edifice (*Martin and Rose, 1981; Vallance et al., 2001*).

The Fuego volcano, one of the most active volcanoes of Central America (*GVP, 2018*), is characterized by very steep (30°– 40°) slopes (*Escobar-Wolf, 2013; GVP, 2018*). The activity of Fuego has been mainly characterized by the emission of basaltic and basaltic-andesitic products, but some of the older rocks are more silicic (Fig. 5.3; *Chesner and Rose, 1984*).

The prehistoric eruptive activity is poorly constrained and stratigraphic data are scarce. Pyroclastic flows have been dated with ^{14}C at 5370 ± 50, 3560 ± 70, 2170 ± 30, 1375 ± 45, 1050 ± 70, and 980 ± 50 years BP (*Vallance et al., 2001; Escobar-Wolf, 2013*).

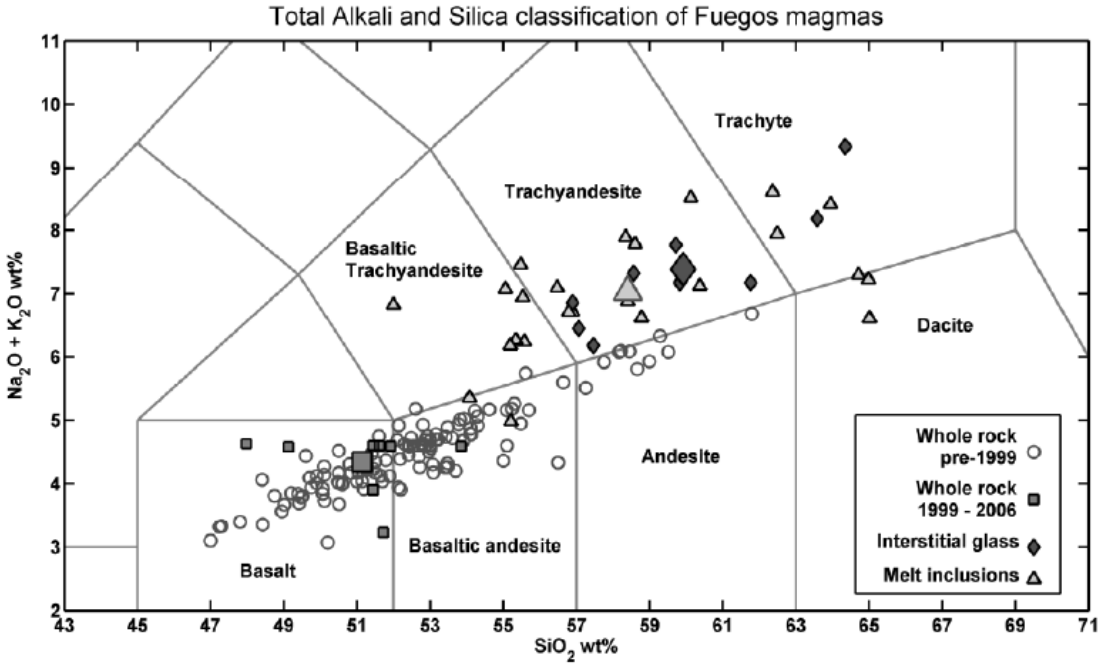

Fig. 5.3 Total alkali-silica (TAS) rock classification diagram with pre-1999 and 1999–2013 rock compositions of Fuego magmas (from *Escobar-Wolf, 2013)*. 1999–2013 rock compositions are published by *Berlo et al. (2012)*; pre-1999 whole-rock compositions are from the RU_CAGeochem database (http://www.iedadata.org/doi?id=100263).

Since the first documented historic eruption of 1524 AD, over 50 violent strombolian and sub-Plinian eruptions of VEI ≥ 2 occurred (*Kurtz, 1913; Rose et al., 2008; Berlo et al., 2012; Waite et al., 2013; Escobar-Wolf, 2013*).

Since 1999, Fuego has been in an eruptive phase characterized by periods of persistent degassing, low-intensity strombolian eruptions, ash-rich explosions and lava flows, punctuated by occasional paroxysms (*Patrick et al., 2007; Lyons et al., 2010; INSIVUMEH, 2012a, 2012b*). The paroxysmal eruptions typically begin with lava effusion and increasing strombolian activity, followed by a phase of sustained explosivity forming a convective plume and small PDCs, before waning (*Naismith et al., 2019*).

From 2015 to 2018, Fuego's volcanic activity was characterized by continuous, mild to strongly energetic, strombolian and fountaining activity, ejecting ash, lapilli and bombs that accumulated on the upper part of the cone. Several lava flows were also produced, mainly funnelled in the Santa Teresa and Las Lajas drainages (in Fig. 5.8), and pyroclastic flows descended into the main valleys (Las Lajas, Trinidad and Santa Teresa valleys). A larger explosive eruption occurred in 2017, during which several pyroclastic flows descending Las Lajas, Trinidad, Ceniza and Santa Teresa valleys, causing the evacuation of some communities. PDCs represent the main hazard for more than 50,000 people that live within 10 km of the volcano and near the radial valleys (*Naismith et al., 2019*).

PDCs are rapidly flowing mixtures of hot volcanic particles and gas that originate from a variety of eruption styles, including pyroclastic fountaining, lateral blasts, and collapse of lava-domes *(Druitt, 1998; Branney and Kokelaar, 2002*). They can transport large volumes of hot debris for several kilometres, depending upon the current's mass flux, the height of any pyroclastic fountaining, the particle concentration and sorting, the topography, and the rates of air ingestion and pyroclastic sedimentation during transport (*Branney and Kokelaar, 2002*). Numerous studies have interpreted depositional facies of PDC deposits (*Sparks et al., 1973; Wilson, 1985; Branney and Kokelaar, 1992; Buesch, 1992; Druitt, 1992; Boudon et al., 1993*; *Sparks et al., 1997; Calder et al., 2000; Gurioli et al., 2002; Saucedo et al., 2004; Cole et al., 2005; Lube et al., 2007; Charbonnier and Gertisser, 2011; Brand et al., 2014*), but there are few reports on the contribution to the PDC mass flux by the incorporation of surface rocks, which can happen by a variety of mechanisms, including collapse, avalanching or erosional entrainment (*Fisher, 1977; Rowley et al., 1981; Wilson, 1985; Kieffer and Sturtevant, 1988; Suzuki-Kamata, 1988; Buesch, 1992; Sparks et al., 1997; Cole et al., 1998; Calder et al., 2000; Brown and Branney, 2004; Mangeney et al., 2010; Farin et al., 2013*).

The June 3rd, 2018 eruption was unexpected for its size and consequences. It formed a 16-km-high sub-plinian eruption column (*Naismith et al., 2019*) and small PDCs along radial valleys; one significantly larger PDC travelled more than 12 km along the Las Lajas valley to the east-southeast (Fig. 5.4), much farther than those from recent previous eruptions (*Naismith et al., 2019*), and buried the village of San Miguel de Los Lotes (San Miguel, hereinafter, 750 m a.s.l.) and caused the deaths of more than two hundred people. This event was accompanied by the formation of a collapse scar from 3,600 to 2,600 m a.s.l. at

the head of the Las Lajas valley, just below the summit of the volcano. Two other radial valleys show some evidence of headwall erosion; however, these are smaller than the collapse scar above the Las Lajas valley, and extensive block-and-ash flow deposits downhill are lacking.

This work reports on an investigation of part of the 2018 Las Lajas block-and-ash flow deposits, mainly regarding a palaeomagnetic study to estimate the emplacement temperatures of PDCs, as well as the source of the materials forming the flows. The aim is to better understand how the fatal PDC originated, to account for its unexpected runout distance, and thereby to help improve the evaluation of hazards at other steep-sided volcanoes.

Fig. 5.4 Photo of Las Lajas gorge after the 3rd June 2018 eruption (from https://medium.com/@UNDP/volc%C3%A1n-de-fuego-inside-the-emergency-response-e0f280834eff).

5.1 Eruption chronology

The 3rd June 2018 volcanic eruption started with features similar to the previous 73 paroxysms (*Lyons et al., 2010*).

The eruption began at 6:00 AM (local time), with strong explosions accompanied by loud rumbling and shockwaves felt by the population. During the morning, the intensity of the

eruption increased and, at 10:00 AM, some pyroclastic flows were reported by INSIVUMEH in Seca, Santa Teresa and Ceniza valleys.

The sustained explosive activity occurred between 11:30 AM and 1:30 PM and reached its acme at 1:10 PM, when the sub-plinian convective plume reached an elevation of ~17 km-high a.s.l. (Fig. 5.5; *Pardini et al., 2019*). During this time interval (between 11:20 and 12:50 AM), the fallout of coarse lapilli occurred on Acatenango volcano (3 km north of Fuego).

After 1:00 PM, despite the intensity of the convective plume starting to decrease, PDC activity continued, and currents moved past La Reunion Golf Resort (LRGR). Just before 2:00 PM, PDCs were observed descending into Seca, Ceniza, Taniluya and Honda valleys and, by 2:24 PM, large PDCs accompanied by moderate convection were filmed descending the in Las Lajas gorge, reaching the bridge along the main road (Ruta Nacional 14, RN-14; Fig. 5.6a) for the first time, filling the channel below the bridge but leaving the bridge still intact.

Between 3:00 and 3:30 PM, when the top of the volcano was hidden in the clouds, PDCs descended again in Las Lajas gorge, spilling over the side of the valley, destroying the bridge, and flowing southwards down a smaller valley to the village of San Miguel, where most of the houses and people were buried.

Filmed images indicate that PDCs first arrived at the Las Lajas bridge on RN-14 between 2:00 and 3:00 PM, when local smartphone footage filmed a fresh, stationary, steaming PDC deposit next to the bridge (Fig. 5.6b). Around 3:09 PM (Fig. 5.6c), a new dilute turbulent cloud of ash and gas descended the Las Lajas gorge, again reaching the bridge. A few minutes later (Fig. 5.6d), the flow passing the bridge visibly waxed, reaching lateral sections of the bridge and overwhelming onlookers on the road hundreds of meters away from and uphill from the bridge, resulting in several casualties. The sudden and simultaneous widening of the flow fronts along the segment of the RN-14 both downhill and uphill suggests that the PDC fronts had quickly widened, spilling laterally beyond the main channel of the Las Lajas valley.

After 3:30 PM, the PDC activity rapidly declined. A second convective plume, possibly of co-ignimbritic origin began at 3:30 PM and reached an elevation of 13-14 km a.s.l. After 4:30 PM the activity decreased.

According to the bulletin reports (GVP, 2013), from 2015 to 2017, the Fuego's activity was continuous and mainly characterized by strombolian -from moderate to intense- activity,

producing lava fountains, lava and pyroclastic flows. Satellite images show that the products (ash, blocks, bombs, and lavas) of this three-year activity filled the steep channels in the upper part of the Las Lajas, in Trinidad, Santa Teresa and Honda valleys, which appeared partially or completely emptied immediately after the eruption (Fig. 5.7).

The June 3rd, 2018, eruption was the largest eruption of the current phase, with an estimated total ejected volume for vent-derived material of 0.04 ± 0.01 km^3 dense rock equivalent (*Pardini et al., 2019*). The volume of PDC deposits from this eruption within the Las Lajas valley has been estimated to be 0.02-0.03 km^3 (*Naismith et al., 2019*).

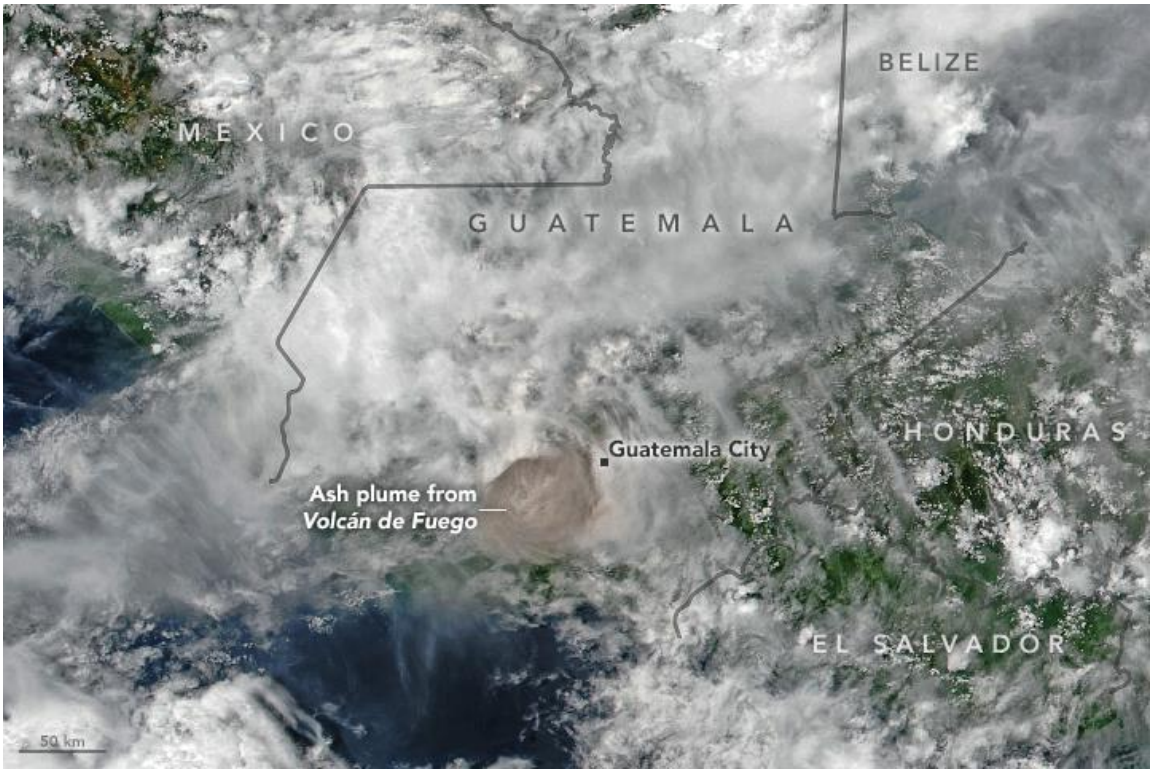

Fig. 5.5 The Visible Infrared Imaging Radiometer Suite (VIIRS) on Suomi NPP acquired this image of the ash plume at 1 p.m. local time (19:00 UT) on June 3, 2018, after the ash (brown) had punched through a deck of clouds (Nasa image from https://disasters.nasa.gov/mount-fuego-eruption-2018).

Fig. 5.6 Frames extracted from eyewitness video (video by Leonid Rosas and Jiuwit Rosas, https://www.youtube.com/watch?v=uQyMq6BdXSo). a) Pyroclastic flows seen from San Juan Alotenango, at 2.24 pm. b) Road bridge along the RN-14 filled by pyroclastic flows at 3.01 PM. c) Arrival of another pyroclastic flow overwhelming the bridge at 3.09 PM. d) Pyroclastic flows invested San Miguel de Los Lotes village.

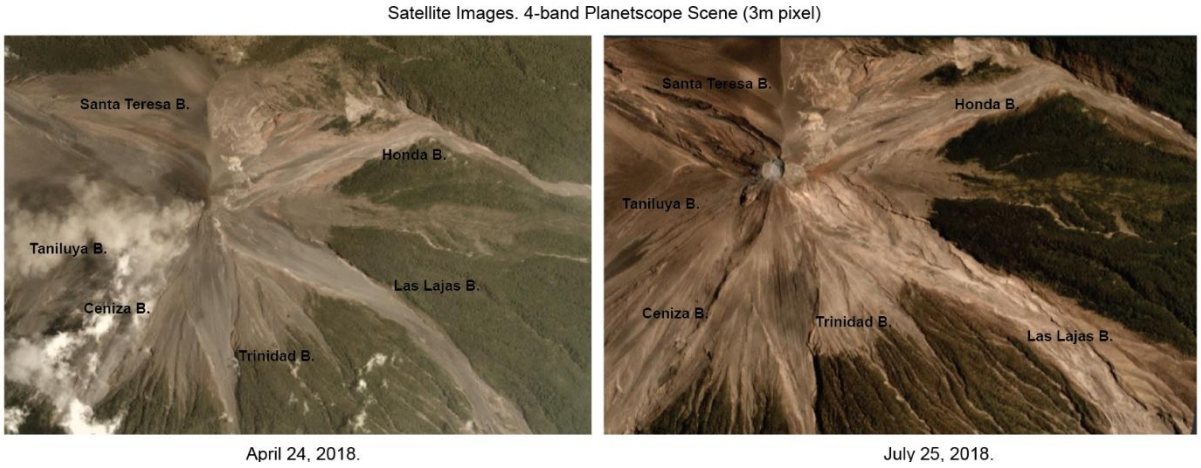

Fig. 5.7 Planetscope satellite images (3m-wide pixel) focused on the Fuego summit and the nearby gorges, obtained before (April 24th, 2018) and after (July 25th, 2018) the eruption. B.= barranca (gorge).

5.3 Sampling and Methods

The complete description of the estimate of T_{emp} using palaeomagnetism is explained in paragraph 2.3: here, a summary is presented.

Accidental volcanic blocks entrained from the substrate or conduit walls contain ferromagnetic minerals with an original magnetic remanence acquired when the rock

initially cooled, some geologic time before the PDC event under consideration. Upon subsequent incorporation into a hot PDC, they are randomly rotated and reheated, effectively producing a thermal demagnetization event. They are then deposited in their final position and continue -or they may reach thermal equilibrium while in the current -, to be re-heated during thermal equilibration to a temperature close to the mean temperature of the initially hot deposit. This erases a portion of the magnetic remanence carried by ferromagnetic grains that have T_b lower than the temperature of the PDC. The time taken to reach the equilibrium temperature depends on the size of the blocks (*Zanella et al., 2015* and reference therein); the larger the lithic clast, the longer time required for thermal equilibrium to be reached (*Marti et al., 1991*; *Cioni et al., 2004*). As the PDC deposit cools, the blocks acquire a new, partial Low-T_b thermal magnetization, oriented along the local Earth's magnetic field direction at the time of cooling. The resultant clasts thus have two magnetic components: a High-T_b component that is randomly oriented because the blocks were rotated in the PDC and emplaced randomly after having acquired it at source; and a Low-T_b component that was acquired during the cooling in situ within the PDC deposit. Different blocks (as well as the entire deposit) within the same deposit thus share the same Low-T_b orientation. The T_r of each clast is estimated to lie between the highest blocking temperature of the Low-T_b component and the lowest blocking temperature of the High-T_b component.

For this study, five sites (FGO12, 06, 08, 13, and 14; Fig. 5.8 and 5.9) upstream of San Miguel village, from north to south within the Las Lajas valley (site information in Table 6), were sampled.

The deposits (between 2 and 15 m thick) were mostly sampled in the middle of the sections. One hundred and fifty-two clasts were collected, of which 125 small hand samples (from 1 to 6 cm, ~4 cm diameter on average, except for one clast -FGO1232- that was 21 cm in diameter). Small samples were selected to minimise thermal heterogeneity effects. For this reason, the definition of T_{emp} from *McClelland et al. (2004)*, which consider the lowest value of the T_r of the sampled clasts, was used. Blocks larger than a few tens of centimetres in diameter were discarded, as they can record an uneven temperature distribution (*Marti et al., 1991; Bardot, 2000*). Thermal heterogeneity (i.e. block temperature different than

deposit temperature) was considered for a limited number (27) of drilled larger blocks (7–67 cm diameter, 21 cm diameter on average).

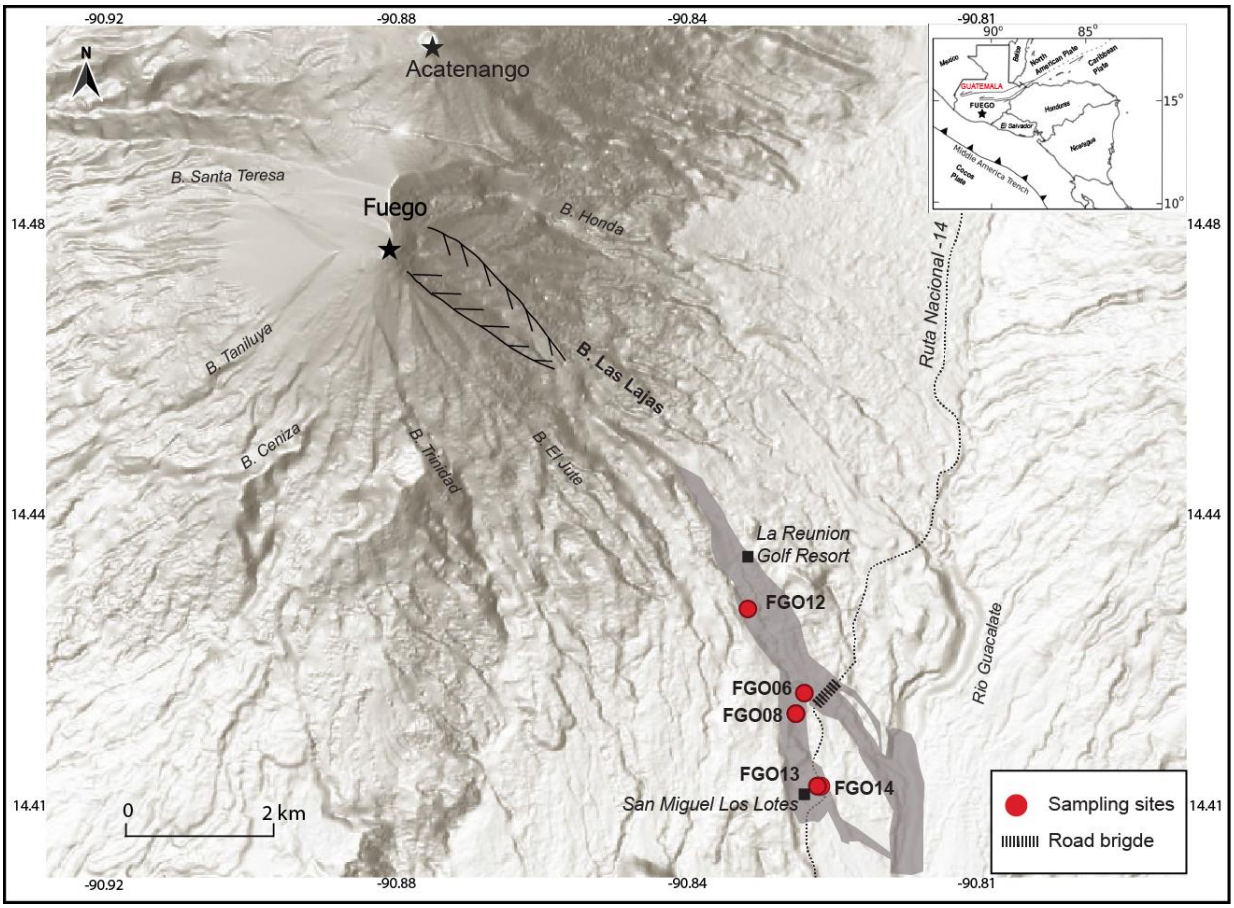

Fig. 5.8 Map of El Fuego volcano, Guatemala (with an inset for general location) showing sites mentioned in the text, and the small radial valleys, including the Las Lajas valley along which the June 2018 PDC travelled, destroying the village of San Miguel de Los Lotes. In dark grey the Las Lajas deposit path is shown. Red dots refer to sampling sites; the segmented line is the Las Lajas road bridge; the dotted line is the Ruta Nacional, RN-14.

Hand sampling was done following the methods of *Lesti et al. (2011)* and *Trolese et al. (2017)*: the dip azimuth and dip value of a roughly flat clast surface were measured in situ using a magnetic compass and a clinometer. Cores of 2.5 cm- diameter were drilled and oriented in situ by both a magnetic and a sun compass.

As the distinction between juvenile and accidental clasts was not readily apparent, all clast types were sampled. Clasts were grouped into four field categories: (1) grey scoria, (2) red scoria (vesicular rounded clasts, with rare white microphenocrysts), (3) grey lava, and (4) red lava (non-vesicular angular or subangular lavas, with rare white phenocrysts). We sampled 79 grey scoria, 23 red scoria, 45 grey lava, and 5 red lava clasts (Table 6).

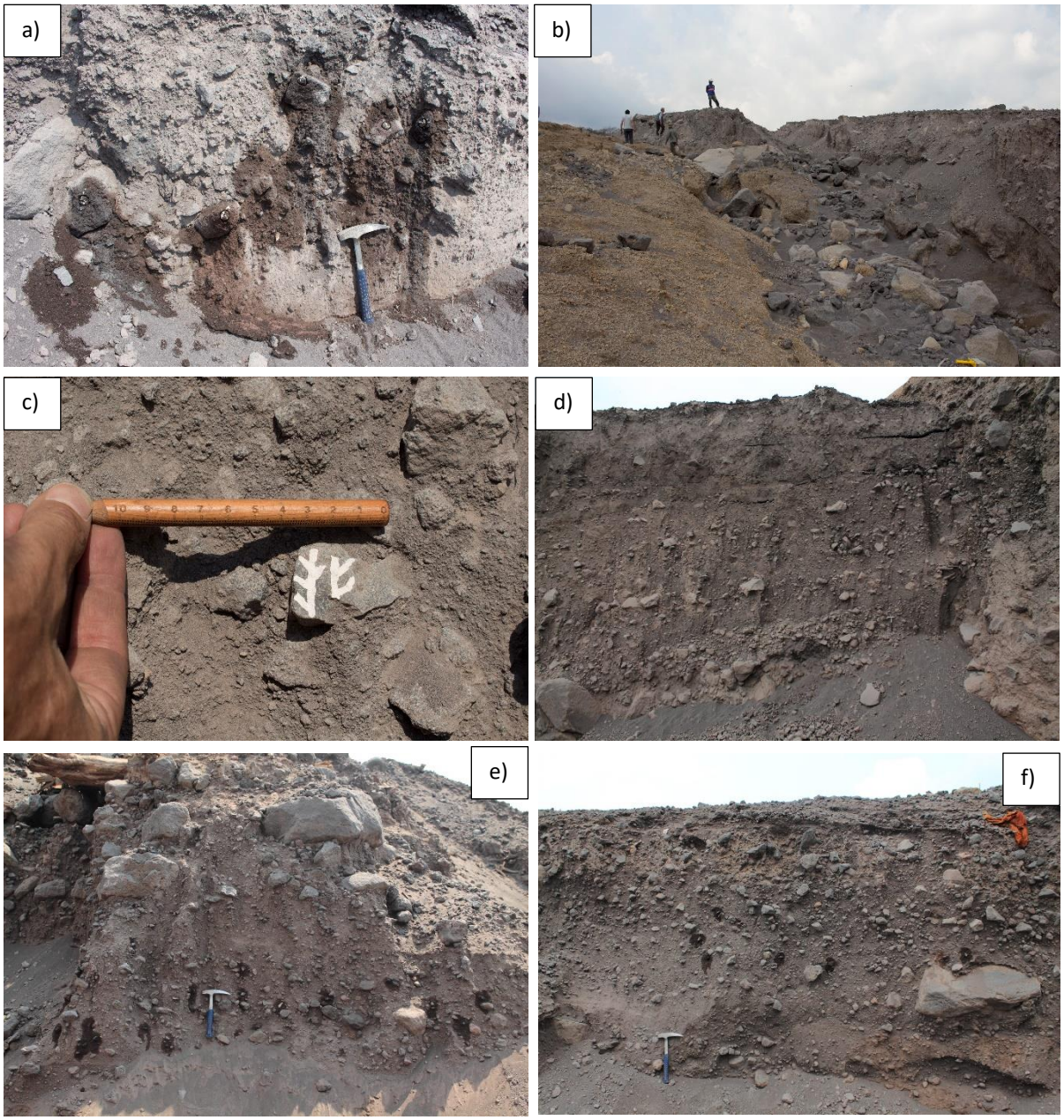

Fig. 5.9 Photos of sampled deposit. a) Drilled cores in FGO12 site. b) FGO08 site. c) Hand sample collected in FGO08 site. d) FGO06 site. e) FGO13 site. f) FGO14 site.

Hand samples and drill cores were cut into 2-cm cubes and 2-cm-long cylindrical specimens, respectively. To evaluate the temperature differences between the inner and outer parts of the few larger (>10 cm) drilled blocks, cores were cut into three sections, and both the external and internal sections were analysed (*Bardot and McClelland, 2000; Porreca et al., 2008*). A total of 54 specimens from cylindrical cores were examined. Inner and outer core extremities were cut in thinner 1 cm-long specimens, to assess the rock thermal behaviour both near the clast surface and at the clast centre.

Thermal demagnetization of all samples was performed using sixteen demagnetization steps from room temperature to 590°C (the first step was set at 100°C), systematically heating samples for 30‘ after having reached rock temperature equilibration. As the deposit temperature was expected to be around 200-300°C, smaller 30°C temperature steps were selected from 100 to 430°C, and larger 40°C steps for higher temperatures. According to *Paterson et al. (2010*), based on the relations between the deposit age and the minimum palaeomagnetic T_{emp}, considering clasts with SD magnetite and Ti-poor magnetite from a 1-year-old deposit, the minimum emplacement temperature that can be estimated is ~100 °C. For this reason, the first demagnetization step was set at 100 °C.

Five samples that could not be demagnetized at 590°C (FGO0615, FGO0807, 15, 23, FGO1412) were heated to 640°C. After each temperature step, the NRM of each sample was measured, and after every three steps of thermal demagnetization, the bulk susceptibility was also measured, to evaluate possible mineralogical changes occurring during heating.

To investigate possible CRM by post-emplacement growth of secondary magnetic minerals (e.g., *Porreca et al., 2008*), the variation of the low-field magnetic susceptibility during heating and cooling cycles in air, from room temperature up to 700°C on crushed powders, for two specimens per lithological group was measured.

Thermal demagnetization data were plotted on orthogonal demagnetization diagrams (*Zijderveld, 1967*) and equal-area stereographic projections and the magnetization components were isolated by principal component analysis (*Kirschvink, 1980*).

Table 6. Location of the Sampling Sites at El Fuego Volcano (Guatemala), and synthesis of the estimated deposit temperatures.

Site	**Latitude,**	**Longitude,**	**N°**	**N°**	**Clast type**				**Clast type**				**T_{emp} (°C)**	**T_{emp} (°C)**
Code	**N°**	**W°**	**Hand samples**	**cores**	**hand samples**				**cores**				**Hand samples**	**Cores**
					GS	**GL**	**RS**	**RL**	**GS**	**GL**	**RS**	**RL**		
FGO12	14.431207	90.836831	21 *Lw*	13 *Lw*	10	6	5	0	4	7	1	1	250	100/190-220
			21 U*p*	4 U*p*	14	4	3	0	0	3	0	1	280	100/310-430
FGO06	14.420898	90.830135	20		14	5	0	1					220-280	
FGO08	14.418387	90.831160	24	10	14	2	7	1	4	2	3	1	250	220
FGO13	14.409516	90.828483	20		11	7	2	0					250	
FGO14	14.409450	90.828187	19		8	9	2	0					280	

Site coordinates were gathered by a Garmin GPS, using the WGS84 datum. N, number of samples. GS, grey scoria; GL, grey lava; RS, red scoria; RL, red lava. Lw, lower lever, Up, upper level.

5.4 Results

5.4.1 Stratigraphy of PDC deposits

As described in the 5.1 paragraph, this study is focused on the PDC deposits in the Las Lajas valley adjacent to the LRGR, and in the small branch that runs south through San Miguel. It was in these areas that the PDCs interacted with buildings and inhabitants. The loose PDC deposits of the June 2018 eruption had been fluvially incised during the 2018 wet season, which exposed the deposit facies and lateral variations, and produced some lahar deposits. A synthetic description of the stratigraphy of the PDC deposits follows.

The PDC deposit distribution was ribbon shaped along the valleys, thickest in the river channel and thinning laterally, locally pinching out abruptly at vertical channel sides with evidence of scouring. They contained no pumice, and therefore the PDC was classified as block-and-ash flow, although the blocks were dominantly basaltic andesite lavas of diverse grain size and crystal content, with fresh and altered scoria of similar composition. The deposits comprise massive, very poorly sorted, heterolithic lapilli-tuff and breccia up to 15 m thick, and with angular and sub-rounded lapilli and blocks of lava (most < 1 m in size; but some > 1.5 m), supported in an ash matrix of similar composition. The deposit contains scattered alluvial cobbles and abraded, allochthonous tree branches.

The PDC deposits can be referred to three principal facies: (1) **Valley-floor deposits**, mainly coarse and up to tens of meters in thickness (valley-confined facies); (2) **thinner deposits** outside the valley floor (overbank facies); and 3) **thin** (<20 cm) **stratified ash cloud deposits**, mostly preserved away from the valley axis.

(1) **The valley-floor deposits** are the coarsest ones, with blocks up to 1.5 m in diameter (Fig. 5.10a). They are observed between 900 and 1150 m a.s.l. The structure varies from massive to weakly normal graded, without any centimetric ground layer beds at the base. However, in some cases, at various heights in the sequence, laterally continuous levels have been noted, characterized by significant granulometric changes. These changes do not indicate pauses in the PDC activity and overlapping of several flow units because of the lack of sharp granulometric variations or discrete ash layers between the units. Sporadically, in the lower sections of the sequence, directly in contact with the 2018 soil, are clast-

supported lenses, a couple of meters thick and tens of meters laterally, composed of strongly angular lava blocks are lenses (Fig. 5.10b). These lenses can be referred as the Jigsaw-type facies of dry volcanic debris avalanche.

(2) **The thinner deposits** outside the valley floor have severely affected the southern part of LRGR and the San Miguel village. These deposits have the same granulometric and structural characteristics of the first type; but they are set outside the main gorges, and their thickness is limited (<1 to 3 meters).

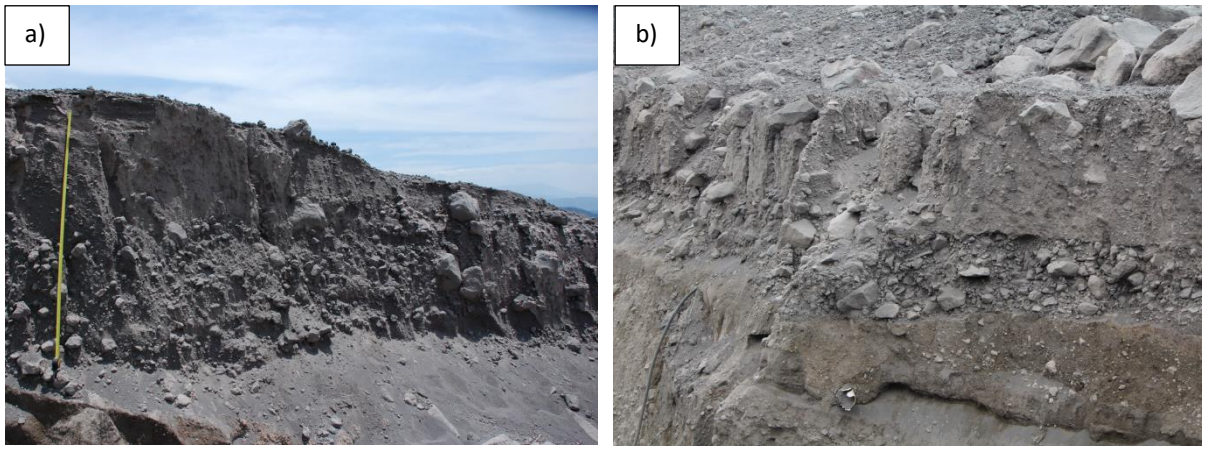

Fig. 5.10 Photos of the valley-floor deposits. (a) Valley-floor PDC deposits (scale is 2 m), 1 km upstream of San Miguel Los Lotes. (b) Clast supported depositional facies, composed of strongly angular lavas blocks observed close to LRGR.

The first deposits that covered San Miguel village are rich in tree trunks, torn from the northern wooded areas; trees affected by the lateral part of the flows remained in life position, but showing strongly abraded trunks up to 1 m high on the side facing the volcano and with abrupt termination upward (Fig. 5.11a). This indicates that the coarser portion of the flow travelled in the dense lower section of the transport system, but with limited thickness and scarce energy. Concentrated abrasion marks, up to 1-2 meters high above the previous soil level, were also noted on trees in life position and on the walls in the southern area of LRGR. Some edges of the reinforced-concrete structures were severely damaged, with the removal of the cement mortar and with the exposition of the metal inlays bent in the flow direction (Fig. 5.11b). Buildings in San Miguel appear partially buried (Fig. 5.12a), but little damaged by the dynamic action of the initial PDC.

Considering the coarseness of the deposits and the presence of metre-sized blocks, the limited mechanical effects indicate initial low flow velocity when it first reached the village. In the upper part of the built-up area, some trees in life position are broken off 1-2 m above the original soil level, suggesting that they were initially partly covered by 1-2 m of deposit, and subsequently broken as the flow velocity increased with time (Fig. 5.12b). The dilute portion that travelled above the coarse and reduced thickness avalanches was able to break the branches, but without any wood abrasion, confirming the abrupt disappearance of centimetric (or bigger) clasts suspended in the PDCs, dilute portions.

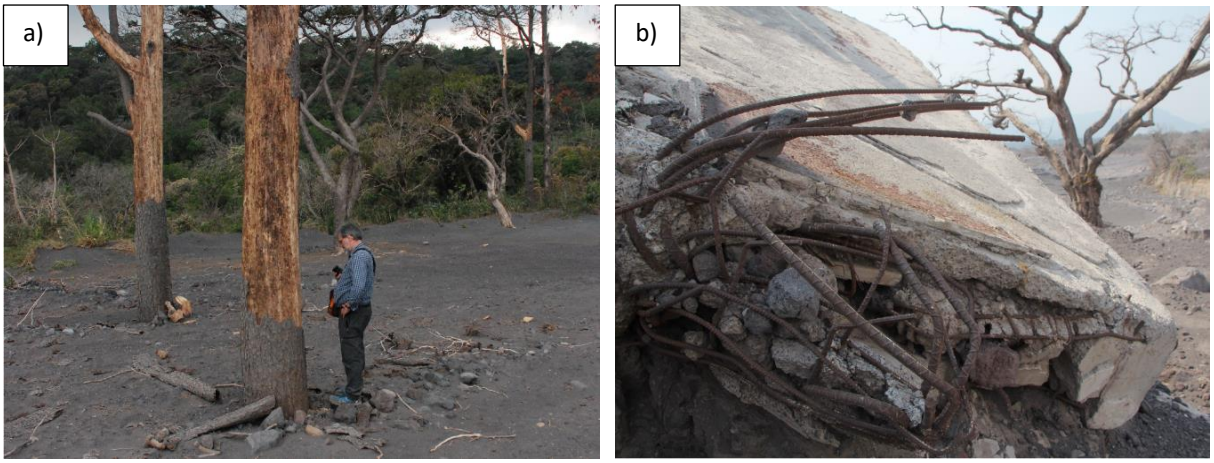

Fig. 5.11 a) Trees incorporated by the lateral part of the flows close to San Miguel Los Lotes, that remained in life position, showing strong abrasion on the side facing the volcano. b) reinforced-concrete structures severely damaged by the flow in LRGR, with the removal of the cement mortar and with the exposition of the metal inlays bent in the flow direction.

(3) **The thin stratified ash deposits** were discontinuous and subordinate at the base and lateral margins of “block-and-ash flow” deposits. At 1-2 km upstream of San Miguel village, they consist of centimetric and multi-centimetric ash and fine lapilli strata, with cross-bedded structure below the block-and-ash flow deposits of 1-2 meters thick (5.13a). These deposits tend to drape the topography (ash-cloud surge) for some tens to meters to the side of coarse deposits. Some fine ash layers, interstratified to the dune-bedded strata, are plane parallel, massive, and vesicular, and may represent ashfall from moist ash (probably a co-ignimbrite ash-fall). In the southern part of LRGR, one of these deposits consisted of a lower layer of massive, fine ash overlain by a layer of poorly sorted coarse ash and fine lapilli with dune-bedding, resting on a well-defined contact (Fig. 5.13b).

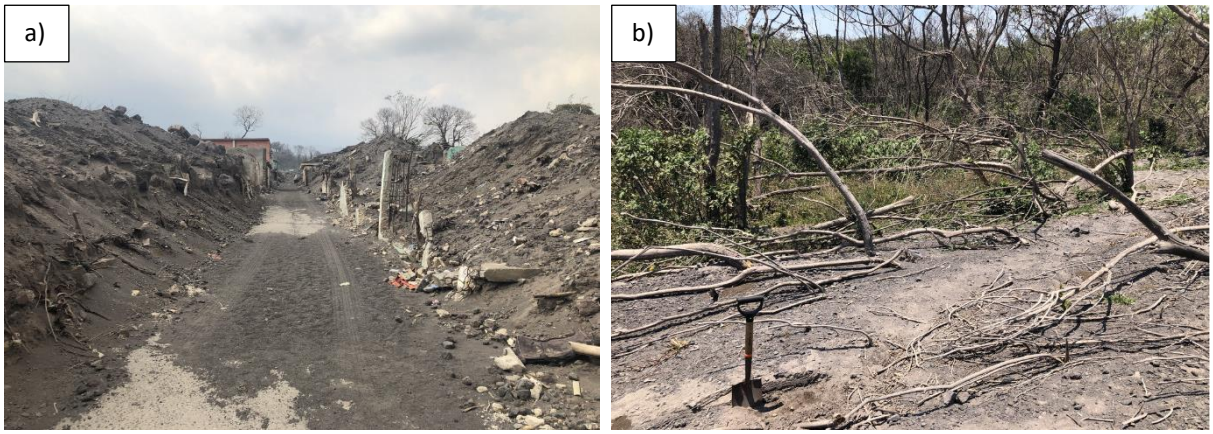

Fig. 5.12 a) Buildings in San Miguel partially buried, but little damaged by the dynamic action of the first-arrived PDCs. b) trees in life position in the upper part of the built-up area of San Miguel, bended or broken off at 1-2 m above the original soil level.

The upper ash-cloud deposit is probably ascribable to the most energetic phase, responsible for having pushed, due to the dynamic pressure, the reinforced-concrete wall bearing the LRGR initials (orthogonally oriented to the flow), and to have uncovered the LRGR structures located nearby (Fig. 5.13c). The stratified ash and fine lapilli deposits located upstream of San Miguel are accompanied by significant mechanical damage to the vegetation (tree felling in the flow direction, branch truncation and drying of the plants). These effects decrease with distance (10's to 100's m) away from the valley axis.

Near the valley axis, the contact with the substrate is locally erosional, with scour of the pre-2018 soil and, in some cases, of the bedrock. Farther from the valley axis, there is little evidence of erosion. The lowest few centimetres of the deposit commonly show reverse grading. When preserved along the valley axis, the top of the deposits is finer grained on average, with internal cross-bedding, and shows a general granulometric decline upwards, indicating a rapid decrease in the transport competence as flow waned. The preliminary field examination indicates a moderately elevated T_{emp} based upon the presence of few centimetres of dark film in the outer part of woody remains and singed zones, evidence of partial and/or total softening/melting of plastic materials in the village and the LRGR structures (Fig. 5.13d).

No rootless phreatic craters or phreatic pipes were observed. This agrees with the paucity of clasts with features indicating high temperature, such as radial jointing and/or glass rind produced by the abrupt cooling of clasts in contact with a cold matrix.

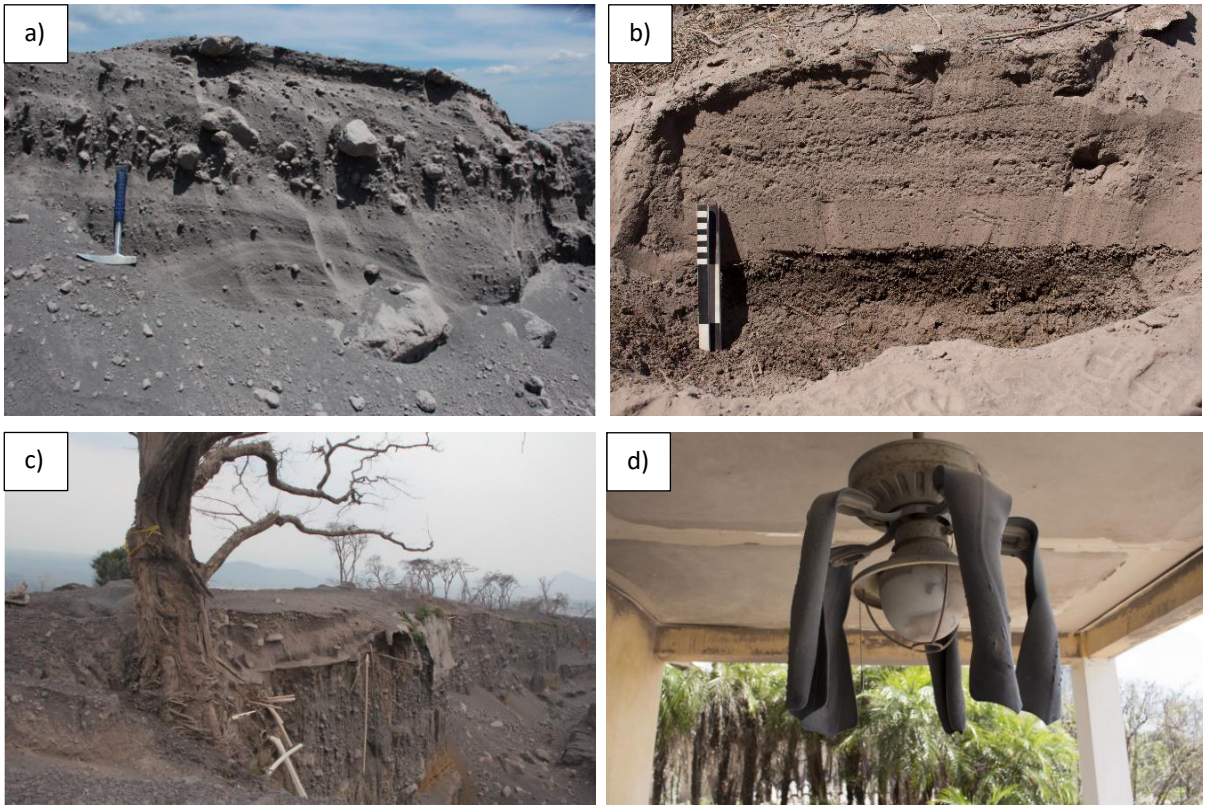

Fig. 5.13 a) Centimetric and pluri-centimetric ash and fine lapilli strata, with cross-bedded structure below the block and ash flow deposits observed 1-2 km upstream to San Miguel village. b) lower layer of massive, fine ash overlain by a layer of poorly sorted coarse ash and fine lapilli with dune-bedding, resting on with a clear-cut contact in the southern part of LRGR. c) uncovered structures, plastic pipes and electric cables swept away by the PDCs in LRGR. d) evidence of partial and/or total softening/melting of different plastic materials present in the village and the golf resort structures is shown by folding of a plastic roof fan.

5.4.2 Palaeomagnetic results

Thermomagnetic curves generally show reversible cycles (Fig. 5.14) except the grey lavas, which yielded lower susceptibility values in the cooling curves. Almost all samples showed Curie temperatures around 580°C, but a few specimens showed an inflection in the heating curve around 450°C. This indicates that all samples contain magnetite, and a few contain minor titanomagnetite. Bulk volume susceptibility values range between $5.5*10^{-2}$ and $1.0*10^{-1}$ SI, with no significant changes during heating, implying that there were no significant transformations of magnetic mineralogy (SF1 in Appendix III). NRM intensities of all clasts range from $2*10^{-3}$ to 140 A/m (17.8 A/m on average).

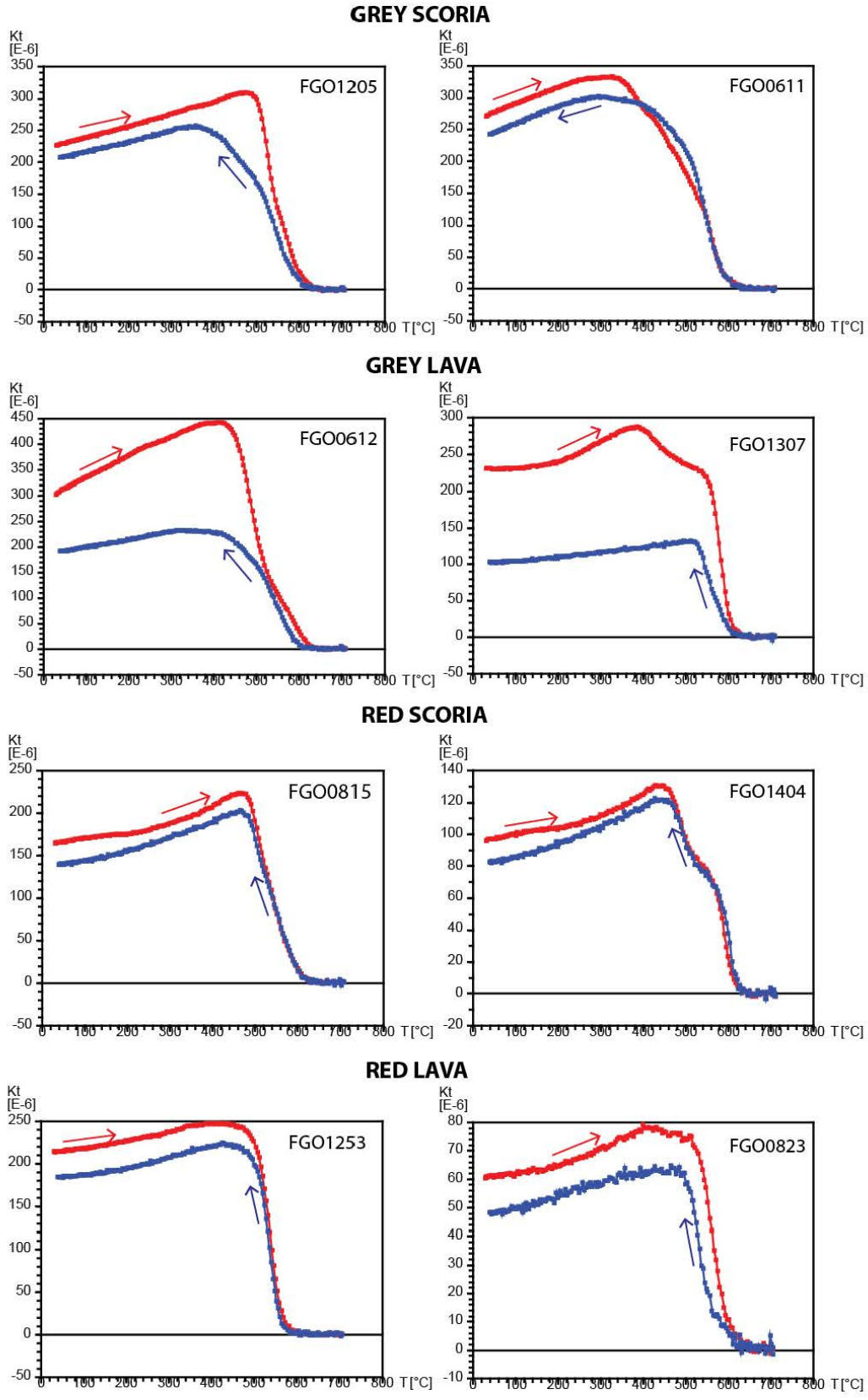

Fig. 5.14 Representative thermomagnetic cycles. *k* is the magnetic susceptibility and *T* is the temperature (°C). Red and blue arrows indicate the heating and cooling cycles, respectively.

The NRM demagnetization patterns have been grouped as in *McClelland et al. (2004)* (Fig. 5.15 a-b):

-Group 1*:* Clasts with a single magnetic component, subparallel to the 2018 geomagnetic field direction at El Fuego (D=1.2°, I=42°, IGRF model https://www.ngdc.noaa.gov/geomag/calculators/magcalc.shtml#igrfwmm). These clasts show only a magnetic component, until complete demagnetization (generally at 590°C; Fig. 5.15). They are thought to have been hotter than 590°C when they were deposited by the Las Lajas PDC. Only ~6% of all samples (of which ~66% of the hand specimens and ~33% of the drill cores) belong to this group.

-**Group 2:** Clasts with both low- and high-temperature components. This group includes samples with two straight-line segments in the orthogonal demagnetization diagram corresponding to two magnetization components (Fig. 5.15). The HT components are the original magnetization directions acquired before the eruption, now randomly orientated by the PDC, and the low-temperature components are the new partial thermoremanences subparallel to the 2018 Earth's magnetic field (Fig. 5.16). Some clasts (9 hand samples and 2 cores) show two high-temperature components. In some of them, the high and low-temperature components are separated by a curved path and the T_r is taken to lie in the temperature range between the highest T_b low-temperature component and the lowest T_b high-temperature component. About 39% of all the samples (of which 82% of the hand specimens and 18% of the drill cores) belong to Group 2.

-***Group 3*****:** Clasts with only a randomly oriented high-temperature component. Clasts in this group did not start demagnetising until being heated to 250-500 °C, and only a randomly oriented HT component could be isolated (Fig. 5.15). These clasts have been considered cooler than the lowest T_b of the high-temperature components isolated; they did not acquire an LT component sub-parallel to the local geomagnetic field due to a lack of ferromagnetic grains with low-temperature Tb spectra. Thus, the lowest T_b of the high-temperature component simply indicates an upper boundary of the possible clast temperature range. About 51% of all samples (of which ~83% of the hand specimens and ~17% of the drill cores) show this pattern.

Five samples (~3 %) showed scattered demagnetization paths and were discarded from further consideration.

A comparison of the T_r gathered from the central and external parts of drilled large blocks was instructive (Figs. 5.17 and 5.18). In four blocks, the central part was hotter than the outer one (430° vs. 310°C in red lava block FGO0831; Fig. 5.17), whereas in another two blocks, the centre was cooler than the outer section (e.g. completely cold centre vs. 310°C outer part, for grey scoria block FGO1252, Fig. 5.18). This demonstrates that the PDCs entrained both completely cold blocks that were heated by the enclosing PDC and by the PDC deposit during thermal equilibration (the block centres remaining cold), and hot blocks (400-500°C), the outer parts of which were cooled at the equilibrium temperature in the deposit (for the two examples shown).

Orientations of the low- and high-temperature components are shown on equal-area stereographic projections (Fig. 5.16). The mean direction of all low-temperature components (D=3.5°, I=44°, α_{95}=5.8°) is consistent (considering its 95% confidence cone) with the local geomagnetic field direction for the 2018 year at El Fuego volcano (see above), while the HT components are randomly oriented (k=1.1 and α_{95}=35.1°).

Generally, hand samples (Fig.s 5.14 and 5.18) recorded temperatures between 200 and 500°C, with a cluster between 300 and 480°C, but a few samples showed low temperatures, between 240 and 300°C. A few clasts of Group 1 are present, and display T>500 °C (only one shows T>220°C, implying a 220°C T_c likely from titanomagnetite).

Cores drilled in blocks display similar characteristics, with some hot blocks at 400-500°C, some hotter than 550°C, and a few recording low temperatures of 100-240°C. These temperatures probably reflect the thermal disequilibrium of large, cold clasts that were not heated to the equilibrium temperature of the deposit. Generally, cores display similar temperatures in the inner and outer sections, except for four (FGO0831-32, FGO1255-58; Fig. 5.17) and two cores (FGO1245-51; Fig. 5.18) in which higher temperatures were observed in the inner and outer rock slices, respectively.

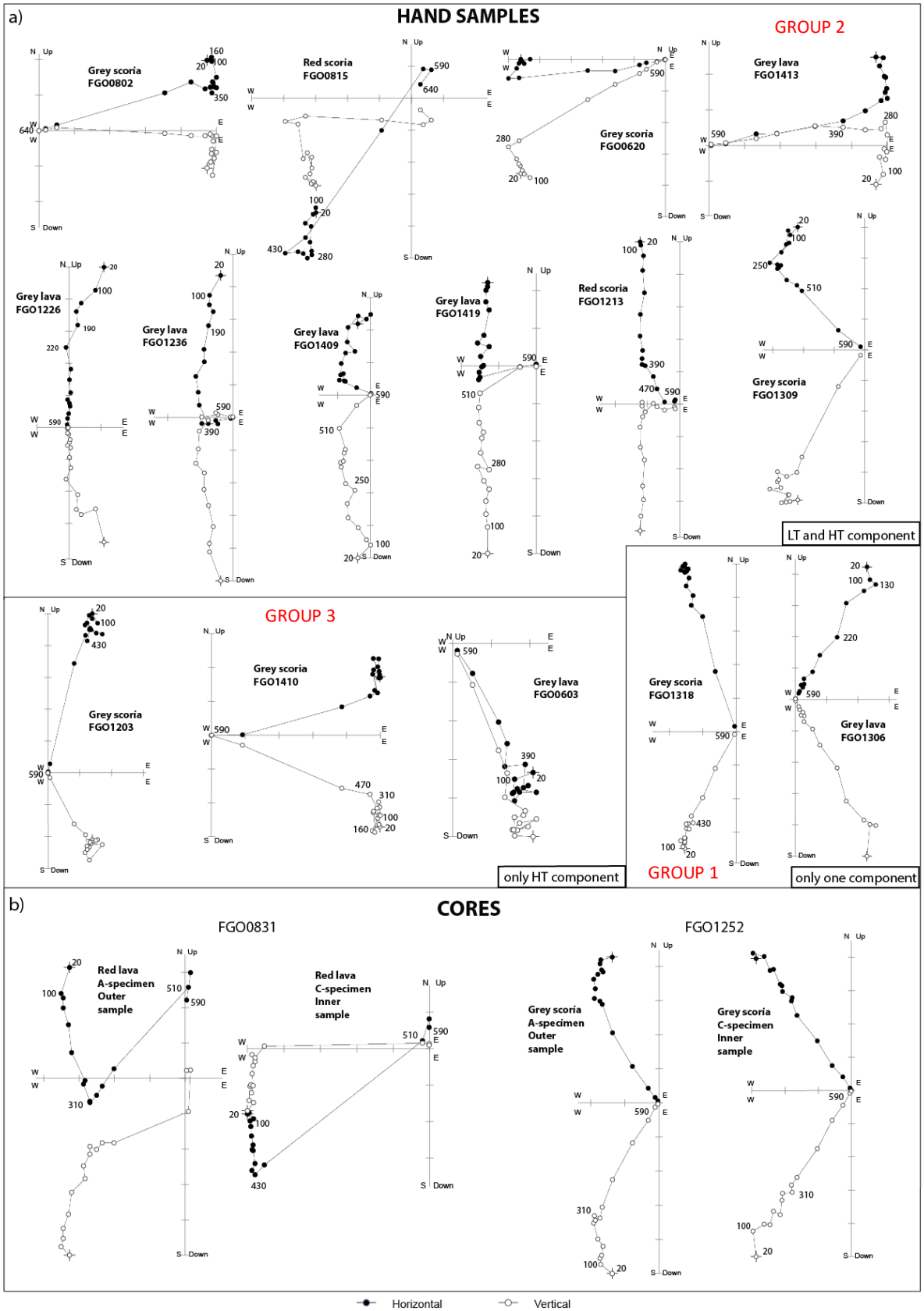

Fig. 5.15 Representative orthogonal vector diagrams of typical demagnetization data, in situ coordinates. Filled and empty dots represent projections on the horizontal and vertical planes, respectively. Demagnetization step values are °C. a) Hand samples. b) drilled cores from big blocks. A-cores and C-cores represent the outer and inner core specimen respectively.

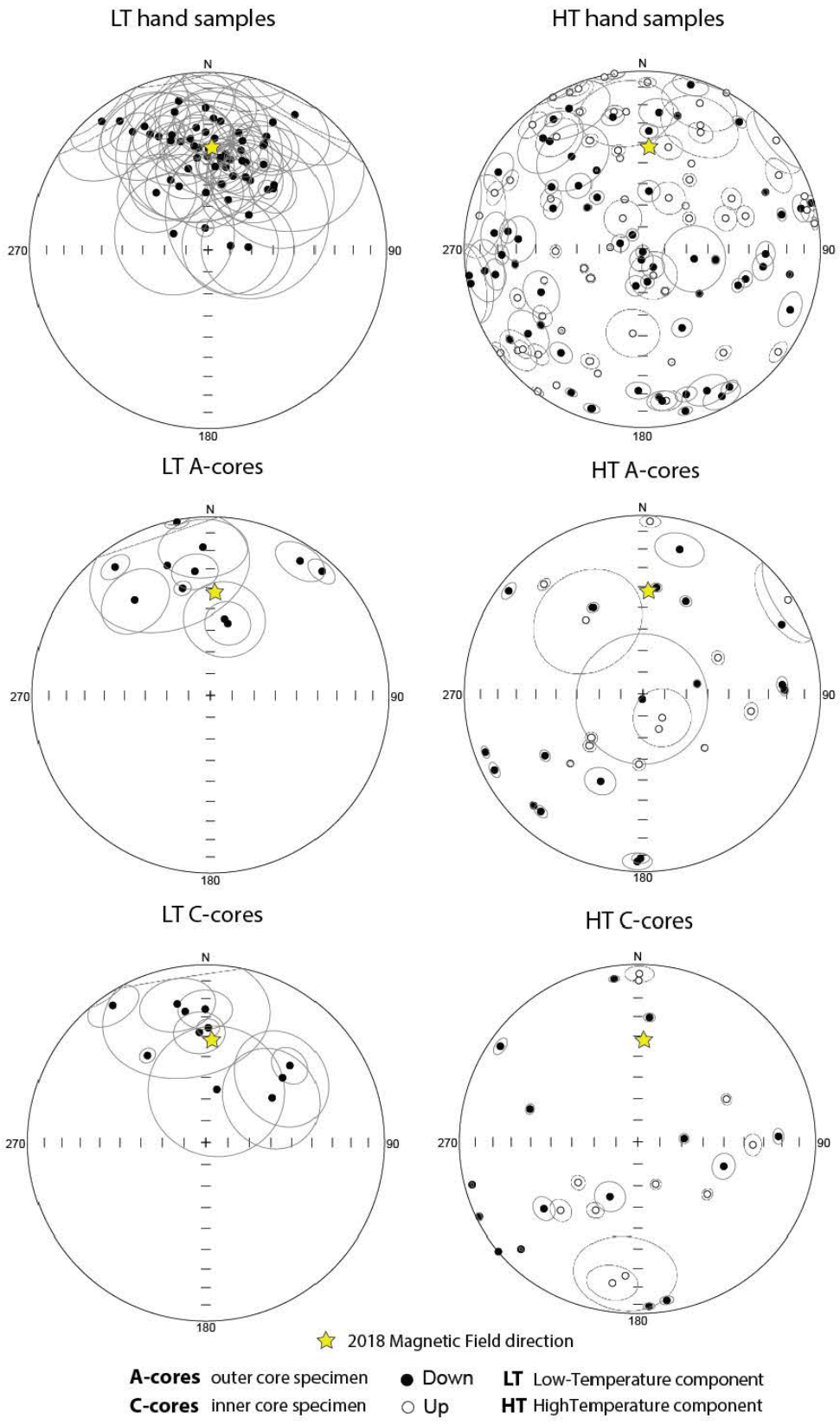

Fig. 5.16 Equal-area projection of high temperature (HT) and low temperature (LT) magnetic components of clasts from the June 2018 Las Lajas PDC deposit, in in-situ coordinates. Yellow stars indicate the 2018 local geomagnetic field direction (IGRF model, June 3rd, 2018). The ellipses around the palaeomagnetic directions are the projections of the relative maximum angular dispersion values.

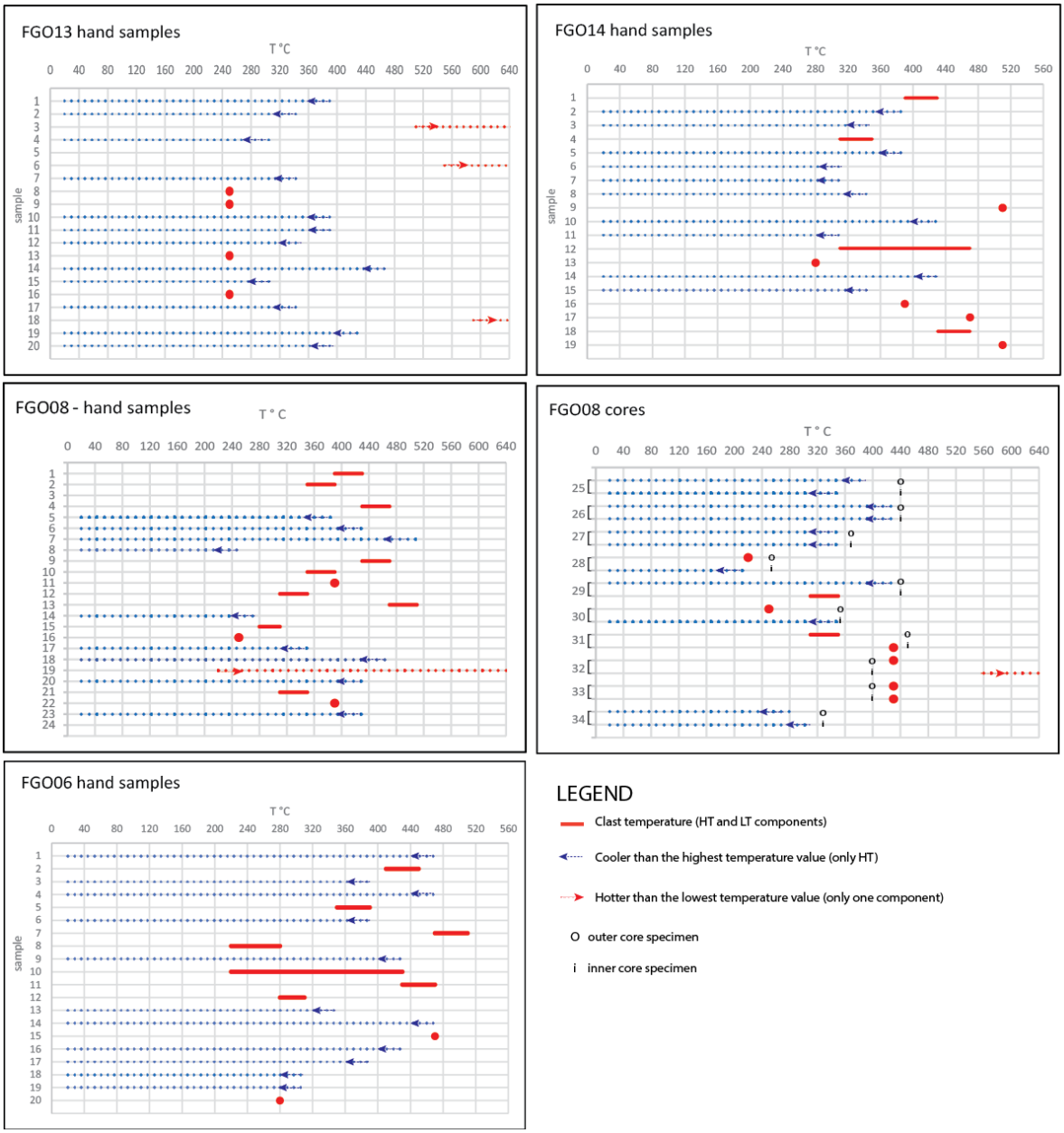

Fig. 5.17 Palaeomagnetically inferred re-heating temperatures of FGO06-13-14-08 sites. Red lines represent the temperature range (HT and LT components). Blue arrows represent clasts with only randomly oriented HT components (only upper bound temperatures can be deduced). Red arrows represent clasts with only one component subparallel to the 2018 local geomagnetic field direction (only lower bound temperatures can be deduced). O and I indicate outer and inner core rock slices, respectively.

As mentioned above (see 5.2 paragraph), to evaluate the T_{emp} the lowest T_r found on each site was considered, following the method by *McClelland et al. (2004).* For the FGO12 site, which was sampled at two different heights, slightly different T_{emp} for hand samples collected along the sequence, with 250°C and 280°C for the lower and upper part of the deposit were found, respectively, whereas cores drilled in big blocks recorded temperatures below 100°C for the whole deposit. If cores drilled in big blocks are not considered (since

they did not reach thermal equilibrium), the T_{emp} range is 190-220°C for the lower part and 310-430°C for the upper part of the deposit. Hand samples and cores of the FGO08 site yield a comparable T_{emp}, 250°C and 220°C, respectively. FGO06 site shows a T_{emp} between 220 and 280°C. Finally, for FGO13 and FGO14 sites, the T_{emp} is 250°C, and 280°C, respectively.

There is a small degree of correlation between magnetic temperatures and clast type (Fig. 5.19). Clasts recording the highest temperatures (>500 °C) are all grey clasts (63 % lavas and 37 % scoria), whereas clasts recording temperatures between 200° and 540°C are hetero-lithologic (20% of grey lava, 17% red scoriae, 4% red lavas and 59% grey scoriae); finally, cold clasts (with T<200 °C) are mainly lavas (75 % grey and 25 % red lavas).

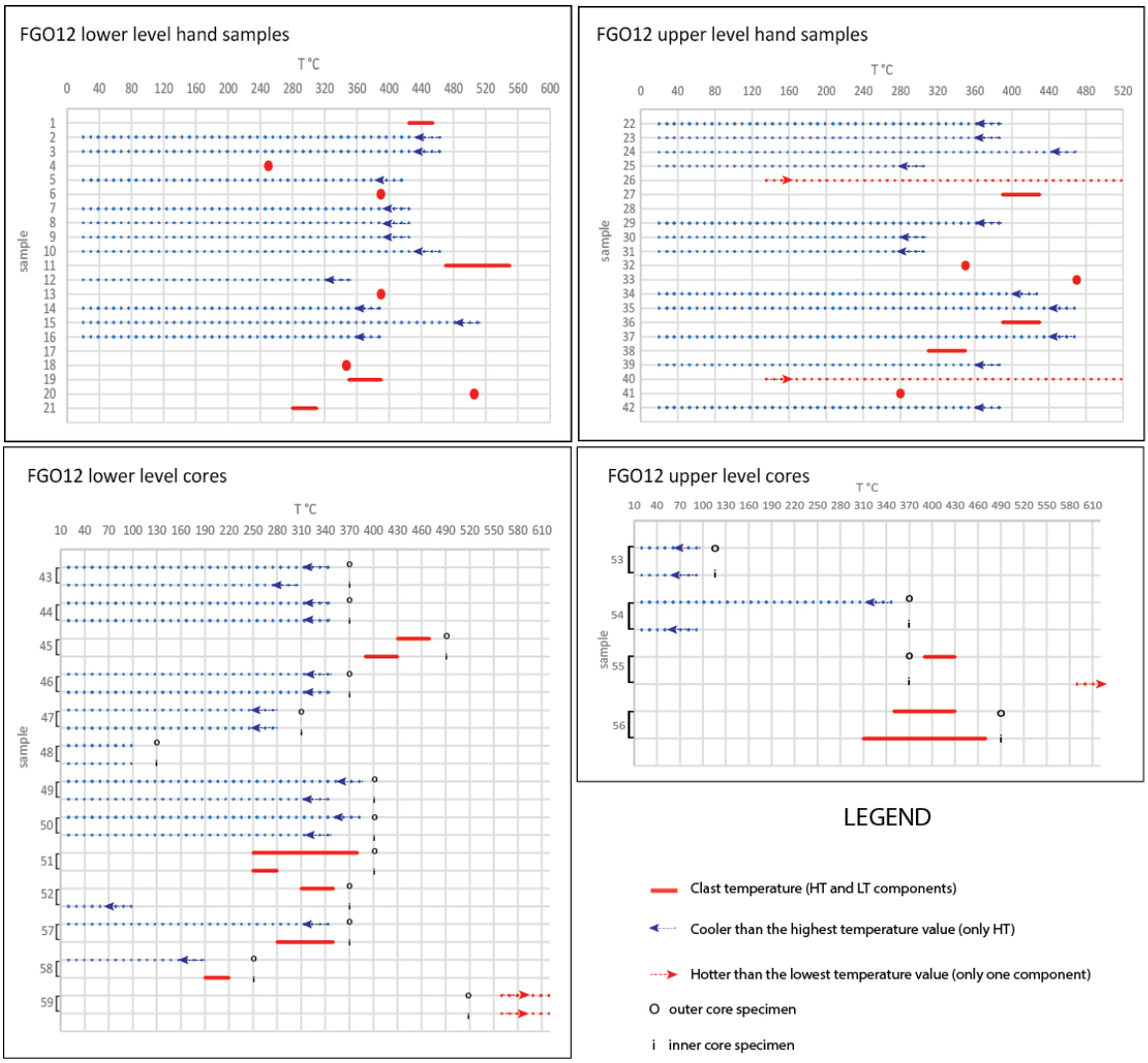

Fig. 5.18 Palaeomagnetically inferred re-heating temperatures of FGO12 site. Red lines represent the temperature range (HT and LT components). Blue arrows represent clasts with only randomly oriented HT components (only upper bound temperatures can be deduced). Red arrows represent clasts with only one component subparallel to the 2018 local geomagnetic field direction (only lower bound temperatures can be deduced). O and I indicate outer and inner core rock slices, respectively.

Fig. 5.19 Palaeomagnetically inferred re-heating temperatures of samples for each lithic category. Grey, orange, black and red colours represent grey scoriae, red scoriae, grey lavas and red lavas, respectively.

5.5 Discussion

5.5.1 Timing and PDCs emplacement dynamics

By combining characteristics of the deposits, eyewitness accounts and magnetic properties of selected clasts, the dynamics of the 2018 eruption have been reconstructed as follows (Fig. 5.20).

PDCs occurred between 2.00 and 3.30 PM (local time), with a peak between 3:00 and 3:30 PM. The short duration of individual pulses and the sustained character of the overall PDCs in the Las Lajas valley are primarily constrained by eyewitnesses and timed images. They are also confirmed in the internal architecture of the PDC deposits, which lack clear evidence for time-breaks, such as stacked flow-units with intercalated remnant ashfall layers commonly deposited during pauses between successive currents. The deposit architecture and the eyewitness accounts agree also with a rapid escalation (waxing) of the PDC at 3:08 PM and with the following rapid waning of the flow. The pulsating nature of the PDC is also consistent with eyewitness reports and with local bedding and vertical grading patterns in the deposit, including discontinuous scours that record local erosion during waxing phases as well as the invasion of wider areas through time.

Several eyewitnesses report that the PDC first reached the Las Lajas bridge on the RN-14 at around 2:30 PM and was initially contained within the ~500 m-wide river channel. Around 3:00 PM, the PDC activity rapidly escalated and reached a peak, in turn represented by two main pulses. The “waves” behaviour with increasing intensity is mainly suggested by the events witnesses on the bridge in the RN-14 route. Several onlookers on the main road were overwhelmed by the PDC, even though they had retreated a few hundred meters from the bridge after the first PDC arrival. The rapid waxing of the PDC is demonstrated by the rapid widening of the flow paths, inundating without any warning all channels and RN-14 road at 3:08 PM. This suggests that the flow suddenly was able to climb over a topographic barrier above the highway, beyond the Las Lajas barranca axis.

The arrival time of the most energetic flow on the RN-14 is reflected in the eyewitness accounts of San Miguel survivors, and in the internal structure of the analysed deposits. Witnesses reports that the arrival of the PDCs at the village soon after (10’ later) their arrival

at the Las Lajas bridge. The internal structure of the deposits in the village confirms the arrival of at least two waves, the second characterized by greater volume and kinetic energy. These “double-peak-phase” flows destroyed the LRGR and San Miguel village. In each case, the destruction seems to have occurred when the valley could not contain all the PDC mass, due to both the narrowing of the Las Lajas valley section upstream of the bridge, and to the abrupt direction change eastward.

This overflow into the small San Miguel drainage may have been facilitated by the partial filling of the Las Lajas river channel during the early stages of PDC activity, thereby lowering the effective height of the topographic barrier from 20 m to a few m. The combined effect is probably the result of a double “overflow” of the mass both on the left (LGRG) and the right (San Miguel village) side. This overflow effect in the San Miguel direction seems, however, to have been favoured by conservation of momentum, as the valley continues towards San Miguel from the Las Lajas valley upstream of the bend.

After this phase, the PDCs activity waned in energy and volume.

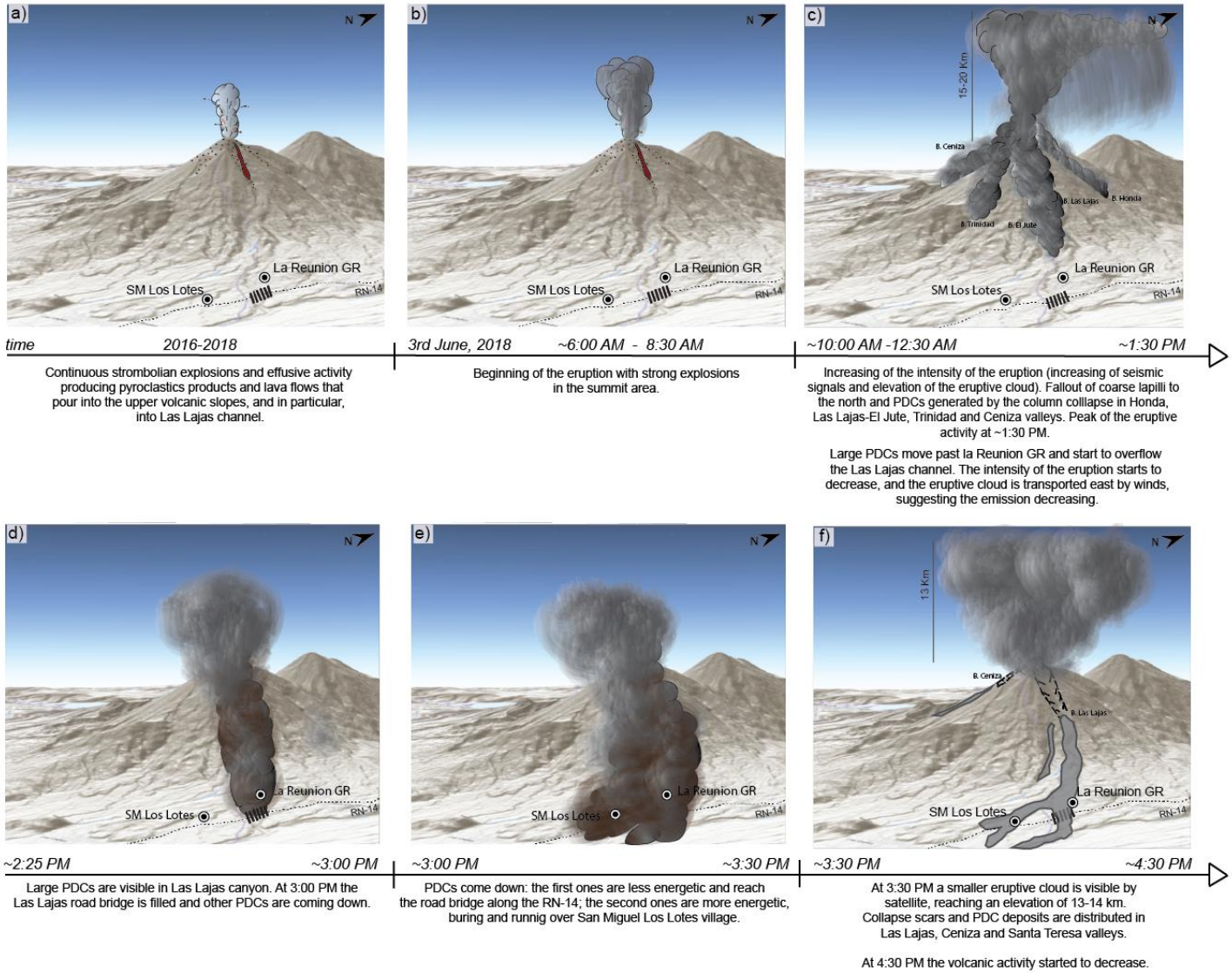

Fig. 5.20 Simplified cartoon with the main phases of the June 3rd, 2018 eruption as reconstructed from deposits analysis, eyewitness accounts and palaeomagnetic data. SM Los Lotes: San Miguel de Los Lotes. La Reunion GR: La Reunion Golf Resort. RN-14: Ruta Nacional 14.

5.5.2 Magnetic analyses and clasts temperatures

Groups 1, 2 and 3 from demagnetization patterns can be interpreted as three different thermal histories:

(1) Clasts belonging to Group 1 are inferred to be very hot juvenile clasts deposited by the Las Lajas PDCs above the T_c of magnetite (590°C) and record the local geomagnetic field direction during in situ cooling within the PDC deposit. It is unlikely that these clasts were heated by a hotter enclosing PDC deposit, because clasts in other groups record lower temperatures (200-300°C).

(2) Clasts belonging to Group 2 show randomly oriented HT components, inferred to have been acquired during geological times older than the June 2018 eruption. The LT magnetic components cluster near the 2018 geomagnetic field direction at El Fuego volcano (Fig. 5.16), and are inferred to record a thermoremanence overprint acquired within the Las Lajas PDC deposit. A few (8%) clasts have two HT components (for example FGO0815 in Fig. 5.15). These may have acquired the first HT component during initial cooling near El Fuego summit, and were then slightly rotated by gravitational adjustment whilst still hot and acquired a second high-temperature component as they continued to cool, before being entrained into the PDC. They were then transported and deposited, and acquired the low temperature component as they finally cooled in situ within the PDC deposit.

(3) Clasts belonging to Group 3 did not demagnetise until medium and high temperatures (250°-500°C), thus they likely lack magnetite and Ti-poor magnetite magnetic grains characterized by low/intermediate unblocking temperatures (e.g., *Cole et al., 2019*). It is not possible to identify a clear T_r. Three cores in this group recorded a very low T_r (<100°C): these were drilled in blocks 15–12 cm in diameter that were probably not heated homogeneously by the PDC, and failed to reach thermal equilibrium (e.g., *Porreca et al., 2008*).

5.5.3 Emplacement temperatures of the deposit

Based on the T_{emp} estimated, the deposit included three types of clasts:

(a) very hot (>590°C) clasts (forming 6% of the deposit clast population) considered to be juvenile and formed during the June eruption;

(b) hot clasts (300°–500°C; average clast temperature 410°C) of lava and scoria erupted from Fuego activity weeks or months before the June 2018 eruption, stacked around the summit and the head of the Las Lajas valley (as recorded on satellite images; Fig. 5.7), and not fully cooled before the June 3 eruption;

(c) cold (~20°C) clasts derived from older volcanic deposits near the summit and entrained during the PDCs, travel along the Las Lajas valley. This category includes clasts for which temperatures between 200° and 300°C cannot be excluded, as the thermoremanent magnetic data do not form a unique cluster (Fig.s 5.17 and 5.18). However, although such temperatures would have made the mean PDC deposit temperature higher (but consider the loss of thermal energy in heating air and driving convection and the phoenix plumes), some large blocks were cooler than 100°C.

Although lithic clasts are commonly used to infer the temperature of the PDC flows, some studies (e.g., *Nakaoka and Suzuki-Kamata, 2014; Rader et al., 2015*) combined information derived by both juvenile and lithic clasts. *Rader et al. (2015),* studying PDCs of Tungurahua and Cotopaxi in Ecuador, found different temperatures: in some cases, they found a low emplacement temperature (<90 °C) in lithic clasts whereas a hot emplacement temperature (>540 °C) in juvenile clasts; in others, deposits recorded cold temperatures for both clast types, and for this reason they were interpreted as lahar deposits; and in others, high temperatures for both juvenile and lithic clasts were found, and therefore they were interpreted as deposits derived from thermally well-mixed PDC. This shows how important is the ratio between the mass of juvenile and lithic clasts involved in the PDC flows, as well as how much lithic clasts incorporated in the flows are cold and how rapidly they conducted the heat between them.

According to the heat transfer equation from *Carlsaw and Jaeger (1959)* and *Bardot (2000), Cioni et al. (2004),* estimated the time for the thermal equilibration between coarse clasts and gas-ash mixture. They found that lithic clasts smaller than 2-3 cm in diameter can reach the equilibrium in a very few minutes (just over a minute for clasts of 1 cm in radii),

whereas larger clasts equilibrate after a very prolongated contact, or when they emplaced in the deposit.

The results of this work confirm that sampling small (2-3 cm) hand clasts yields a better temperature estimate for the deposit than drilling larger blocks (10's of cm), because the large blocks (both cold and hot blocks) did not reach thermal equilibrium before the deposit finally cooled. Most of the 2-3 cm wide clasts attained thermal equilibration and may faithfully represent the deposit temperature**.**

5.5.4 Origin of PDCs

PDCs may be generated by pyroclastic fountaining during Plinian and Vulcanian eruptions, from lateral blasts, phreatic and hydrovolcanic explosions, or from the decrepitation of growing lava domes (*Branney et al., 2020*). None of these mechanisms adequately accounts for the fatal June 3rd, 2018 PDCs of Fuego. The data presented here implicate the collapse of recently deposited rocks around the summit of the steep-sided, frequently active volcano.

Arc volcanoes with steep slopes generally result from frequent eruptions of mafic and intermediate compositions. Summit areas of the stratocones are typically constructed of thick deposits of loose ash, lapilli and bombs from strombolian eruptions interstratified with laterally continuous spatter layers and proximal lava flows. The deposits dip at angles close to their angles of repose, and have internal downslope-dipping weaknesses, such as loose tephra layers and autobreccia zones. As deposits aggrade, they become unstable, particularly as they start to become undercut by the headwall advance of erosional gullies. Their gravitational instability can be further increased by faulting and tilting caused by gravitational spreading or magma intrusion, seismic shaking during and immediately after strong explosive crisis, changes in the hydrothermal system, heavy rain, ice-melting, or erosion by pyroclastic density currents.

Volcano instability may variously lead to debris avalanches, rockfalls, lahars, and block-and-ash flows. Debris avalanches form giant landslides, typically much larger than the June 1980 event at Fuego, and they characteristically leave arcuate sector-collapse scarps near the source and widespread hummocky deposit sheets in quasi-flat areas or open valleys with

pervasive internal microbrecciation, block facies and matrix facies (*Glicken, 1998; de Vries and Delcamp, 2015*). No such features formed in the 2018 Fuego eruption, so a debris avalanche origin can be discounted. Rockfalls typically produce well-sorted talus cones and fans of angular blocks with lens-type repose bedding quite different from the June 2018 deposits. Lahar emplacement also can be discounted because of the eye-witness reports, which describe high temperatures (e.g. charring) and scarcity of water.

Block-and-ash flows are small PDCs, characterized by abundant dense, poorly to moderately vesicular hot juvenile blocks, predominantly non-pumiceous ash of similar composition, and entrained air (*Branney and Kokelaar, 2002*). They commonly form from the explosive disruption, decrepitation and gravitational collapse of growing, perched lava domes or lavas (e.g., Merapi, *Komorowski et al., 2013*; Unzen, *Nakada et al., 1999*; Santiaguito, *Rose 1987*; Soufriere Hills, *Carn et al., 2004*; Mt. St. Helens, *Vallance et al., 2008*). They are predominantly monolithologic but may include a range of textural varieties of the lava, including chilled juvenile blocks from dome exteriors. Their deposits are typically loose and largely valley confined. The proportion of ash matrix may be less than that in ignimbrite because the juvenile clasts are non-pumiceous and so less friable; however, breakage of poorly vesicular, but partly cooled, decompressed and thermally-stressed blocks readily generates abundant fine ash (e.g., *Mellors et al., 1988*).

The formation of the Las Lajas scarp is consistent with the addition of blocks to the PDC from pre-existing volcanic products coming from the retrogressive slope failure, in which an initial small collapse causes further instability triggering larger subsequent collapses. The sudden pulsed supply of abundant blocks to the PDC probably increased the mass flux and led to the increasing runout distance with time somehow triggered by the eruption.

The mass detached from the upper part of Las Lajas was composed of volcanic products, such as lapilli, ash, bombs, blocks, lavas, and pyroclastic flow deposits accumulated during the previous three years at least, that were presumably partially still hot. If we consider the cooling time of a lava flow, it depends on several factors, such as the initial temperature of the lava, the heat losses due to radiation and convection, air temperature, rainfall, wind, etc. (*Harris and Rowland, 2015*), but one of the most influential factors is the thickness of the flow. According to *Kilburn (2015)*, the time needed for a lava to cool is related to its

thickness and thermal diffusivity. For example, for the 10-15 m thick lava flows produced by the 2018 lower East Rift Zone eruption on Kilauea Volcano (Hawaii), the estimated time for the complete cooling was from 8 months to 1.5 years (https://www.usgs.gov/center-news/volcano-watch-how-do-lava-flows-cool-and-how-long-does-it-take). Using similar criteria, the time needed to cool for a lava flow emitted by El Fuego of 2-5 m-thick would be from a dozen days to 2-3 months. These estimates, however, do not take into consideration the emplacement of multiple flows close in time, and the rapid burying by pyroclastic deposits produced by the frequent strombolian activity. Therefore, these timing can be considered as a minimum estimate.

Another important point is the increase of the deposit thickness over time. Recently, *Albino et al. (2020)* studied the 2018 eruption of El Fuego, applying a bi-static interferometry producing pre- and post- eruptive DEMs (TanDEM-x DEM) with the aim of measure the topographic changes caused by the eruption. Considering three 3 different periods (pre-eruptive, 18 and 29 October, 2015; co-eruptive, 29 October and 06 August, 2018; post-eruptive, 06 august and 8 September 2018), the authors noted that, near the summit, even before the 2018 eruption, negative elevation changes (~30 m) had occurred, and during the co-eruptive period, a major one (~68 m) took place. We tried to investigate in detail the topographic changes occurred during the period between the end of 2015 and the 2018 eruption. We examined the satellite images on Google Earth and measured the topographic elevation in three different heights within the Las Lajas gorge in different time within the period considered. However, the results are not accurate and reliable, so these data were not used.

Albino et al. (2020) also calculated the total deposit volume of $15.1\pm4.2\times10^6 m^3$, in agreement with the volume estimated by *Naismith et al. (2019)* ($20–30x10^6$ m^3) and by *Ferres and Escobar Wolf (2018*) ($18.6 \pm 12.4 \times 10^6$ m^3 in channel). Their data highlight that mass removal of volcanic material occurs repetitively; based on their calculations, the total volume of PDCs increased due to the bulking process, especially in the upper part of Las Lajas gorge. Therefore, their data concur with the data provided by this work and show that the large run-out distance reached by PDCs was caused by the inclusion of material located near the vent that had gravitationally collapsed.

An additional explanation for the increasing runout of the PDCs can be given by the gradual filling of the Las Lajas channel, allowing the PDCs to spill over the outside bend into the San Miguel drainage to reach the village, and also the higher gravitational energy and volume of the late sliding masses compared to the earlier ones caused by the destabilization front migrated towards higher elevation and also towards the deepest and wider parts of the left scar.

5.5.5 From landslide-derived to block-and-ash flow deposit

The deposit of Las Lajas gorge shows characteristics of block-and-ash flow: ribbon-like structure, limited volume (~10^6 m^3), and a chaotic internal structure with the presence of metre-sized boulders of lava dispersed in the matrix. There is also evidence that the flow moved like a pyroclastic flow, producing dilute ash cloud surges on the sides of the valleys and also upward-directed buoyant phoenix plumes. The deposits, however, diverge from typical block-and-ash flows in the high lithological variability of the components, with a predominance of spongy scoriae and subordinate lava blocks of variable composition.

Considering a possible landslide origin, factors that allowed the transformation from a landslide-derived deposit to a pyroclastic flow deposit similar to a block-and-ash flow are:

1) The slide mass consisted of medium-hot materials (200-300°C). The thermal energy likely enhanced the mobility of the system, making the process different from a typical cold dry debris avalanche.

2) The landslide mass was primarily constituted by loose and fragile material (spongy scoriae). Some of the fine material needed to produce PDC-type behaviour of the transport system may have already been present in the pre-failure deposit and some may be derived from grinding the fragile clasts during transport.

3) The high potential energy of the sliding mass (around 2 km vertical elevation drop), combined with the narrow valley in which it was forced to flow, enhancing mechanical disaggregation.

One of the main problems encountered during palaeomagnetic sampling and the interpretation of the laboratory analyses was the nomenclature of clasts. The standard classification that separates the juvenile clasts from the cognate ones of the tephra is here not easily applicable, because of the nuanced difference between the material emitted on June 3rd and those of similar composition and characteristics emitted in hours, days, weeks before. This is because the cognate clasts, which typically are cold and not always fresh, are in this case still warm and fresh. Nearly all clasts in the Las Lajas deposit were probably derived from recently erupted products before the 2018 eruption, and the truly 'accidental' clasts could be clasts entrained from much older, cold deposits, like alluvial cobbles on the Las Lajas valley floor.

5.5.6 Implications for hazard at other volcanoes

PDCs may be generated by the collapse of unstable rock accumulations at craters rims and slopes, as recorded by several volcanoes such as Mayon (Philippines*; Moore and Melson, 1969; Rodolfo, 1989; Rodolfo et al., 1989*), Tungurahua (Ecuador; *Hall et al., 1999; 2013; Le Pennec et al., 2008, 2013*), Stromboli and Etna (Italy; *Rittmann, 1931; De Fino et al., 1988; Barberi et al., 1993; Rosi et al., 2006; Pioli et al., 2008; Pistolesi et al., 2008; Di Roberto et al., 2014; Calvari et al., 2016; Salvatici et al., 2016; Andronico et al., 2018*), Arenal (Costa Rica; *Alvarado and Soto, 2002; Cole et al., 2005*), Fuji (Japan; *Yamamoto et al., 2005*) and Fuego (*Davies et al., 1978).*

Most deposits produced by these collapses are small volume, hot, and have long runout distances (*Davies et al., 1978; Nairn and Self, 1978; Hazlett et al., 1991; Yamamoto et al., 2005; Miyabuchi et al., 2006; Di Roberto et al., 2014*). Intense fallout of coarse pyroclastic fragments on steep upper slopes of Mount Fuji (Japan) has been invoked to account for avalanching with formation of PDCs that travelled more than 8 km from source (*Yamamoto et al., 2005*).

All gradations may exist between vent-derived PDCs that entrain variable amounts of accidental lithic material (e.g., heterolithic breccias in ignimbrites derived from avalanching

from growing fault scarps during caldera collapse) to completely deposit-derived PDCs (as described months after the June 1991 eruption of Mount Pinatubo, *Torres et al., 1996*).

The example reported in this study highlights that retrogressive collapse of recently formed deposits can significantly increase the mass flux of the PDCs, thereby substantially increasing its runout distance (*Bursik and Woods, 1996; Branney and Kokelaar, 2002*). This demonstrably increased the hazard of the volcano with fatal consequences.

Older block-and-ash flow deposits underlie the 2018 Las Lajas PDC deposit at the RN-14 road bridge (Fig. 5.21). This also demonstrates the importance of evaluating the stratigraphy and genesis of pre-historic deposits in undertaking hazard assessments. Hazard policies should not be based entirely upon historical records and monitoring.

At other volcanoes, deposit-derived PDCs may be common. Therefore, the potential of recently emplaced volcanic deposits to remobilise should be evaluated in monitoring programs and hazard assessments. The deposit-derived PDC origin of some ignimbrites and block-and-ash flow deposits may be challenging to discern from pre-historic and ancient deposits (*Torres et al., 1996*), but we have demonstrated that careful palaeomagnetic investigations coupled with fieldwork may be the best way to make this important distinction.

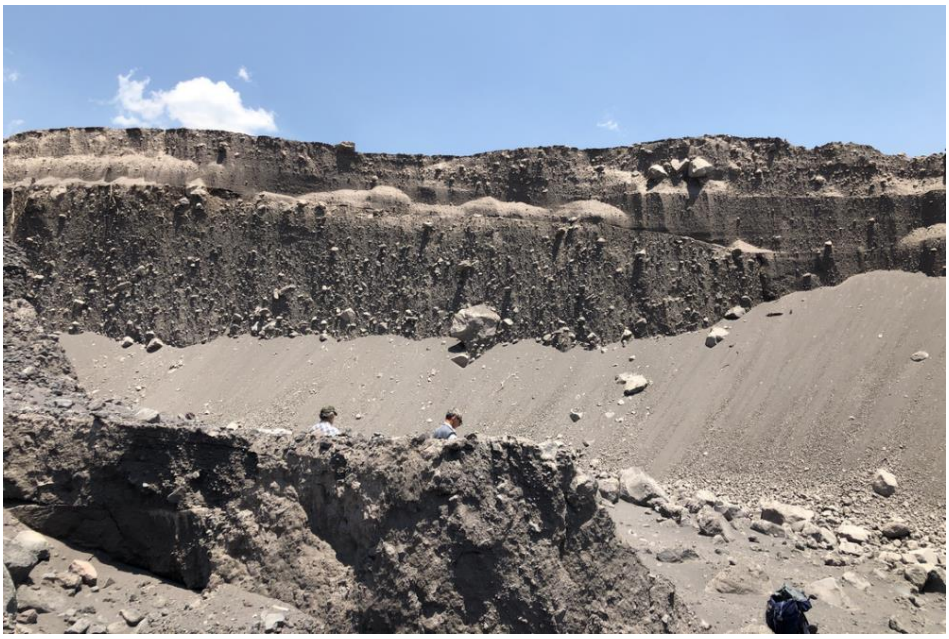

Fig. 5.21 Older block-and-ash flow deposits underlie the 2018 Las Lajas PDC deposit at the RN-14 road bridge.

5.6 Conclusions

A field and palaeomagnetic study of the June 3rd, 2018 PDC deposits that accumulated in the lower segment of the Las Lajas gorge helped to unravel the origin and dynamics of the dramatic events that killed more than two hundred people. The following main points can be highlighted:

1) The PDCs had estimated T_{emp} between 220° and 280°C, and overall lithological features similar to a block-and-ash flow. However, they resulted from the progressive collapse of the apical segment of the Las Lajas gorge, where large amount of partly hot, incoherent, mafic and intermediate materials (ash, lapilli, bombs and lavas), produced by strombolian activity, accumulated during the last years of Fuego's activity before 2018.

2) Palaeomagnetic analysis reveals that very hot juvenile clasts were scarce, whereas a large amount of hot clasts (with a temperature between 300 and 500 °C) was piled at the edge of the Las Lajas gorge, which later constituted the deposit. Therefore, the heat was probably not given by juvenile material but was mainly from hot cognate clasts.

3) Deposit destabilization started after 2:00 PM and rapidly increased between 3:00 and 3:20 PM, about one hour after the end of a sub-plinian eruption producing a 19 km-high plume and the formation of a vent-derived PDC. After the onset, the destabilization quickly progressed through a mechanism of rock retrogressive collapse of the unstable, perched deposits, evidenced by the appearance of a new collapse scar.

4) The process was triggered by initial erosion by the early, vent-derived PDCs and seismic shaking during and immediately after the paroxysmal sub-plinian explosive eruption.

5) This study demonstrates that deposit-derived PDCs with unexpected runout distances can pose a significant hazard at frequently active, steep volcanoes, where a large volume of loose, fines-rich, unstable deposits exist in the apical part of the cones. The retrogressive collapse of unstable stacks of hot and cool volcanic material can generate rock avalanches, which can transform into genuine PDC systems.

6) The involvement of masses of unstable materials either by increasing the mass flux of the density currents by bulking up or retrogressive sliding of unstable detritus masses can cause the further PDC runout and is thus worth investigating in future studies. This

phenomenon may be common at other steep-sided volcanoes, so the accumulation of lavas and pyroclastic deposits on volcanic slopes should be properly evaluated during hazard assessments.

References

Albino, F., Biggs, J., Escobar-Wolf, R., Naismith, A., Watson, M., Phillips, J. C., Marroquin, G. C. (2020). Using TanDEM-X to measure pyroclastic flow source location, thickness and volume: Application to the 3rd June 2018 eruption of Fuego volcano, Guatemala. J. Volcanol. Geotherm. Res., 406, 107063.

Alvarado, G.E., Soto, G.J. (2002). Pyroclastic flow generated by crater–wall collapse and outpouring of the lava pool of Arenal Volcano, Costa Rica. Bull. Volcanol. 63 (8):557–568. https://doi.org/10.1007/s00445–001–0179–9.

Álvarez-Gómez, J.A., Meijer, P.T., Martínez-Díaz, J.J., Capote, R. (2008). Constraints from finite element modelling on the active tectonics of northern Central America and the Middle America Trench. Tectonics 27 (1). https://doi.org/10.1029/2007TC002162.

Andronico, D., Di Roberto, A., De Beni, E., Behncke, B., Bertagnini, A., Del Carlo, P., & Pompilio, M. (2018). Pyroclastic density currents at Etna volcano, Italy: The 11 February 2014 case study. Journal of Volcanology and Geothermal Research, 357, 92-105.

Authemayou, C., Brocard, G., Teyssier, C., Simon-Labric, T., Gutiérrez, A., Chiquín, E.N., Morán, S. (2011). The Caribbean–North America–Cocos Triple Junction and the dynamics of the Polochic–Motagua fault systems: pull-up and zipper models. Tectonics 30 (3). https://doi.org/10.1029/2010TC002814.

Barberi, F., Rosi, M., Sodi, A. (1993).Volcanic hazard assessment at Stromboli based on re-view of historical data. Acta Vulcanol. 3, 173–187.

Bardot, L. (2000). Emplacement temperature determinations of proximal pyroclastic deposits on Santorini, Greece, and their implications. Bull. Volcanol.61, 450–467. http://dx.doi.org/10.1007/PL00008911.

Basset, T. S. (1996). Histoire éruptive et évaluation des aléas du volcan Acatenango (Guatemala) (Vol. 3). Université de Genève. 309 p.

Berlo, K., Stix, J., Roggensack, K., Ghaleb, B. (2012). A tale of two magmas, Fuego, Guatemala. Bull. Volcanol. 74 (2), 377–390. https://doi.org/10.1007/s00445-011-0530-8.

Boudon, G., Camus, G., Gourgaud, A., Lajoie, J. (1993). The 1984 nuéeardente deposits of Merapi volcano, Central Java, Indonesia: stratigraphy, textural characteristics, and transport mechanisms. Bull. Volcanol. 55(5), 327–342.

Brand, B.D., Mackaman-Lofland, C., Pollock, N.M., Bendaña, S., Dawson, B., Wichgers, P., (2014). Dynamics of pyroclastic density currents: conditions that promote substrate erosion and self-channelization - Mount St Helens, Washington (USA). J Volcanol Geotherm Res 276:189–214.

Branney, M.J., Kokelaar, B.P. (1992). A reappraisal of ignimbrite emplacement: progressive aggradation and changes from particulate to non-particulate flow during emplacement of high-grade ignimbrite. Bulletin of Volcanology, 54, 504-520.

Branney, M. J., Kokelaar, P. (2002). Pyroclastic Density Currents and the Sedimentation of Ignimbrites. Geological Society, London, Memoirs, 27. 142 pp.

Branney, M.J., Brown, R.J., Calder, E. (2020). Pyroclastic rocks. In: Encyclopedia of Geology. 2nd Ed. Elsevier. p. xx–xx (in press).

Brown, R.J., Branney, M.J. (2004). Bypassing and diachronous deposition from density currents: evidence from a giant regressive bed form in the Poris ignimbrite, Tenerife, Canary Islands. Geology 32, 445–448.

Buesch, D.C. (1992). Incorporation and redistribution of locally derived lithic fragments within a pyroclastic flow. Geol. Soc. Am. Bull. 104(9): 1193–1207

Burkart, B., Self, S. (1985). Extension and rotation of crustal blocks in northern Central America and effect on the volcanic arc. Geology 13 (1), 22–26. https://doi.org/ 10.1130/0091-761313b22:EAROCBN2.0.CO;2.

Bursik, M., Woods, A. (1996). The dynamics and thermodynamics of large ash flows. Bull Volcanol 58, 175–193. https://doi.org/10.1007/s004450050134

Calder, E.S., Sparks R.S.J., Gardeweg M.C. (2000). Erosion, transport and segregation of pumice and lithic clasts in pyroclastic flows inferred from ignimbrite at Lascar Volcano, Chile. J. Volcanol. Geotherm. Res. 104(1–4):201–235.

Calvari, S., Intrieri, E., Di Traglia, F., Bonaccorso, A., Casagli, N., Cristaldi, A. (2016). Monitoringcrater-wall collapse at active volcanoes: a study of the 12 January 2013 event at Stromboli. Bull. Volcanol. 78 (5), 1–16.http://dx.doi.org/10.1007/s00445-016-1033-4.

Carlsaw, H. S., Jaeger, J. C. (1959), Conduction of Heat in Solids, 510 pp., Oxford Univ. Press, New York

Carn, S.A.,Watts, R.B., Thompson, G., Norton, G.E. (2004). Anatomy of a lava dome collapse: the 20 March 2000 event at Soufrière Hills Volcano, Montserrat. J. Volcanol. Geotherm. Res. 131(3–4): 241–264.

Cioni, R., Gurioli, L., Lanza, R., Zanella, E. (2004). Temperatures of the AD 79 pyroclastic density current deposits (Vesuvius, Italy). J. Geophys. Res., Solid Earth 109, B02207. http://dx.doi.org/10.1029/2002JB002251.

Charbonnier, S.J., Gertisser, R. (2011). Deposit architecture and dynamics of the 2006 block-and-ash flows of Merapi Volcano, Java, Indonesia. Sedimentology 58(6):1573–1612.

Chesner, C.A., Rose Jr., W.I. (1984). Geochemistry and evolution of the Fuego volcanic complex, Guatemala. J. Volcanol. Geotherm. Res. 21 (1–2), 25–44. https://doi.org/10.1016/0377-0273(84)90014-3.

Co-ordinadora Nacional para la Reducción de Desastres (CONRED) (2018). Volcán De Fuego Te compartimos los datos de personas albergadas, atendidas e incidentes registrados hasta el momento por la erupción del volcán de Fuego. #PrevenirParaVivir #TodosSomosResponsables. 19 June 2018 Retrieved from: https://twitter.com/ ConredGuatemala/status/1009088485368745985, Accessed date: 12 April 2018.

Cole, P. D., Calder, E. S., Druitt, T. H., Hoblitt, R., Robertson, R., Sparks, R. S. J., Young, S. R. (1998). Pyroclastic flows generated by gravitational instability of the 1996–97 lava dome of Soufriere Hills Volcano, Montserrat. Geophysical Research Letters, 25(18), 3425-3428.

Cole, P.D., Fernandez, E., Duarte, E., Duncan, A.M. (2005). Explosive activity and generation mechanisms of pyroclastic flows at Arenal volcano, Costa Rica between 1987 and 2001. Bull. Volcanol. 67(8):695–716

Cole, R. P., Ohneiser, C., White, J. D. L., Townsend, D. B., Leonard, G. S. (2019). Paleomagnetic evidence for cold emplacement of eruption-fed density current deposits beneath an ancient summit glacier, Tongariro volcano, New Zealand. Earth and Planetary Science Letters, 522, 155-165.

Davies, D. K., Quearry, M. W., Bonis, S. B. (1978). Glowing avalanches from the 1974 eruption of the volcano Fuego, Guatemala. Geological Society of America Bulletin, 89(3), 369-384.

De Fino, M., La Volpe, L., Falsaperla, S., Frazzetta, G., Neri, G., Francalanci, L., Rosi, M., Sbrana, A., 1988. The Stromboli eruption of December 6, 1985–April 25, 1986: volcanological, petrological and seismological data. Rend. Soc. Ital. Mineral. Petrol. 43, 1021–1038.

de Vries, B. V. W., Delcamp, A. (2015). Volcanic debris avalanches. In: Landslide Hazards, Risks and Disasters, eds J. F. Shroder and T. Davies (Cambridge, MA: Elsevier), 131–157. doi: 10.1016/B978-0-12-396452-6.00005-7

Di Roberto, A., Bertagnini, A., Pompilio, M., Bisson, M. (2014). Pyroclastic density currents at Stromboli volcano (Aeolian Islands, Italy): a case study of the 1930 eruption. Bull.Volcanol. 76 (6), 1–14.http://dx.doi.org/10.1007/s00445-014-0827-5

Druitt, T. H. (1992). Emplacement of the 18 May 1980 lateral blast deposit ENE of Mount St. Helens, Washington. Bulletin of Volcanology, 54(7), 554-572.

Druitt, T. H. (1998). Pyroclastic density currents. In: Gilbert, J.S., Sparks, R.S.J. (eds) The physics of explosive volcanic eruptions. Geological Society, London, Special Publications, 145(1), 145-182.

Escobar Wolf, R.P. (2013). Volcanic processes and human exposure as elements to build a risk model for Volcan de Fuego, Guatemala, Unpubl Dissertation, Michigan Technological University, 2013. 216 pp. https://digitalcommons.mtu.edu/etds/638

Farin, M., Mangene, A., Roche, O. (2013). Fundamental changes of granular flow dynamics, deposition and erosion processes at high slope angles: insights from laboratory experiments. J. Geophys. Res. Earth. Surf. 119(3), 504-532.

Ferres, D., Escobar Wolf, R. (2018). Informe Tecnico: Volcan de Fuego. Technical Report. Cooperacion Espanola. http://bibliotecadigital.aecid.es/bibliodig/i18n/consulta/registro.cmd?id=8751.

Fisher, R. V. (1977), Erosion by volcanic base-surge density currents—U-shaped channels. Geological Society of America Bulletin, v. 88, p. 1287-1297.

Glicken, H (1998). Rockslide-debris avalanche of May 18, 1980, Mount St Helens Volcano, Washington. Geological Survey of Japan Bulletin, 49, 55–106.

Global Volcanism Program, (2013). Fuego (342090) in Volcanoes of the World, v. 4.9.4 (17 Mar 2021). Venzke, E (ed.). Smithsonian Institution. Downloaded 30 Apr 2021 (https://volcano.si.edu/volcano.cfm?vn=342090). https://doi.org/10.5479/si.GVP.VOTW4-2013

Global Volcanism Program (2018). In: Venzke, E. (ed.), [Fuego (342090)] in Volcanoes of the World, v. 4.6.7. Smithsonian Institution https://volcano.si.edu/volcano.cfm?vn=342090.

Gurioli, L., Cioni, R., Sbrana, A., Zanella, E. (2002). Transport and deposition of pyroclastic density currents over an inhabited area: the deposits of the AD 79 eruption of Vesuvius at Herculaneum, Italy. Sedimentology, 49(5):929–953.

Hall, M. L., Robin, C., Bernardo, B., Mothes, P., Monzier, M. (1999). Tungurahua Volcano, Ecuador: structure, eruptive history and hazards. J. Volcanol. Geotherm. Res. 91:1–21.

Hall, M. L., Steele, A. L., Mothes, P.A., Ruiz, M.C. (2013). Pyroclastic density currents (PDC) of the 16–17 August 2006 eruptions of Tungurahua volcano, Ecuador: geophysical registry and characteristics. J. Volcanol. Geotherm. Res. 265, 78–93.

Harris, A. J., Rowland, S. K. (2015). Lava flows and rheology. In The encyclopedia of volcanoes (pp. 321-342). Academic Press.

Hazlett, R.W., Buesch, D., Anderson, J.L., Elan, R., Scandone, R. (1991). Geology, failure conditions, and implications of seismogenic avalanches of the 1944 eruption at Vesuvius, Italy. J. Volcanol. Geotherm. Res. 47 (3–4), 249–264. http://dx.doi.org/10.1016/0377-0273(91)90004-J.

Instituto Nacional de Sismología, Vulcanología, Meteorología e Hidrología (INSIVUMEH) (2012a). Folleto sobre Volcán de Fuego. Retrieved from:. http://www.insivumeh.gob.gt, Accessed date: 12 July 2018.

Instituto Nacional de Sismología, Vulcanología, Meteorología e Hidrología (INSIVUMEH) (2012b). Reporte preliminar de la erupción del Volcán de Fuego 13 de septiembre 2012. Retrieved from:http://www.insivumeh.gob.gt/folletos/REPORTE%20ERUPCION%20DE%20FUEGO%2013%20SEP%202012%20%28OK%29.pdf, Accessed date: 12 July 2018.

Kieffer, S. W., Sturtevant, B. (1988). Erosional furrows formed during the lateral blast at Mount St. Helens, May 18, 1980. Journal of Geophysical Research: Solid Earth, 93(B12), 14793-14816.

Kilburn, C. R. (2015). Lava flow hazards and modeling. In The encyclopedia of volcanoes (pp. 957-969). Academic Press.

Kirschvink, J.L. (1980). The least-square line and plane and the analysis of paleomagnetic data, Geophys. J., 62, 699–718.

Komorowski, J. C., Jenkins, S., Baxter, P. J., Picquout, A., Lavigne, F., Charbonnier, S., et al. (2013). Paroxysmal dome explosion during the Merapi 2010 eruption: Processes and facies relationships of associated high-energy pyroclastic density currents. Journal of Volcanology and Geothermal Research, 261, 260-294.

Kurtz, A.W. (1913). Documentos Antiguos: Copia de dos cartas manuscritas de Don Pedro de Alvarado a Hernando Cortes, 11 de abril y 28 de julio 1524. Tip. – Arenales hijos. Retrieved from: https://www.scribd.com/doc/213352772/Cartas-de-Pedro-de-Alvarado-a-Hernan-Cortes, Accessed date: 12 July 2018.

Le Pennec, J.-L, D. Jaya, P. Samaniego, P. Ramón, S. Moreno, J. Egred, J. van der Plicht (2008).The AD 1300–1700 eruptive periods at Tungurahua volcano, Ecuador, revealed by historical narratives, stratigraphy, and radio-carbon dating J. Volcanol. Geotherm. Res., 176, pp. 70-81.

Le Pennec, J.-L., de Saulieu, G., Samaniego, P., Jaya, D., Gaillerm L. (2013). A devastating Plinian eruption at Tungurahua Volcano reveals formative occupation at ~1100 cal BC in Central Ecuador. Radiocarbon 55(3–4) 1199-1214.

Lesti, C., Porreca, M., Giordano, G., Mattei, M., Cas, R.A.F., Wright, H.M.N., Folkes, C.B., Viramonte, J. (2011). High-temperature emplacement of the Cerro Galán and Toconquis Group ignimbrites (Puna plateau, NW Argentina) determined by TRM analyses. Bull. Volcanol.73, 1535–1565. http://dx.doi.org/10.1007/s00445-011-0536-2.

Lube, G., Cronin, S.J., Platz, T., Freundt, A., Procter, J.N., Henderson, C., Sheridan, M.F. (2007). Flow and deposition of pyroclastic granular flows: a type example from the 1975 Ngauruhoe eruption, New Zealand. J. Volcanol. Geotherm. Res. 161(3):165–186.

Lloyd, A.S., Plank, T., Ruprecht, P., Hauri, E.H., Rose,W. (2013). Volatile loss from melt inclusions in pyroclasts of differing sizes. Contrib. Mineral. Petrol. 165 (1), 129–153.

Lloyd, A.S., Ruprecht, P., Hauri, E.H., Rose, W., Gonnermann, H.M., Plank, T. (2014). NanoSIMS results from olivine-hosted melt embayments: magma ascent rate during explosive basaltic eruptions. J. Volcanol. Geotherm. Res. 283, 1–18.

Lyons, J.J.,Waite, G.P., Rose,W.I., Chigna, G. (2010). Patterns in open vent, strombolian behaviour at Fuego volcano, Guatemala, 2005–2007. Bull. Volcanol. 72 (1), 1. https://doi.org/10.1007/s00445-009-0305-7.

Mangeney, A., Roche, O., Hungr, O., Mangold, N., Faccanoni, G., Lucas, A. (2010). Erosion and mobility in granular collapse over sloping beds. J. Geophys. Res., 115(F3), F03040.

Marti, J.J., Diez-Gil, J.L, Ortiz, R. (1991). Conduction model for the thermal influence of lithic clasts in mixtures of hot gases and ejecta, J. Geophys. Res., 96, 21,879– 21,885.

Martin, D.P., Rose Jr., W.I. (1981). Behavioral patterns of Fuego volcano, Guatemala. J. Volcanol. Geotherm. Res. 10 (1–3), 67–81. https://doi.org/10.1016/0377-0273(81)90055-X.

McClelland, E. A., Druitt, T.H (1989). Palaeomagnetic estimates of emplacement temperatures of pyroclastic deposits on Santorini, Greece, Bull. Volcanol., 51, 16–27.

McClelland, E., Wilson, C.J.N., Bardot, L. (2004). Palaeotemperature determinations for the 1.8-ka Taupo ignimbrite, New Zealand, and implications for the emplace-ment history of a high-velocity pyroclastic flow. Bull. Volcanol.66, 492–513. http://dx.doi.org/10.1007/s00445-003-0335-5.

Mellors R.A., Waite R.B., Swanson, D.A. (1988). Generation of pyroclastic flows and surges by hot rock avalanches from the dome of Mount St Helens volcano, USA. Bulletin of Volcanology, 50, 14–25.

Miyabuchi, Y.,Watanabe, K., Egawa, Y. (2006). Bomb-rich basaltic pyroclastic flow deposit from Nakadake, Aso Volcano, southwestern Japan. J. Volcanol. Geotherm. Res. 155 (1–2), 90–103. http://dx.doi.org/10.1016/j.jvolgeores.2006.02.007.

Moore, J.G., Melson, W.J. (1969). Nuées Ardentes of the 1968 Eruption of Mayon Volcano, Philippines, Bull. Volcanol. 33: 600. https://doi.org/10.1007/BF02596528

Nairn, I.A., Self, S. (1978). Explosive eruptions and pyroclastic avalanches from Ngauruhoe in February 1975. J. Volcanol. Geotherm. Res. 3 (1–2), 39–60.

Naismith, A. K., Watson, I. M., Escobar-Wolf, R., Chigna, G., Thomas, H., Coppola, D., Chun, C. (2019). Eruption frequency patterns through time for the current (1999–2018) activity cycle at Volcán de Fuego derived from remote sensing data: Evidence for an accelerating cycle of explosive paroxysms and potential implications of eruptive activity. Journal of Volcanology and Geothermal Research, 371, 206-219.

Nakada, S., Shimizu, H., Ohta., K. (1999). Overview of the 1990–1995 eruption at Unzen Volcano. Journal of Volcanology and Geothermal Research, 89(1-4), 1-22.

Nakaoka, R., Suzuki-Kamata, K. (2014). Rock magnetic evidence for the low-temperature emplacement of the Habushiura pyroclastic density current, Niijima Island, Japan. Geological Society, London, Special Publications, 396, 51-66, https://doi.org/10.1144/SP396.7

Pardini, F., Queißer, M., Naismith, A., Watson, I. M., Clarisse, L., Burton, M. R. (2019). Initial constraints on triggering mechanisms of the eruption of Fuego volcano (Guatemala) from 3 June 2018 using IASI satellite data. Journal of Volcanology and Geothermal Research, 376, 54-61.

Paterson, G.A., Roberts, A.P., Mac Niocaill, C., Muxworthy, A.R., Gurioli, L., Viramonté, J.G., Navarro, C., Weider, S. (2010). Paleomagnetic determination of emplacement temperatures of pyroclastic deposits: an under-utilized tool. Bull. Volcanol.72, 309–330. http://dx.doi.org/10.1007/s00445-009-0324-4.

Patrick, M.R., Harris, A.J., Ripepe, M., Dehn, J., Rothery, D.A., Calvari, S. (2007). Strombolian explosive styles and source condition: insights from thermal (FLIR) video. Bull. Volcanol. 69 (7), 769–784. https://doi.org/10.1007/s00445-006-0107-0

Pérez-Rodríguez, N., Morales, J., Goguitchaichvili, A., García-Tenorio, F. (2019). A comprehensive paleomagnetic study from the last Plinian eruptions of Popocatepetl volcano: absolute chronology of lavas and estimation of emplacement temperatures of PDCs. Earth Planets Space. 71: 80. https://doi.org/10.1186/s40623-019-1059-x

Pioli, L., Rosi, M., Calvari, S., Spampinato, L., Renzulli, A., Di Roberto, A. (2008). The eruptive activity of 28 and 29 December 2002, Stromboli volcano: an integrated study of the 2002–2003 eruption. American Geophysical Union, Washington, USA,pp. 105–115http://dx.doi.org/10.1029/182GM10.

Pistolesi, M., Rosi, M., Pioli, L., Renzulli, A., Bertagnini, A., Andronico, D. (2008). The paroxysmal event and its deposits. In: Calvari, S., Inguaggiato, S., Puglisi, G., Ripepe, M., Rosi, M., Eds.,Stromboli Volcano: an Integrated Study of the 2002–2003 eruption. American Geophysical Union, Washington, USA, pp. 317–330.

Porreca, M., Mattei, M., MacNiocaill, C., Giordano, G., McClelland, E., Funiciello, R. (2008). Paleomagnetic evidence for low-temperature emplacement of the phreatomagmatic Peperino Albano ignimbrite (Colli Albani volcano, Central Italy). Bull. Volcanol., 70, 877–893. http://dx.doi.org/10.1007/s00445-007-0176-8.

Rader, E., Geist, D., Geissman, J., Dufek, J., Harpp, K. (2015). Hot clasts and cold blasts: thermal heterogeneity in boiling-over pyroclastic density currents. Geological Society, London, Special Publications, 396(1), 67-86.

Rittmann, A. (1931). Der Ausbruch des Stromboli am 11. September 1930. Z. Vulkanologie 14, 47–77.

Rodolfo, K. S. (1989). Origin and early evolution of lahar channel at Mabinit, Mayon Volcano, Philippines: Geological Society of America Bulletin, v. 101, p. 414–26 .

Rodolfo, K.S., Arguden, A.T., Solidum, R.U. Umbal, J.V. (1989). Anatomy and behaviour of a post-eruptive rain lahar triggered by a typhoon on Mayon volcano, Philippines. Bulletin of the International Association of Engineering Geology 40, 55–66. https://doi.org/10.1007/BF02590341

Rose, Jr.,W.I., Anderson Jr., A.T.,Woodruff, L.G., Bonis, S.B. (1978). The October 1974 basaltic tephra from Fuego volcano: description and history of the magma body. J. Volcanol. Geotherm. Res. 4 (1–2), 3–53. https://doi.org/10.1016/0377-0273(78)90027-6.

Rose, W.I. (1987). Volcanic activity at Santiaguito Volcano 1976-1984. Geol. Soc. Am. Spec. Pap. 212: 17–27

Rose, W.I., Self, S., Murrow, P.J., Bonadonna, C., Durant, A.J., Ernst, G.G.J., (2008). Nature and significance of small volume fall deposits at composite volcanoes: Insights from the October 14, 1974 Fuego eruption, Guatemala. Bull. Volcanol. 70 (9), 1043–1067. https://doi.org/10.1007/s00445-007-0187-5.

Rosi, M., Bertagnini, A., Harris, A.J.L., Pioli, L., Pistolesi, M., Ripepe, M. (2006). A case history of paroxysmal explosion at Stromboli: timing and dynamics of the April 5, 2003 event. Earth Planet. Sci. Lett. 243 (3), 594–606.http://dx.doi.org/10.1016/j.epsl.2006.01.035

Rowley, P. D., Kuntz, M. A., MacLeod, N. S. (1981). Pyroclastic-flow deposits, in Lipman, P. W., Mullineaux, D. R., eds., The 1980 eruptions of Mount St. Helens, Washington: U-S. Geological Survey Professional Paper 1250, p. 489-512.

Salvatici, T., Di Roberto, A., Di Traglia, F., Bisson, M., Morelli, S., Fidolini, F., et al. (2016). From hot rocks to glowing avalanches: Numerical modelling of gravity-induced pyroclastic density currents and hazard maps at the Stromboli volcano (Italy). Geomorphology, 273, 93-106.

Saucedo, R., Macías, J., Bursik, M. (2004). Pyroclastic flow deposits of the 1991 eruption of Volcán de Colima, Mexico. Bull Volcanol 66(4): 291–306.

Sparks, R.S.J., Self, S., Walker, G.P.L. (1973). Products of ignimbrite eruptions. Geology 1: 115–118

Sparks, R.S.J., Gardeweg ,M.C., Calder, E.S., Matthews, S.J. (1997). Erosion by pyroclastic flows on Lascar Volcano, Chile. Bull. Volcanol. 58: 557–565.

Stoiber, R., Carr, M. (1973). Quaternary volcanic and tectonic segmentation of Central America. Bull. Volcanol. 37 (3), 304–325. https://doi.org/10.1007/BF02597631.

Suzuki-Kamata, K. (1988). The ground layer of Ata pyroclastic flow deposit, southwestern Japan—Evidence for the capture of lithic fragments. Bull. Volcanol. 50(2), 119-129.

Torres, R. C., Self, S., Martinez, M. L. (1996). Secondary pyroclastic flows from the June 15, 1991, ignimbrite of Mount Pinatubo. In: Newhall, C. G. & Punongbayan, S. (eds) Fire and Mud: Eruptions of Mount Pinatubo, Philippines. Philippine Institute of Volcanology and Seismology, Quezon City, University of Washington Press, Seattle, 665-678

Trolese, M., Giordano, G., Cifelli, F., Winkler, A., Mattei, M. (2017). Forced transport of thermal energy in magmatic and phreatomagmatic large volume ignimbrites: Paleomagnetic evidence from the Colli Albani volcano, Italy. Earth and Planetary Science Letters, 478, 179-191.

Turner, G.M., Alloway, B.V., Dixon, B.J., Atkins, C.B. (2018). Thermal history of volcanic debris flow deposits on the eastern flanks of Mt. Taranaki, New Zealand: Implications for future hazards. J. Volcanol. Geortherm. Res., 353, 55–67.

Uehara, D., Cas, R.A.F., Folkes, C., Takarada, S., Oda, H., Porreca, M. (2015). Using thermal remanent magnetisation (TRM) to distinguish block and ash flow and debris flow deposits, and to estimate their emplacement temperature: 1991–1995 lava dome eruption at Mt. Unzen Volcano, Japan. J. Volcanol. Geotherm. Res., 303, 92–111. http://dx.doi.org/10.1016/j.jvolgeores.2015.07.019.

Vallance, J.W., Siebert, L., Rose Jr., W.I., Girón, J.R., Banks, N.G. (1995). Edifice collapse and related hazards in Guatemala. J. Volcanol. Geotherm. Res. 66 (1–4), 337–355. https://doi.org/10.1016/0377-0273(94)00076-S.

Vallance, J.W., Schilling, S.P., Matías, O., Rose,W., Howell, M.M. (2001). Volcano Hazards at Fuego and Acatenango, Guatemala. US Geological Survey Retrieved from: https:// pubs.usgs.gov/of/2001/0431/, Accessed date: 12 July 2018.

Vallance, J.W., Schneider, D.J., Schilling, S.P. (2008). Growth of the 2004–2006 Lava-Dome Complex at Mount St. Helens, Washington. In: Sherrod, D.R., Scott, W.E., Stauffer, P.H., eds. A Volcano Rekindled: The Renewed Eruption of Mt St Helens, 2004–2006. U.S. Geol. Surv. Professional Paper 1750, pp 169–208.

VanKirk, J., Bassett-VanKirk, P. (1996). Remarkable Remains of the Ancient Peoples of Guatemala. University of Oklahoma Press, Norman, Oklahoma.

Waite, G.P., Nadeau, P.A., Lyons, J.J. (2013). Variability in eruption style and associated very long period events at Fuego volcano, Guatemala. J. Geophys. Res. Solid Earth 118 (4), 1526–1533. https://doi.org/10.1002/jgrb.50075.

Wallace, P.J. (2001). Volcanic SO2 emissions and the abundance and distribution of exsolved gas in magma bodies. J. Volcanol. Geotherm. Res. 108, 85–106.

Wilson, C.J.N. (1985). The Taupo eruption, New Zealand II. The Taupo ignimbrite. Royal Society of London Philosophical Transactions, ser. A, v. 314, p. 229–310, doi:10.1098/rsta.1985.0020.

Yamamoto, T., Takada, A., Ishizuka, Miyaji, Y. N., Tajima, Y. (2005). Basaltic pyroclastic flows of Fuji volcano, Japan: characteristics of the deposits and their origin. Bull. Volcanol., 67: 622. https://doi.org/10.1007/s00445-004-0398-y

Zanella, E., Sulpizio, R., Gurioli, L., Lanza, R. (2015). Temperatures of the pyroclastic density currents deposits emplaced in the last 22 kyr at Somma-Vesuvius (Italy). Geol. Soc. Lond. Spec. Publ. 396, 13–33. http://dx.doi.org/10.1144/sp396.4.

Zijderveld, J.D.A. (1967). AC demagnetization of rocks: analysis of results. In: Collinson, D.W., Creer, K. M., Runcorn, S.K. (Eds.), Methods in Palaeomagnetism, Elservier, pp. 254–28.54–28.

PART IV

6 Conclusive remarks

The palaeomagnetic method can give crucial information to better evaluate the volcanic hazards, in both volcanoes mainly characterized by effusive activity and those in which more energetic and dangerous explosive eruptions occur.

Palaeomagnetic techniques were applied in this work to investigate two different volcanological problems, both crucial for a proper hazard assessment, i.e. 1) to date the Holocene effusive volcanic eruptions at Tenerife and El Hierro Islands (Canary Islands), and 2) to estimate the emplacement temperature and investigate the origin of pyroclastic flows that occurred in June 2018 at El Fuego Volcano (Guatemala).

1) The use of palaeomagnetism in active volcanoes such as Tenerife and El Hierro Islands, in the Canary Islands, helped to better detail the Holocene volcanic history, which is fundamental to understand how volcanic systems operate, and to elaborate more realistic scenarios for future eruptive activity, including the eruption type, intensity, and frequency. At Tenerife and El Hierro (Canary Islands), the palaeomagnetic method applied on large lava flows was useful to determine the eruption age interval, in most cases with higher detail than previously determined by stratigraphic constraints and/or by other radiometric methods.

The comparison between the new palaeomagnetic ages and the previous age data (obtained with ^{14}C and K/Ar dating methods) for the eruptions of Abejera Alta, Roques Blancos, Mña Reventada, Boca Cangrejo in Tenerife and Mña del Tesoro, Mña Chamuscada and Lomo Negro in El Hierro, point out that, for three of them (Boca Cangrejo, Mña Reventada and Lomo Negro), the different dating methods yield comparable results, whereas for the remaining eruptions (Abejera Alta, Roques Blancos and Mña del Tesoro, Mña Chamuscada), they produced significantly different ages. This highlights that the use and comparison between different dating methods is often necessary to get reliable eruption ages. Palaeomagnetic results for eruptions of Tenerife that were only stratigraphically constrained (Pico Cabras, Mña Bilma, Mña Botija, Mña Cascajo) produced much narrower age ranges than those previously available. In one case, palaeomagnetic dating allowed constraining with high accuracy (789-723 BC) the age of Mña Grande eruption, adding this event to the list of the Holocene eruptions of Tenerife. Results of El Hierro show that several Holocene eruptions

occurred in the three rift zones of the island, prevalently concentrated during the last few thousands of years and clustered from ~2000 BC to ~1500 AD. However, the absence of previous age data or geological information for most of the studied eruptions, made many possible ages. Further investigations are thus necessary to build a solid chronological reconstruction of the Holocene volcanic activity.

These data highlight the need for a re-assessment of the volcanic hazards, especially along the east coast of Tenerife, which is very close to the locality where one of the last eruptions occurred (the Arafo Eruption in 1706 AD), and on El Hierro, where few studies on the Holocene volcanic activity have been carried out.

Considering the whole archipelago of the Canary Islands and only the historic period (the last 500 years) approximately fifteen eruptions occurred, some of which almost simultaneously, with an average of three eruptions/100 year. Most of these eruptions occurred along rift zones and outside central edifices, in areas that are now densely inhabited. If similar eruptions took place today, the urbanized and industrialized affected areas would be very large.

The data presented in this work further confirm the relevance of the volcanic hazard at the scale of individual islands of Tenerife and El Hierro but also at the scale of the whole Canarian volcanic system. Both the regional scientific authorities engaged in volcano monitoring and eruption forecasting and the regional operational civil protection authority responsible for emergency planning should thus pay appropriate attention to this issue, developing in peacetime the necessary tools and procedures to be ready to respond effectively in case a volcano crisis occurs.

2) Palaeomagnetism is one of the best tools to estimate the emplacement temperatures of pyroclastic flows, helping to quantify risks for regional assessments. Moreover, it is a valuable tool to investigate the formation mechanism of peculiar pyroclastic flows. The study carried out at El Fuego volcano (Guatemala) showed that the block-and-ash flows of 3rd June 2018 recorded an emplacement temperature of 220-280°C. Palaeomagnetic analyses identified also hot clasts (with 300°C<T<500 °C), that had been stacked near the crater summit area and were remobilized by the retrogressive collapse of the apical portion of the Las Lajas gorge. This mechanism was probably triggered by erosion by the early, vent-derived PDCs and the seismic

shaking during and immediately after the sub-Plinian explosive eruption. In addition to the already known possibility to correlate deposits of ignimbrites and to determine the emplacement temperature of pyroclastic flows, the palaeomagnetic method proves to be powerful also in tracing and quantifying the different processes that contribute to the generation of the materials that form the pyroclastic flows. When appropriately planned, it may permit a better evaluation of surface-embedding processes of materials that may be added to those directly derived from the eruptive process. This mechanism is essential to give more mass and mobility to flows and, generally, to assess the danger of these phenomena.

These new data underline how palaeomagnetism, still poorly used in volcanology, represents a valuable technique for the study of volcanological issues. This thesis contributes to further extend the vast potential that paleomagnetic studies have for solving a great variety of volcanological challenges, and the results achieved are promising and confirm that their increasing use in volcanology is desirable.

APPENDIX I

Palaeomagnetic dating

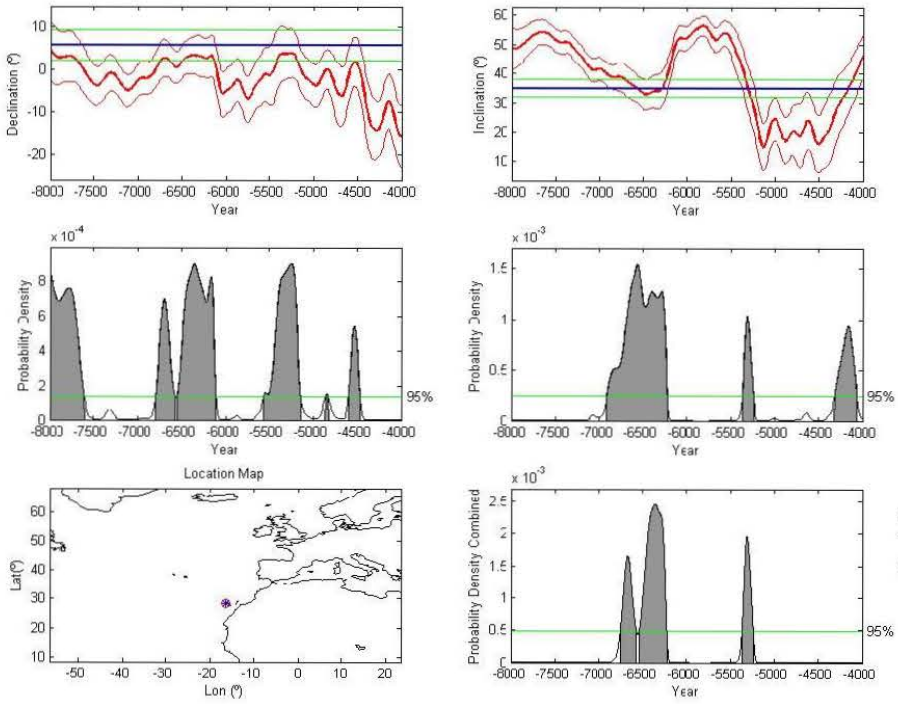

Dating : PICO CABRAS TE\30-32 samples

Combining Probability Density Functiors

Threshold = 0.00048363 (Confidence = 95%)

Between t = 8000BC and 4000BC

[6753BC 6571BC]

[6540BC 6228BC]

[5368BC 5241BC]

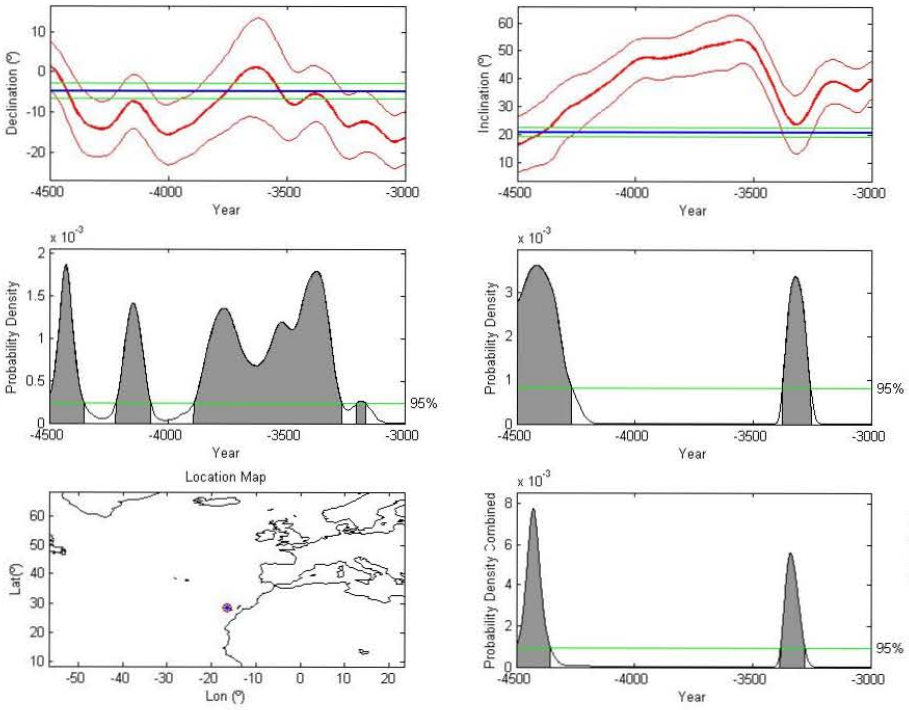

Dating : ABEJERA ALTA samples

Combining Probability Density Functions

Threshold = 0.0009232 (Confidence = 95%)

Between t = 4500BC and 3000BC

[4500BC 4356BC]

[3382BC 3279BC]

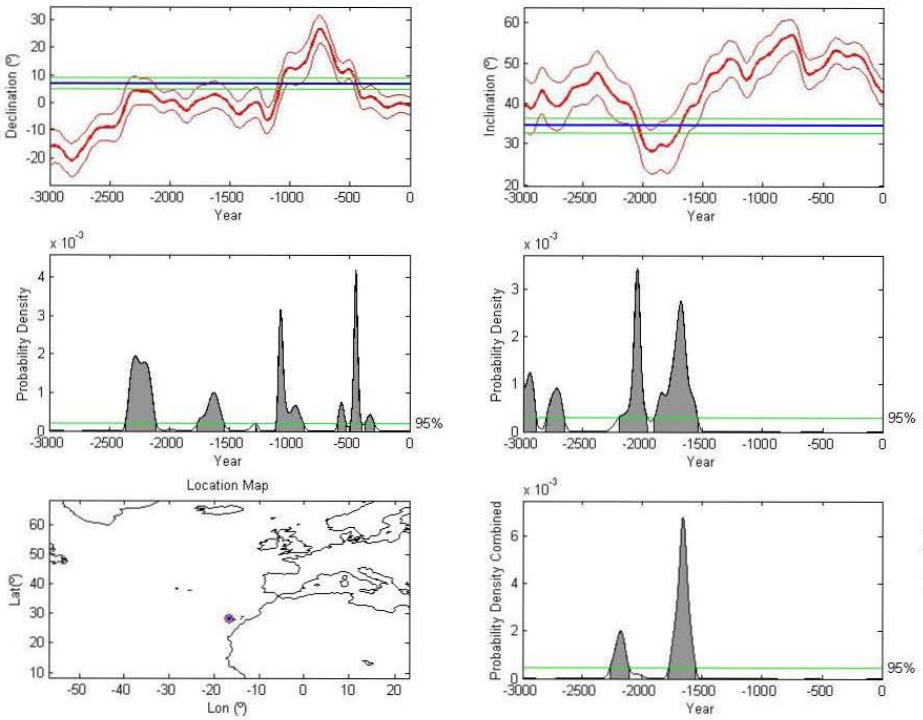

Dating : BOTIJA samples
Combining Probability Density Functions
Threshold = 0.0004689 (Confidence = 95%)
Between t = 3000BC and 0AD
[2267BC 2109BC]
[1777BC 1550BC]

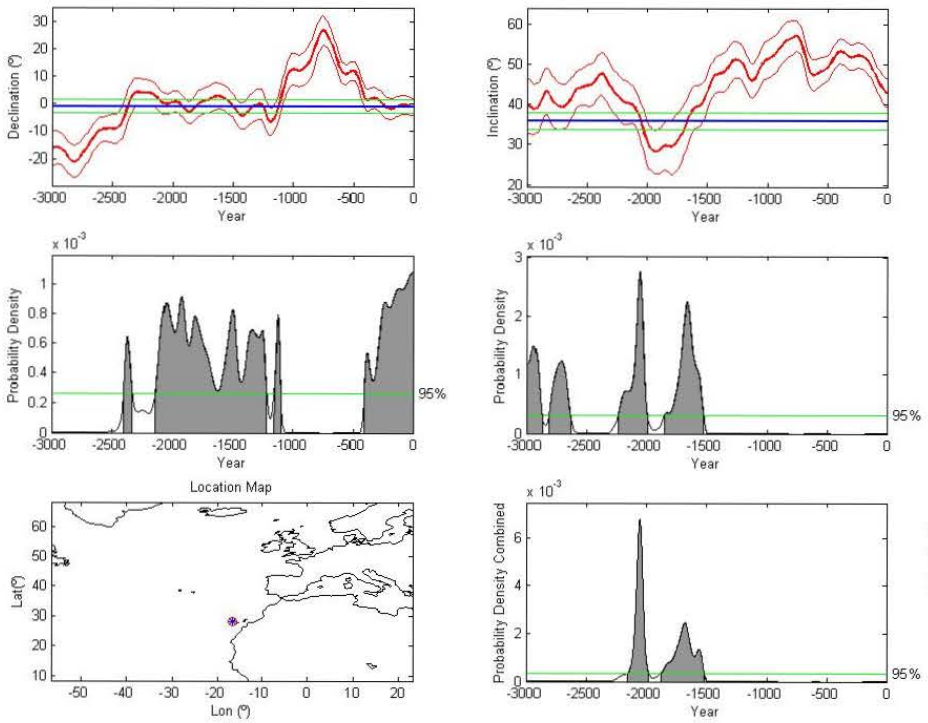

Dating : CASCAJO samples
Combining Probability Density Functions
Threshold = 0.00033311 (Confidence = 95%)
Between t = 3000BC and 0AD
[2159BC 1981BC]
[1879BC 1516BC]

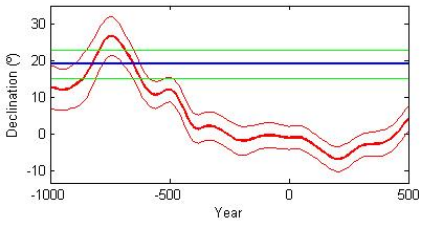

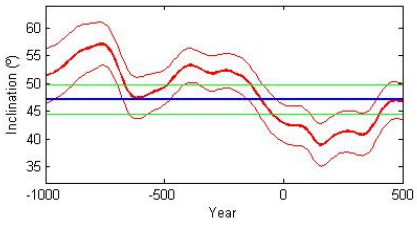

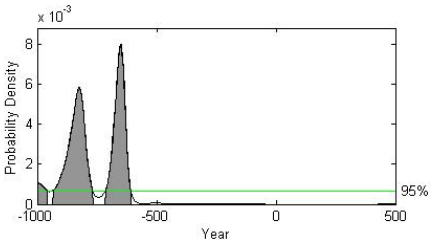

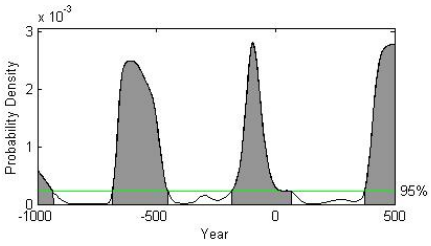

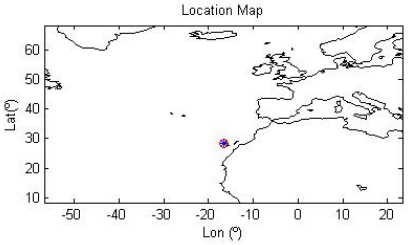

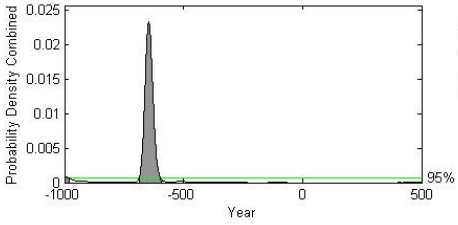

Dating : ROQUES BLANCOS samples

Combining Probability Density Functions

Threshold = 0.00063099 (Confidence = 95%)

Between t = 1000BC and 500AD

[1000BC 981BC]

[686BC 596BC]

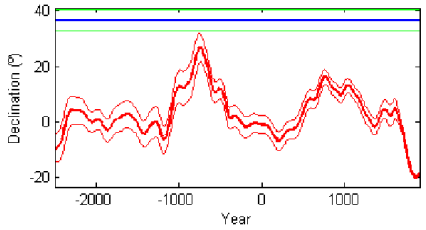

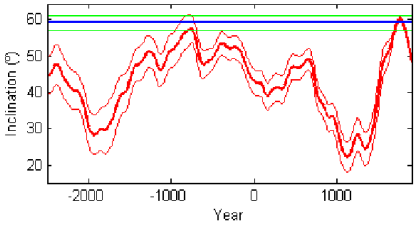

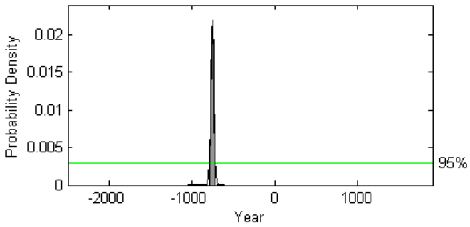

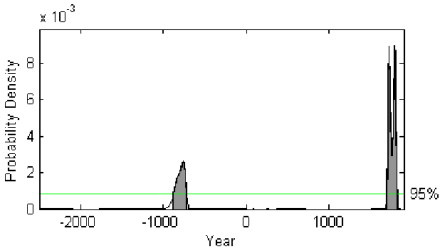

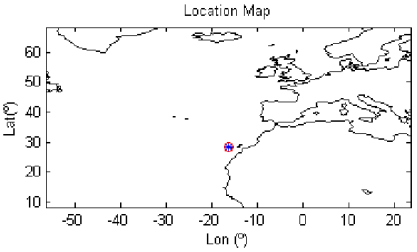

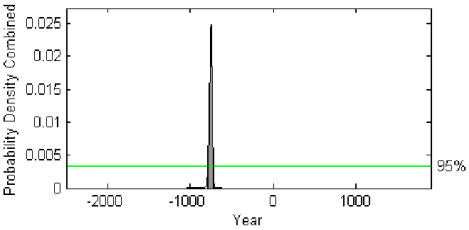

Dating : Mna Grande

Combining Probability Density Functions

Threshold = 0.003404 (Confidence = 95%)

Between t = 2500BC and 1900AD

[789BC 725BC]

^{14}C dating

Marine shells under Mña Grande lavas

BetaCal 3.21

Calibration of Radiocarbon Age to Calendar Years

(highest probability ranges: MARINE13)

(Variables: d13C = +4.0 o/oo : Delta-R = 114 ± 30 : Glob res = -200 to 500)

Laboratory number **Beta-513848**

Conventional radiocarbon age **4200 ± 30 BP**

4086 ± 42 Adjusted for local reservoir correction

95.4% probability

(95.4%) 2316 - 2030 cal BC (4265 - 3979 cal BP)

68.2% probability

(68.2%) 2259 - 2120 cal BC (4208 - 4069 cal BP)

GUIM_PLA_1

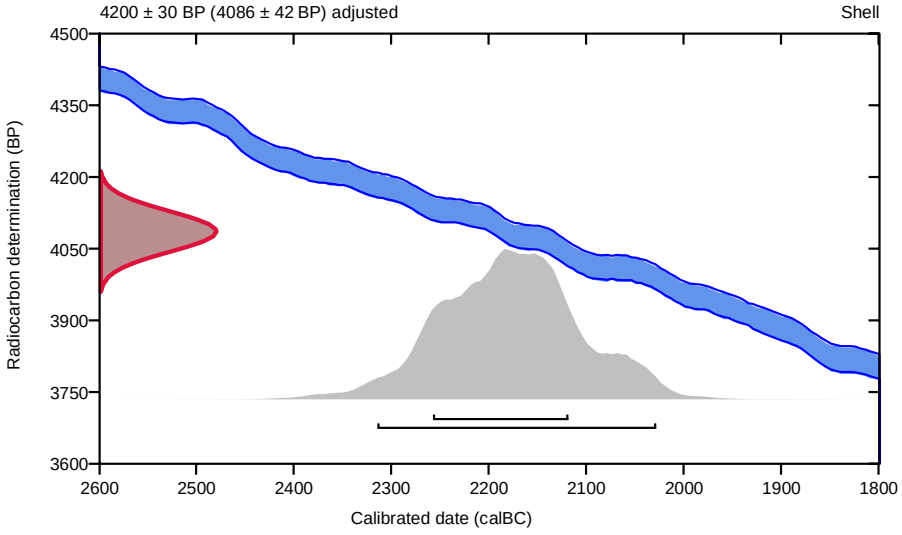

Database used

MARINE13

References

References to Probability Method

Bronk Ramsey, C. (2009). Bayesian analysis of radiocarbon dates. Radiocarbon, 51(1), 337-360.

References to Database MARINE13

Reimer, et.al., 2013, Radiocarbon 55(4).

Beta Analytic Radiocarbon Dating Laboratory
4985 S.W. 74th Court, Miami, Florida 33155 • Tel: (305)667-5167 • Fax: (305)663-0964 • Email: beta@radiocarbon.com

APPENDIX II

Palaeomagnetic dating

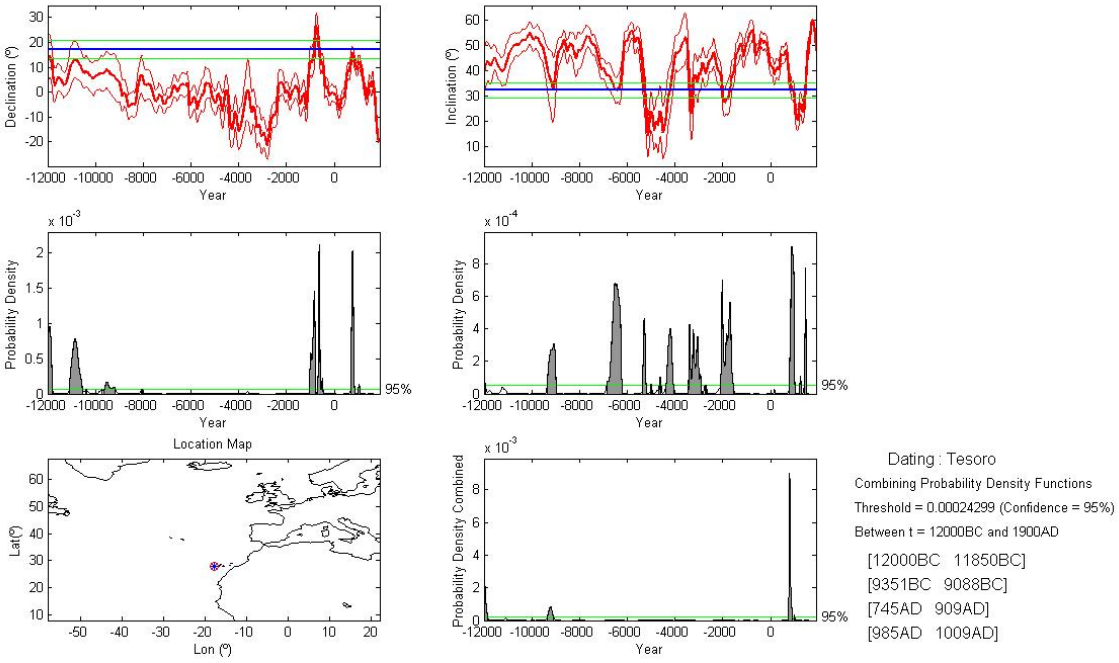

Dating : Tesoro

Combining Probability Density Functions

Threshold = 0.00024299 (Confidence = 95%)

Between t = 12000BC and 1900AD

[12000BC 11850BC]
[9351BC 9088BC]
[745AD 909AD]
[985AD 1009AD]

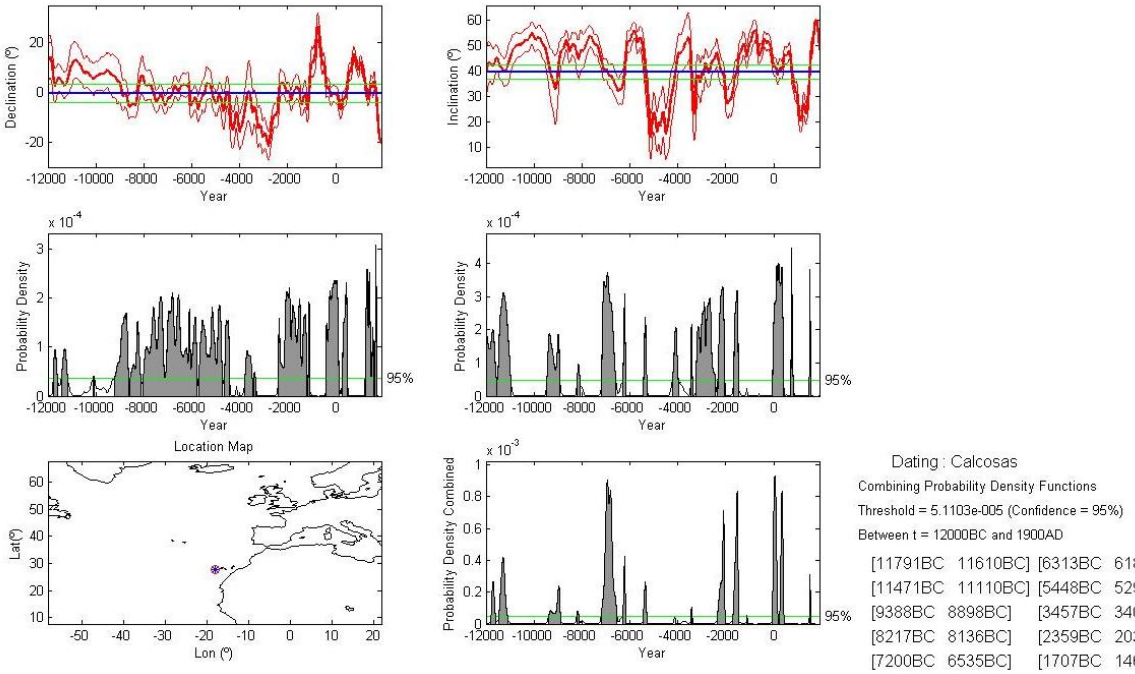

Dating : Calcosas

Combining Probability Density Functions

Threshold = 5.1103e-005 (Confidence = 95%)

Between t = 12000BC and 1900AD

[11791BC 11610BC] [6313BC 6181BC] [1123BC 1116BC]
[11471BC 11110BC] [5448BC 5295BC] [71BC 168AD]
[9388BC 8898BC] [3457BC 3402BC] [236AD 418AD]
[8217BC 8136BC] [2359BC 2035BC] [1480AD 1532AD]
[7200BC 6535BC] [1707BC 1464BC]

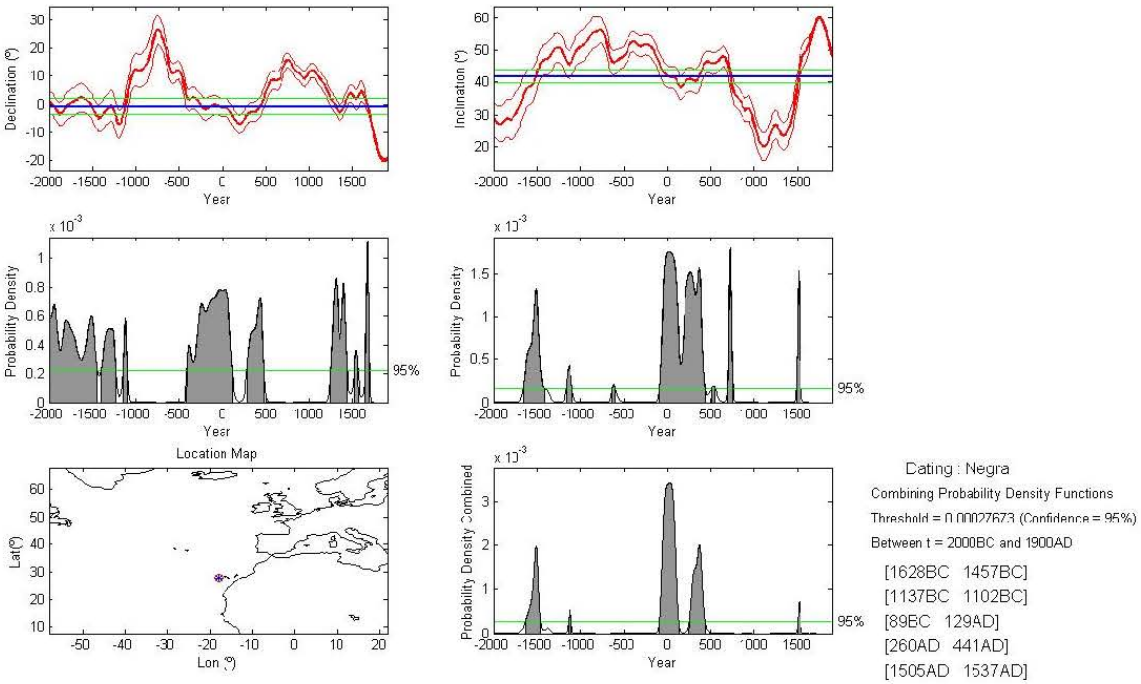
Declination (°)
Year
Inclination (°)
Year
x 10^-3
Probability Density
95%
Year
x 10^-3
Probability Density
95%
Year
Location Map
Lat(°)
Lon (°)
x 10^-3
Probability Density Combined
95%
Year
Dating : Negra
Combining Probability Density Functions
Threshold = 0.0002673 (Confidence = 95%)
Between t = 2000BC and 1900AD
[1628BC 1457BC]
[1137BC 1102BC]
[89BC 129AD]
[260AD 441AD]
[1505AD 1537AD]

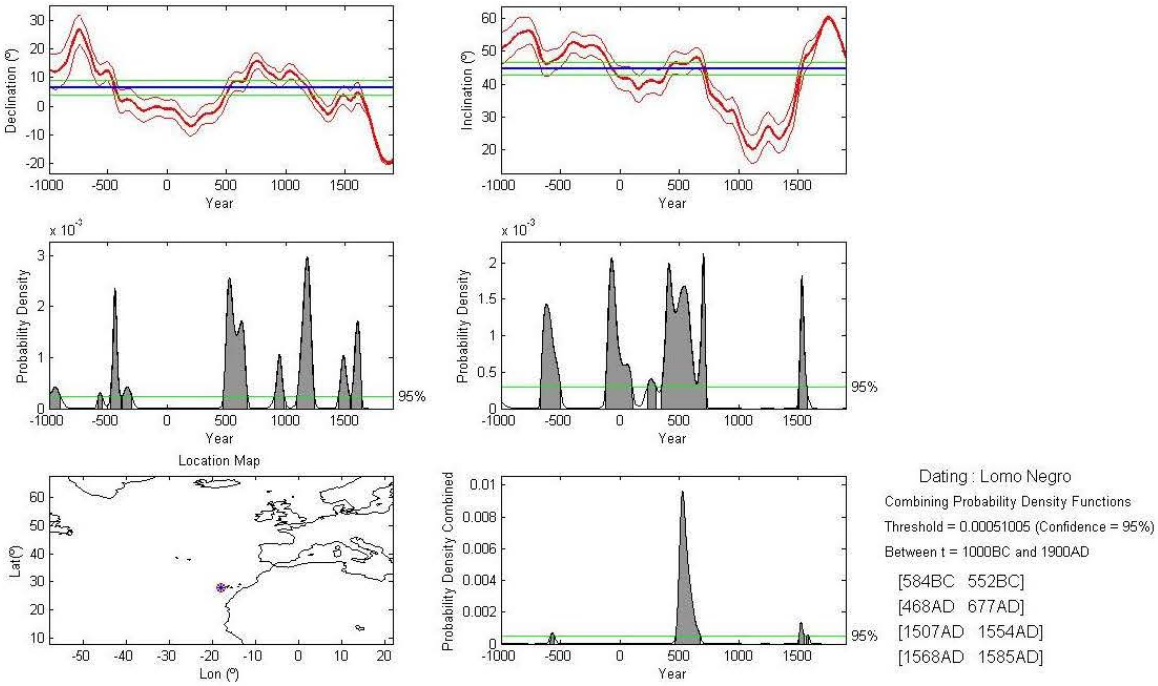
Declination (°)
Year
Inclination (°)
Year
x 10^-3
Probability Density
95%
Year
x 10^-3
Probability Density
95%
Year
Location Map
Lat(°)
Lon (°)
Probability Density Combined
95%
Year
Dating : Lomo Negro
Combining Probability Density Functions
Threshold = 0.00051005 (Confidence = 95%)
Between t = 1000BC and 1900AD
[584BC 552BC]
[468AD 677AD]
[1507AD 1554AD]
[1568AD 1585AD]

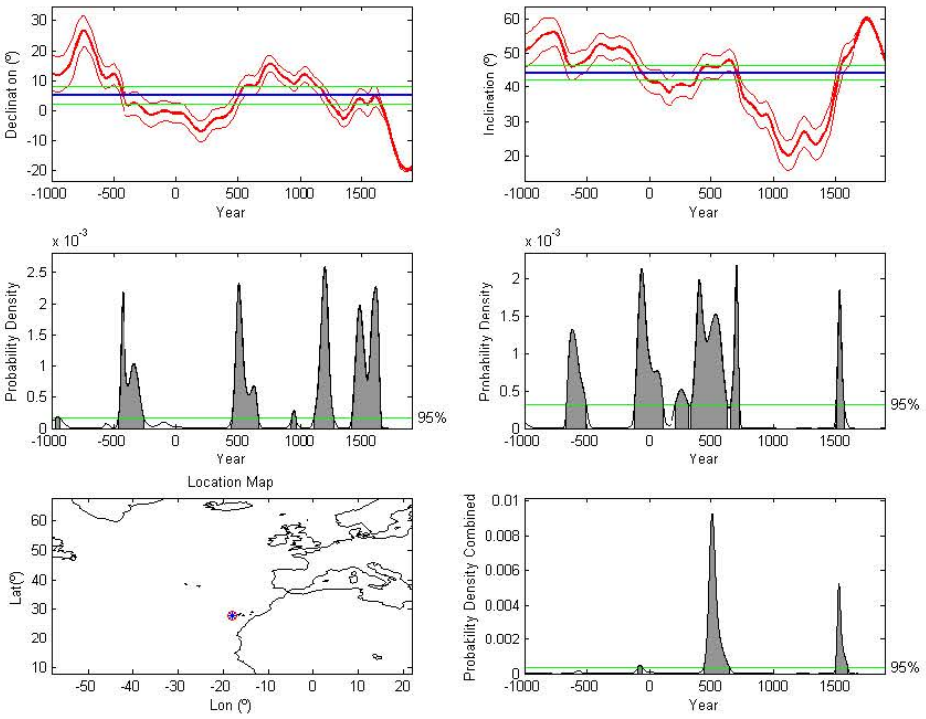

Dating : LOMO NEGRO all
Combining Probability Density Functions
Threshold = 0.00037977 (Confidence = 95%)
Between t = 1000BC and 1900AD
[92BC 57BC]
[443AD 649AD]
[1498AD 1595AD]

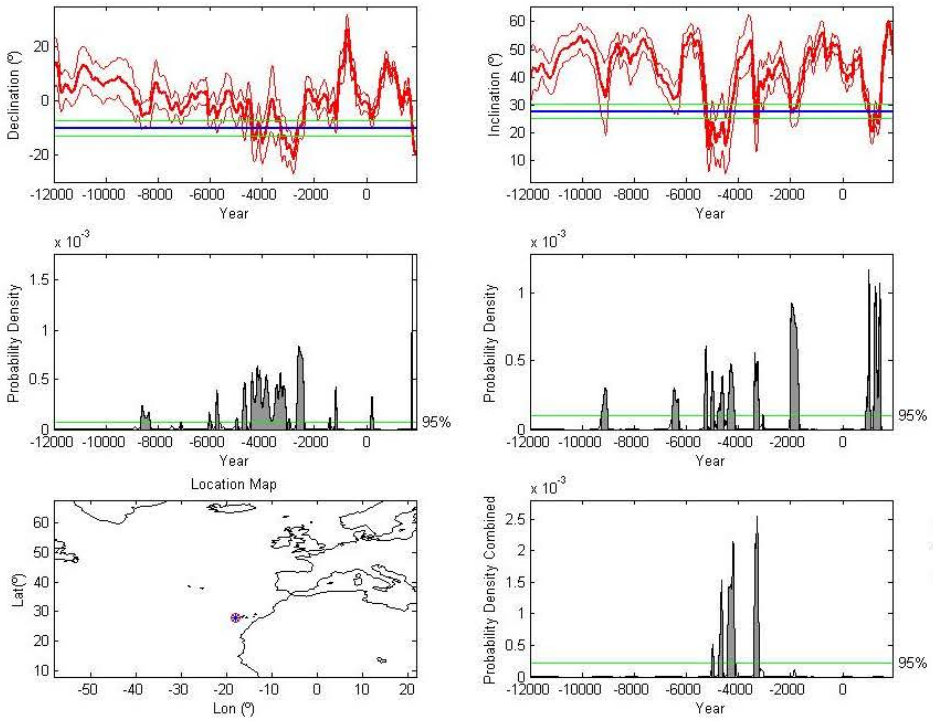

Dating : Under Lomo Negro
Combining Probability Density Functions
Threshold = 0.00022661 (Confidence = 95%)
Between t = 12000BC and 1900AD
[5031BC 4958BC]
[4764BC 4598BC]
[4437BC 4120BC]
[3420BC 3198BC]

^{14}C dating

Charchoal found under a lapilli outcrop of Mña Chamuscada

BetaCal 3.9

Calibration of Radiocarbon Age to Calendar Years

(High Probability Density Range Method (HPD): INTCAL13)

(Variables: d13C = -24.0 o/oo)

Laboratory number **Beta-480840**

Conventional radiocarbon age **3410 ± 30 BP**

95.4% probability

(93.1%)	1773 - 1627 cal BC	(3722 - 3576 cal BP)
(2.3%)	1865 - 1849 cal BC	(3814 - 3798 cal BP)

68.2% probability

(68.2%)	1746 - 1665 cal BC	(3695 - 3614 cal BP)

Cham_Casas

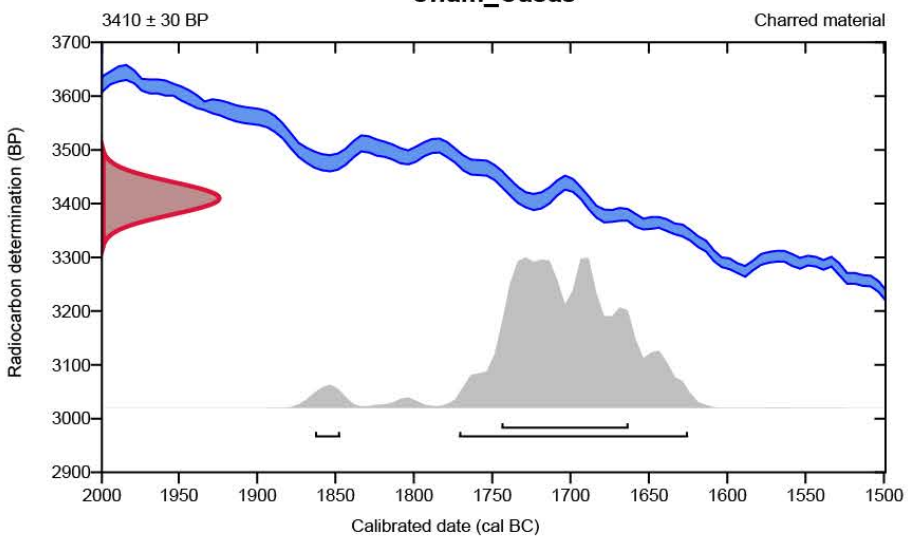

Database used

INTCAL13

References

References to Probability Method

Bronk Ramsey, C. (2009). Bayesian analysis of radiocarbon dates. Radiocarbon, 51(1), 337-360.

References to Database INTCAL13

Reimer, et.al., 2013, Radiocarbon55(4).

Beta Analytic Radiocarbon Dating Laboratory
4985 S.W. 74th Court, Miami, Florida 33155 • Tel: (305)667-5167 • Fax: (305)663-0964 • Email: beta@radiocarbon.com

Charchoal found within Mña Chamuscada lavas

BetaCal 3.9

Calibration of Radiocarbon Age to Calendar Years

(High Probability Density Range Method (HPD): INTCAL13)

(Variables: d13C = -23.9 o/oo)

Laboratory number **Beta-480839**

Conventional radiocarbon age **320 ± 30 BP**

95.4% probability

(95.4%) 1482 - 1646 cal AD (468 - 304 cal BP)

68.2% probability

(53.5%) 1518 - 1594 cal AD (432 - 356 cal BP)
(14.7%) 1618 - 1640 cal AD (332 - 310 cal BP)

Cham_Tronco

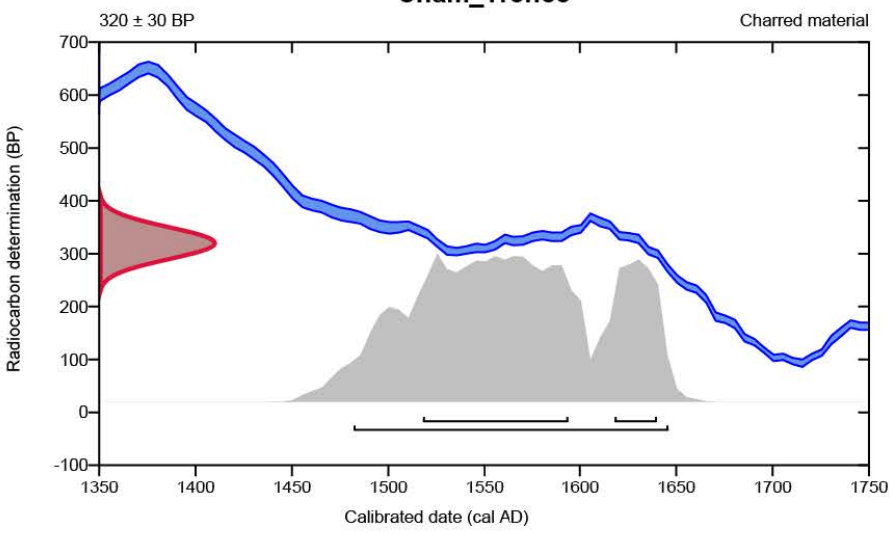

Database used

INTCAL13

References

References to Probability Method

Bronk Ramsey, C. (2009). Bayesian analysis of radiocarbon dates. Radiocarbon, 51(1), 337-360.

References to Database INTCAL13

Reimer, et.al., 2013, Radiocarbon55(4).

Beta Analytic Radiocarbon Dating Laboratory
4985 S.W. 74th Court, Miami, Florida 33155 • Tel: (305)667-5167 • Fax: (305)663-0964 • Email: beta@radiocarbon.com

Charchoal found within Lomo Negro lavas

BetaCal 3.9

Calibration of Radiocarbon Age to Calendar Years

(High Probability Density Range Method (HPD): INTCAL13)

(Variables: d13C = -22.6 o/oo)

Laboratory number **Beta-480841**

Conventional radiocarbon age **380 ± 30 BP**

95.4% probability

(61.6%)	1445 - 1524 cal AD	(505 - 426 cal BP)
(33.8%)	1558 - 1632 cal AD	(392 - 318 cal BP)

68.2% probability

(53.8%)	1450 - 1514 cal AD	(500 - 436 cal BP)
(14.4%)	1600 - 1617 cal AD	(350 - 333 cal BP)

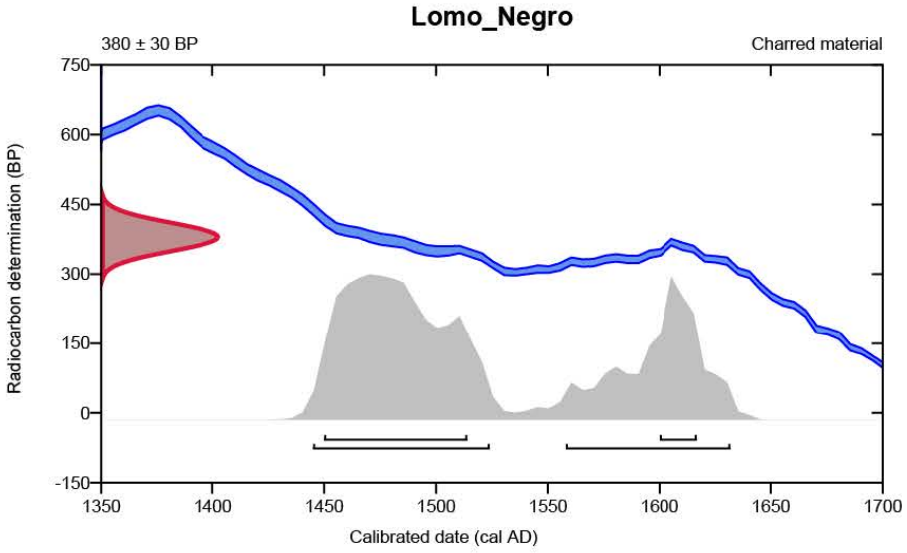

Database used

INTCAL13

References

References to Probability Method

Bronk Ramsey, C. (2009). Bayesian analysis of radiocarbon dates. Radiocarbon, 51(1), 337-360.

References to Database INTCAL13

Reimer, et.al., 2013, Radiocarbon55(4).

Beta Analytic Radiocarbon Dating Laboratory

4985 S.W. 74th Court, Miami, Florida 33155 • Tel: (305)667-5167 • Fax: (305)663-0964 • Email: beta@radiocarbon.com

APPENDIX III

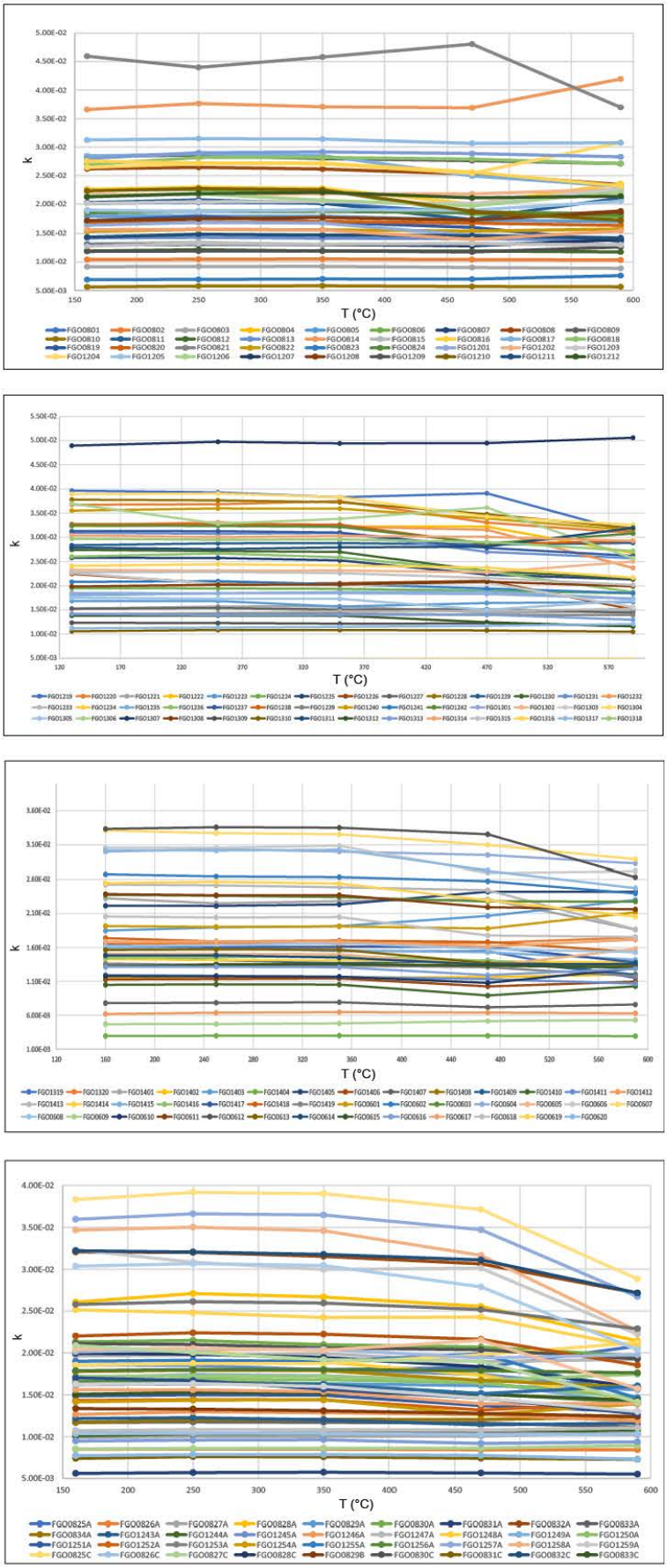

SF1. Variation of magnetic susceptibility for each sample after each heating step. k is the magnetic susceptibility and T is the temperature (°C).

Acknowledgments

(la parte più difficile di questa tesi)

Non pensavo di arrivare a questo punto, e invece eccomi qui.
Questa tesi non è solo un lungo testo, e spero non troppo difficile da leggere, composto da circa 270 pagine. È il frutto di tre anni di duro lavoro e impegno, e il risultato di un percorso costellato da molteplici e difficili sfide, professionali ma soprattutto personali. Non è stato facile cominciarlo, e ancor meno proseguirlo.
Il dottorato è, a mio avviso, una delle esperienze più formanti della vita; dovrebbero, però, cambiarne il nome in uno più simile al concetto di *metamorfosi*.
Perché il dottorato, se fatto bene, deve cambiarti. Deve prendere tutto ciò che sei e stravolgerlo. E il cambiamento, il più delle volte, può far male. Deve farti uscire dalla tua comfort-zone e gettarti nel buio. È un percorso che trasforma ciò che eri in ciò che sarai, da un semplice studente…in (si spera) un Ricercatore. E lo fa in ogni modo possibile, con forza, aggressività e brutalità.
Ciò che sicuramente ho compreso nel corso di tutti questi anni universitari è che il mondo scientifico basa tutto *sull'errore*. Quando si fa un esperimento, si deve trovare la giusta combinazione tra tutte le variabili, si devono cioè escludere uno alla volta tutti quei valori sbagliati che non porteranno alla soluzione dell'equazione.
E come fare a capire se un valore, un dato, e perfino e un'idea sono sbagliati?
Si deve necessariamente sbagliare. Sbagliare una, dieci, mille volte prima di trovare il giusto equilibrio, la giusta soluzione, la strada da percorrere.
Quindi prima di tutto, si deve *accettare* di sbagliare. Si deve accettare di non essere perfetti, di non avere sempre la soluzione, e di aver completamente sbagliato strada. Si devono accettare ed ammettere i propri limiti davanti al mondo intero, e in primis a sé stessi. E si deve avere la capacità, la voglia e la forza di *continuare e riprovare*, probabilmente sbagliando nuovamente.
Questi tre anni sono stati per me molto difficili: come continuare a seguire una strada se si inizia a dubitare di essa? Come continuare a credere che la soluzione sia in fondo, anche se non si vede?
Continuando.
Devo, quindi ringraziare una persona: me. Ringrazio me stessa per aver continuato; per essere stata testarda, per non essermi arresa, pur dubitando ferocemente di me stessa, delle mie abilità, delle mie capacità di giudizio, delle mie decisioni, pur sentendomi continuamente inadeguata, sbagliata, insufficiente, fuori posto. Ringrazio me stessa per non essermi arresa anche quando era facile farlo.
Tuttavia, non avrei mai potuto fare nulla di tutto ciò senza il sostegno e l'aiuto di alcune persone, poche ma di elevatissima qualità, che mi hanno permesso di arrivare fin qui. Ognuna di esse ha contribuito ad arricchire, direttamente e non, il mio percorso scientifico, lavorativo e soprattutto personale.
In questi anni, ho avuto il privilegio di lavorare con Ricercatori e Professori di altissimo livello, che hanno accresciuto il mio bagaglio culturale in modo straordinario. Desidero ringraziare tutto il "team" dei miei "tutors", ufficiali e non, che si sono rivelati più che semplici guide e che mi hanno scortato e supportato nel fantastico (e terribile) mondo della Ricerca. Ringrazio il Prof. Rosi, per avermi dato l'onore di essere la sua "ultima" dottoranda; il Prof. Marco Pistolesi, un imprevedibile amico e una splendida persona con cui chiacchierare e confrontarsi, fonte di preziosi consigli; la Dott.ssa Paola del Carlo, in grado di regalarmi sempre un sorriso e la grinta necessaria per affrontare tutte le difficoltà che si sono poste davanti al mio percorso; i Dott. Alessio Di Roberto e Massimo Pompilio, con quali ho potuto condividere una delle più belle campagne fatte sin ora. Desidero ringraziare il Dott. Stavros Meletlidis, per il suo fondamentale aiuto sul campo e per la sua innata simpatia, che hanno reso il lavoro svolto durante le campagne di campionamento alle Canarie una bellissima esperienza.
Infine, ma mai ultimi, devo ringraziare il Dott. Fabio Speranza e (come sempre e per sempre) il Prof. Rotolo, senza i quali non avrei mai cominciato questo percorso, ai quali devo ogni singolo risultato raggiunto sino ad oggi.
Voglio ringraziare anche i miei colleghi "paleomagnetisti": Arianna, Andrea, Alessandro e Gaia, con i quali è stato sempre un piacere confrontarsi e aiutarsi.

Desidero ringraziare tutte quelle persone che mi hanno supportato, ascoltato, incoraggiato, sostenuto più di quanto avrei mai potuto immaginare, e che mi hanno aiutato a focalizzarmi sull'obiettivo, a vedere in me stessa quello che spesso, ancora adesso, continuo a non vedere.
Mi hanno aiutato a vedere sempre il lato positivo, anche quando questo voleva dire andare via da casa e ambientarsi nuovamente in una nuova città e ripartire da zero. Voglio ringraziare le meravigliose coinquiline che ho avuto la fortuna di incontrare, quelle che la sera, stanca e distrutta, mi hanno sempre strappato, anche con forza, un sorriso. Ringrazio Silvia e Valentina, che hanno reso il mio arrivo a Pisa un po' meno traumatico e solitario; Nicole, Alisea, Giusy, Marica R. che in pochissimo tempo mi hanno accolto come una di loro a Roma. Ringrazio Brigida, che con la sua incredibile forza e gioia di vivere mi ha strappato giorno dopo giorno da quella stanzetta microscopica per riportarmi alla "vita vera".
Ringrazio i miei colleghi, tutti quanti: Simone C., Alessandro, Fabrizio, Luca, Diego, Simone V., Duccio, ed in particolare Irene e Marica (che dovrei, a onor del vero, inserire tra le mie amiche ormai!), per avermi accolto come una di voi, e avere condiviso gioie e dolori di questo dottorato. E ringrazio anche Silas e Martjin, per aver sopportato il mio maccheronico inglese. Anzi più che ringraziarvi, mi scuso, che è meglio.
Devo ringraziare poi le mie sorelle: Roberta, Mariangela, Vanessa e Cecilia. Voi siete sempre il punto d'appoggio quando sto per cadere, la mano che ho afferrato e afferro ogni volta nel buio, quella costante che aggiusta tutte le equazioni.
Voglio ringraziare mio "cognato" Simone, che più di tutti mi ha insegnato che, a prescindere dalle difficoltà della vita, si possono sempre superare i propri limiti e dare il meglio di sé, per ritornare a splendere.

Voglio e devo poi ringraziare una *Persona*, l'unica che più di tutti merita tutta la mia riconoscenza.
Te, Francesco, che da quando sei entrato nella mia vita l'hai riempita di tutto quello di cui era sempre stata priva; l'hai pervasa di allegria, gioia e felicità, ridandomi *luce*.
Te, che mi sei stato vicino sempre; che mi hai spronato a dare in ogni occasione, e a qualsiasi costo, il meglio di me, mostrandomi per ciò che *sono;* che mi hai *rimproverato* quando pensavo di non farcela e mi hai incoraggiato e sostenuto nei momenti di difficoltà, ricordandomi, anche quotidianamente, tutti i motivi per cui ho intrapreso questo cammino.
Te, che sei stato in grado di ridarmi il sorriso anche quando in me c'erano solo lacrime. Te, che hai visto tutte le mie debolezze, e mi hai costretto ad accettarle e trasformarle in punti di forza. Te, che hai accettato tutti i miei cambiamenti, comprendendoli e rassicurandomi.
Te, che non c'è stato giorno in cui non ti ho sentito vicino, nonostante la continua, maledetta distanza che ci ha separato in questi anni, e nonostante tutte le difficoltà e i momenti difficili che la vita ci ha messo davanti.
Te, che non ti sei mai stancato e mai abituato davanti a quella distanza che ci ha diviso.
Te, che anche quando ero una barca in mezzo alla tempesta, strattonata dai venti di burrasca e a un passo dal ribaltarmi, mi hai dato stabilità, e mi hai guidato a casa come un *faro sulla terraferma.*
Te, che a prescindere dalle strade che seguiranno le nostre vite,
sei stato e sarai sempre parte della *mia metamorfosi*.